

**A HETEROGENEOUS MULTIRATE SIMULATION
APPROACH FOR WIDE-BANDGAP-BASED ELECTRIC
DRIVE SYSTEMS**

by

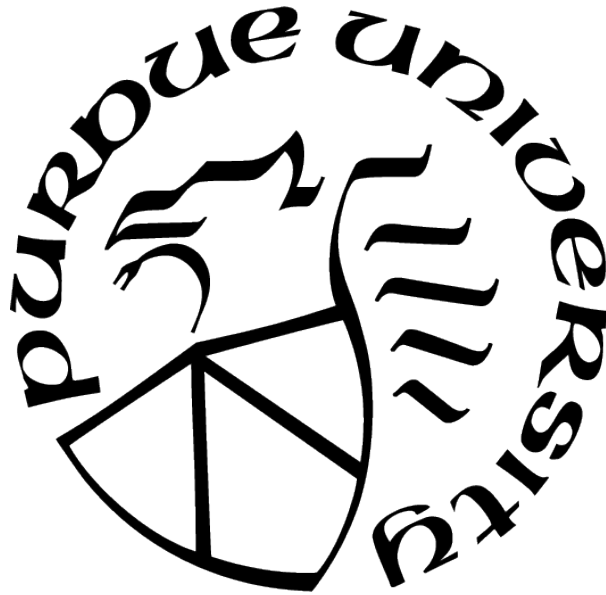
Olatunji T. Fulani

A Dissertation

Submitted to the Faculty of Purdue University

In Partial Fulfillment of the Requirements for the degree of

Doctor of Philosophy



School of Electrical and Computer Engineering

West Lafayette, Indiana

August 2021

**THE PURDUE UNIVERSITY GRADUATE SCHOOL
STATEMENT OF COMMITTEE APPROVAL**

Dr. Oleg Wasynczuk, Chair

School of Electrical and Computer Engineering

Dr. Dallas Morisette

School of Electrical and Computer Engineering

Dr. Dionysios C. Aliprantis

School of Electrical and Computer Engineering

Dr. Steven D. Pekarek

School of Electrical and Computer Engineering

Approved by:

Dr. Dimitri Peroulis

Head of the School of Electrical and Computer Engineering

To Mummy Ajayi.

ACKNOWLEDGMENTS

Several people played pivotal roles towards the conclusion of my graduate studies at Purdue. I would like to acknowledge them for their support. First, there is my major advisor, Professor Oleg Wasynczuk, whose insight in research and technology is a constant inspiration. He first introduced and guided me through the obscure paths of research. I will continue to treasure his care and support through my studies at Purdue. I would also like to thank Professors Aliprantis, Morisette, and Pekarek for their insightful comments and invaluable inputs in my research.

Special thanks to Tom Craddock, a great friend who, as a grad student, was a co-laborer in this work. Thanks to Dr. Minyu Cai, whose initial efforts were the foundation for this work. Tim Donnelly was kind enough to allow me to pick his brain and engage him on numerous occasions; I am privileged to call him a friend. I am also grateful for the never-ending support I received from friends and fellow graduate students. Words fail me to tell of Emily, Jeff, Horane, Tobi, Jaron, Ibukun, Derrick, Andrew, Samantha, Marquette, Danae, Thembi, Olamide, and Purdue Chi Alpha. They were part of different *kairos* moments during my studies.

Finally, I would like to thank my family; my lovely wife Jerica for her encouragement and patience when I burned the midnight oil; mummy Ajayi, whose wings have covered me since my dad went home to be with the Lord; my brother Tolu for his unflinching support; my big brothers Dele, Segun, and Sola for challenging me to leave my comfort zone and being the greatest influence in my education; my big sister Funmi and husband Biodun for always reaching out and believing in me; my big sister Sola and husband Wale for always putting up with me despite my quiriness; Tina, Dami Ajayi, and Dami for becoming my sisters and encouraging me; my sister Isioma for her support and laughter. I have been fortunate to have them cheer me on to the finish.

TABLE OF CONTENTS

LIST OF TABLES	8
LIST OF FIGURES	9
ABBREVIATIONS	14
ABSTRACT	15
1 BACKGROUND AND OBJECTIVES	16
1.1 Literature Review	17
1.2 Motivation and Objectives	23
1.3 Thesis Outline	25
2 ELECTRIC MACHINE MODELING AND PARAMETERIZATION	27
2.1 Low-Frequency Model	27
2.2 Determination of the Low-Frequency Parameters	33
2.3 Limitations of the Low-Frequency Model	42
2.4 Wideband Model	43
2.5 Parameterization of Wideband Model	44
2.6 Complete Large-Displacement Wideband Model	52
2.7 Modal Frequencies of the Wideband Model	53
2.8 Alternative Formulation of the Wideband Model	58
2.9 Summary	66

3	WIDEBAND INVERTER MODEL AND PARAMETERIZATION	68
3.1	Inverter Phase Leg	68
3.2	MOSFET Model Parameters	72
3.3	Source Model	76
3.4	Characterization of Source Model	77
3.5	Validation of Source Model Parameters	83
3.6	Summary	84
4	ELECTRIC DRIVE SYSTEM SIMULATION	85
4.1	Experimental Study of Electric Drive System	85
4.2	MNA-based Simulation of Wideband Model	88
4.3	State-space-based Simulation of Wideband Model	96
4.4	The Computational Cost of Simulation and the Stiffness Problem	100
4.5	Sparse Tableau Formulation of System Model	102
4.6	Summary	111
5	NEW HETEROGENEOUS MULTIRATE SIMULATION STRATEGY	113
5.1	The Low-frequency Model	113
5.2	Simulation of Low-frequency Model	120
5.3	The High-frequency Model	124
5.4	Simulation of High-frequency Model	126
5.5	High-frequency Transients with Machine Ground Wire Disconnected	133

5.6	Summary	133
6	COMPARISON OF MEASURED AND SIMULATED HIGH-FREQUENCY TRANSIENTS	136
6.1	Switching Transients of Inverter Test Circuit	136
6.2	Switching Transients of Electric Drive System	145
6.3	Summary	151
7	FINAL RESULTS, CONCLUSIONS, AND AREAS OF POTENTIAL FURTHER RESEARCH	152
7.1	Review of Prior Results	153
7.2	Combining Results of Low- and High-frequency Models	154
7.3	Example Study: Evaluation of Conduction and Switching Losses for Rated Operating Conditions	170
7.4	Conclusions	173
7.5	Areas of Future Research	173
	REFERENCES	175
A	MNA-BASED SIMULATION OF THE ELECTRIC DRIVE SYSTEM	182
	VITA	185

LIST OF TABLES

2.1	Low-frequency model parameters.	39
2.2	Open-circuit characterization results.	41
2.3	DM equivalent circuit parameters.	50
2.4	CM equivalent circuit parameters.	51
2.5	Frequency modes of the DM circuit.	56
2.6	Frequency modes of the CM circuit.	58
2.7	Low-frequency state model parameters.	61
2.8	Wideband DM state model parameters.	63
2.9	Wideband CM state model parameters.	65
3.1	SiC MOSFET parameters.	76
3.2	Parameters in segment c - P - N - f	79
3.3	Parameters in segment b - c - f - e	80
3.4	Parameters in segment a - b - e - d	82
4.1	Steady-state operating-point values.	87
4.2	MNA simulation statistics.	93
4.3	State-space simulation statistics.	97
5.1	Simulation statistics using low-frequency model.	122
6.1	Simulated results of phase leg turn-on event.	141
6.2	Results from phase leg turn-on event of inverter test circuit.	144
6.3	Results from turn-on event of a phase leg.	148
7.1	Summary of average power losses and efficiency	173

LIST OF FIGURES

1.1	Typical three-phase inverter topology.	17
1.2	Electric machine drive system.	24
2.1	A two-pole three-phase PMAC machine, adapted from [55]	28
2.2	Low-frequency classical model at a fixed rotor position.	30
2.3	Rotor reference frame equivalent circuits for the classical model.	32
2.4	Rotor reference frame equivalent circuits for the low-frequency model.	34
2.5	DM test circuit for realizing low-frequency parameters.	35
2.6	Measured and fitted low-frequency per-phase impedance of the PMAC machine.	39
2.7	Low-frequency per-phase equivalent circuit of PMAC machine.	40
2.8	Measured and fitted open-circuit voltages.	42
2.9	Calculated low-frequency impedance compared with measured wideband data.	43
2.10	Wideband equivalent circuit.	44
2.11	Test circuit for DM impedance measurement.	45
2.12	Test circuit for CM impedance measurement.	46
2.13	Wideband DM equivalent circuit.	48
2.14	Measured and fitted wideband DM impedance.	49
2.15	Wideband CM equivalent circuit.	50
2.16	Measured and fitted wideband CM impedance.	51
2.17	Complete large-displacement wideband model of the surface-mount PMAC machine.	52
2.18	DM circuit.	54
2.19	CM circuit.	58
2.20	State-space-based wideband model of the PMAC machine and cable.	59
2.21	Measured and fitted low-frequency per-phase impedance using the state-space-based approach.	60
2.22	Block diagram representation of wideband DM state model.	63
2.23	Measured and fitted wideband DM impedance using the state-space-based approach.	64

2.24	Measured and fitted wideband CM impedance using the state-space-based approach.	66
3.1	Equivalent circuit of one phase leg of an inverter.	69
3.2	The MOSFET model, adapted from [60].	70
3.3	MOSFET capacitances versus drain-to-source voltage	73
3.4	Measured and fitted output characteristics, $T_j = 25\text{ }^{\circ}\text{C}$, $v_{gs} = 20\text{ V}$	74
3.5	Cross section of a broken inverter module (all dimensions in millimeters). . .	76
3.6	The inverter with detailed source model.	77
3.7	Test circuit for segment $c\text{-}P\text{-}N\text{-}f$	78
3.8	Measured and fitted impedance of segment $c\text{-}P\text{-}N\text{-}f$	79
3.9	Test circuit for segment $b\text{-}c\text{-}f\text{-}e$	80
3.10	Measured and fitted impedance of segment $b\text{-}c\text{-}f\text{-}e$	81
3.11	Test circuit for segment $a\text{-}b\text{-}e\text{-}d$	82
3.12	Measured and fitted impedance of segment $a\text{-}b\text{-}e\text{-}d$	83
3.13	Calculated source model impedance compared with measured data.	84
4.1	The electric machine drive system.	86
4.2	Block diagram of sine-triangle modulator with third harmonic injection. . . .	87
4.3	Measured phase currents for selected operating point ($d = 1$, $\phi_v = 0.0657\text{ rad}$). .	88
4.4	Measured a -phase current showing multiple time scales.	89
4.5	The SPICE algorithm for transient analysis, adapted from [65].	90
4.6	Top-level LTspice block diagram of the electric machine drive system.	92
4.7	Simulated phase currents using LTspice.	93
4.8	Expanded view of simulated a -phase current.	94
4.9	Simulated phase-to-ground voltage, v_{ag} using LTspice.	94
4.10	Step size taken in MNA-based simulation.	95
4.11	Top-level block diagram of the state-space-based simulation of the system. .	97
4.12	Simulated phase currents using state-space-based approach.	98
4.13	Expanded view of a -phase current.	98
4.14	Simulated phase-to-ground voltage, v_{ag}	99
4.15	Step size taken in state-space-based simulation.	99

4.16	rL circuit.	106
4.17	gC circuit.	107
4.18	(a) Example circuit, (b) directed graph.	108
4.19	Flow chart for sparse tableau algorithm.	112
5.1	Low-frequency circuit representation of drive system.	114
5.2	Low-frequency model of PMAC machine and interconnecting cable.	115
5.3	Top-level block diagram of low-frequency model.	120
5.4	Inverter simulation block diagram (low frequency).	121
5.5	Simulated phase currents using low-frequency model.	122
5.6	Expanded view of simulated a -phase current using low-frequency model.	123
5.7	High-frequency circuit model of the inverter and source.	124
5.8	Block diagram of high-frequency model of electric machine and interconnecting cable.	125
5.9	Code snippet for initializing model parameters and variables.	127
5.10	Code snippet for instantiating the high-frequency model.	128
5.11	Function for defining and instantiating the phase leg of the inverter circuit.	129
5.12	Code snippet for establishing converged solution.	130
5.13	Simulated voltage, current, and power loss in lower MOSFET.	131
5.14	Simulated voltage, current, and power loss in upper MOSFET.	131
5.15	Simulated phase currents.	132
5.16	Simulated phase currents in the stationary reference frame.	132
5.17	Simulated transients in lower MOSFET.	134
5.18	Simulated transients in upper MOSFET.	134
5.19	Simulated machine currents.	135
6.1	Circuit diagram for test setup.	137
6.2	Definition and initialization of variables.	138
6.3	Definition and instantiation of test circuit.	138
6.4	Code snippet for test-circuit analysis solution.	139
6.5	Simulated voltage, current, and power loss in lower MOSFET.	139
6.6	Simulated voltage, current, and power loss in upper MOSFET.	140

6.7	Simulated dc input voltage and currents to inverter circuit.	141
6.8	Measured results for turn-on event of a phase leg.	142
6.9	Zoomed-in measurements for turn-on event of a phase leg.	143
6.10	Measured and filtered simulated results for turn-on event of a phase leg of the test circuit.	144
6.11	Measured currents for turn-on event of a phase leg.	145
6.12	Measured voltages for turn-on event of a phase leg.	146
6.13	Simulated phase currents during turn-on event of a phase leg.	147
6.14	Simulated voltages during turn-on event of a phase leg.	148
6.15	Measured and filtered simulated currents during turn-on event of a phase leg.	149
6.16	Measured and filtered simulated voltages during turn-on event of a phase leg.	150
7.1	Simulation structure for establishing the high-frequency dynamics for different operating points.	155
7.2	Turn-on switching energy losses for phase-leg a ; $[S_a \ S_b \ S_c]_{\text{init}} = [0 \ 0 \ 0]$; $[S_a \ S_b \ S_c]_{\text{final}} = [1 \ 0 \ 0]$	157
7.3	Turn-off switching energy losses for phase-leg a ; $[S_a \ S_b \ S_c]_{\text{init}} = [1 \ 0 \ 0]$; $[S_a \ S_b \ S_c]_{\text{final}} = [0 \ 0 \ 0]$	158
7.4	Switching transients in a -phase upper MOSFET for $\theta_e = 0$ and $i_{\text{peak}} = 10 \text{ A}$; $[S_a \ S_b \ S_c]_{\text{init}} = [0 \ 0 \ 0]$; $[S_a \ S_b \ S_c]_{\text{final}} = [1 \ 0 \ 0]$	159
7.5	Switching transients in a -phase lower MOSFET for $\theta_e = 0$ and $i_{\text{peak}} = 10 \text{ A}$; $[S_a \ S_b \ S_c]_{\text{init}} = [0 \ 0 \ 0]$; $[S_a \ S_b \ S_c]_{\text{final}} = [1 \ 0 \ 0]$	159
7.6	Switching transients in a -phase upper MOSFET during phase a turn-on event ($\theta_e = \pi$ and $i_{\text{peak}} = 10 \text{ A}$).	160
7.7	Switching transients in a -phase lower MOSFET during phase a turn-on event ($\theta_e = \pi$ and $i_{\text{peak}} = 10 \text{ A}$).	161
7.8	Switching transients in a -phase upper MOSFET during phase a turn-off event ($\theta_e = \pi$ and $i_{\text{peak}} = 10 \text{ A}$).	162
7.9	Switching transients in a -phase lower MOSFET during phase a turn-off event ($\theta_e = \pi$ and $i_{\text{peak}} = 10 \text{ A}$).	163
7.10	Switching transients in a -phase upper MOSFET during phase a turn-on event ($i_{\text{peak}} = 0$).	164
7.11	Switching transients in a -phase lower MOSFET during phase a turn-on event ($i_{\text{peak}} = 0$).	165

7.12	Energy transferred to electric machine during turn-on event; $[S_a \ S_b \ S_c]_{\text{init}} = [0 \ 0 \ 0]$; $[S_a \ S_b \ S_c]_{\text{final}} = [1 \ 0 \ 0]$	166
7.13	Energy transferred to electric machine during turn-off event; $[S_a \ S_b \ S_c]_{\text{init}} = [1 \ 0 \ 0]$; $[S_a \ S_b \ S_c]_{\text{final}} = [0 \ 0 \ 0]$	167
7.14	Turn-on transients in high-frequency circuit ($\theta_e = 0$ and $i_{\text{peak}} = 10 \text{ A}$); $[S_a \ S_b \ S_c]_{\text{init}} = [0 \ 0 \ 0]$; $[S_a \ S_b \ S_c]_{\text{final}} = [1 \ 0 \ 0]$	168
7.15	Turn-off transients in high-frequency circuit ($\theta_e = 0$ and $i_{\text{peak}} = 10 \text{ A}$); $[S_a \ S_b \ S_c]_{\text{init}} = [1 \ 0 \ 0]$; $[S_a \ S_b \ S_c]_{\text{final}} = [0 \ 0 \ 0]$	169
7.16	Switching energy loss in phase-leg a	171
7.17	Energy transferred to/ from electric machine during switching of phase-leg a	171
7.18	Conduction loss in inverter.	172
A.1	LTspice implementation of the extended sine-triangle modulation strategy.	182
A.2	LTspice circuit diagram of the inverter.	183
A.3	LTspice circuit diagram of the machine cables.	183
A.4	LTspice circuit diagram of the surface-mount PMAC machine.	184

ABBREVIATIONS

BDF	backward differential formulae
CM	common-mode
DM	differential-mode
EMI	electromagnetic interference
FET	field-effect transistor
GaN	gallium nitride
GOSET	genetic optimization system engineering tool
HF	high-frequency
IGBT	insulated-gate bipolar transistor
LF	low-frequency
MOSFET	metal-oxide-semiconductor field-effect transistor
NDF	numerical differentiation formula
NdFeB	neodymium-iron-boron
PMAC	permanent-magnet ac
SiC	silicon carbide
Si	silicon
SPICE	simulation program with integrated circuit emphasis
WBG	wide-bandgap

ABSTRACT

Recent developments in semiconductor device technology have seen the advent of wide-bandgap (WBG) based devices that enable operation at high switching frequencies. These devices, such as silicon carbide (SiC) metal-oxide-semiconductor field-effect transistors (MOS-FETs), are becoming a favored choice in inverters for electric drive systems because of their lower switching losses and higher allowable operating temperature. However, the fast switching of such devices implies increased voltage edge rates (high dv/dt) that give rise to various undesirable effects including large common-mode currents, electromagnetic interference, transient overvoltages, insulation failure due to the overvoltages, and bearing failures due to microarcs. With increased use of these devices in transportation and industrial applications, it is imperative that accurate models and efficient simulation tools, which can predict these high-frequency effects and accompanying system losses, be established. This research initially focuses on establishing an accurate wideband model of a surface-mount permanent-magnet ac machine supplied by a WBG-based inverter. A new multirate simulation framework for predicting the transient behavior and estimating the power losses is then set forth. In this approach, the wideband model is separated into high- and low-frequency models implemented using two different computer programs that are best suited for the respective time scales. Repetitive execution of the high-frequency model yields look-up tables for the switching losses in the semiconductors, electric machine, and interconnecting cable. These look-up tables are then incorporated into the low-frequency model that establishes the conduction losses. This method is applied to a WBG-based electric drive comprised of a SiC inverter and permanent-magnet ac machine. Comparisons of measured and simulated transients are provided.

1. BACKGROUND AND OBJECTIVES

Wide-bandgap (WBG) power semiconductor devices are becoming more prevalent in modern electric drive systems. The benefits of WBG semiconductor devices such as silicon carbide (SiC) or gallium nitride (GaN) metal-oxide-semiconductor field-effect transistors (MOSFETs) include their switching times that are much shorter than their silicon counterparts. This property is the principal reason for the reduced switching losses and consequential high efficiencies seen in power electronic circuits such as dc-to-ac inverters and dc-to-dc converters that use WBG-based devices [1]–[14]. Such circuits are instrumental in providing the voltages and currents that drive variable-speed electric machines.

Typically, an inverter supplies the voltages to a three-phase electric machine, such as the permanent-magnet ac (PMAC) machine. A common three-phase inverter topology is shown in Figure 1.1. Therein, diodes are connected anti-parallel to semiconductor switches to provide a path for inductive current when the corresponding switch that was originally conducting current of that polarity is turned off. In general, the switches are MOSFETs as shown in Figure 1.1, or insulated-gate bipolar transistors (IGBTs), which are typically silicon-based. Research and development in this area have yielded WBG transistors whose switching times are now on the order of tens of nanoseconds [15], [16]. With fast transistors, inverters with high switching frequencies can be realized as the turn-on/off events are completed in very short periods of time. This attribute is desirable since short turn-on or turn-off transients yield reduced switching losses resulting in inverter efficiencies on the order of 98-99% [2], [14], [17], [18].

Although the benefits of using fast transistors in inverters are laudable, some unfavorable effects have been introduced due to their use. Much of these are deleterious to electric machine drive systems and have been attributed to the increased voltage edge rates that come from the fast switching of the transistors. Fast switching implies that the rate at which the inverter output voltage changes (dv/dt) is high. Increased voltage edge rates give rise to a number of undesirable effects including large common-mode currents, electromagnetic interference, transient overvoltages, insulation failure due to the overvoltages, and pitting of mechanical bearings due to micro arcs [19]–[25]. In order to study these issues, the modeling

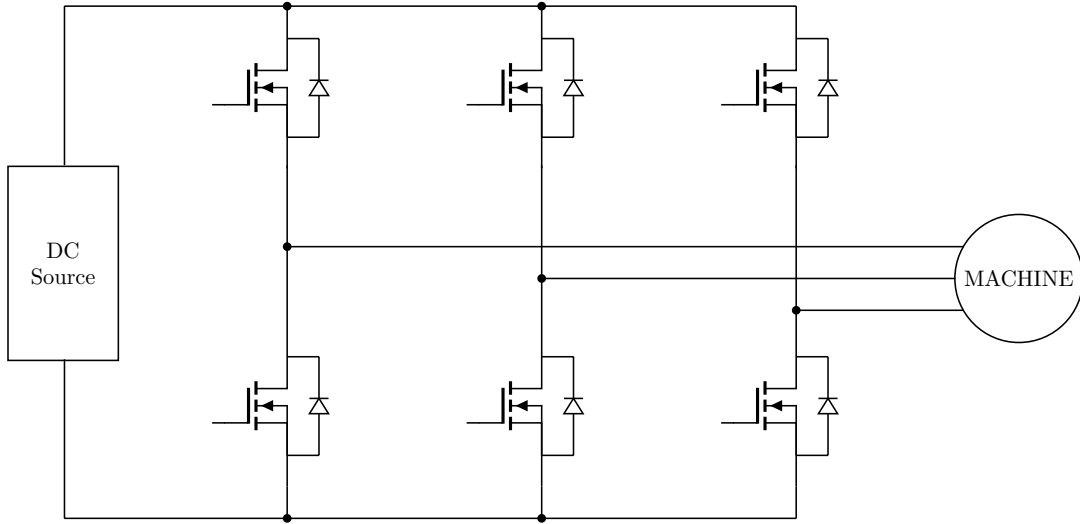


Figure 1.1. Typical three-phase inverter topology.

and simulation of WBG-based electric drives must accurately capture the high-frequency switching transients including their effects on the overall losses and efficiency of the system.

The goal of this research is to achieve an accurate and efficient simulation framework for WBG-based electric drive systems. As suggested in [26], it is imperative that focus should not only be given to the simulation of the electric machine as this is not sufficient to predict the behavior of the complete drive system. Instead, a complete system simulation including the inverter and electric machine, which can accurately capture both the low- and high-frequency dynamics of the electric drive system, is the focus in this research.

1.1 Literature Review

Substantial research has previously been conducted on developing computer models and simulation methods for predicting the dynamic performance of various electric drive systems. In the following discussion, it is important to distinguish the terms *modeling* and *simulation*. The term *modeling* refers to the identification of the physical phenomena that are relevant to the system being studied and the expression of that physics in the form of partial, differential, and/or algebraic equations (PDAEs). On the other hand, the term *simulation* involves the conversion of the PDAEs into sequential linear algebraic equations that can be solved

numerically using direct or iterative methods. The simulation approach generally involves discretization of time and/or spacial coordinates and manipulation of the ensuing algebraic equations into the form of a sequential algorithm.

Focusing first on modeling aspects, computer models of electric machinery (induction, synchronous, permanent-magnet) have been available since the early part of the 20th century. The classical models are based on Ohm's, Ampere's, and Faraday's laws. They are now presented in undergraduate textbooks [27], [28] and are standard in commercially available simulation packages such as Simulink [29] as part of the Simscape/Electrical/Electromechanical library. Simulink also includes semiconductor and converter models as part of the Simscape/Electrical/Semiconductors & Converters library.

In a traditional simulation, an ideal or semi-ideal model of a semiconductor switch is used. In an ideal switch or diode model, the voltage drop is completely neglected when the device is on or conducting and its current is assumed zero otherwise. In a semi-ideal model, the voltage drop is modeled as a resistive (MOSFET) or constant (IGBT) voltage drop. Switching from on-state to off-state is often assumed to be instantaneous. Switching losses are then estimated after-the-fact. For example, in a turn-off event, the current in the device before turn-off and voltage across the device after turn-off are recorded. The turn-off energy is often approximated as one-half the product of the dc voltage, load current, and the manufacturer-supplied turn-off time.

The aforementioned model will be referred to as a traditional low-frequency (LF) model of the inverter. Such models are readily implemented in Simulink. They are computationally efficient, useful for control system development and analysis, and have been used to approximate the switching and conduction losses and overall efficiency. This approach was reasonable when switching times were on the order of 1 to 5 μs ; however, as switching times have become smaller, the assumptions made in estimating switching losses are no longer valid. In particular, with switching times now less than 100 ns, it is necessary to revisit and revise the models used to represent all aspects of the drive system including the semiconductor devices, the discrete circuit elements (capacitors, inductors), the electric machine, and the cables connecting the inverter to the machine and the dc source to the inverter. Recent relevant efforts in these areas are described below.

Numerous wideband (WB) machine models capturing both low- and high-frequency (HF) characteristics have been proposed in [30]–[36]. For example, in [30], a WB model of an interior permanent-magnet ac machine was set forth. Particular efforts were made to include the so-called parasitic circuit elements of the machine as well as those due to the cable leads of the machine. Parasitic circuit elements include small unintentional capacitances and inductances that are attributed to the electric and/or magnetic coupling associated with the interconnections between the physical windings, inductors, and/or capacitors in the circuit. In a traditional LF simulation, the parasitic circuit elements are neglected. In [31]–[34], various induction machine WB models were presented. A WB wound-rotor induction machine model along with characterization techniques were presented in [31]. Although, saturation effects were considered, its validity at frequencies exceeding 50 kHz has not been proven. Boglietti and Carpeneto describe another WB induction motor model based on lumped parameters in [32]. The model essentially entails components representing the winding-to-ground and turn-to-turn capacitances, resistance for capturing eddy current effects, low-frequency leakage inductance, and the stator and rotor aggregate resistance. In [33], a simple induction machine model for fast simulation was introduced. Here, the winding-to-ground parasitics are modeled to contain resistances and capacitances. Also, Wang et. al. propose a WB modeling method for a long-cable-fed induction machine drive system in [34]. The authors give special attention to improved cable models that account for HF effects using transmission-line modeling techniques.

A WB multi-resolutional model of a surface-mount permanent-magnet ac machine including the inverter was presented in [36]. Although a detailed machine model was presented, the inverter was represented using behavioral IGBT models to establish the results. While this approach was reasonable at the time when switching times were on the order of 1 μ s, this approach does not suffice for the accurate prediction of the overall behavior of an electric drive using fast WBG devices.

In [26], a HF inverter model was introduced wherein the MOSFET was represented as a subcircuit containing junction capacitances, resistances, and a dependent current source. This is commonly referred to as the SPICE Level 1 [37] or Shichman-Hodges model [38]. Also, in [39], a pair of simple *RLC* equivalent-circuit models that portray the turn-on and

turn-off transients of a SiC MOSFET were presented. It was shown that the models may be used to capture the ringing associated with the switching of fast transistors. However, using these models for an inverter in a WBG-based electric drive system simulation may prove to be challenging. This is because the stage between the turn-on and turn-off events, which is essential in the simulation of electric drive systems, was not considered in [39]. Another behavioral electrothermal gallium nitride (GaN) MOSFET model was presented in [40] for use in SPICE. The model couples a GaN FET electrical model with an RC network to account for thermal effects due to the device temperature changes during operation.

A method for developing physics-based models for a PIN diode that is based on the detailed coupled drift, diffusion, and continuity equations was proposed in [41]. Although the simulation of physics-based models is generally slow, an efficient variable-structure variable-order method was introduced in [41]. It was shown that by using a variable-structure variable-order simulation approach, wherein the structure and order of the simulation is dynamically changed based on the states (active or inactive) of devices, the simulation runtime for the physics-based model of a full-bridge rectifier can be reduced by more than 400%. However, its application to power MOSFETs and electric drive system simulation remains an open area of research.

With well-defined models, the analysis of modern electric drive systems becomes less ambiguous. However, realizing an efficient and accurate simulation technique for such systems is a relatively difficult task. Much of this is because the model is numerically stiff. A numerically stiff model is characterized by the fact that it portrays both fast and slow dynamic behaviors of the system. For example, in a silicon-based electric drive system, the time constants associated with the semiconductor switching are on the order of microseconds whereas the time constants associated with the electrical transients of an electric machine may be in tens of milliseconds. With fast switching devices as in WBG-based electric drive systems, the stiffness problem is greatly exacerbated as the disparity between the largest and smallest time constants is even larger.

Typically, to solve a system of stiff differential equations, implicit integration algorithms are chosen as they bear a history of handling such problems better than explicit algorithms. If explicit algorithms (such as Runge-Kutta or forward Euler) are used to solve a stiff problem,

the time step cannot be selected to be larger than the smallest time constant in the system even if fast transients have subsided. Often, Gear’s backward differential formulae (BDF) are used for such problems [42], [43]; the second-order Gear’s and modified trapezoidal algorithms are the featured integration algorithms in LTspice, a general-purpose circuit simulator of SPICE origins. However, circuit simulation based upon modified nodal analysis (MNA) used in SPICE generally uses a fixed small time step even after the fast transients have subsided. Thus, these are inefficient for numerically stiff systems when the longer term dynamics are also of interest.

In state-space-based simulation approaches such as those used in Simulink, there are several implicit algorithms suitable for numerically stiff systems. However, in implicit algorithms, there is a significant overhead in having to solve a large set of nonlinear algebraic equations at each time step. This generally involves a Newton-Raphson (NR) iteration that requires the formation of a Jacobian (typically non-sparse) and the solution of a large set of linear equations in each NR iteration. For systems with a large number of states, this can be problematic.

The simulation methods previously described are generally referred to as a single-rate simulation. Here, the dynamics of the system are determined by considering the system as an unpartitioned network. Other techniques for simulating stiff models involve partitioning techniques for the application of multirate integration methods [44]. Usually, the stiff model is decoupled into fast and slow subsystem models for the short- and long-term dynamics of the drive system, respectively. In the multirate method, a step size for the fast dynamics, h_f is chosen smaller than that for the slow dynamics, h_s , such that $h_s = kh_f$, where k is an integer. For every step h_s made, the variables contained in the slow subsystem are predicted for the next step. These predicted results are interpolated for each fast step, h_f by some interpolation technique. Typically, linear interpolation is used to establish these interpolated slow variables which are saved. The saved interpolated variables are then used in establishing the fast variables at each step, h_f made. Next, the entire system is solved and the updated slow variables are compared against the initial predicted values. The process is continued to the next interval if the specified tolerance is met or repeated with interpolated slow variables from the updated values if the tolerance test fails. This method has been

used for power systems simulations as outlined in [45] and [46]. Although, the method suggests that there are only two subsystems and thus two time scales, a potential n-time scale multirate simulation method for power systems was discussed in [47] and [48].

A variant form of the multirate method for power systems was set forth in [49] and [50]. Here, a change in network topology, due to the switching properties of the converter, determines the time step that is used. When a switching event occurs, communication between the fast and slow subsystems is established at some communication interval $h_c \geq h_s$. The slow state variables are predicted from derivatives obtained at the previous communication step and used in integrating the fast subsystem. Next, the fast variables are averaged and supplied into the slow subsystem equations when advancing the slow subsystem. To continue to the next communication interval, the rate of change of the slow states is evaluated and the calculated slow states are compared against their approximates. If the specified tolerance is exceeded, the process is repeated; otherwise, the cycle is repeated for the next communication interval. It is important to note that this method yielded significant savings in simulation time for power-electronic-based systems [50] compared to their single-rate counterparts. However, its application in high-frequency-inverter-based machine drives is yet to be explored.

Another multirate simulation technique was used for power systems simulation in [51]. The slow subsystem is taken into account when solving for the fast transients by an interpolation of its Thévenin equivalent voltage source. During the slow interval, an average of currents linking the subsystems is used to account for the variation of the fast subsystem. In [52], a multirate method that divides a power-electronic-based system into subcircuits was proposed. By selecting different step sizes for partitioned subcircuits, the analysis may be carried out efficiently.

Singular perturbation techniques may also be employed for solving partitioned models. In this approach, the solution of the entire system is obtained from the sum of two less complex subsystem models that are derived from two major assumptions. In the first subsystem, it is assumed that the fast transients have decayed. This assumption significantly mitigates stiffness difficulties [53]. With slow states evaluated, the fast states are then obtained assuming the slow states are constant. Also, by employing multi-resolutional techniques on detailed

models of power electronic circuits, it has been shown that a significant improvement in simulation speed may be achieved [54].

The complete simulation of the overall characteristics of a stiff system such as an electric drive can be computationally expensive and time-consuming. This certainly depends on the simulation method that is chosen. For instance, in [26], Simulink is used to describe the system in block diagram form from which the state equations are established and solved numerically using the provided ode15s (stiff/NDF) algorithm, a multi-step solver that computes the system's state using variable-order numerical differentiation formulae (NDF). It should be noted that the runtime for the simulation study for a single operating point was approximately 6 minutes for a simulation time of 20 ms. This simulation method is evidently slow, though it offers the designer the benefit of not relying on the pre-programmed models of devices that are defined in circuit simulators such as SPICE and its derivatives.

At the writing of this thesis, there is not a significant body of literature on techniques used for the complete or thorough simulation of electric drive systems that utilize wide-bandgap transistors. It should be noted that the classical methods have depended on general-purpose simulators such as SPICE or its derivatives using built-in transistor models and user-developed machine models as proposed in [30]. Other simulators such as Simulink have also proven useful as one may choose from a number of stiff integration algorithms. In many cases, to ensure that the simulation is computationally efficient, approximate or semi-ideal transistor models are used as in [36]. As has been noted before, the accuracy of the simulation may be sacrificed and the errors may be significant for wide-bandgap-based electric drives.

1.2 Motivation and Objectives

The advent of ultra-fast transistors such as SiC MOSFETs in electric drives has generated significant interest in the WB modeling of machines and inverters as well as efficient techniques for the simulation of the dynamics of electric drive systems. Much of the interest has been inspired by HF effects including electromagnetic interference (EMI), common-mode currents, and transient overvoltages that accompany the use of such fast transistors. As wide-bandgap transistors grow in usage in electric drive systems, it is imperative that de-

sign engineers are assured of their designs through simulation. Moreover, it is necessary that the simulation accurately predicts the losses in the various components of the system. Of importance are the switching and conduction losses of the inverter. However, a careful consideration of the impact of HF effects on the electric drive system shown in Figure 1.2 suggests that significant losses may also occur elsewhere in the system. As such, an overall simulation of the system is necessary to determine all of the losses within the system.

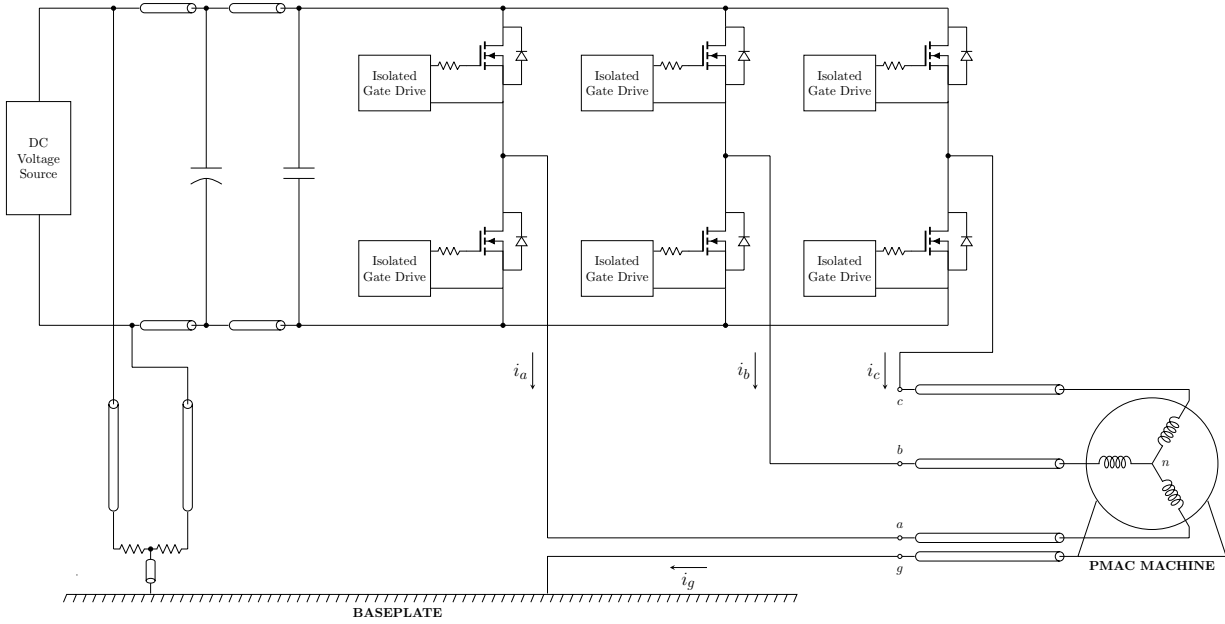


Figure 1.2. Electric machine drive system.

The primary objective of this research is to establish a computationally efficient heterogeneous multirate simulation framework for predicting the overall dynamics of a WBG-based electric drive system including the losses in the system. The approach is based upon establishing the machine currents from the simulation of a derived low-frequency model of the drive system and using the currents at switching instants as initial conditions to the simulation of a HF model.

The specific system to be studied is shown in Figure 1.2. As shown, the drive system comprises a PMAC machine and an inverter circuit whose switches are controlled using the outputs of gate drives. Moreover, a dc source with an accompanying dc filter circuit

provides the dc voltage to the inverter circuit. The PMAC machine used in this study is a commercially available surface-mount PMAC machine with the nameplate data: Sanyo Denki P50B08100, 3000 rpm rated speed, 1000 W rated power, 9.6 A rated current. The MOSFETs used constitute a six-pack Cree inverter module with model number CCS020M12CM2. Also, the isolated gate drives and polypropylene capacitor shown depict important components of a gate driver circuit used in the study. This gate driver circuit is the Cree CGD15FB45P1 gate driver board. In addition, a Cornell Dubilier electrolytic capacitor with model number DCMC102T4450BB2B was used in the dc filter circuit. The resistors used in the resistive potential divider are a pair of the Vishay Sfernice RCH50S47000JS06 thin-film resistors. For the drive system simulation, accurate models are needed for the cables, physical capacitors, transistors, and the surface-mount permanent-magnet ac machine. Accordingly, another objective of this research is to establish accurate models for all of the components of the electric drive system to be studied.

1.3 Thesis Outline

The outline of this thesis is as follows. The wideband model of a surface-mount PMAC machine is introduced in Chapter 2. Starting from classical models of the PMAC machine, a low-frequency model that takes account of the effects due to eddy currents in the permanent magnets is introduced. This model is further expanded to establish a wideband model that ensures that the low- and high-frequency characteristics of the machine are captured in a simulation. The characterization and parameterization of the selected PMAC machine is also discussed. A model of a wide-bandgap-based inverter is described in Chapter 3. Techniques for the characterization and parameterization of a SiC inverter and its manufacturer-supplied gate-driver board are also outlined in Chapter 3. The wideband models set forth in Chapters 2 and 3 are implemented using established simulators in Chapter 4. Specifically, conventional single-rate simulation methods are used to show the need for a more computationally efficient simulation strategy. In Chapter 5, a new heterogeneous multirate simulation framework for the electric drive system is set forth. Comparisons of simulated and measured high-frequency

transients are presented in Chapter 6. In Chapter 7, final results and conclusions from the research conducted and avenues of potential future research are discussed.

2. ELECTRIC MACHINE MODELING AND PARAMETERIZATION

A model of a surface-mount PMAC machine is presented in this chapter. Emphasis is given to developing a wideband model that captures the low- and high-frequency dynamics. Starting from the classical model, an improved low-frequency model is introduced that accounts for the effects of eddy currents in the Neodymium-Iron-Boron (NdFeB) permanent magnets used in modern PMAC machines. This improved low-frequency model sets the stage for the development and parameterization of the wideband model that forms an important part of the simulation framework presented in Chapter 5.

2.1 Low-Frequency Model

A two-pole, three-phase PMAC machine with identical stator windings displaced 120° from one another is shown in Figure 2.1. Each stator winding has N_s turns and resistance r_s . The classical model is based on Ohm's and Faraday's laws [55]

$$\mathbf{v}_{abcs} = r_s \mathbf{i}_{abcs} + p \boldsymbol{\lambda}_{abcs} \quad (2.1)$$

$$\boldsymbol{\lambda}_{abcs} = \mathbf{L}_s \mathbf{i}_{abcs} + \boldsymbol{\lambda}'_m \quad (2.2)$$

where

$$(\mathbf{f}_{abcs})^T = \begin{bmatrix} f_{as} & f_{bs} & f_{cs} \end{bmatrix} \quad (2.3)$$

Here, f is a variable that can represent current, voltage, or flux linkage, r_s represents the stator winding resistance, p is the derivative-with-respect-to-time (d/dt) operator, and \mathbf{L}_s is a matrix of the stator self and mutual inductances. \mathbf{L}_s may be expressed as [55]

$$\mathbf{L}_s = \begin{bmatrix} L_{aa} & L_{ab} & L_{ac} \\ L_{ba} & L_{bb} & L_{bc} \\ L_{ca} & L_{cb} & L_{cc} \end{bmatrix} \quad (2.4)$$

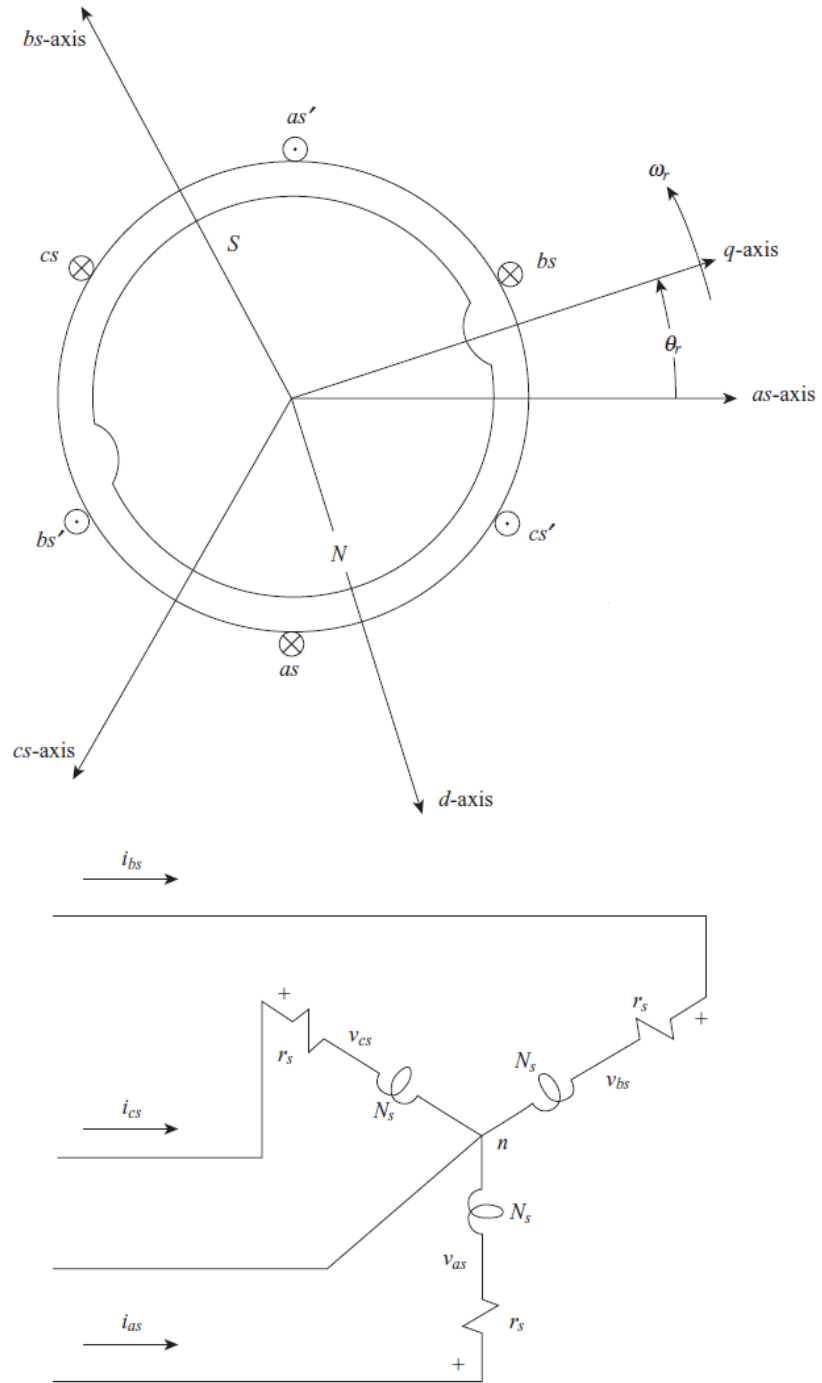


Figure 2.1. A two-pole three-phase PMAC machine, adapted from [55]

where the self inductances are denoted as L_{aa} , L_{bb} , and L_{cc} for phases a , b , and c , respectively, and the mutual inductances as L_{ab} for phases a and b , L_{bc} for phases b and c , and L_{ac} for phases a and c . The self and mutual inductances may be approximated as

$$\begin{aligned}
L_{aa} &= L_{ls} + L_{ms} + L_{\theta} \cos 2\theta_r \\
L_{bb} &= L_{ls} + L_{ms} + L_{\theta} \cos 2(\theta_r - 2\pi/3) \\
L_{cc} &= L_{ls} + L_{ms} + L_{\theta} \cos 2(\theta_r + 2\pi/3) \\
L_{ab} &= L_{ba} = -L_{ms}/2 + L_{\theta} \cos 2(\theta_r - \pi/3) \\
L_{bc} &= L_{cb} = -L_{ms}/2 + L_{\theta} \cos 2(\theta_r + \pi) \\
L_{ac} &= L_{ca} = -L_{ms}/2 + L_{\theta} \cos 2(\theta_r + \pi/3)
\end{aligned} \tag{2.5}$$

The electrical rotor angle is θ_r . In particular, it is defined as

$$\theta_r = \frac{P}{2} \theta_{rm} \tag{2.6}$$

where P is the number of poles and θ_{rm} is the mechanical rotor angle. In a surface-mount PMAC machine, $L_{\theta} = 0$ whereupon

$$\begin{aligned}
L_{aa} &= L_{bb} = L_{cc} = L_{ls} + L_{ms} = L_s \\
L_{ab} &= L_{ba} = L_{bc} = L_{cb} = L_{ac} = L_{ca} = -L_{ms}/2
\end{aligned} \tag{2.7}$$

Here, the self inductance L_s is an aggregate of the leakage L_{ls} and magnetizing inductance L_{ms} . The mutual inductance is $-L_{ms}/2$. Thus, (2.4) may be re-written as

$$\mathbf{L}_s = \begin{bmatrix} L_s & -\frac{1}{2}L_{ms} & -\frac{1}{2}L_{ms} \\ -\frac{1}{2}L_{ms} & L_s & -\frac{1}{2}L_{ms} \\ -\frac{1}{2}L_{ms} & -\frac{1}{2}L_{ms} & L_s \end{bmatrix} \tag{2.8}$$

Further, the flux linkage λ'_m may be expressed as

$$\lambda'_m = \lambda'_m \begin{bmatrix} \sin \theta_r \\ \sin (\theta_r - 2\pi/3) \\ \sin (\theta_r + 2\pi/3) \end{bmatrix} \quad (2.9)$$

where λ'_m is the amplitude of the stator flux linkages due to the permanent magnet. It may be obtained from the measured open-circuit line-to-line voltages induced in the stator phase windings, which have an amplitude of $\sqrt{3}\omega_r\lambda'_m$, where ω_r is the electrical rotor speed.

Using appropriate substitutions in (2.1), the voltage equations that define the classical model for the surface-mount PMAC machine may be expressed as

$$\begin{aligned} v_{as} &= r_s i_{as} + L_s p i_{as} - \frac{1}{2} L_{ms} p i_{bs} - \frac{1}{2} L_{ms} p i_{cs} + \omega_r \lambda'_m \cos(\theta_r) \\ v_{bs} &= r_s i_{bs} - \frac{1}{2} L_{ms} p i_{as} + L_s p i_{bs} - \frac{1}{2} L_{ms} p i_{cs} + \omega_r \lambda'_m \cos(\theta_r - 2\pi/3) \\ v_{cs} &= r_s i_{cs} - \frac{1}{2} L_{ms} p i_{as} - \frac{1}{2} L_{ms} p i_{bs} + L_s p i_{cs} + \omega_r \lambda'_m \cos(\theta_r + 2\pi/3) \end{aligned} \quad (2.10)$$

A circuit diagram for this model at a fixed rotor position is shown in Figure 2.2. Here, each phase is represented as an rL branch.

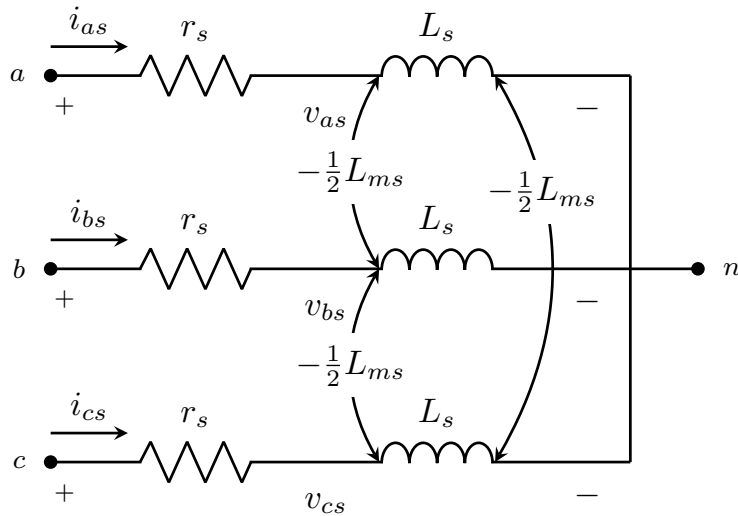


Figure 2.2. Low-frequency classical model at a fixed rotor position.

The variables in the model may be transformed to the rotor reference frame using Park's transformation [56]. In particular,

$$\mathbf{f}_{qd0s}^r = \mathbf{K}_s^r \mathbf{f}_{abcs} \quad (2.11)$$

where

$$\mathbf{K}_s^r = \frac{2}{3} \begin{bmatrix} \cos \theta_r & \cos(\theta_r - 2\pi/3) & \cos(\theta_r + 2\pi/3) \\ \sin \theta_r & \sin(\theta_r - 2\pi/3) & \sin(\theta_r + 2\pi/3) \\ 1/2 & 1/2 & 1/2 \end{bmatrix} \quad (2.12)$$

By applying the transformation to (2.10), the voltage equations in the rotor reference frame become

$$\mathbf{v}_{qd0s}^r = \mathbf{r}_s \mathbf{i}_{qd0s}^r + \omega_r \boldsymbol{\lambda}_{dqs}^r + p \boldsymbol{\lambda}_{qd0s}^r \quad (2.13)$$

where

$$\boldsymbol{\lambda}_{dqs}^r = \begin{bmatrix} \lambda_{ds}^r & -\lambda_{qs}^r & 0 \end{bmatrix}^T \quad (2.14)$$

$$\boldsymbol{\lambda}_{qd0s}^r = \begin{bmatrix} L_{ls} + \frac{3}{2}L_{ms} & 0 & 0 \\ 0 & L_{ls} + \frac{3}{2}L_{ms} & 0 \\ 0 & 0 & L_{ls} \end{bmatrix} \begin{bmatrix} i_{qs}^r \\ i_{ds}^r \\ i_{0s}^r \end{bmatrix} + \lambda_m' \begin{bmatrix} 0 \\ 1 \\ 0 \end{bmatrix} \quad (2.15)$$

In terms of transformed variables, the equivalent circuits of the machine are illustrated in Figure 2.3. It is important to note that this model does not account for the effects of eddy currents induced in the rotor of the machine. Nonetheless, it is widely used since the induced eddy currents are typically small and do not significantly affect the electromechanical dynamics.

Modern permanent-magnet ac machines use NdFeB magnets, which are relatively good conductors [57]. Therefore, the eddy currents induced may be significant and cannot be neglected when considering the wideband dynamics. Their effects may be modeled by adding damper windings to the q - and d -axis equivalent circuits of Figure 2.3. The circuit diagrams for the resulting model are shown in Figure 2.4. Here, the pairs of parallel rL branches of r_{kq1} - L_{lkq1} and r_{kq2} - L_{lkq2} for the q -axis equivalent circuit and r_{kd1} - L_{lkd1} and r_{kd2} - L_{lkd2} for

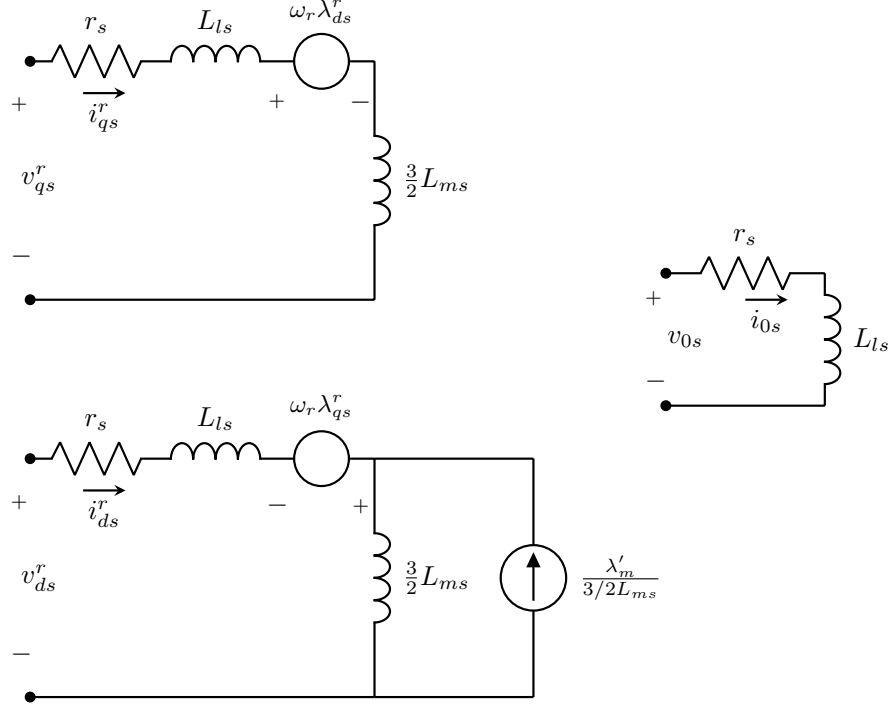


Figure 2.3. Rotor reference frame equivalent circuits for the classical model.

the d -axis equivalent circuit, represent the damper windings necessary for describing the effects due to the induced eddy currents. Thus, the expressions for the flux linkages may be expanded as

$$\lambda_{qs}^r = L_{ls} i_{qs}^r + \frac{3}{2} L_{ms} (i_{qs}^r + i_{kq1} + i_{kq2}) \quad (2.16)$$

$$\lambda_{ds}^r = L_{ls} i_{ds}^r + \frac{3}{2} L_{ms} (i_{ds}^r + i_{kd1} + i_{kd2}) + \lambda_m' \quad (2.17)$$

$$\lambda_{0s} = L_{ls} i_{0s} \quad (2.18)$$

The flux linkages due to the added branches are

$$\lambda_{kq1} = L_{lkq1} i_{kq1} + \frac{3}{2} L_{ms} (i_{qs}^r + i_{kq1} + i_{kq2}) \quad (2.19)$$

$$\lambda_{kq2} = L_{lkq2} i_{kq2} + \frac{3}{2} L_{ms} (i_{qs}^r + i_{kq1} + i_{kq2}) \quad (2.20)$$

$$\lambda_{kd1} = L_{lk d1} i_{kd1} + \frac{3}{2} L_{ms} (i_{ds}^r + i_{kd1} + i_{kd2}) \quad (2.21)$$

$$\lambda_{kd2} = L_{lk d2} i_{kd2} + \frac{3}{2} L_{ms} (i_{ds}^r + i_{kd1} + i_{kd2}) \quad (2.22)$$

Due to the symmetry of the surface-mount PMAC machine, the q - and d -axis resistances and inductances are equal. Specifically,

$$r_{kq1} = r_{kd1} = r_{d1} \quad (2.23)$$

$$L_{lkq1} = L_{lk d1} = L_{d1} \quad (2.24)$$

$$r_{kq2} = r_{kd2} = r_{d2} \quad (2.25)$$

$$L_{lkq2} = L_{lk d2} = L_{d2} \quad (2.26)$$

Consequently, the parameters that are needed for the the new low-frequency model are r_s , L_{ls} , L_{ms} , r_{d1} , L_{d1} , r_{d2} , L_{d2} , and λ'_m . Experimental procedures for establishing these parameters are described in the next section.

2.2 Determination of the Low-Frequency Parameters

The low-frequency parameters may be obtained by measuring the open-circuit voltages while the device is spun by another motor and from impedance measurements in which the machine terminals are connected in so-called differential mode (DM).

Differential Mode Test

To establish the low-frequency parameters, r_s , L_{ls} , L_{ms} , r_{d1} , L_{d1} , r_{d2} , and L_{d2} , a blocked-rotor, 20 Hz to 2 kHz frequency sweep was performed with the stator windings connected as shown in Figure 2.5 to a Keysight E4990A impedance analyzer. As shown in the figure, nodes a , b , and c denote the a - b - and c -phase machine terminals while node n represents the machine neutral, which is not accessible. In addition, node a is connected to the positive lead of the impedance analyzer while nodes b and c are connected to the negative lead. The

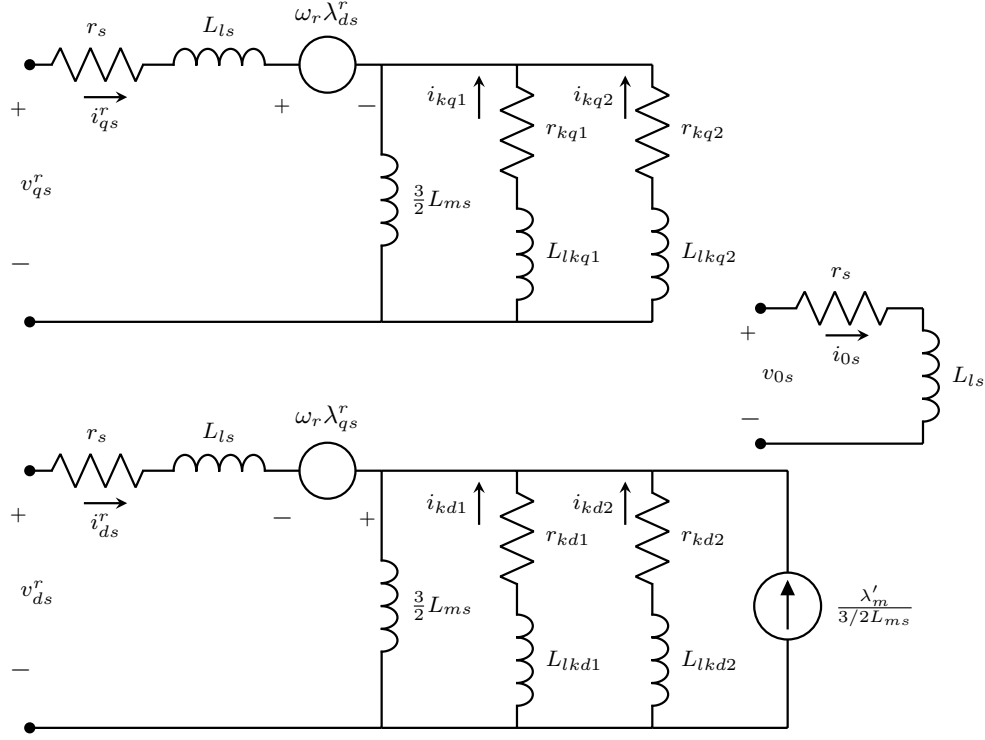


Figure 2.4. Rotor reference frame equivalent circuits for the low-frequency model.

currents through the a - b - and c -phase of the machine are i_{as} , i_{bs} , and i_{cs} , respectively. It should be noted that the windings are identical and displaced 120° . Also, v_{in} and i_{in} are sinusoidal functions of time that represent the input voltage and current, respectively.

Before describing the relationship between the currents and voltages indicated in Figure 2.5, it would be useful to define the phase voltages of the machine. The voltages v_{as} , v_{bs} , and v_{cs} are, respectively, the a - b - and c -phase voltages of the machine relative to the neutral node n . From Figure 2.5,

$$\begin{aligned} v_{bs} &= v_{cs} \\ v_{as} &= v_{bs} + v_{in} \end{aligned} \tag{2.27}$$

Using Park's transformation as described by (2.11) and (2.12), a relationship between the q -axis equivalent impedance, the d -axis equivalent impedance, and the impedance measured

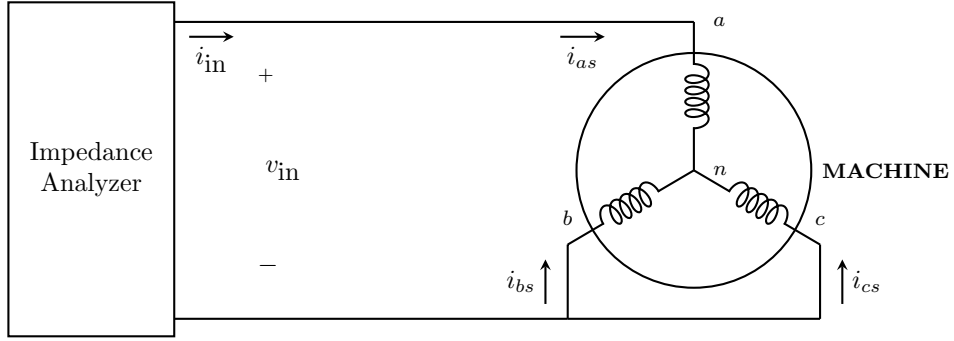


Figure 2.5. DM test circuit for realizing low-frequency parameters.

by the impedance analyzer may be established. First, the q - and d -axis voltages may be expressed.

$$v_{qs}^r = \frac{2}{3} \left[v_{as} \cos \theta_r + v_{bs} \cos(\theta_r - 120^\circ) + v_{cs} \cos(\theta_r + 120^\circ) \right] \quad (2.28)$$

$$v_{ds}^r = \frac{2}{3} \left[v_{as} \sin \theta_r + v_{bs} \sin(\theta_r - 120^\circ) + v_{cs} \sin(\theta_r + 120^\circ) \right] \quad (2.29)$$

Substituting (2.27) into (2.28) and simplifying using trigonometric identities, the q -axis voltage becomes

$$v_{qs}^r = \frac{2}{3} \left[v_{as} \cos \theta_r + v_{bs} \cos(\theta_r - 120^\circ) + v_{cs} \cos(\theta_r + 120^\circ) \right] \quad (2.30)$$

$$= \frac{2}{3} \left[v_{as} - v_{bs} \right] \cos \theta_r \quad (2.31)$$

This implies that

$$v_{qs}^r = \frac{2}{3} v_{in} \cos \theta_r \quad (2.32)$$

In the same manner, the d -axis voltage may be expressed as

$$v_{ds}^r = \frac{2}{3} v_{in} \sin \theta_r = \frac{2}{3} v_{in} \cos(\theta_r - 90^\circ) \quad (2.33)$$

Furthermore, from Figure 2.5,

$$\begin{aligned} i_{as} &= i_{\text{in}} \\ i_{bs} &= i_{cs} \\ i_{as} &= -i_{bs} - i_{cs} = -2i_{bs} \end{aligned} \tag{2.34}$$

Thus, the q -axis current may be expressed as

$$i_{qs}^r = \frac{2}{3} [i_{as} \cos \theta_r + i_{bs} \cos(\theta_r - 120^\circ) + i_{cs} \cos(\theta_r + 120^\circ)] \tag{2.35}$$

$$= \frac{2}{3} [i_{as} \cos \theta_r + i_{bs} \cos(\theta_r - 120^\circ) + i_{bs} \cos(\theta_r + 120^\circ)] \tag{2.36}$$

$$= \frac{2}{3} [i_{as} \cos \theta_r - \frac{1}{2}i_{as} \cos(\theta_r - 120^\circ) - \frac{1}{2}i_{as} \cos(\theta_r + 120^\circ)] \tag{2.37}$$

$$= \frac{2}{3} [\frac{3}{2}i_{as} \cos \theta_r] \tag{2.38}$$

$$= i_{as} \cos \theta_r \tag{2.39}$$

This implies

$$i_{qs}^r = i_{\text{in}} \cos \theta_r \tag{2.40}$$

Similarly, the d -axis current may be shown to be

$$i_{ds}^r = i_{\text{in}} \sin \theta_r = i_{\text{in}} \cos(\theta_r - 90^\circ) \tag{2.41}$$

Based on the simplified expressions for the q - and d -axis voltages and currents, it is possible to establish a relationship between the equivalent-circuit impedances and the impedance measured by the impedance analyzer. To do this, it is useful to consider the q -axis voltage and q -axis current at $\theta_r = 0^\circ$ and those for the d -axis at $\theta_r = 90^\circ$. When $\theta_r = 0^\circ$,

$$\begin{aligned} v_{qs}^r &= \frac{2}{3}v_{\text{in}} \\ i_{qs}^r &= i_{\text{in}} \end{aligned} \tag{2.42}$$

and when $\theta_r = 90^\circ$,

$$\begin{aligned} v_{ds}^r &= \frac{2}{3}v_{\text{in}} \\ i_{ds}^r &= i_{\text{in}} \end{aligned} \tag{2.43}$$

From (2.42), the phasor voltage and current equations for the q -axis may be established.

In particular,

$$\begin{aligned}\tilde{V}_{qs}^r &= \frac{2}{3}\tilde{V}_{\text{in}} \\ \tilde{I}_{qs}^r &= \tilde{I}_{\text{in}}\end{aligned}\tag{2.44}$$

where \tilde{V}_{qs}^r , \tilde{V}_{in} , \tilde{I}_{qs}^r , and \tilde{I}_{in} represent the phasor forms of v_{qs}^r , v_{in} , i_{qs}^r , and i_{in} , respectively. Due to the symmetrical construction of the surface-mount PMAC machine, q -axis impedance is independent of rotor position. As such, the equivalent q -axis impedance can be obtained from the phasor voltage and current relationship as

$$Z_q = \frac{\tilde{V}_{qs}^r}{\tilde{I}_{qs}^r}\tag{2.45}$$

$$= \frac{\frac{2}{3}\tilde{V}_{\text{in}}}{\tilde{I}_{\text{in}}}\tag{2.46}$$

$$= \frac{2}{3}Z_{\text{in}}\tag{2.47}$$

where Z_{in} represents the impedance measured by the impedance analyzer.

Conversely, (2.43) can be written in phasor form as

$$\begin{aligned}\tilde{V}_{ds}^r &= \frac{2}{3}\tilde{V}_{\text{in}} \\ \tilde{I}_{ds}^r &= \tilde{I}_{\text{in}}\end{aligned}\tag{2.48}$$

with \tilde{V}_{ds}^r and \tilde{I}_{ds}^r representing the phasor forms of v_{ds}^r and i_{ds}^r respectively. Solving for the d -axis impedance gives

$$Z_d = \frac{\tilde{V}_{ds}^r}{\tilde{I}_{ds}^r}\tag{2.49}$$

$$= \frac{\frac{2}{3}\tilde{V}_{\text{in}}}{\tilde{I}_{\text{in}}}\tag{2.50}$$

$$= \frac{2}{3}Z_{\text{in}}\tag{2.51}$$

Thus, the q - and d -axis impedance are both equal to two-thirds times the impedance measured using the impedance analyzer.

To set the stage for the development of the wideband model, it is instructive to see how Z_d and Z_q are related to the low-frequency impedance in abc variables. The per-phase low-frequency impedance at a fixed rotor position will be denoted as Z_{lf} . This is the same for each phase because of the similarity of the stator windings. Furthermore, the machine symmetry ensures that the low-frequency impedance is independent of rotor position. For the purpose of simplicity, Z_{lf} will represent the aggregate low-frequency impedance evaluated from the stator resistance, self inductance, and impedance obtained from simplified expressions of voltage drops due to mutual inductances and eddy current effects. From (2.27) and (2.34), it can be inferred that

$$\begin{aligned}\tilde{V}_{in} &= \tilde{V}_{as} - \tilde{V}_{bs} \\ \tilde{I}_{in} &= \tilde{I}_{as} \\ \tilde{I}_{as} &= -2\tilde{I}_{bs}\end{aligned}\tag{2.52}$$

where \tilde{V}_{as} , \tilde{V}_{bs} , \tilde{I}_{as} , and \tilde{I}_{bs} represent the phasor forms of v_{as} , v_{bs} , i_{as} , and i_{bs} , respectively. Consequently, the impedance measured by the impedance analyzer may be written as

$$Z_{in} = \frac{\tilde{V}_{in}}{\tilde{I}_{in}} = \frac{\tilde{V}_{as} - \tilde{V}_{bs}}{\tilde{I}_{in}} = \frac{\tilde{V}_{as}}{\tilde{I}_{as}} + \frac{\tilde{V}_{bs}}{2\tilde{I}_{bs}} = \frac{3}{2}Z_{lf}\tag{2.53}$$

Thus,

$$Z_q = Z_{lf}\tag{2.54}$$

This implies that the parameters for the q - and d -axis equivalent circuits are the same as those of the per-phase equivalent circuit (i.e. $Z_q = Z_d = Z_{lf}$). Therefore, the parameters to be established using the q - and d -axis equivalent circuits also describe the aggregate low-frequency impedance Z_{lf} .

With the machine terminals connected to the impedance analyzer, impedance measurements across a frequency sweep (20 Hz to 2 kHz) were taken and fitted to the rotor reference frame equivalent circuits shown in Figure 2.4 by applying a population-based curve fitting routine using the genetic algorithm toolbox, GOSET [58]. For the fit, the speed-voltage terms $\omega_r \lambda_{qs}^r$ and $\omega_r \lambda_{ds}^r$ are zero as the measurements were obtained from a blocked-rotor

test. The result of the fit is shown in Figure 2.6 with associated parameter values in Table 2.1. The low-frequency equivalent circuit of the PMAC machine is shown in Figure 2.7.

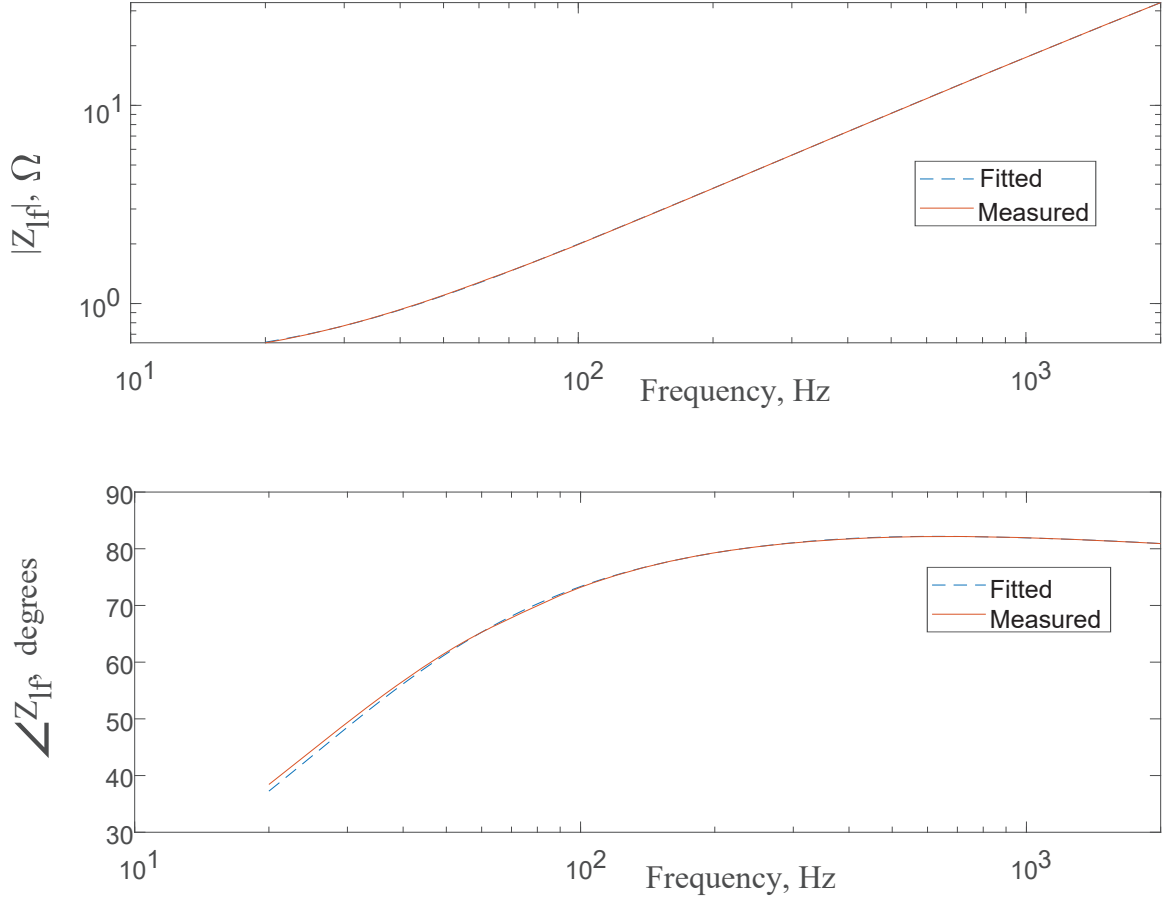


Figure 2.6. Measured and fitted low-frequency per-phase impedance of the PMAC machine.

Table 2.1. Low-frequency model parameters.

Parameter	Value
r_s	0.3465Ω
L_{ls}	$38.487 \mu\text{H}$
$\frac{3}{2}L_{ms}$	0.002 H
r_{d1}	142.5438Ω
L_{d1}	4.9 mH
r_{d2}	72.7298Ω
L_{d2}	21.3 mH

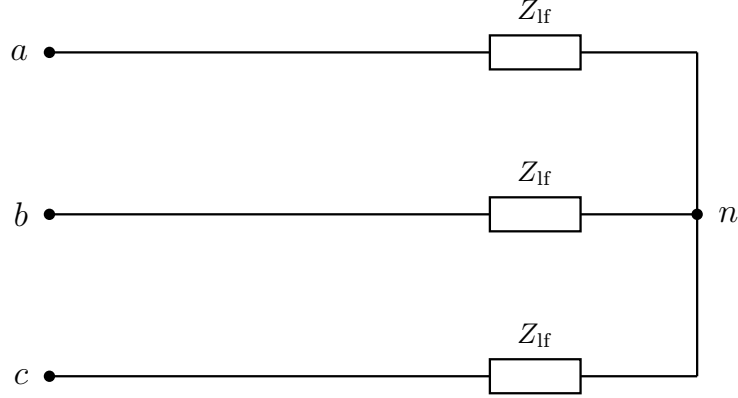


Figure 2.7. Low-frequency per-phase equivalent circuit of PMAC machine.

Open-circuit Test

The flux linkage λ'_m and the number of poles P of the surface-mount PMAC machine also form part of the low-frequency parameters that are needed for the simulation of the machine. The open-circuit test, which was used to establish the relevant parameters, is described.

For this test, the surface-mount PMAC machine was spun clockwise at a mechanical rotor speed of 360 rpm and the open-circuit line-to-line voltages e_{ac} and e_{bc} were captured using a Lecroy 24Xs-A oscilloscope; the corresponding encoder signal data was also captured. From the measured data, the open-circuit phase voltage e_{as} was determined analytically. Herein,

$$\begin{aligned}
 e_{ac} &= e_{as} - e_{cs} \\
 e_{bc} &= e_{bs} - e_{cs} \\
 0 &= e_{as} + e_{bs} + e_{cs}
 \end{aligned} \tag{2.55}$$

From the previous equations, e_{as} may be established from measured data as

$$e_{as} = \frac{2}{3}e_{ac} - \frac{1}{3}e_{bc} \tag{2.56}$$

With the terminals open-circuited, the a -phase voltage takes the form

$$v_{as} = e_{as} = \omega_r \lambda'_m \cos \theta_r \quad (2.57)$$

This implies that the open-circuit voltage e_{as} is a sinusoidal signal. Thus, the data analytically determined from (2.56) was fitted to the equation

$$e_{as} = k_1 \cos \theta_{ra} + k_2 \sin \theta_{ra} = \sqrt{k_1^2 + k_2^2} \cos(\theta_{ra} + \theta_{r,\text{offset}}) \quad (2.58)$$

using the method of least squares. Here,

$$\theta_r = \theta_{ra} + \theta_{r,\text{offset}} \quad (2.59)$$

$$\theta_{r,\text{offset}} = \frac{P}{2} \theta_{\text{offset}} = \tan^{-1}(-k_2/k_1) \quad (2.60)$$

From the least-squares fit solution,

$$k_1 = -8.5334 \text{ V}; \quad k_2 = 0.1012 \text{ V}$$

$$\theta_{r,\text{offset}} = 179.3208^\circ \approx \pi \text{ rad}$$

The results of the least-squares fit superimposed onto the measured data are shown in Figure 2.8. The encoder signal is also shown. From the figure, there are two peaks of the open-circuit voltage in one revolution. Thus, it can be concluded that the number of pole pairs of the machine is two ($P = 4$). Also, from the fitted data, the electrical rotor speed ω_r can be determined and used to establish the flux constant λ'_m by relating the peak of the realized waveform to $\omega_r \lambda'_m$. Table 2.2 summarizes the results for the parameters established.

Table 2.2. Open-circuit characterization results.

Parameter	Value
P	4
λ_m	0.1133 Vs
$\theta_{r,\text{offset}}$	π rad

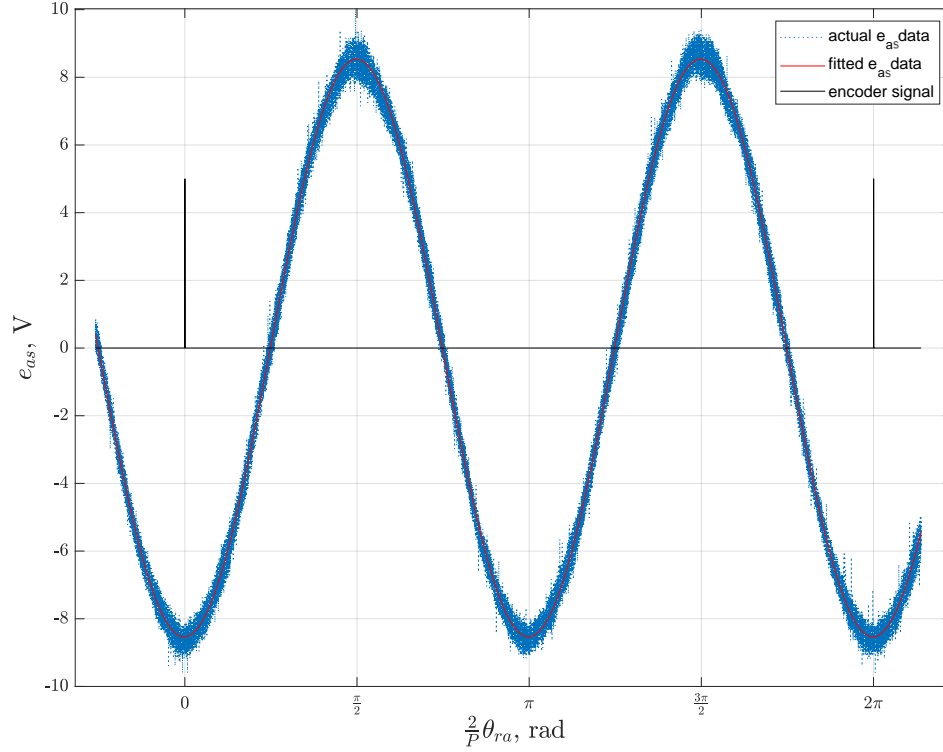


Figure 2.8. Measured and fitted open-circuit voltages.

2.3 Limitations of the Low-Frequency Model

The low-frequency model that has been described may be adequate for predicting the dominant electromechanical characteristics of the surface-mount PMAC machine but it falls short in predicting the undesirable high-frequency effects including transient overvoltages, common-mode (CM) currents and EMI associated with wide-bandgap-based electric drive systems. Accordingly, a wideband model that represents the low- and high-frequency dynamics of the machine is necessary.

The deficiency of the low-frequency model may be seen by comparing the measured DM impedance with that calculated using the low-frequency parameters for a frequency sweep between 20 Hz and 100 MHz. This comparison is illustrated in Figure 2.9. While it has been shown that $Z_q = Z_d = Z_{lf} = 2Z_{in}/3$ for the low-frequency model, it is apparent from

the figure that this relationship should be reviewed for frequencies beyond 100 kHz. Here, the calculated low-frequency impedance fails to match the measured wideband data.

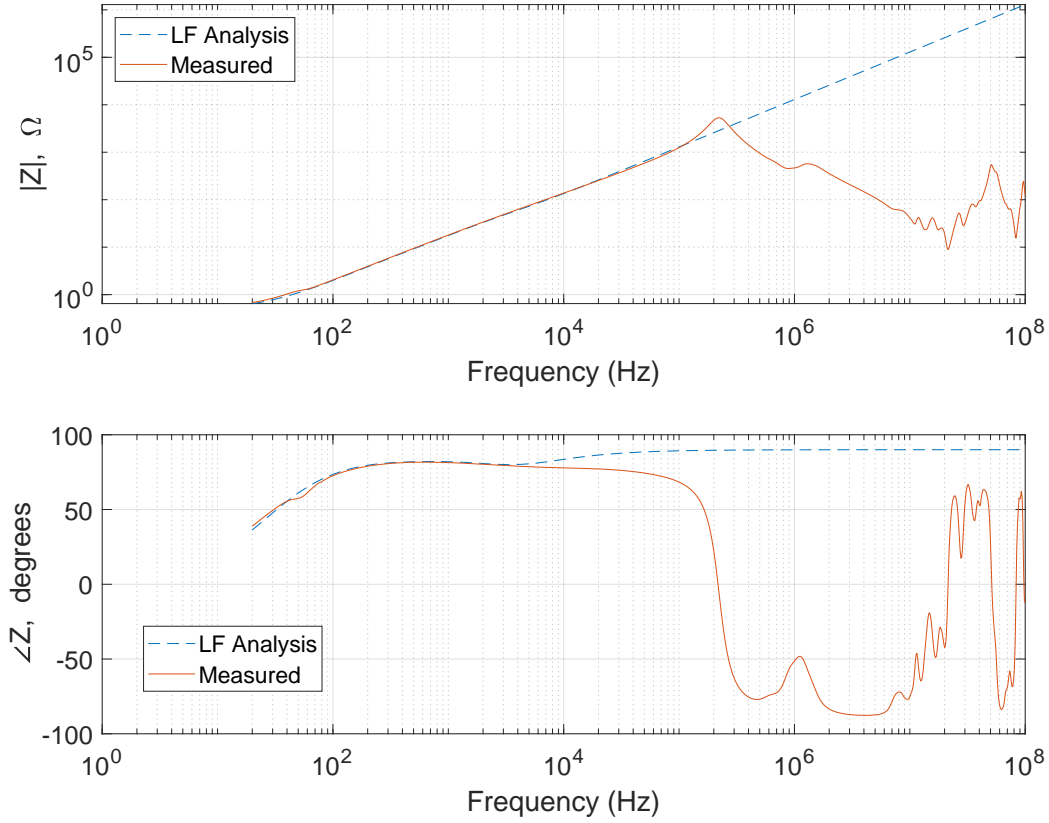


Figure 2.9. Calculated low-frequency impedance compared with measured wideband data.

2.4 Wideband Model

A wideband model of the surface-mount PMAC machine is introduced here. Its need is based on the grounds that fast-switching semiconductor devices introduce undesirable high-frequency effects. The wideband model is realized by including additional branches to the low-frequency circuit model resulting in the equivalent circuit shown in Figure 2.10. Here Z_{lf} , as previously noted, represents the aggregate low-frequency impedance evaluated from

the stator resistance, self inductance, and impedance obtained from simplified expressions of voltage drops due to mutual inductances and eddy current effects. The impedance Z_{C1} is used to denote the parasitic capacitance and resistance between the stator windings and the machine case. In addition, Z_{C2} represents the parasitics (capacitive and resistive) between the neutral point and the motor case. The next section discusses the parameterization of these parasitic components based on differential-mode (DM) and common-mode (CM) test setups.

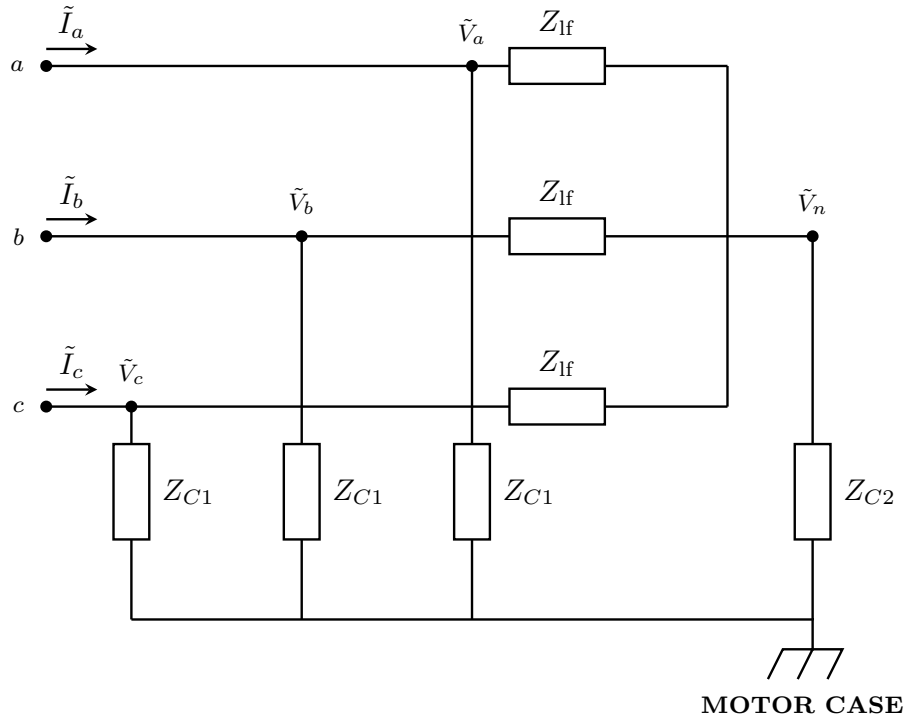


Figure 2.10. Wideband equivalent circuit.

2.5 Parameterization of Wideband Model

To establish the parasitic components introduced in Figure 2.10, DM and CM tests were conducted on the machine as shown in Figure 2.11 and Figure 2.12. As shown, the machine terminals were connected to an impedance analyzer and impedance measurements were taken

across a frequency sweep (20 Hz to 100 MHz). Following the tests, the parameters established in the previous section were held fixed, and the sought-after parameters were treated as genes in a population-based optimization routine to match the measured impedance data.

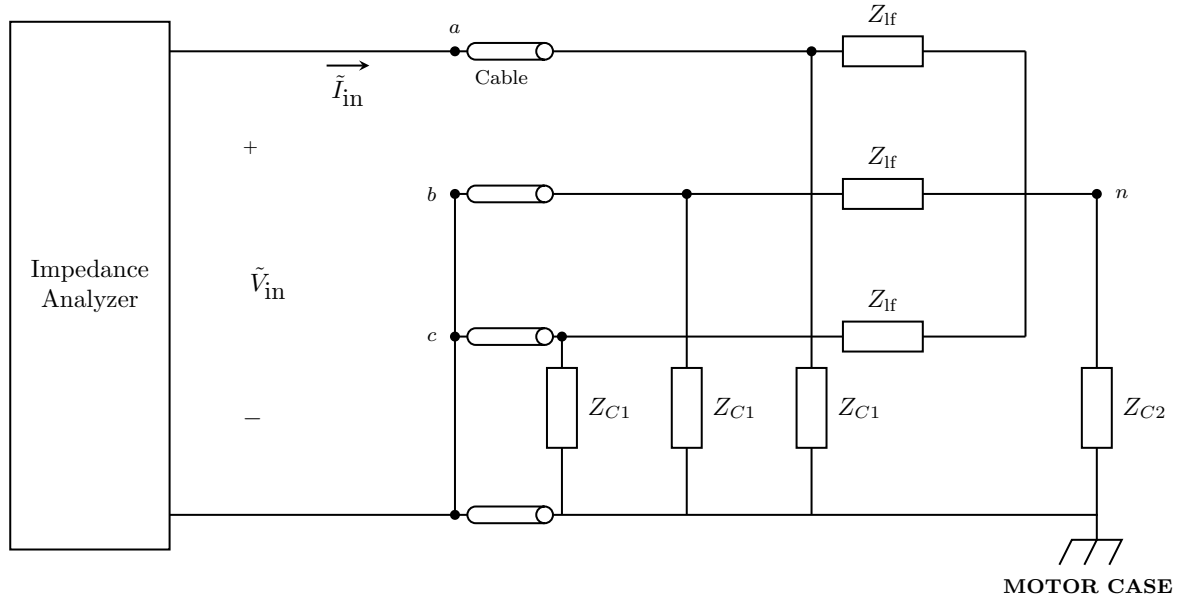


Figure 2.11. Test circuit for DM impedance measurement.

In addition to these parameters, it is important to characterize the cable impedance as well. Rather than attempt to establish a per-phase, magnetically and electrically coupled model for the 4-wire cable connecting the inverter to the machine, the cable and machine can be characterized simultaneously in a DM and CM sense using Clarke's ($\alpha\beta 0$) transformation [59].

The model used to establish the DM and CM test circuits is shown in Figure 2.10. By applying Kirchoff's Current Law, equations relating the voltages seen at the terminals of the machine to the current flowing into the machine can be established. Also, a relationship between the input voltages and the neutral point voltage may be deduced.

Before continuing, it is necessary to define the notations used in describing the relationships. The voltages v_a , v_b , v_c , and v_n will respectively denote the nodal voltages at nodes a ,

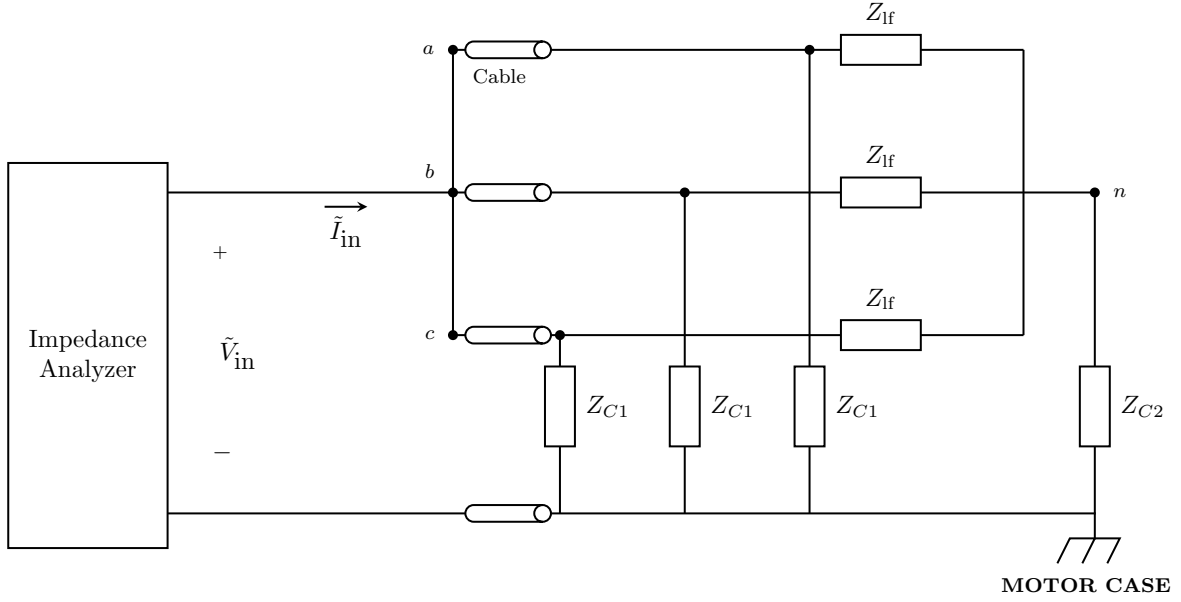


Figure 2.12. Test circuit for CM impedance measurement.

b , c , and n , and their phasor forms will be denoted as \tilde{V}_a , \tilde{V}_b , \tilde{V}_c , and \tilde{V}_n . Also, the currents \tilde{I}_a , \tilde{I}_b , and \tilde{I}_c , will respectively represent the phasor forms of i_a , i_b , and i_c . By applying nodal analysis techniques to the circuit shown in Figure 2.10, it can be shown that

$$\begin{aligned}\tilde{I}_a &= \frac{\tilde{V}_a}{Z_{C1}} + \frac{\tilde{V}_a - \tilde{V}_n}{Z_{lf}} \\ \tilde{I}_b &= \frac{\tilde{V}_b}{Z_{C1}} + \frac{\tilde{V}_b - \tilde{V}_n}{Z_{lf}}\end{aligned}\tag{2.61}$$

$$\tilde{I}_c = \frac{\tilde{V}_c}{Z_{C1}} + \frac{\tilde{V}_c - \tilde{V}_n}{Z_{lf}}$$

$$\frac{\tilde{V}_n}{Z_{C2}} = \frac{\tilde{V}_a - \tilde{V}_n}{Z_{lf}} + \frac{\tilde{V}_b - \tilde{V}_n}{Z_{lf}} + \frac{\tilde{V}_c - \tilde{V}_n}{Z_{lf}}\tag{2.62}$$

Solving for \tilde{V}_n in (2.62) and substituting the resulting expression into (2.61), gives the resulting matrix equation,

$$\begin{bmatrix} \tilde{I}_a \\ \tilde{I}_b \\ \tilde{I}_c \end{bmatrix} = \begin{bmatrix} a-b & -b & -b \\ -b & a-b & -b \\ -b & -b & a-b \end{bmatrix} \begin{bmatrix} \tilde{V}_a \\ \tilde{V}_b \\ \tilde{V}_c \end{bmatrix} \quad (2.63)$$

where

$$a = \frac{1}{Z_{C1}} + \frac{1}{Z_{lf}}$$

and

$$b = \frac{Z_{C2}}{Z_{lf}(3Z_{C2} + Z_{lf})}$$

By applying Clarke's transformation to (2.63), the $\alpha\beta 0$ variables may be established as

$$\begin{bmatrix} \tilde{I}_\alpha \\ \tilde{I}_\beta \\ \tilde{I}_0 \end{bmatrix} = C \begin{bmatrix} a-b & -b & -b \\ -b & a-b & -b \\ -b & -b & a-b \end{bmatrix} C^{-1} \begin{bmatrix} \tilde{V}_\alpha \\ \tilde{V}_\beta \\ \tilde{V}_0 \end{bmatrix} \quad (2.64)$$

where

$$C = \frac{2}{3} \begin{bmatrix} 1 & -\frac{1}{2} & -\frac{1}{2} \\ 0 & -\frac{\sqrt{3}}{2} & \frac{\sqrt{3}}{2} \\ \frac{1}{2} & \frac{1}{2} & \frac{1}{2} \end{bmatrix}$$

Evaluating (2.64), a simplified admittance equation may be realized as

$$\begin{bmatrix} \tilde{I}_\alpha \\ \tilde{I}_\beta \\ \tilde{I}_0 \end{bmatrix} = \begin{bmatrix} a & 0 & 0 \\ 0 & a & 0 \\ 0 & 0 & a-3b \end{bmatrix} \begin{bmatrix} \tilde{V}_\alpha \\ \tilde{V}_\beta \\ \tilde{V}_0 \end{bmatrix} \quad (2.65)$$

As such, it can be deduced from (2.65) that for the alpha and beta components, the impedance of the motor is $1/a$, the parallel combination of the phase-terminal-to-case impedance Z_{C1} and the per-phase low-frequency impedance Z_{lf} . Further, the zero-sequence impedance is

$1/(a - 3b)$. By careful manipulation, it can be shown that $1/(a - 3b)$ is equivalent to the parallel combination of the phase-terminal-to-case impedance Z_{C1} with the series combination of the low-frequency zero-sequence motor impedance and thrice the neutral-point-to-case impedance $Z_{lf,0s} + 3Z_{C2}$. It is important to note that at low frequencies, the term $Z_{lf,0s}$ in $(Z_{lf,0s} + 3Z_{C2})$ is inconsequential as Z_{C2} , which is capacitive, is as an open circuit. As such, the zero-sequence impedance of the motor is simply the parallel combination of the phase-terminal-to-case impedance Z_{C1} and thrice the neutral-point-to-case impedance $3Z_{C2}$.

The alpha- beta- and zero-sequence impedances are the bases from which the DM and CM impedances can be determined. For the DM test circuit shown in Figure 2.11, it can be shown that the measured Thévenin impedance is equal to three-halves times the alpha-sequence impedance. As such, the alpha-sequence impedance, which is equal to the beta-sequence impedance, was obtained by scaling the measured impedance by two-thirds and then extracting parameters for the wideband DM equivalent circuit shown in Figure 2.13 using GOSET.

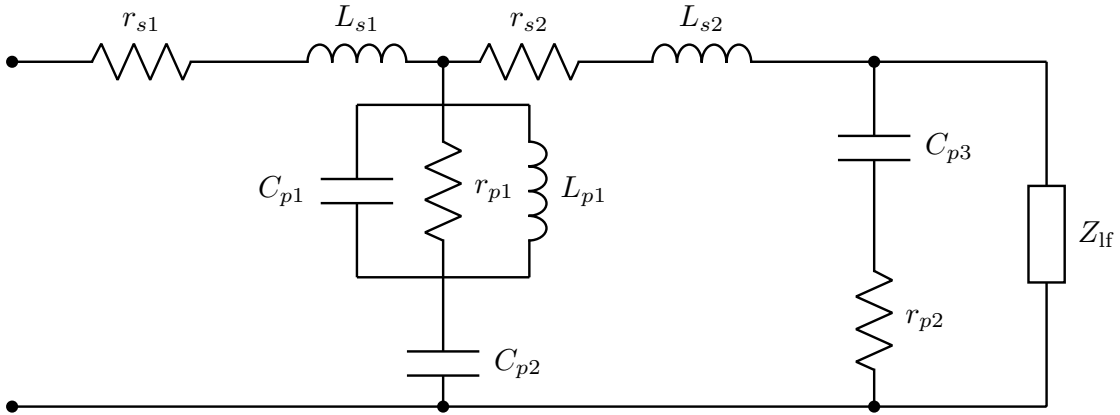


Figure 2.13. Wideband DM equivalent circuit.

Here, parameters r_{s1} , L_{s1} , r_{s2} , L_{s2} , C_{p1} , r_{p1} , L_{p1} , and C_{p2} represent attributes of the machine's cable impedance; r_{s1} , L_{s1} , r_{s2} , and L_{s2} represent segments of the cable's aggregate resistance and inductance; C_{p2} represents the capacitance between wires and its susceptibility

to fluctuations with changing frequency is reason for the parallel rLC branch composed of r_{p1} , L_{p1} , and C_{p1} . The series rC branch of r_{p2} and C_{p3} represents the previously described phase-terminal-to-case impedance Z_{C1} and Z_{lf} is the aggregate low-frequency impedance. The measured and fitted impedance are shown in Figure 2.14 with associated parameters in Table 2.3.

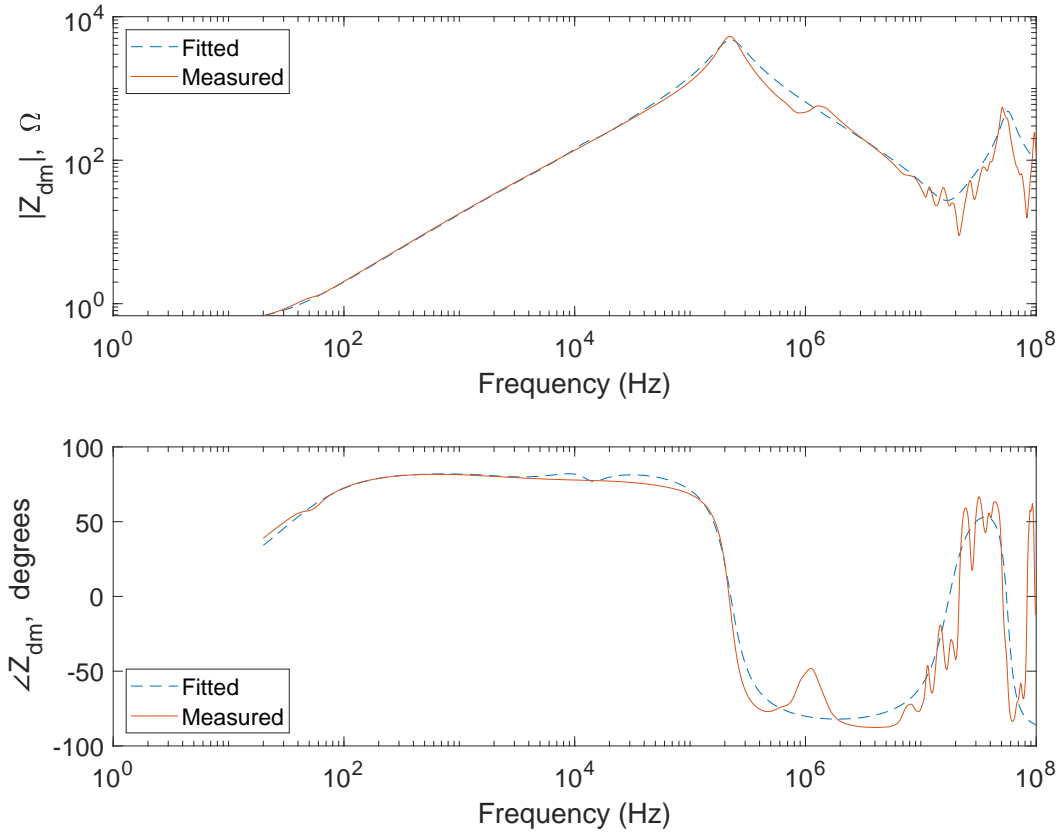


Figure 2.14. Measured and fitted wideband DM impedance.

For the CM test circuit shown in Figure 2.12, the measured Thèvenin impedance can be shown to be equal to one-third times the zero-sequence impedance. Thus, the zero-sequence impedance was obtained by scaling the measured impedance by three and then extracting the associated parameters of the wideband CM equivalent circuit shown in Figure 2.15. As in Figure 2.13, r_{s3} , L_{s3} , r_{s4} , and L_{s4} represent portions of the cable's aggregate resistance and

Table 2.3. DM equivalent circuit parameters.

Parameter	Value
r_{s1}	12 m Ω
L_{s1}	1.2019 pH
r_{s2}	17.9 m Ω
L_{s2}	246.76 nH
C_{p1}	35.413 pF
r_{p1}	3.219 k Ω
L_{p1}	2.1 mH
C_{p2}	6.4855 nF
C_{p3}	346.33 pF
r_{p2}	18.4772 Ω

inductance; C_{p5} represents the capacitance between wires and the rLC branch, composed of r_{p3} , L_{p2} , and C_{p4} , makes up for the fluctuations in the capacitance between wires. The series rC branch of r_{p4} and C_{p6} represents the parallel combination of the phase-terminal-to-case impedance and thrice the neutral-point-to-case impedance $\frac{3Z_{C2}Z_{C1}}{Z_{C1} + 3Z_{C2}}$. The measured and fitted impedance are shown in Figure 2.16 with associated parameters in Table 2.4.

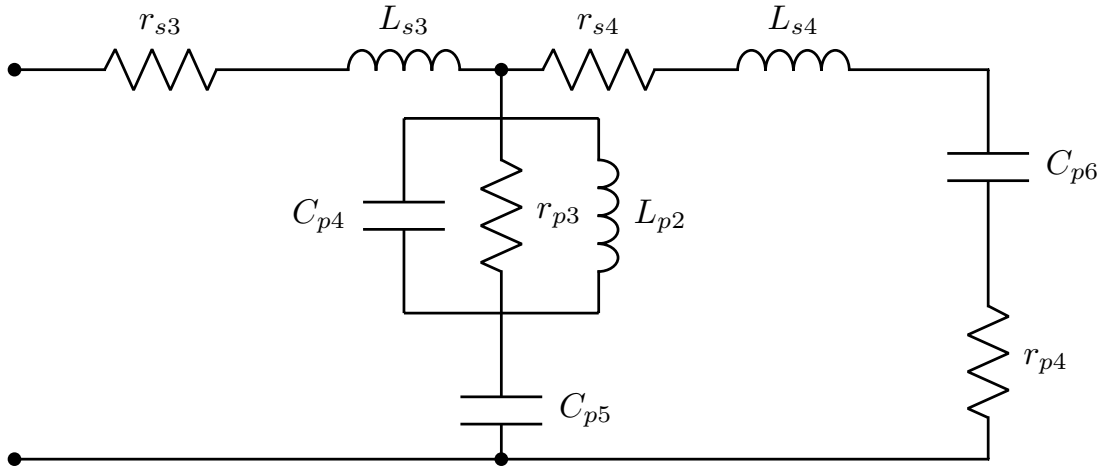


Figure 2.15. Wideband CM equivalent circuit.

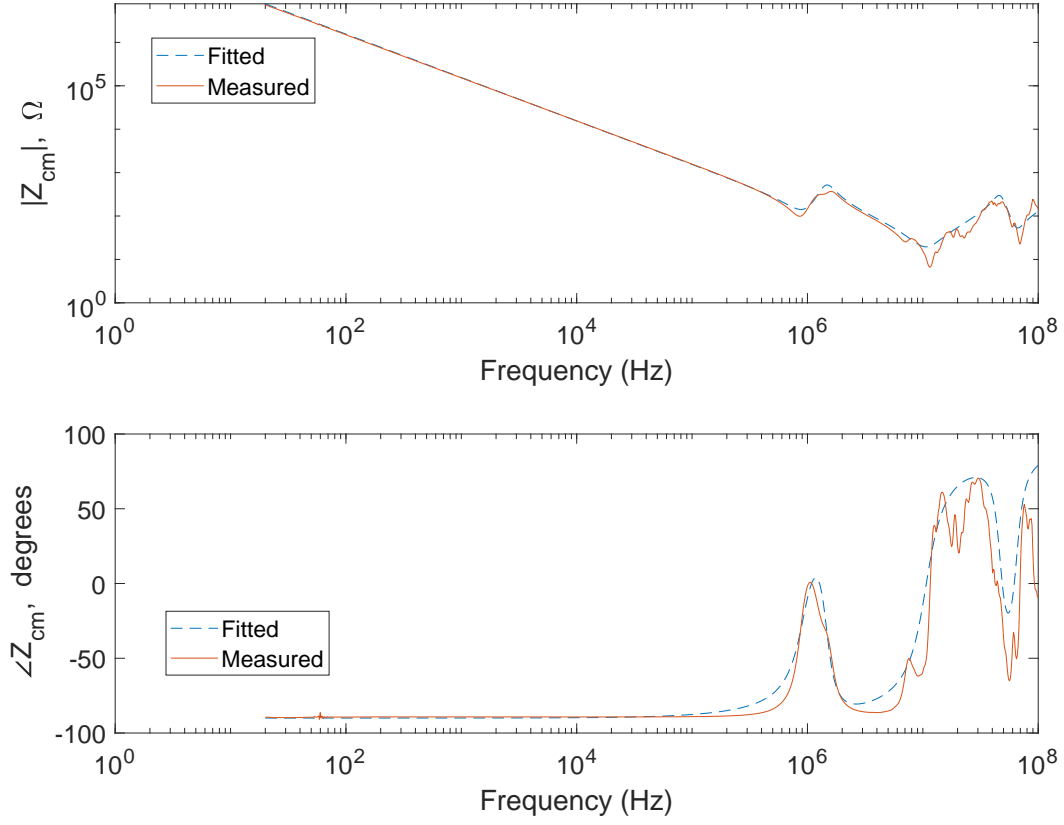


Figure 2.16. Measured and fitted wideband CM impedance.

Table 2.4. CM equivalent circuit parameters.

Parameter	Value
r_{s3}	55.6026 Ω
L_{s3}	799.42 nH
r_{s4}	39.7 m Ω
L_{s4}	142.52 μ H
C_{p4}	17.16 pF
r_{p3}	793.23 Ω
L_{p2}	672.32 nH
C_{p5}	146.58 pF
C_{p6}	195.65 pF
r_{p4}	419.86 Ω

2.6 Complete Large-Displacement Wideband Model

The wideband DM and CM equivalent circuits portray the small displacement dynamic characteristics of the PMAC machine and cable. The large-displacement model is depicted in Figure 2.17. Therein, v_{ag} , v_{bg} , and v_{cg} denote the phase-to-ground voltages at the cable terminals. These are transformed into the so-called stationary reference frame using

$$\begin{bmatrix} v_{qL}^s \\ v_{dL}^s \\ v_{0L} \end{bmatrix} = \frac{2}{3} \begin{bmatrix} 1 & -\frac{1}{2} & -\frac{1}{2} \\ 0 & -\frac{\sqrt{3}}{2} & \frac{\sqrt{3}}{2} \\ \frac{1}{2} & \frac{1}{2} & \frac{1}{2} \end{bmatrix} \begin{bmatrix} v_{ag} \\ v_{bg} \\ v_{cg} \end{bmatrix} \quad (2.66)$$

The q , d , and 0 components in the stationary reference frame are equivalent to the α , β , and 0 components of Clarke's transformation. The transformed voltages are coupled to the DM and CM circuits using dependent sources. The DM and CM circuits are, in turn, coupled to a large-displacement low-frequency model of the PMAC machine using dependent current sources.

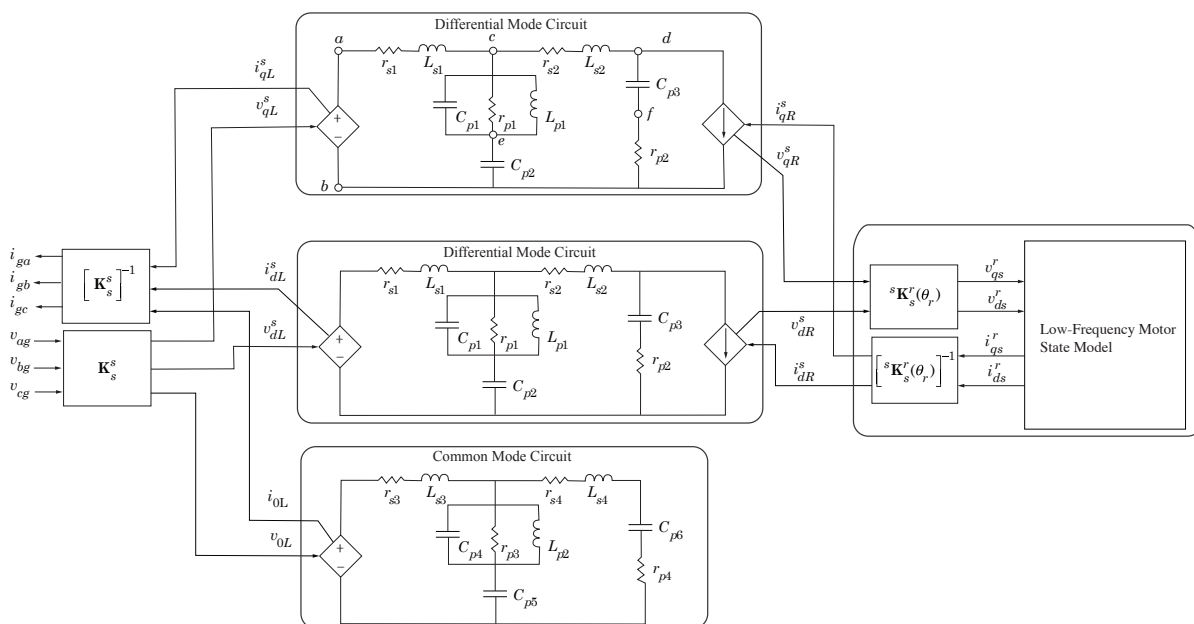


Figure 2.17. Complete large-displacement wideband model of the surface-mount PMAC machine.

The DM currents at the cable terminals are denoted as i_{qL}^s , i_{dL}^s , and the CM current as i_{0L} . These are transformed back to physical variables using

$$\begin{bmatrix} i_{ga} \\ i_{gb} \\ i_{gc} \end{bmatrix} = \begin{bmatrix} 1 & 0 & 1 \\ -\frac{1}{2} & -\frac{\sqrt{3}}{2} & 1 \\ -\frac{1}{2} & \frac{\sqrt{3}}{2} & 1 \end{bmatrix} \begin{bmatrix} i_{qL}^s \\ i_{dL}^s \\ i_{0L} \end{bmatrix} \quad (2.67)$$

The physical currents are supplied to the wideband inverter model described in the next chapter. The inverter model will supply the input voltages to the large-displacement wideband model of Figure 2.17.

2.7 Modal Frequencies of the Wideband Model

From the established wideband model, the state-space representation of the high-frequency DM and CM dynamics may be established. The DM circuit in Figure 2.17 is shown again in Figure 2.18 from which the following linear differential equations can be established.

$$p i_{Ls1} = \frac{1}{L_{s1}} \left[-r_{s1} i_{Ls1} - v_{cp1} - v_{cp2} + v_{qL}^s \right] \quad (2.68)$$

$$p i_{Ls2} = \frac{1}{L_{s2}} \left[-r_{s2} i_{Ls2} + v_{cp1} + v_{cp2} - v_{cp3} - r_{p2} (i_{Ls2} - i_{qR}^s) \right] \quad (2.69)$$

$$p i_{Lp1} = \frac{1}{L_{p1}} v_{cp1} \quad (2.70)$$

$$p v_{cp1} = \frac{1}{C_{p1}} \left[i_{Ls1} - i_{Ls2} - i_{Lp1} - v_{cp1}/r_{p1} \right] \quad (2.71)$$

$$p v_{cp2} = \frac{1}{C_{p2}} \left[i_{Ls1} - i_{Ls2} \right] \quad (2.72)$$

$$p v_{cp3} = \frac{1}{C_{p3}} \left[i_{Ls2} - i_{qR}^s \right] \quad (2.73)$$

where v_{cp1} , v_{cp2} , and v_{cp3} are the voltages across the respective capacitors, C_{p1} , C_{p2} , and C_{p3} represented in the circuit. Furthermore, the output voltage, v_{qR}^s and current i_{qL}^s may be expressed as

$$v_{qR}^s = v_{cp3} + r_{p2} \left[i_{Ls2} - i_{qR}^s \right] \quad (2.74)$$

$$i_{qL}^s = -i_{Ls1} \quad (2.75)$$

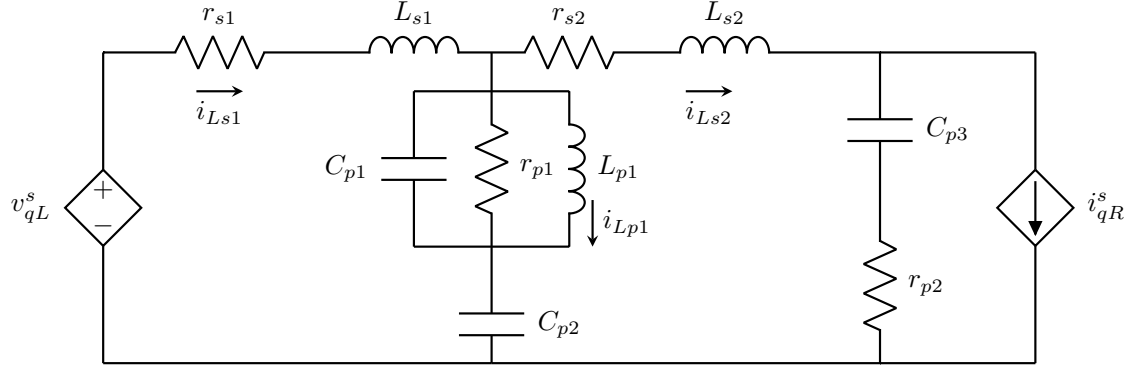


Figure 2.18. DM circuit.

The state equations for the DM circuit may be represented as

$$p \begin{bmatrix} i_{Ls1} \\ i_{Ls2} \\ i_{Lp1} \\ v_{cp1} \\ v_{cp2} \\ v_{cp3} \end{bmatrix} = \mathbf{A}_{\text{dm}} \begin{bmatrix} i_{Ls1} \\ i_{Ls2} \\ i_{Lp1} \\ v_{cp1} \\ v_{cp2} \\ v_{cp3} \end{bmatrix} + \mathbf{B}_{\text{dm}} \begin{bmatrix} v_{qL}^s \\ i_{qR}^s \end{bmatrix} \quad (2.76)$$

where

$$\mathbf{A}_{\text{dm}} = \begin{bmatrix} -r_{s1}/L_{s1} & 0 & 0 & -1/L_{s1} & -1/L_{s1} & 0 \\ 0 & -(r_{s2} + r_{p2})/L_{s2} & 0 & 1/L_{s2} & 1/L_{s2} & -1/L_{s2} \\ 0 & 0 & 0 & 1/L_{p1} & 0 & 0 \\ 1/C_{p1} & -1/C_{p1} & -1/C_{p1} & -1/(r_{p1}C_{p1}) & 0 & 0 \\ 1/C_{p2} & -1/C_{p2} & 0 & 0 & 0 & 0 \\ 0 & 1/C_{p3} & 0 & 0 & 0 & 0 \end{bmatrix}$$

and

$$\mathbf{B}_{\text{dm}} = \begin{bmatrix} 1/L_{s1} & 0 \\ 0 & r_{p2}/L_{s2} \\ 0 & 0 \\ 0 & 0 \\ 0 & 0 \\ 0 & -1/C_{p3} \end{bmatrix}$$

In addition, the output equations may be represented as

$$\begin{bmatrix} i_{qL}^s \\ v_{qR}^s \end{bmatrix} = \mathbf{C}_{\text{dm}} \begin{bmatrix} i_{Ls1} \\ i_{Ls2} \\ i_{Lp1} \\ v_{cp1} \\ v_{cp2} \\ v_{cp3} \end{bmatrix} + \mathbf{D}_{\text{dm}} \begin{bmatrix} v_{qL}^s \\ i_{qR}^s \end{bmatrix} \quad (2.77)$$

where

$$\mathbf{C}_{\text{dm}} = \begin{bmatrix} -1 & 0 & 0 & 0 & 0 & 0 \\ 0 & r_{p2} & 0 & 0 & 0 & 1 \end{bmatrix}; \quad \mathbf{D}_{\text{dm}} = \begin{bmatrix} 0 & 0 \\ 0 & -r_{p2} \end{bmatrix}$$

From the state equations, the frequency modes associated with the DM circuit may be determined. In particular, the eigenvalues of the matrix \mathbf{A}_{dm} provide a means for determining the damped, ω_d , and natural, ω_n , frequencies as well as the damping ratios, ζ . The magnitudes of the real parts of the eigenvalues give the products of the damping ratios and the natural frequencies i.e. $\zeta\omega_n$; the imaginary parts give the damped frequencies and their absolute values the natural frequencies. Using the parameters of the wideband model, the eigenvalues of \mathbf{A}_{dm} are evaluated as: $-4.9964 \times 10^9 \pm j1.5362 \times 10^{11}$, $-3.7488 \times 10^7 \pm j1.0147 \times 10^8$, and $-2.3823 \times 10^4 \pm j2.6918 \times 10^5$. As such the three damped frequencies $\{1.5362 \times 10^{11}$, 1.0147×10^8 , $2.6918 \times 10^5\}$ rad/s that are associated with the DM circuit correspond to the

natural frequencies $\{1.5370 \times 10^{11}, 1.0817 \times 10^8, 2.7023 \times 10^5\}$ rad/s and damping ratios $\{0.0325, 0.3466, 0.0882\}$.

It can be inferred from these results that there are three modes associated with the DM circuit. For classification purposes, each mode may be designated as one of

- ultra-high-frequency mode
- high-frequency mode
- low-frequency mode

The frequencies and damping ratios for each mode that is represented are given in Table 2.5.

Table 2.5. Frequency modes of the DM circuit.

Mode	ω_n (rad/s)	f_n	ζ
Ultra-high-frequency	1.5370×10^{11}	24.462 GHz	0.0325
High-frequency	1.0817×10^8	17.216 MHz	0.3466
Low-frequency	2.7023×10^5	43.009 kHz	0.0882

The results of this analysis imply that the cable parameters have a moderate effect on the low-frequency dynamics of the machine. This discovery will have an impact on the new simulation framework that is set forth in Chapter 5.

In the same vein, the modal frequencies of the CM circuit shown in Figure 2.19 may be established. Here, the state and output equations are given as

$$p \begin{bmatrix} i_{Ls3} \\ i_{Ls4} \\ i_{Lp2} \\ v_{cp4} \\ v_{cp5} \\ v_{cp6} \end{bmatrix} = \mathbf{A}_{\text{cm}} \begin{bmatrix} i_{Ls3} \\ i_{Ls4} \\ i_{Lp2} \\ v_{cp4} \\ v_{cp5} \\ v_{cp6} \end{bmatrix} + \mathbf{B}_{\text{cm}} \begin{bmatrix} v_{0L} \end{bmatrix} \quad (2.78)$$

$$i_{0L} = \mathbf{C}_{\text{cm}} \begin{bmatrix} i_{Ls3} \\ i_{Ls4} \\ i_{Lp2} \\ v_{cp4} \\ v_{cp5} \\ v_{cp6} \end{bmatrix} \quad (2.79)$$

where v_{cp4} , v_{cp5} , and v_{cp6} are the voltages across the respective capacitors, C_{p4} , C_{p5} , and C_{p6} of the CM circuit, and the matrices \mathbf{A}_{cm} , \mathbf{B}_{cm} , and \mathbf{C}_{cm} are

$$\mathbf{A}_{\text{cm}} = \begin{bmatrix} -r_{s3}/L_{s3} & 0 & 0 & -1/L_{s3} & -1/L_{s3} & 0 \\ 0 & -(r_{s4} + r_{p4})/L_{s4} & 0 & 1/L_{s4} & 1/L_{s4} & -1/L_{s4} \\ 0 & 0 & 0 & 1/L_{p2} & 0 & 0 \\ 1/C_{p4} & -1/C_{p4} & -1/C_{p4} & -1/(r_{p3}C_{p4}) & 0 & 0 \\ 1/C_{p5} & -1/C_{p5} & 0 & 0 & 0 & 0 \\ 0 & 1/C_{p6} & 0 & 0 & 0 & 0 \end{bmatrix}$$

$$\mathbf{B}_{\text{cm}} = \begin{bmatrix} 1/L_{s3} \\ 0 \\ 0 \\ 0 \\ 0 \\ 0 \end{bmatrix}; \quad \mathbf{C}_{\text{cm}} = \begin{bmatrix} -1 & 0 & 0 & 0 & 0 & 0 \end{bmatrix}$$

As in the case of the DM circuit, three pairs of damped and natural frequencies may be derived from the eigenvalues of \mathbf{A}_{cm} which are $-5.2705 \times 10^7 \pm j4.0303 \times 10^8$, $-1.8613 \times 10^7 \pm j6.4364 \times 10^7$, and $-1.6650 \times 10^6 \pm j5.7442 \times 10^6$; their corresponding damping ratios are 0.1297, 0.2778, and 0.2784, respectively. Based on the magnitudes of the natural frequencies, all of the modes are classified as *high-frequency* and are summarized in Table 2.6.

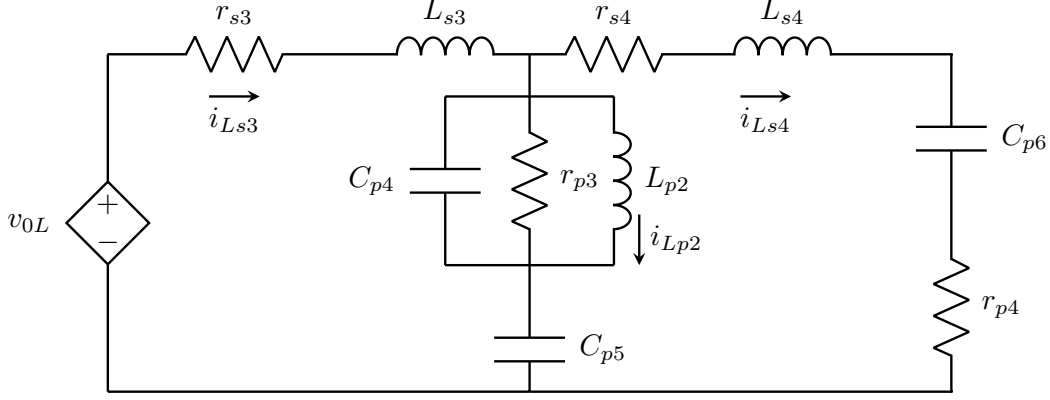


Figure 2.19. CM circuit.

Table 2.6. Frequency modes of the CM circuit.

Mode	ω_n (rad/s)	f_n	ζ
High-frequency	4.0646×10^8	64.690 MHz	0.1297
High-frequency	6.7001×10^7	10.664 MHz	0.2778
High-frequency	5.9807×10^6	0.9519 MHz	0.2784

The wideband model of the machine may be symbolically illustrated by the block diagram representation shown in Figure 2.20. It should be noted that the state \mathbf{x} of the DM state model is distinct from that of the CM state model. For the DM state model, $\mathbf{x} = [i_{Ls1}, i_{Ls2}, i_{Lp1}, v_{cp1}, v_{cp2}, v_{cp3}]^T$ as demonstrated by (2.76); and based on (2.78), $\mathbf{x} = [i_{Ls3}, i_{Ls4}, i_{Lp2}, v_{cp4}, v_{cp5}, v_{cp6}]^T$ for the CM state model. The block diagram representation of the wideband model will be useful for establishing a computer simulation of the complete electric drive system. This will be part of the discussion of Chapter 5.

2.8 Alternative Formulation of the Wideband Model

The state-based representation of the wideband model described heretofore was derived from the circuit-based representation of the dynamics of the PMAC machine and cable. Instead of relying on the circuit-based model, the state-space-based wideband model may be realized directly from the measured wideband data. An alternative approach to realizing the state-based wideband model shown in Figure 2.20 is described here.

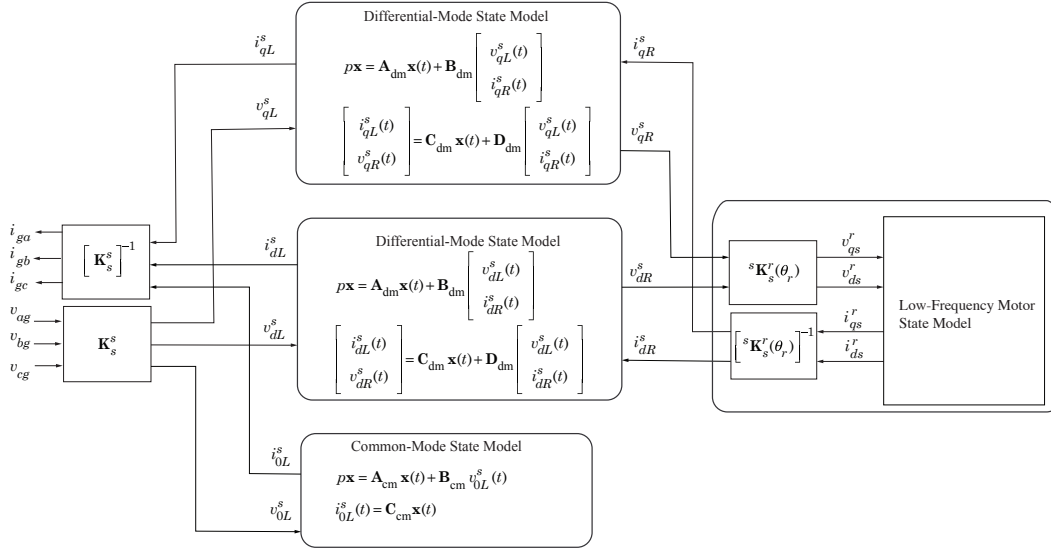


Figure 2.20. State-space-based wideband model of the PMAC machine and cable.

Low-Frequency State Model

Data taken from the low-frequency differential mode test for a frequency sweep between 20 Hz and 2 kHz may be fitted to the state-based form given by

$$p\mathbf{x} = \mathbf{A}_{lf}\mathbf{x} + \mathbf{B}_{lf}\mathbf{u} \quad (2.80)$$

$$\mathbf{y} = \mathbf{C}_{lf}\mathbf{x} \quad (2.81)$$

where the input \mathbf{u} can be voltage quantities v^s_{qR} or v^s_{dR} and the output \mathbf{y} can be current i^s_{qR} or i^s_{dR} . In the model, the matrix \mathbf{A}_{lf} may be set up such that its eigenvalues are $-\alpha_1 \pm j\omega_1$ and $-\alpha_2$ to make

$$\mathbf{A}_{lf} = \begin{bmatrix} -\alpha_1 & -\omega_1 & 0 \\ \omega_1 & -\alpha_1 & 0 \\ 0 & 0 & -\alpha_2 \end{bmatrix}$$

Also, \mathbf{B}_{lf} may be in the form $\mathbf{B}_{\text{lf}} = \begin{bmatrix} b_1 & b_2 & b_3 \end{bmatrix}^T$ and \mathbf{C}_{lf} in the form $\mathbf{C}_{\text{lf}} = \begin{bmatrix} 1 & 1 & 1 \end{bmatrix}$. From these definitions, the transfer admittance relating the output \mathbf{y} to the input \mathbf{u} can be evaluated in the Laplace domain as

$$\frac{\mathbf{Y}(s)}{\mathbf{U}(s)} = \mathbf{C}_{\text{lf}}[s\mathbf{I}_3 - \mathbf{A}_{\text{lf}}]^{-1}\mathbf{B}_{\text{lf}} \equiv \mathbf{L}(s) \quad (2.82)$$

where \mathbf{I}_3 is a 3×3 identity matrix. The transfer admittance is basis for the fit that is necessary for establishing the parameters α_1 , ω_1 , α_2 , b_1 , b_2 , and b_3 . A curve fitting routine yielded the fitted characteristics shown in Figure 2.21. The associated parameters are given in Table 2.7.

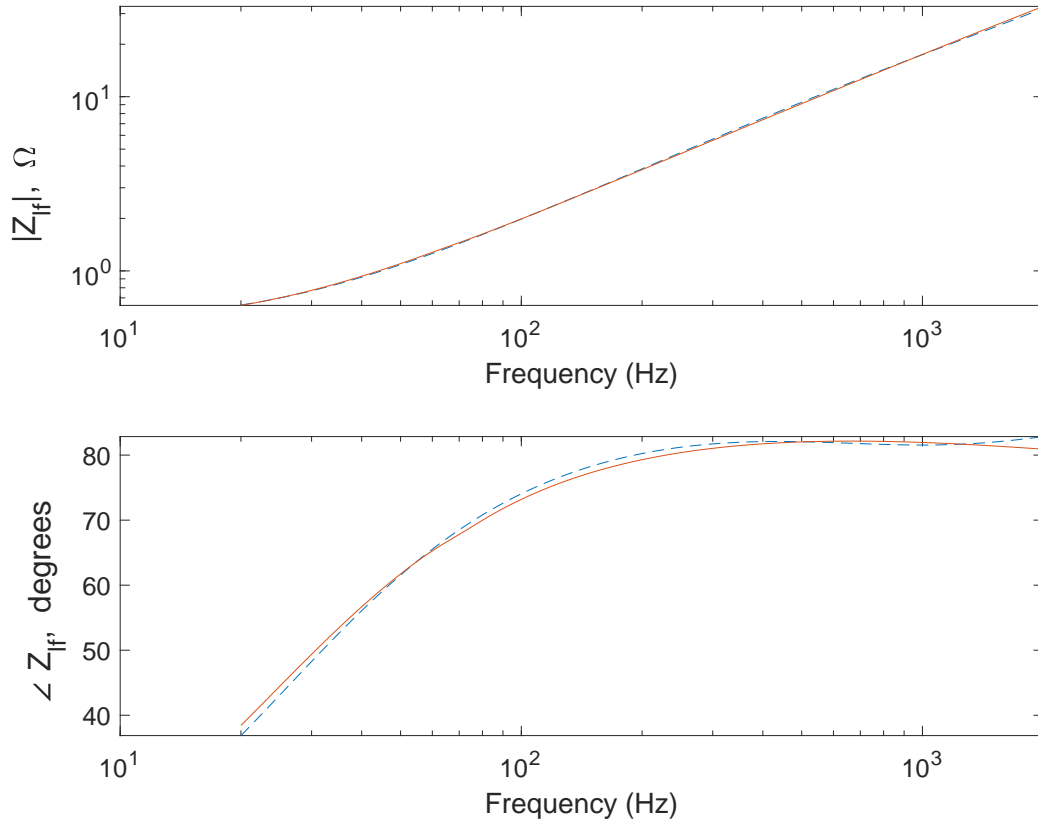


Figure 2.21. Measured and fitted low-frequency per-phase impedance using the state-space-based approach.

Table 2.7. Low-frequency state model parameters.

Parameter	Value
α_1	9.1182×10^3
ω_1	1×10^3
α_2	166.2451
b_1	89.4127
b_2	51.4459
b_3	488.0888

Wideband Differential Mode State Model

The wideband DM state model represented in Figure 2.20 may be established by considering the low-frequency state model in the routine to establish a curve fit to the measured wideband DM characteristics shown in Figure 2.14. Therein, the DM state model of the machine cable and parasitics is expressed as

$$p\mathbf{x} = \mathbf{A}_{\text{dm}}\mathbf{x} + \mathbf{B}_{\text{dm}}\mathbf{u} \quad (2.83)$$

$$\mathbf{y} = \mathbf{C}_{\text{dm}}\mathbf{x} + \mathbf{D}_{\text{dm}}\mathbf{u} \quad (2.84)$$

Here, the output \mathbf{y} and the input \mathbf{u} are respectively given as

$$\mathbf{y} = \begin{bmatrix} i_{\delta L}^s & v_{\delta R}^s \end{bmatrix}^T \quad \text{and} \quad \mathbf{u} = \begin{bmatrix} v_{\delta L}^s & i_{\delta R}^s \end{bmatrix}^T$$

where δ denotes q or d for the q - and d -axis, respectively and the superscript s denotes the stationary reference frame. For notational convenience, the superscript s is dropped in the rest of this section.

In realizing a fit to the wideband data, the matrix \mathbf{A}_{dm} may be formed such that its eigenvalues are $-\alpha_1 \pm j\omega_1$, $-\alpha_2 \pm j\omega_2$, and $-\alpha_3 \pm j\omega_3$. Specifically,

$$\mathbf{A}_{\text{dm}} = \begin{bmatrix} -\alpha_1 & -\omega_1 & 0 & 0 & 0 & 0 \\ \omega_1 & -\alpha_1 & 0 & 0 & 0 & 0 \\ 0 & 0 & -\alpha_2 & -\omega_2 & 0 & 0 \\ 0 & 0 & \omega_2 & -\alpha_2 & 0 & 0 \\ 0 & 0 & 0 & 0 & -\alpha_3 & -\omega_3 \\ 0 & 0 & 0 & 0 & \omega_3 & -\alpha_3 \end{bmatrix}$$

Moreover, \mathbf{B}_{dm} , \mathbf{C}_{dm} , and \mathbf{D}_{dm} can be respectively expressed in the forms,

$$\mathbf{B}_{\text{dm}} = \begin{bmatrix} b_1 & b_2 & b_3 & b_4 & b_5 & b_6 \\ 0 & 0 & 0 & 0 & b_7 & b_8 \end{bmatrix}^T, \quad \mathbf{C}_{\text{dm}} = \begin{bmatrix} 1 & 0 & 1 & 0 & 1 & 0 \\ 1 & 0 & 1 & 0 & 1 & 0 \end{bmatrix}, \quad \text{and}$$

$$\mathbf{D}_{\text{dm}} = \begin{bmatrix} d_1 & d_2 \\ d_3 & d_4 \end{bmatrix}$$

Using these definitions, the output may be expressed in the Laplace domain as

$$\mathbf{Y}(s) = [\mathbf{C}_{\text{dm}}[sI_6 - \mathbf{A}_{\text{dm}}]^{-1}\mathbf{B}_{\text{dm}} + \mathbf{D}_{\text{dm}}] \mathbf{U}(s) \equiv \mathbf{T}_{\text{dm}}(s)\mathbf{U}(s) \quad (2.85)$$

where $\mathbf{Y}(s) = \begin{bmatrix} I_{\delta L}(s) & V_{\delta R}(s) \end{bmatrix}^T$, $\mathbf{U}(s) = \begin{bmatrix} V_{\delta L}(s) & I_{\delta R}(s) \end{bmatrix}^T$, and I_6 is a 6×6 identity matrix. The output and input are related to the low-frequency state model as shown in Figure 2.22.

From surveying the block diagram given by Figure 2.22, the output-input relationship may be revised as

$$\begin{bmatrix} I_{\delta L}(s) \\ V_{\delta R}(s) \end{bmatrix} = \mathbf{T}_{\text{dm}}(s) \begin{bmatrix} V_{\delta L}(s) \\ I_{\delta R}(s) \end{bmatrix} \quad (2.86)$$

Assuming the measured wideband DM impedance may be represented in the Laplace domain as $\mathbf{H}^{-1}(s)$, it follows that

$$\begin{bmatrix} I_{\delta L}(s) \\ V_{\delta R}(s) \end{bmatrix} = \begin{bmatrix} \mathbf{H}(s)V_{\delta L}(s) \\ \mathbf{L}^{-1}(s)I_{\delta R}(s) \end{bmatrix} \equiv \begin{bmatrix} \mathbf{H}(s) & 0 \\ 0 & \mathbf{L}^{-1}(s) \end{bmatrix} \begin{bmatrix} V_{\delta L}(s) \\ I_{\delta R}(s) \end{bmatrix} \quad (2.87)$$

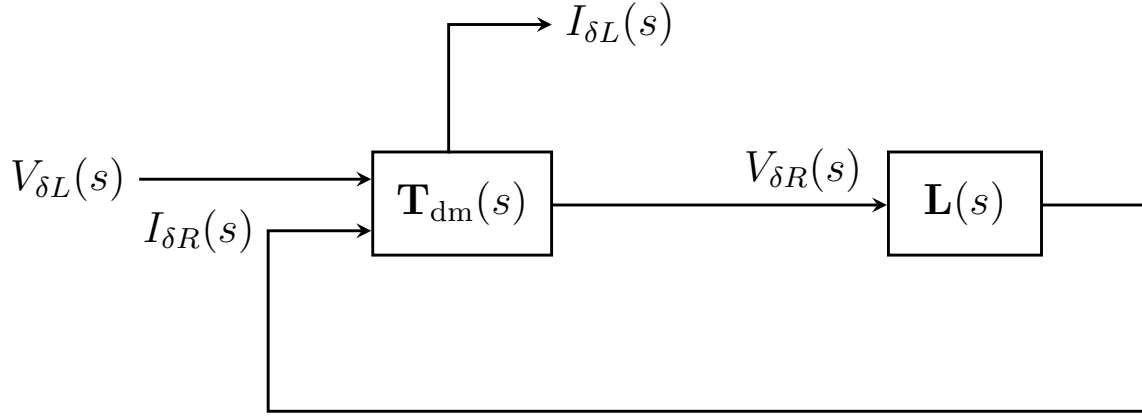


Figure 2.22. Block diagram representation of wideband DM state model.

As such,

$$\mathbf{T}_{dm}(s) = \begin{bmatrix} \mathbf{H}(s) & 0 \\ 0 & \mathbf{L}^{-1}(s) \end{bmatrix} = [\mathbf{C}_{dm}[s\mathbf{I}_6 - \mathbf{A}_{dm}]^{-1}\mathbf{B}_{dm} + \mathbf{D}_{dm}] \quad (2.88)$$

$$\begin{bmatrix} \mathbf{H}(s) \\ 1 \end{bmatrix} = [\mathbf{C}_{dm}[s\mathbf{I}_6 - \mathbf{A}_{dm}]^{-1}\mathbf{B}_{dm} + \mathbf{D}_{dm}] \begin{bmatrix} 1 \\ \mathbf{L}(s) \end{bmatrix} \quad (2.89)$$

The relationship given by (2.89) is basis for the fit that is necessary for establishing the DM state model parameters. A curve fitting routine gave the fitted characteristics shown in Figure 2.23 and the parameters in Table 2.8.

Table 2.8. Wideband DM state model parameters.

Parameter	Value	Parameter	Value
α_1	2.1124×10^7	b_4	2.7893×10^3
ω_1	8.7655×10^9	b_5	3.5675×10^6
α_2	9.8503×10^5	b_6	1.0119×10^6
ω_2	4.9399×10^6	b_7	15.8015
α_3	3.0045×10^7	b_8	0.0286
ω_3	1.1020×10^8	d_1	0.0010
b_1	2.4656×10^9	d_2	0.6954
b_2	4.4336×10^6	d_3	0.9981
b_3	1.0000×10^3	d_4	1.2163×10^{-6}

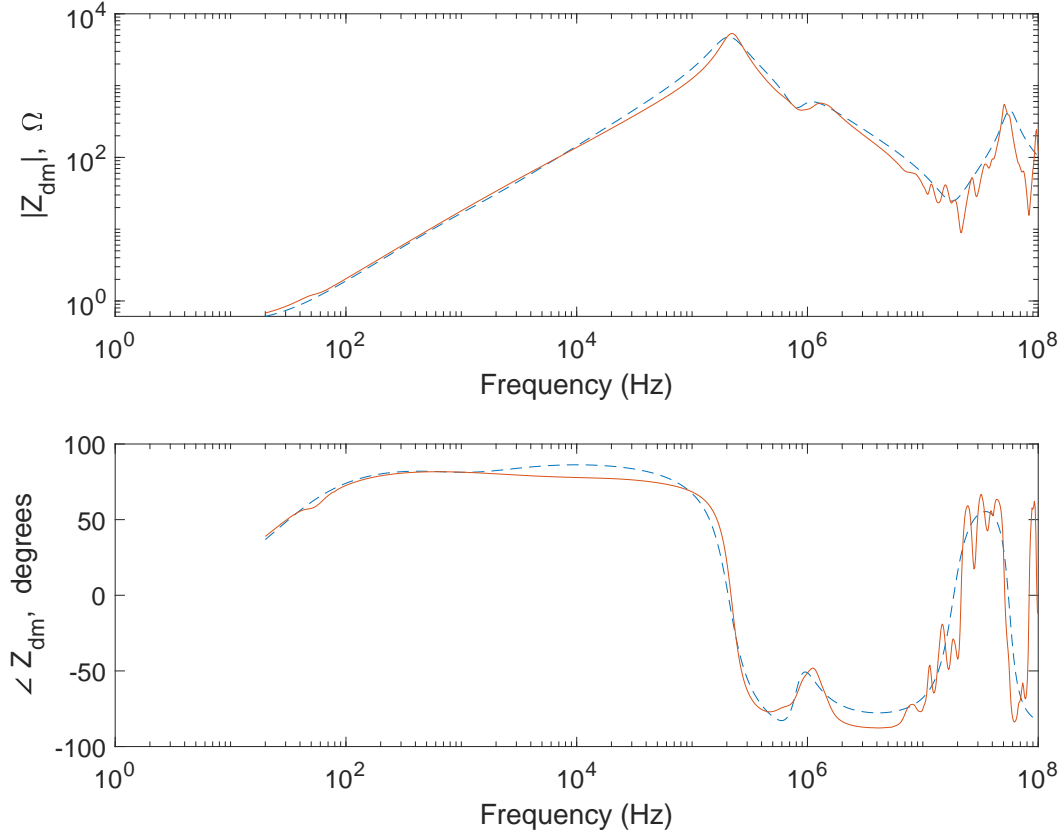


Figure 2.23. Measured and fitted wideband DM impedance using the state-space-based approach.

Wideband Common Mode State Model

The wideband CM state model can also be established from the measured wideband CM characteristics shown in Figure 2.16. As indicated in Figure 2.20, the measured characteristics can be fitted to the state-based form given by

$$p\mathbf{x} = \mathbf{A}_{\text{cm}}\mathbf{x} + \mathbf{B}_{\text{cm}}\mathbf{u} \quad (2.90)$$

$$\mathbf{y} = \mathbf{C}_{\text{cm}}\mathbf{x} \quad (2.91)$$

Here, \mathbf{A}_{cm} , \mathbf{B}_{cm} , and \mathbf{C}_{cm} are respectively in the forms,

$$\mathbf{A}_{\text{cm}} = \begin{bmatrix} -\alpha_1 & -\omega_1 & 0 & 0 & 0 & 0 \\ \omega_1 & -\alpha_1 & 0 & 0 & 0 & 0 \\ 0 & 0 & -\alpha_2 & -\omega_2 & 0 & 0 \\ 0 & 0 & \omega_2 & -\alpha_2 & 0 & 0 \\ 0 & 0 & 0 & 0 & -\alpha_3 & -\omega_3 \\ 0 & 0 & 0 & 0 & \omega_3 & -\alpha_3 \end{bmatrix}, \quad \mathbf{B}_{\text{cm}} = \begin{bmatrix} b_1 \\ b_2 \\ b_3 \\ b_4 \\ b_5 \\ b_6 \end{bmatrix}, \quad \text{and} \quad \mathbf{C}_{\text{cm}} = \begin{bmatrix} 1 \\ 0 \\ 1 \\ 0 \\ 1 \\ 0 \end{bmatrix}^T$$

These definitions see that the transfer admittance relating the output \mathbf{y} to the input \mathbf{u} be expressed as

$$\frac{\mathbf{Y}(s)}{\mathbf{U}(s)} = \mathbf{C}_{\text{cm}}[s\mathbf{I}_6 - \mathbf{A}_{\text{cm}}]^{-1}\mathbf{B}_{\text{cm}} \equiv \mathbf{T}_{\text{cm}}(s) \quad (2.92)$$

The transfer admittance is basis for the fit used in establishing the CM state model parameters. The curve fitting results are shown in Figure 2.24 and the associated parameters in Table 2.9.

Table 2.9. Wideband CM state model parameters.

Parameter	Value	Parameter	Value
α_1	7.2733×10^6	b_1	8.2107×10^5
ω_1	7.4497×10^7	b_2	9.9571×10^4
α_2	6.1463×10^7	b_3	1.9634×10^6
ω_2	4.7337×10^8	b_4	40.2827
α_3	1.0989×10^6	b_5	5.5144×10^3
ω_3	5.4559×10^6	b_6	2.6519×10^3

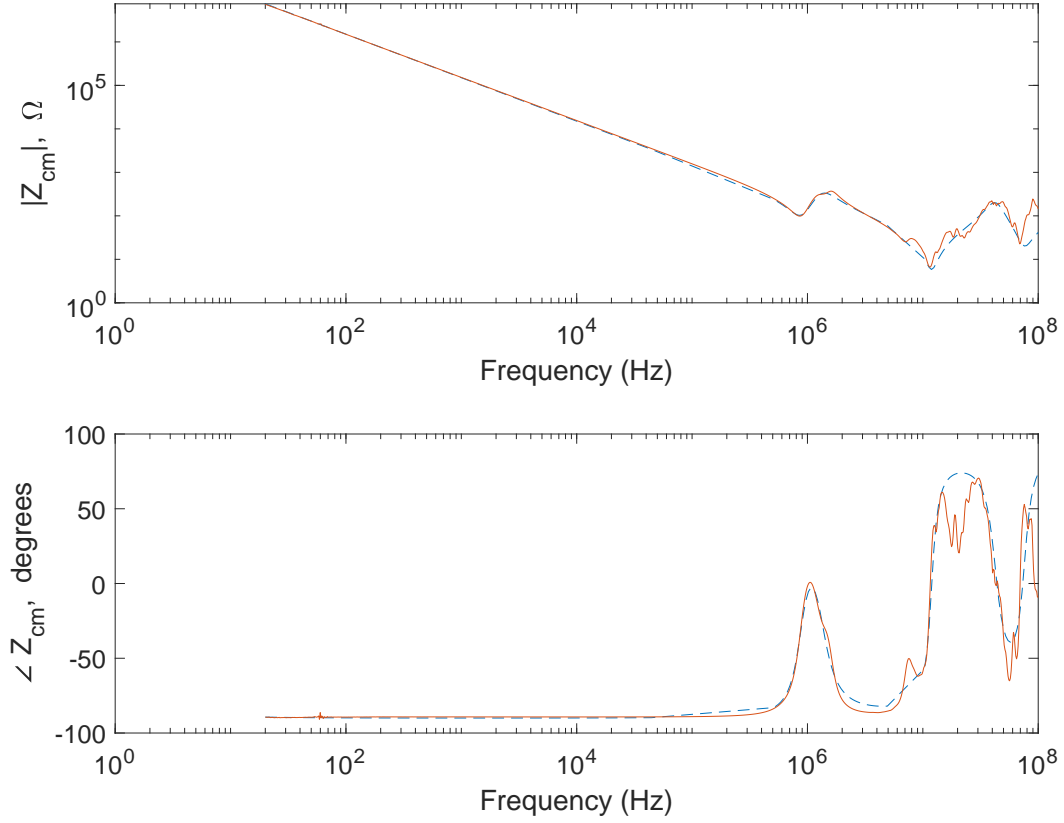


Figure 2.24. Measured and fitted wideband CM impedance using the state-space-based approach.

2.9 Summary

In this chapter, a new wideband model of a surface-mount PMAC machine has been set forth. It incorporates the low- and high-frequency dynamics that are associated with widebandgap-based electric drive systems. Moreover, frequency modes were established for the state models of the high-frequency DM and CM circuits. These modes will have an impact on the simulation framework set forth later. An alternative formulation of the wideband model was also described. Specifically, a state-space-based wideband model was realized directly from measured wideband data. In state-space-based simulation approaches, the alternative

wideband model can be used in lieu of the state models derived from the high-frequency DM and CM circuits.

3. WIDEBAND INVERTER MODEL AND PARAMETERIZATION

Inverters are necessary for providing the voltages that drive poly-phase electric machines. In this chapter, a wide-bandgap-based inverter model is described. The parameterization of this wide-bandgap-based inverter model is also presented.

3.1 Inverter Phase Leg

The equivalent circuit of one phase leg of a three phase inverter is shown in Figure 3.1. As depicted, the phase leg is supplied by a dc voltage V_s , which is defined by a source model described later in this chapter. The source model includes models of an electrolytic capacitor, polypropylene capacitors, thin-film resistors, and connecting cables. Also shown are capacitances $C_{pg, \text{cree}}$, $C_{ng, \text{cree}}$, and $C_{xg, \text{cree}}$ that represent stray capacitances between nodes p , n , and x and the baseplate of the inverter module. In particular, $C_{pg, \text{cree}}$, $C_{ng, \text{cree}}$, and $C_{xg, \text{cree}}$ are used to denote the upper-rail-to-module-baseplate, lower-rail-to-module-baseplate, and mid-rail-to-module-baseplate capacitances, respectively. The MOSFET model is based on the large-signal circuit model set forth in [38], [60]. It includes a diode that represents both the MOSFET body diode and an external diode. A combination of the MOSFET, diode, and mid-rail-to-module-baseplate capacitance form one of three phase legs that make up a three-phase inverter circuit.

MOSFET Model

The equivalent circuit of an individual MOSFET is shown in Figure 3.2 [60]. It consists of resistors r_g , r_d , and r_s that represent the internal gate, drain, and source resistances, respectively. The gate voltage, represented as u , dictates the turn-on or turn-off of the MOSFET device and the dependent current source represents the drain-to-source current, i_{ds} ¹. Specifically, i_{ds} is voltage dependent and is defined by the well-known Shichman-Hodges equations [38] for the cut-off, linear, and saturation regions of the device.

¹The symbols i_{ds} and v_{ds} used in this chapter should not be confused with the d -axis component of the stator current and voltage of the electric machine.

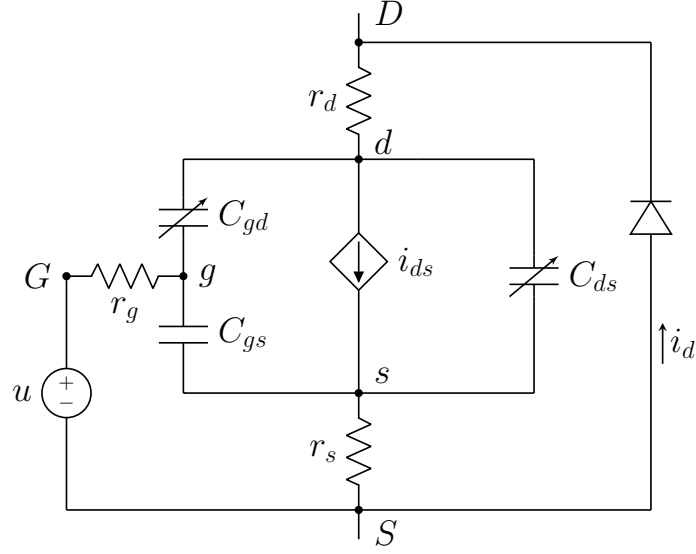


Figure 3.2. The MOSFET model, adapted from [60].

For the cut-off region where $v_{gs} < V_{th}$, the drain-to-source current is

$$i_{ds} = 0 \quad (3.1)$$

In the linear region, with $v_{gs} \geq V_{th}$ and $v_{ds} < v_{gs} - V_{th}$, the drain-to-source current is

$$i_{ds} = K_p \left[(v_{gs} - V_{th})v_{ds} - v_{ds}^2/2 \right] (1 + \lambda v_{ds}) \quad (3.2)$$

In the saturation region, with $v_{gs} \geq V_{th}$ and $v_{ds} \geq v_{gs} - V_{th}$, the drain-to-source current is

$$i_{ds} = \frac{1}{2} K_p (v_{gs} - V_{th})^2 (1 + \lambda v_{ds}) \quad (3.3)$$

In (3.1) - (3.3),

- K_p is a gain constant relating the channel current to the drain-to-source and gate-to-source voltages
- v_{gs} is the gate-to-source voltage

- v_{ds} is the drain-to-source voltage
- V_{th} is the threshold gate voltage
- λ is the channel length modulation parameter

The MOSFET model also contains junction capacitances C_{gd} , C_{gs} , and C_{ds} that represent the gate-to-drain, gate-to-source, and drain-to-source capacitances, respectively. These capacitances are derived from the measured input, output, and reverse transfer capacitances, which are nonlinear functions that depend on the drain-to-source voltage, v_{ds} . In practice, the input capacitance C_{iss} is the capacitance measured between the gate and source terminals of the MOSFET at a specified dc voltage when an ac signal of high frequency (usually 1 MHz) is applied across the gate and source terminals and the drain and source terminals alternately short-circuited. The input capacitance is defined as

$$C_{iss} = C_{gs} - C_{gd} \quad (3.4)$$

The output capacitance C_{oss} is the capacitance measured between the drain and source terminals with the gate and source terminals short-circuited.

$$C_{oss} = C_{ds} - C_{gs} \quad (3.5)$$

The reverse transfer capacitance C_{rss} or Miller capacitance is the capacitance measured between the drain and gate terminals with the source terminal grounded.

$$C_{rss} = C_{gd} \quad (3.6)$$

From these definitions, C_{gs} and C_{ds} may be obtained as

$$C_{gs} = C_{iss} - C_{rss} \quad (3.7)$$

$$C_{ds} = C_{oss} + C_{rss} \quad (3.8)$$

Since C_{iss} , C_{oss} , and C_{rss} are voltage dependent, it follows that the gate-to-source, gate-to-drain, and drain-to-source junction capacitances are also voltage dependent. It should be noted that the gate-to-source capacitance C_{gs} is known to have a small standard deviation. As such it is modeled as a constant capacitance in the MOSFET model while the other junction capacitances (C_{gd} and C_{ds}) are functions of v_{ds} .

Furthermore, the diode shown in the model represents both the MOSFET body diode and an external Schottky diode connected antiparallel to the MOSFET. This diode acts as a freewheeling diode [61] and dominates the switch current when the drain-to-source voltage v_{ds} is negative. The current i_d through the diode may be modeled in a computer simulation using the Shockley diode equation [62]. In particular,

$$i_d = I_0 \left[\exp \left(\frac{qv_d}{nkT} \right) - 1 \right] \quad (3.9)$$

where I_0 is the saturation current, q the electron charge, v_d the diode voltage, n the ideality factor, k the Boltzmann constant and T the absolute temperature. These and the other parameters of the MOSFET model are necessary for the simulation described in Chapter 5 and are presented next.

3.2 MOSFET Model Parameters

The parameters defined in the previous section were realized from the manufacturer-supplied datasheet of the Cree module used in this research. It should be noted that experimental measurements of these parameters were not feasible due to the fact that the MOSFETs and diodes are encased in a single hermetically sealed package. Alternate extraction methods of the parameters are discussed here.

Junction Capacitances C_{gd} , C_{ds} , and C_{gs}

To establish C_{gd} and C_{ds} , data points of the capacitances C_{iss} , C_{oss} , and C_{rss} were extracted directly from the datasheet plots. The drain-to-source and gate-to-drain capacitances are shown in Figure 3.3. The results indicate that C_{gd} varies between 5.7 pF and 600 pF and

C_{ds} varies between 175.6 pF and 2400 pF. On the other hand, C_{gs} was evaluated from the datasheet typical values for C_{iss} (900 pF) and C_{rss} (5.9 pF). Using (3.7), C_{gs} was obtained as 894.1 pF.

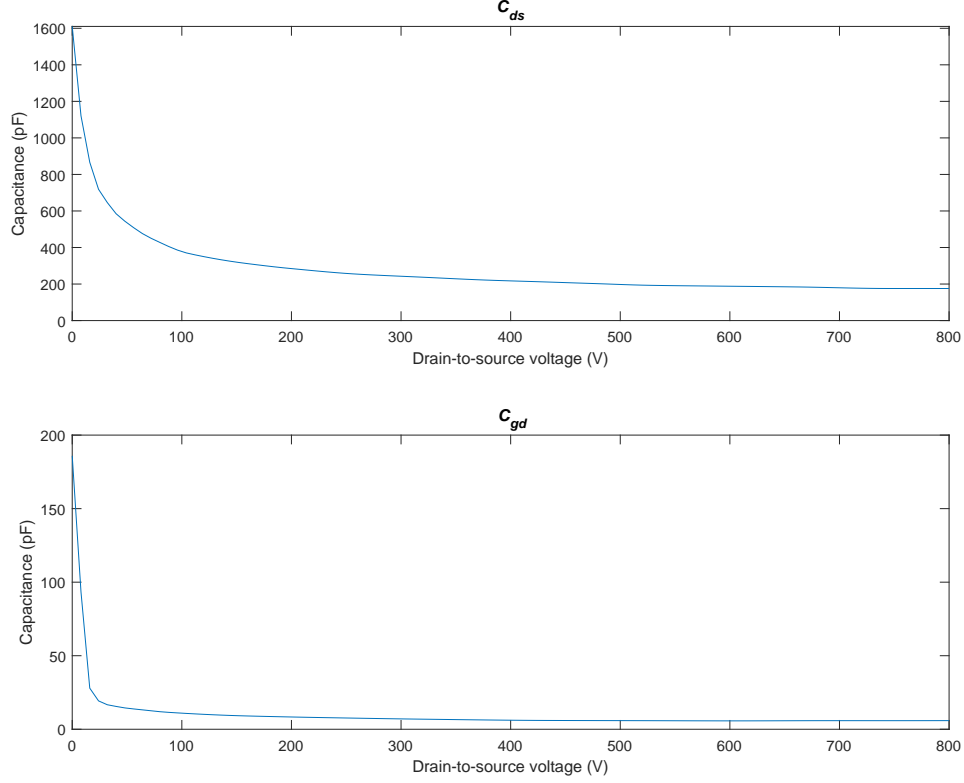


Figure 3.3. MOSFET capacitances versus drain-to-source voltage

Gain K_p and Channel Length Modulation Parameter λ

Typically, the appropriate method for obtaining the channel length modulation parameter λ involves a linear extrapolation of the output characteristics of the saturation region. As the output characteristics showing the saturation region phenomenon is not provided in the datasheet, the linear-region output characteristics could only be depended upon for establishing the terms K_p and λ . Initial efforts to obtain these parameters by using a least-

squares-fit method on the data points of the measured output characteristics with a gate-to-source voltage v_{gs} of 20 V, and a junction temperature T_j of 25 °C yielded a negative λ . This in itself is physically impossible as the channel length modulation parameter is typically a positive number less than 0.1. For this reason, the channel modulation parameter λ was set to zero prior to the implementation of the least-squares-fit method. The data points were extracted from the datasheet using the application Grabit[63]. The result of the consequent fit gave the parameter K_p and is shown in Figure 3.4.

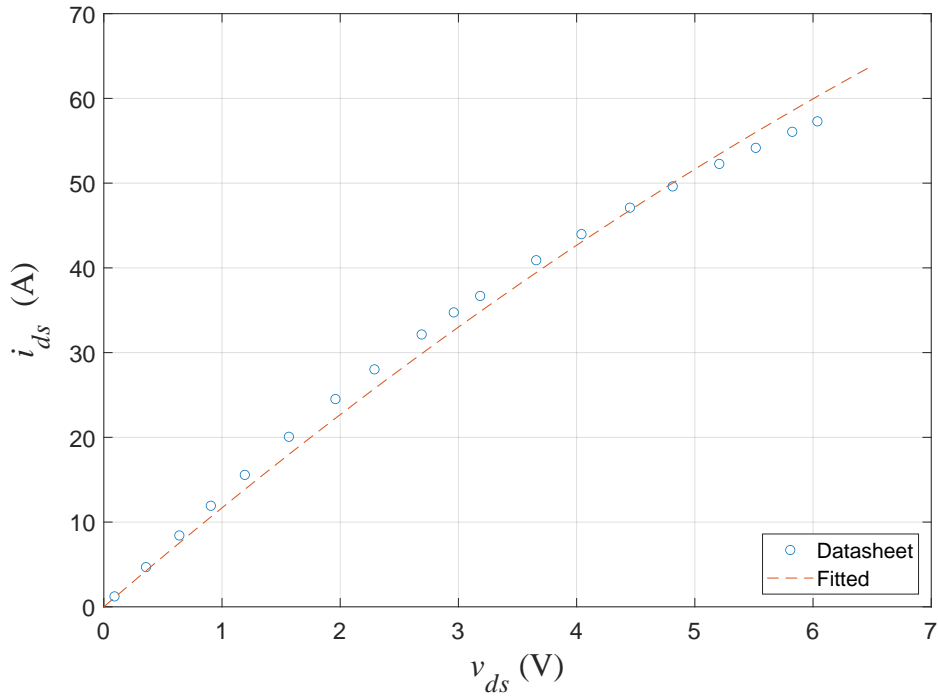


Figure 3.4. Measured and fitted output characteristics, $T_j = 25$ °C, $v_{gs} = 20$ V.

Gate Voltages and Internal Resistances r_g , r_d , and r_s

A threshold voltage of 2 V was chosen for simplicity. It should be noted that, from the datasheet, this is the average of the threshold voltages for junction temperatures of 25 °C (2.3 V) and 150 °C (1.7 V). Also, the internal gate resistance r_g was deduced from the datasheet as 3.8 Ω . The drain resistance r_d was set to 10 m Ω and the source resistance r_s

was neglected. In addition, the turn-on and turn-off gate voltages were obtained from the datasheet specifications of the gate driver circuit for the six-pack module. These voltages are given as 20 and -5 V for the turn-on and turn-off stages, respectively.

Diode Parameters

For the diode parameters, the saturation current I_0 was selected as $1e^{-6}$ A, the ideality factor n as 1, and the absolute temperature as 293 K. These choices are adequate for a computer simulation of the model. The diode characteristics may also be implemented as a lookup table obtained from the information given in the datasheet.

Stray Capacitances $C_{pg, \text{cree}}$, $C_{ng, \text{cree}}$, and $C_{xg, \text{cree}}$

Using an impedance analyzer, the capacitance $C_{xg, \text{cree}}$ between the mid-rail terminal of a phase leg of the Cree module and inverter baseplate was established to be equal to 43.4 pF. To establish the stray capacitances $C_{pg, \text{cree}}$ and $C_{ng, \text{cree}}$, capacitance calculations were made based on area measurements obtained from the Cree module. These measurements were taken from the cross section revealed from a cutout of the inverter module. The cross section is shown in Figure 3.5. Here, sections labeled **U**, **M**, and **L** represent areas associated with the upper-rail-to-module-baseplate, mid-rail-to-module-baseplate, and lower-rail-to-module-baseplate capacitance, respectively. Based on the dimensions shown, the areas particular to $C_{pg, \text{cree}}$, $C_{ng, \text{cree}}$, and $C_{xg, \text{cree}}$ were noted as 490.2 mm², 50.85 mm², and 132.9 mm², respectively. From these measurements, $C_{pg, \text{cree}}$ and $C_{ng, \text{cree}}$ were established by scaling $C_{xg, \text{cree}}$ with respect to their areas. In particular,

$$C_{pg, \text{cree}} = \frac{490.22}{132.9} C_{xg, \text{cree}} = 160.1 \text{ pF}$$

$$C_{ng, \text{cree}} = \frac{50.85}{132.9} C_{xg, \text{cree}} = 16.6 \text{ pF}$$

The established parameters are summarized in Table 3.1.

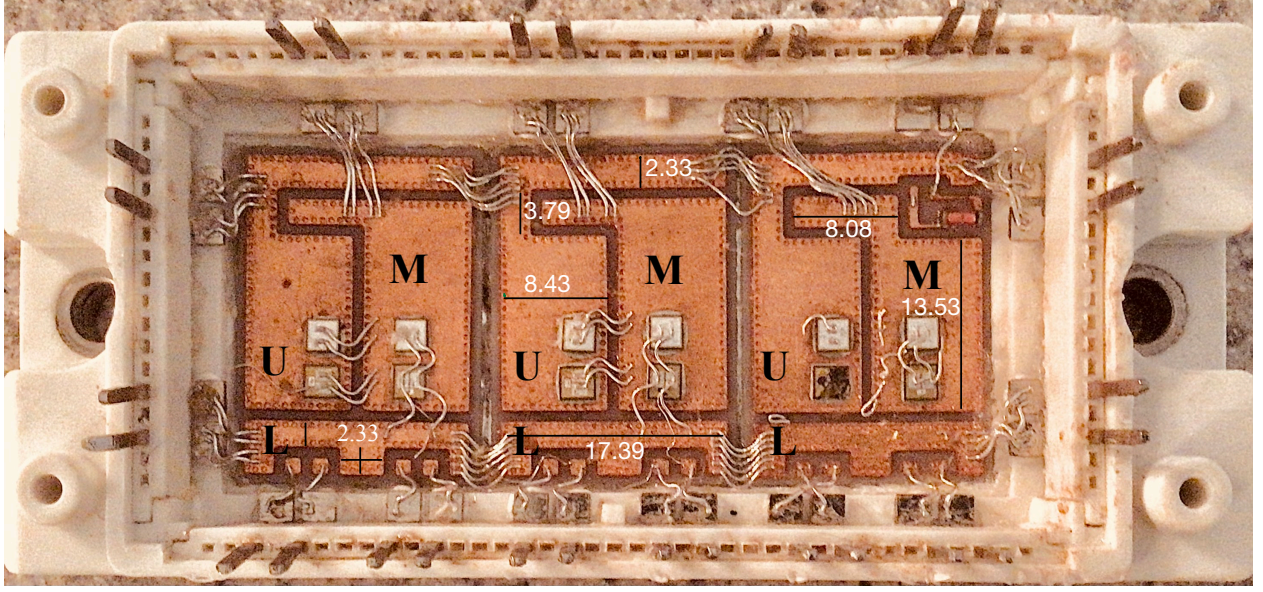


Figure 3.5. Cross section of a broken inverter module (all dimensions in millimeters).

Table 3.1. SiC MOSFET parameters.

Parameter	Value	Parameter	Value	Parameter	Value
C_{gs}	894.1 pF	r_g	3.8Ω	I_0	$1 \times 10^{-6} \text{ A}$
$C_{pg, \text{ cree}}$	160.1 pF	r_d	$10 \text{ m}\Omega$	n	1
$C_{ng, \text{ cree}}$	16.6 pF	λ	0 V^{-1}	k	$8.617 \times 10^{-5} \text{ eV/K}$
$C_{xg, \text{ cree}}$	43.4 pF	K_p	0.6751 AV^{-2}	T	293 K
$u \text{ (on/off)}$	20/-5 V	V_{th}	2 V	q	$1.6 \times 10^{-19} \text{ C}$

3.3 Source Model

The source model contains models of sub-components that affect the voltage supplied to the six-pack MOSFET module. The detailed source model is shown in Figure 3.6. Here, V_{dc} is the dc voltage supplied from a dc source, the Sorensen DHP-series dc supply with 400-V/25-A ratings. The series rL branch containing r_r and L_r is the model of the cable that connects a pair of thin-film resistors to the inverter. The thin-film resistors, although non-inductive, behave like capacitors at high frequencies; hence, a parallel rC branch showing parameters r and C is included.

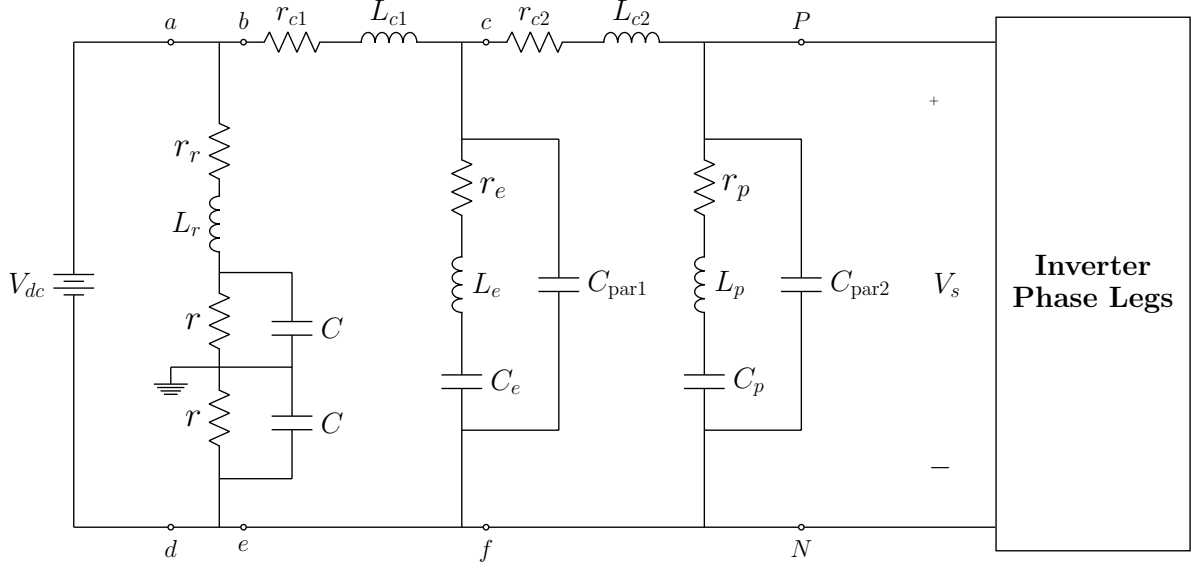


Figure 3.6. The inverter with detailed source model.

The branch containing r_e , L_e , C_e , and C_{par1} form the model for the electrolytic dc link capacitor while r_{c1} and L_{c1} represent the cable connection between the dc source and the electrolytic capacitor. The branch containing r_p , L_p , C_p , and C_{par2} form the model for the polypropylene capacitors that are part of the gate driver circuit for the six-pack module. The resistance r_{c2} and inductance L_{c2} are used to model the connecting cable between the gate driver board and electrolytic capacitor.

3.4 Characterization of Source Model

It is difficult to accurately establish all of the source model parameters simultaneously by applying a population-based curve fitting routine to impedance measurements of the model. This is mainly due to the large number of parameters that may cause the curve-fitting routine to yield results that are not physically interpretable. As such, it is more judicious to divide the source model into three segments and characterize each individually. The segments include segment $a-b-e-d$, segment $b-c-f-e$, and segment $c-P-N-f$, as shown in Figure 3.6.

Polypropylene Capacitors and Cable

Segment c - P - N - f make up the model for the polypropylene capacitors of the gate driver circuit and the adjoining cable. The segment was connected to a Keysight E4990A impedance analyzer as shown in Figure 3.7 and a frequency sweep from 20 Hz to 100 MHz was performed. The resulting data measurements were fitted to the circuit shown in Figure 3.7 by treating the parameters as genes in a population-based curve fitting routine using the genetic algorithm toolbox, GOSET. The fitted results are shown in Figure 3.8 and the parameter results are also summarized in Table 3.2.

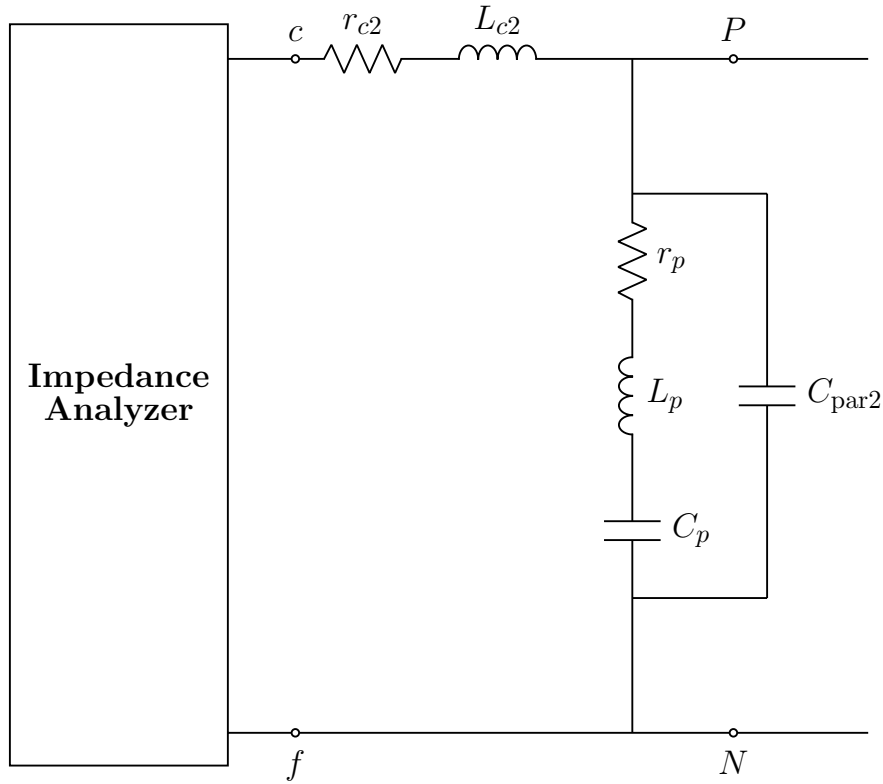


Figure 3.7. Test circuit for segment c - P - N - f .

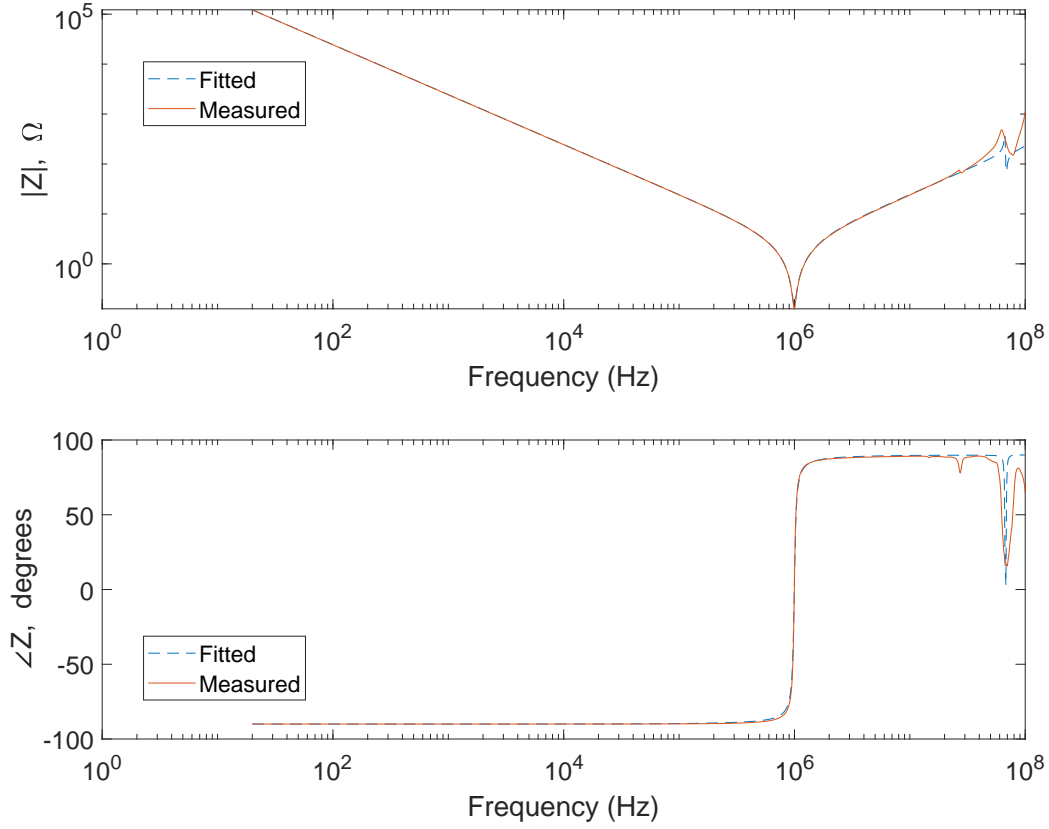


Figure 3.8. Measured and fitted impedance of segment c - P - N - f .

Table 3.2. Parameters in segment c - P - N - f .

Parameter	r_p	L_p	C_p	C_{par2}	r_{c2}	L_{c2}
Value	0.1203 Ω	15.946 nH	64.721 nF	357.28 pF	1.0047 $\mu\Omega$	61.46 nH

Electrolytic Capacitor and Cable

The electrolytic capacitor, which acts as a dc link capacitor in the inverter circuit, is a component of segment b - c - f - e . Alongside the connecting cable represented by the series r_{c2} - L_{c2} in the model, the electrolytic capacitor was connected to the impedance analyzer and a frequency sweep (20 Hz to 100 MHz) was performed as in the case for segment c - P - N - f . The test circuit is shown in Figure 3.9.

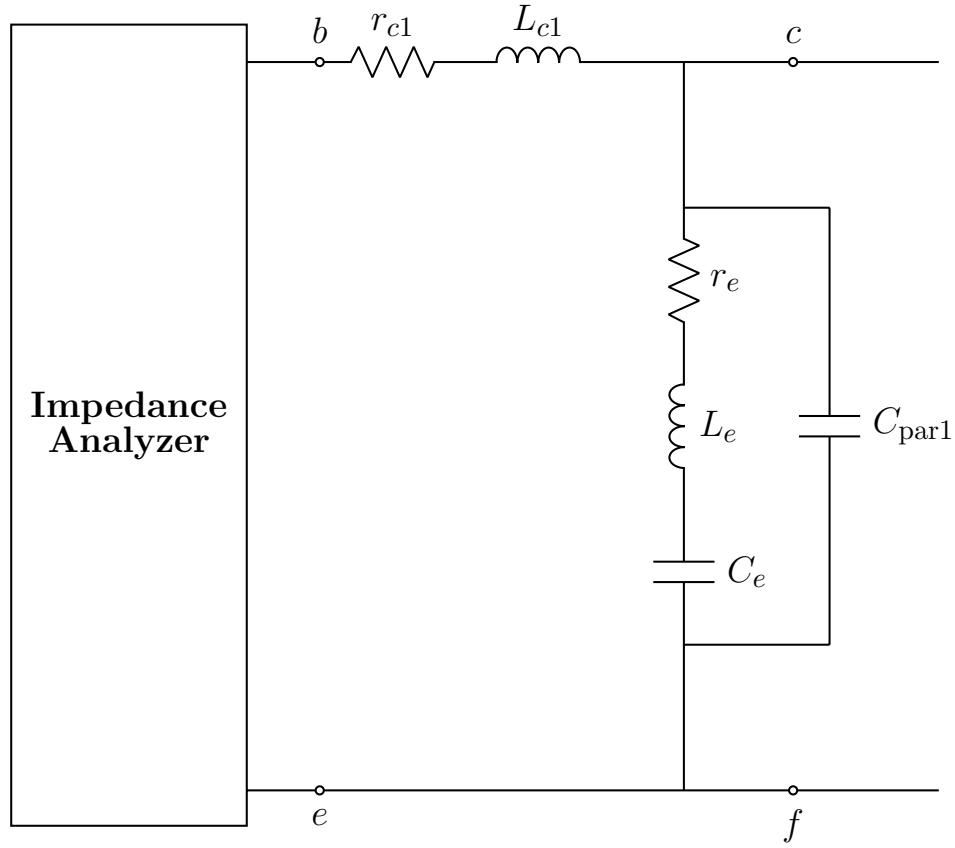


Figure 3.9. Test circuit for segment b - c - f - e .

The parameters of the test circuit were then established using the population-based algorithm toolbox, GOSET. The measured and fitted results of the routine are shown in Figure 3.10 and the established parameters summarized in Table 3.3.

Table 3.3. Parameters in segment b - c - f - e .

Parameter	r_e	L_e	C_e	C_{par1}	r_{c1}	L_{c1}
Value	0.0498 Ω	68.065 nH	0.95495 mF	95.95 pF	1.3696 $\mu\Omega$	132.44 nH

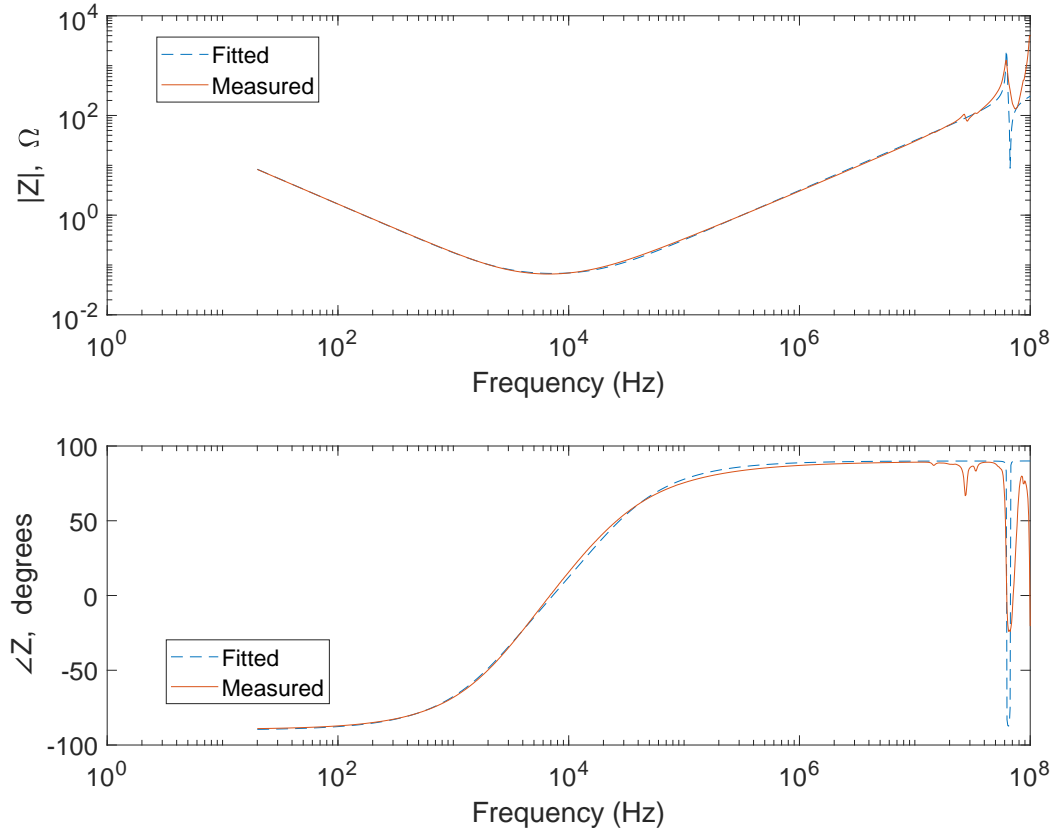


Figure 3.10. Measured and fitted impedance of segment $b-c-f-e$.

Thin-film Resistors and Cable

The third segment, $a-b-e-d$, containing the thin-film resistors and connecting cable was connected to the impedance analyzer as shown in Figure 3.11. Impedance measurements were obtained for the test circuit for frequencies between 20 Hz and 100 MHz and the data consequently fitted to the circuit using GOSET. Although the results shown in Figure 3.12 are not a perfect fit due to the variability of the capacitance of the thin-film resistor, it is still adequate as the deviation is not significant. The parameters obtained are summarized in Table 3.4.

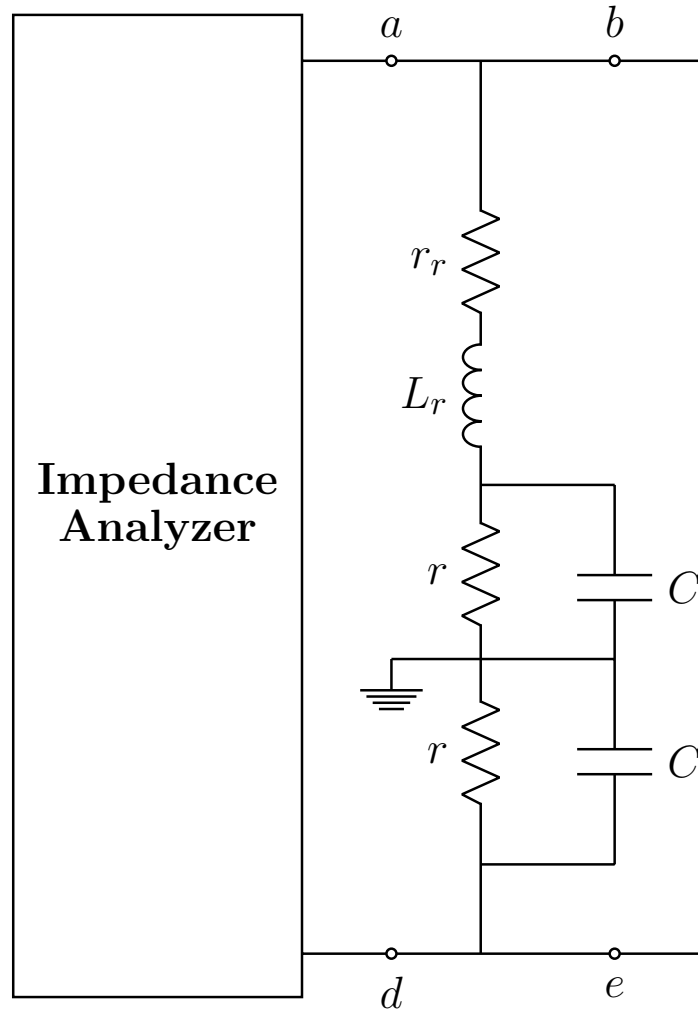


Figure 3.11. Test circuit for segment a - b - e - d .

Table 3.4. Parameters in segment a - b - e - d .

Parameter	r	C	r_r	L_r
Value	4.7 k Ω	30.129 pF	24.3031 Ω	1 pH

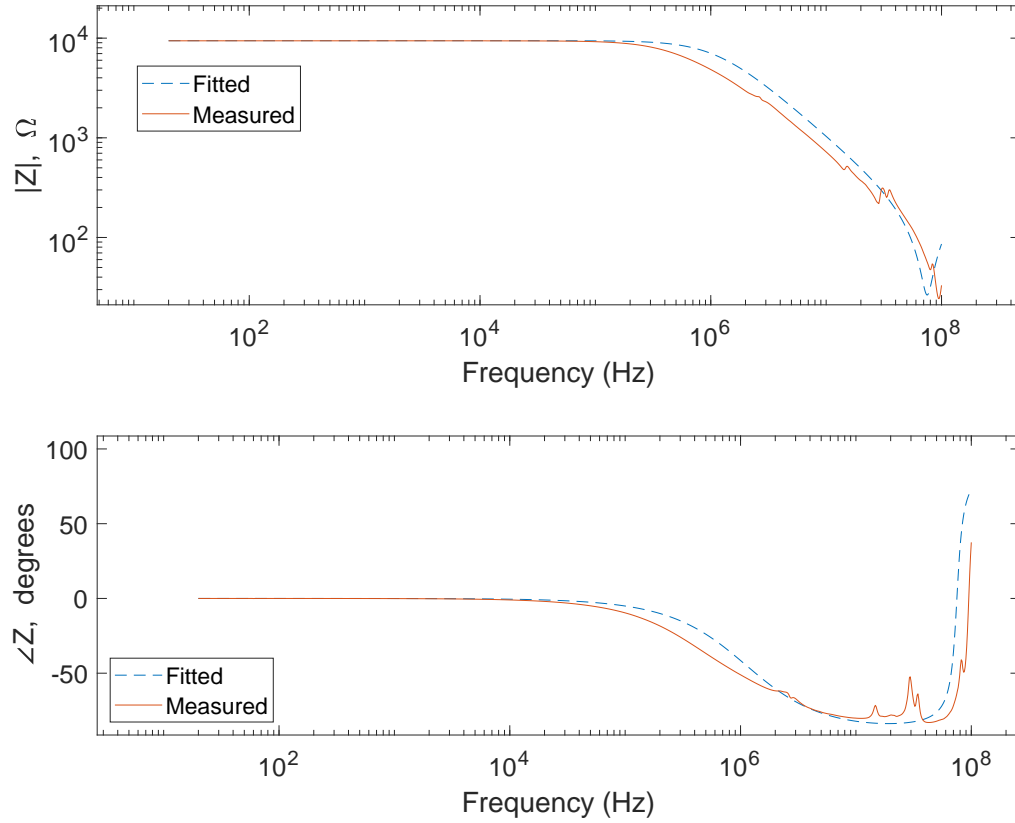


Figure 3.12. Measured and fitted impedance of segment *a-b-e-d*.

3.5 Validation of Source Model Parameters

Following the establishment of the parameters in the previous section, the segments were joined side-by-side as shown in Figure 3.6 and then connected to the impedance analyzer for impedance measurements for frequencies between 20 Hz and 100 MHz. An analytical solution of the Thévenin impedance based on the established parameters was then compared to the measured frequency response. The analytical results superimposed on the measured impedance are shown in Figure 3.13. The results show that the established parameters are fairly accurate and may be used in a computer simulation of the model.

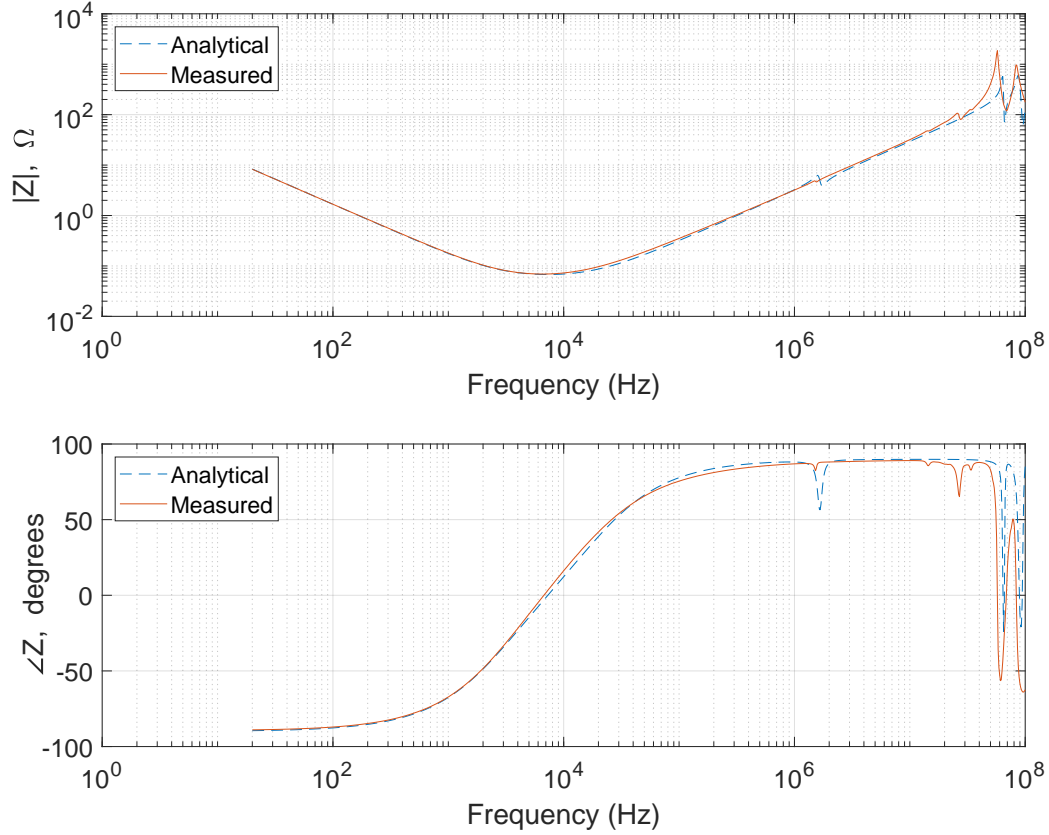


Figure 3.13. Calculated source model impedance compared with measured data.

3.6 Summary

In this chapter, a wideband inverter model has been described. Specifically, the SiC MOSFETs are represented using the well-known SPICE Level 1 model that is based on the Shichman-Hodges equations. Also, efforts have been made to establish models and parameters for the different components that complement the three pairs of SiC MOSFETs in the six-pack inverter module. These include models for the dc link capacitor, thin-film resistors and polypropylene capacitors of the gate driver circuit. The models and their associated parameters will form an integral part of the simulations described in later chapters.

4. ELECTRIC DRIVE SYSTEM SIMULATION

The simulation of the electric drive system introduced in Section 1.2 is presented in this chapter. As shown in Figure 1.2, it is comprised of subsystems including a voltage-source inverter and a surface-mount PMAC machine with cable connections. Models for each of these subsystems have been described in the preceding chapters. The primary focus of this chapter is on simulation. In particular, the models are implemented using established simulation methods including modified nodal analysis (MNA) and state-space-based approaches. The computational efficiencies of these conventional techniques will be compared to a heterogeneous multirate simulation approach set forth in the next chapter.

4.1 Experimental Study of Electric Drive System

In order to set the stage for future comparisons, it is useful to examine experimental data obtained from the steady-state operation of the electric drive system shown in Figure 4.1, which is Figure 1.2 repeated here for convenience. For the experimental procedure, the dc source voltage, V_{dc} of the inverter circuit was set to 30 V and the switches of the inverter were controlled by implementing the sine-triangle modulation strategy with third harmonic injection in which duty cycle waveforms are defined as [55]

$$d_a = d \cos \theta_c - d_3 \cos(3\theta_c) \quad (4.1)$$

$$d_b = d \cos(\theta_c - \frac{2\pi}{3}) - d_3 \cos(3\theta_c) \quad (4.2)$$

$$d_c = d \cos(\theta_c + \frac{2\pi}{3}) - d_3 \cos(3\theta_c) \quad (4.3)$$

A block diagram of the modulator is shown in Figure 4.2. Here, d , which may be chosen from the range $[0, 2/\sqrt{3}]$, was selected as 1 whereupon the peak amplitude of the fundamental component of ac voltage becomes

$$\sqrt{(V_{qs}^r)^2 + (V_{ds}^r)^2} = \frac{V_{dc}}{2} d \quad (4.4)$$

Here, V_{qs}^r and V_{ds}^r are the respective notations for the steady-state q - and d -axis components of the ac voltages in the rotor reference frame. In addition, d_3 is the third harmonic term selected to be $d/6$ and θ_c is the converter angle [55] which may be expressed as

$$\theta_c = \theta_r + \phi_v \quad (4.5)$$

where θ_r is the electrical rotor position and

$$\phi_v = \tan^{-1} \left(\frac{-V_{ds}^r}{V_{qs}^r} \right) \quad (4.6)$$

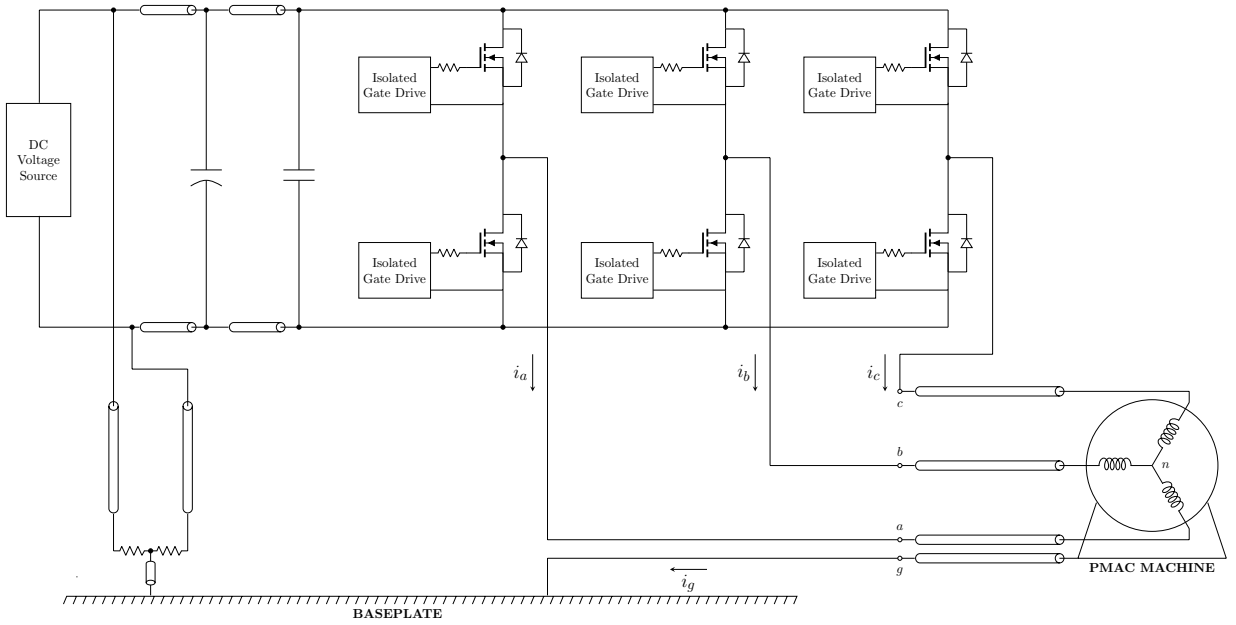


Figure 4.1. The electric machine drive system.

For the chosen operating point, ϕ_v was selected as 0.0657 rad so as to minimize the d -axis component of the ac current that does not contribute to torque. Additionally, it should be noted that the voltages V_{qs}^r and V_{ds}^r may be deduced from the definitions given by (4.4) and (4.6). In particular,

$$V_{qs}^r = \frac{1}{2}dV_{dc} \cos \phi_v = 14.97 \text{ V}$$

$$V_{ds}^r = -\frac{1}{2}dV_{dc} \sin \phi_v = -0.98 \text{ V}$$

A summary of the steady-state operating-point values is given in Table 4.1.

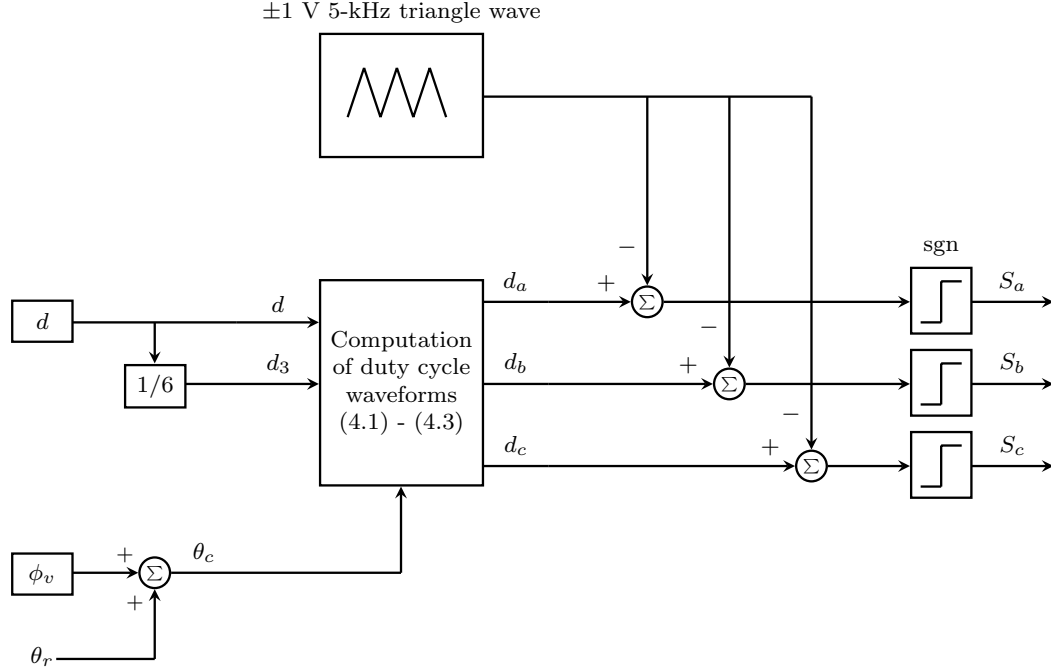


Figure 4.2. Block diagram of sine-triangle modulator with third harmonic injection.

Table 4.1. Steady-state operating-point values.

Parameter	Value	Parameter	Value	Parameter	Value
d	1	V_{dc}	30 V	V_{qs}^r	14.97 V
d_3	1/6	ϕ_v	0.0657 rad	V_{ds}^r	-0.98 V

The measured phase currents are shown in Figures 4.3 and 4.4. These measurements were obtained using a Yokogawa 701933 current probe connected to a 100 MS/s module on a Yokogawa DL850 oscilloscope. Examination of the measured phase currents, i_{as} , i_{bs} , and i_{cs} indicates that multiple time scales are associated with the dynamics of the system. As illustrated in Figure 4.4, each switching event, which takes only a few nanoseconds, results in a high-frequency transient that subsides in less than a microsecond. The time taken for each switching event is in contrast to the elapsed time between switching events. Careful examination of the current waveforms indicates that the time between switching events is on the order of tens of microseconds. This characteristic of WBG-based electric drive systems

is the primary reason for the high computational cost of simulating such systems. In the next section, a detailed simulation of the given drive system is presented to highlight this problem.

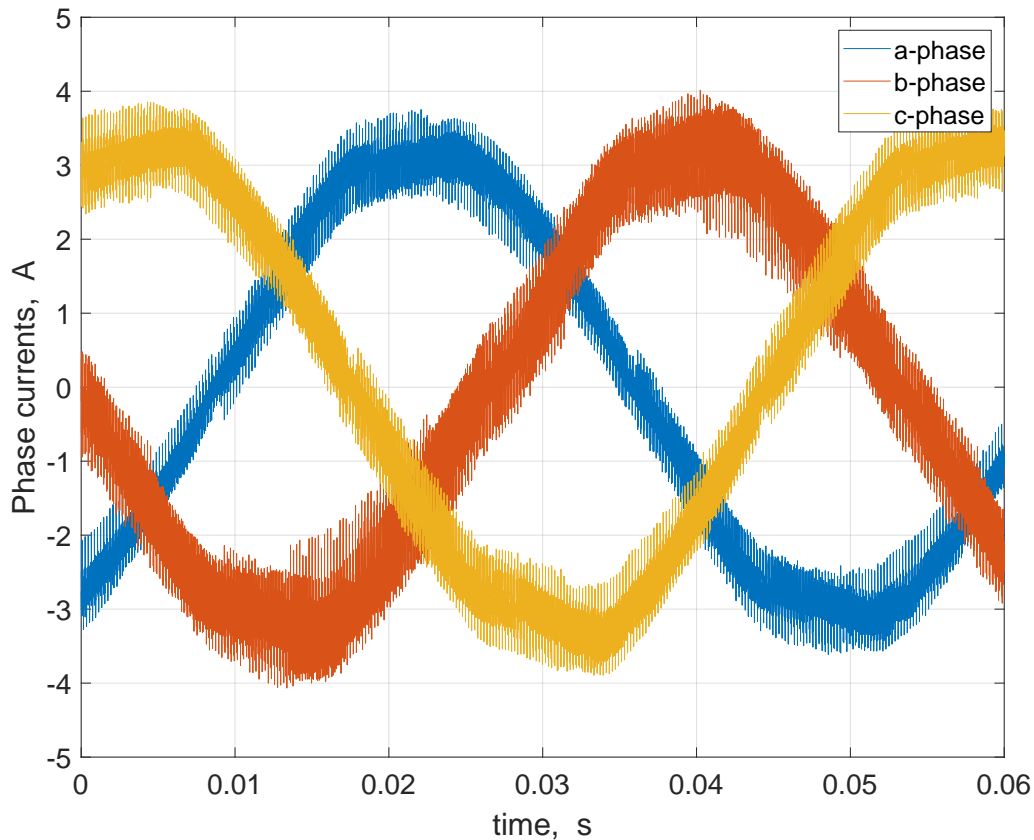


Figure 4.3. Measured phase currents for selected operating point ($d = 1$, $\phi_v = 0.0657$ rad).

4.2 MNA-based Simulation of Wideband Model

Modified nodal analysis (MNA), described by Ho et al. [64], is commonly used for equation formulation for large-scale circuit analysis by circuit simulators such as SPICE and its many derivatives. In order to understand the limitations of the SPICE algorithm, it is useful to describe its salient features. A top-level flowchart for transient analysis using SPICE is

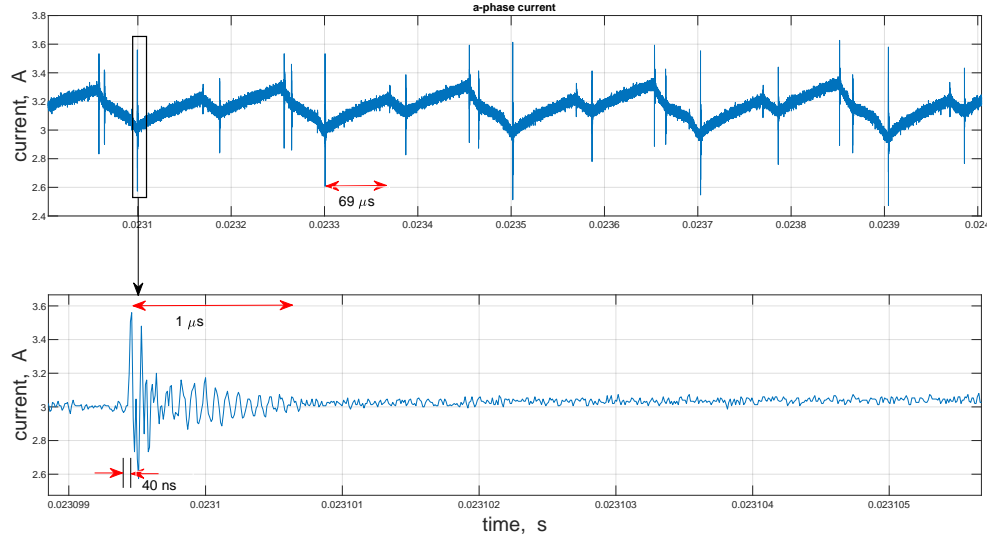


Figure 4.4. Measured a -phase current showing multiple time scales.

shown in Figure 4.5 [65]. It is assumed in this discussion that the initial operating point is a known input. The first stage of the algorithm involves the conversion of all two-terminal elements (inductors, resistors, nonlinear circuit elements whose current-versus-voltage (I - V) characteristics are known) into so-called linear or resistor-companion models consisting of a conductance g in parallel with a current source i . The values of the conductance and current source depend on the value of capacitance, inductance, or slope of the I - V characteristic at the present time step and, for inductors and capacitors, they depend on the specific algorithm (e.g. trapezoidal) and time step.

The next step involves the formation of the node admittance matrix and source vector in the nodal equation.

$$\mathbf{G}\mathbf{v} = \mathbf{i} \quad (4.7)$$

The i th diagonal element of \mathbf{G} represents the sum of conductances connected to node i and the nonzero off-diagonal elements g_{ij} represent the negative of the conductance connected between nodes i and j . The i th element of \mathbf{i} represents the sum of current sources into node i , and \mathbf{v} represents the vector of node voltages. Since \mathbf{G} is of large dimension but sparse,

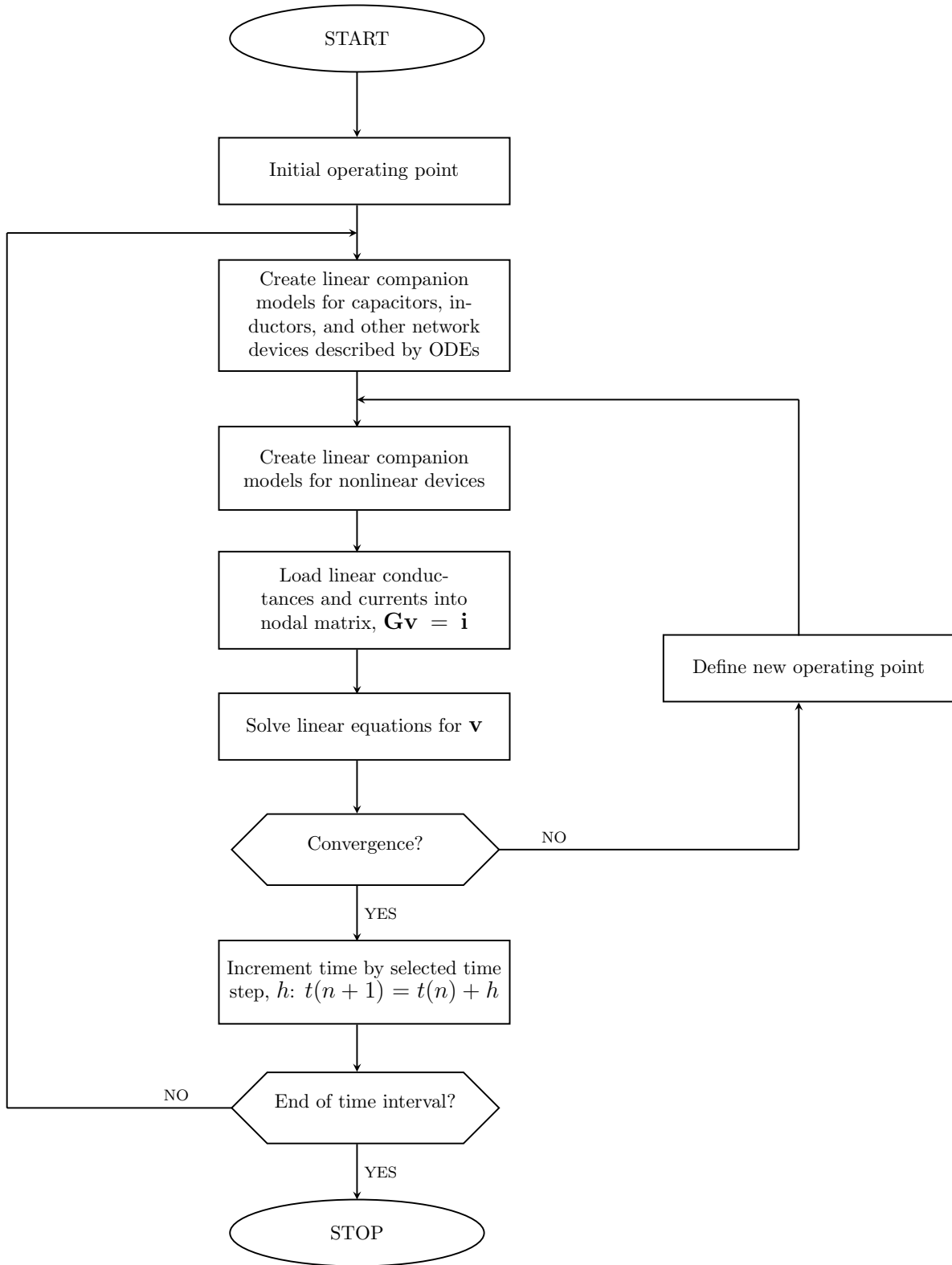


Figure 4.5. The SPICE algorithm for transient analysis, adapted from [65].

sparse matrix methods must be used to solve (4.7). This stage represents the key bottleneck in the SPICE algorithm.

After the node voltages are established, the conductance and current-source values of nonlinear branches are updated and the program flow loops back to recalculation of \mathbf{G} and \mathbf{i} in (4.7). This inner loop is often referred to as a Newton-Raphson loop. Once converged, the time step is advanced and if the accumulated time is less than the stop time, the conductances and current source values for all inductors and capacitors are then updated. They are all updated if the time step or algorithm changes. Only the time-varying or voltage/current dependent capacitors and inductors are updated otherwise. Other calculations performed in SPICE not shown in the flowchart include the calculation of branch voltages and currents from the nodal voltages. This step is not time consuming since it involves direct matrix-vector multiplication.

As can be deduced from Figure 4.5, the SPICE algorithm was developed for studying electric circuits. The program inputs include a list of branches. Each branch entry specifies the branch type, its parameters, and the two nodes to which the branch is connected. In power electronic circuits, the transistors are controlled by other components in the system including gate drive circuits, modulators, current/voltage regulators, and at the outermost layers, speed or position regulators. Each of these components are often described in block-diagram or state-space form.

MNA-based programs such as LTspice allow for incorporation of block-diagram-based models through the use of dependent voltage and/or current sources. The manner in which the corresponding equations are integrated into the flowchart in Figure 4.5 is not apparent. This would likely involve the discretization of the state-space models using the same algorithm used to generate the resistor-companion models to form a set of linear difference equations relating new states to old states and inputs, and sequentially executing the circuit and state-space solvers in a cascaded fashion.

For the WBG-based electric drive system shown in Figure 4.1, a single-rate MNA simulation was implemented in LTspice using the models and parameters established in the previous chapters. The top-level LTspice block diagram of the electric drive system is shown in Figure 4.6. Here, block diagrams of the inverter, machine cable, and motor are connected

as indicated by the circuit diagram in Figure 4.1. The controller block establishes the sine-triangle (with third harmonic injection) modulation strategy that is depicted in Figure 4.2. To set this up, SR flip-flops are used to establish the switching signals that are necessary for inverter control. An implementation of the controller block in LTspice is shown in Figure A.1 in Appendix A. The LTspice circuit diagrams for the inverter, cable, and motor are also detailed in Appendix A. It should be noted that, specific to the inverter circuit, the junction capacitances of the MOSFET model were set as constants in the simulation since using variable capacitance models for the junction capacitances would have added more overhead to the simulation.

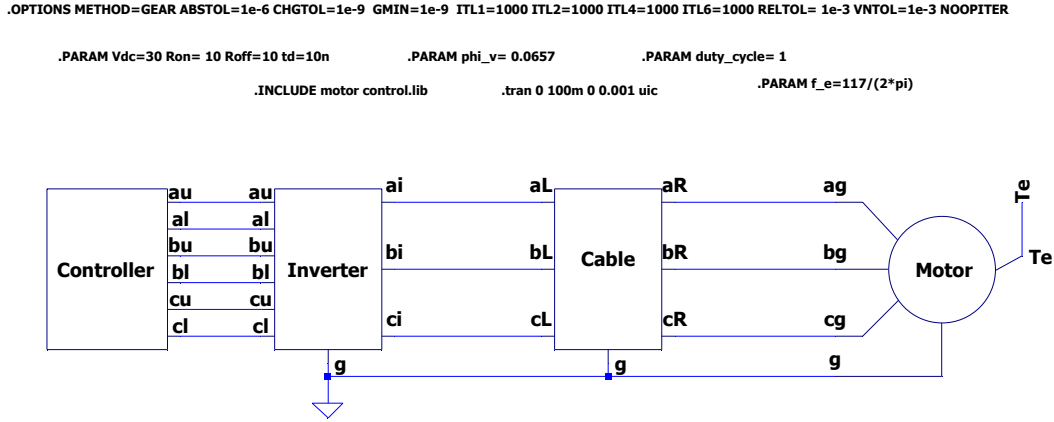


Figure 4.6. Top-level LTspice block diagram of the electric machine drive system.

For the computer study, the operating point for the 4-pole surface-mount PMAC machine was selected as outlined previously. From the measurements taken, the electrical rotor speed was found to be approximately 117 rad/s. This corresponds to a rotor speed ω_{rm} of 558 rpm as

$$\omega_r = \frac{P}{2} \omega_{rm} \quad (4.8)$$

where P is the number of poles of the electric machine. Thus, in the computer simulation, the electrical rotor speed was set to 117 rad/s. Moreover, the relative error tolerance was

set to 0.001, the absolute current and voltage tolerances were selected as $1\text{ }\mu\text{A}$ and 1 mV , respectively, and the integration method was set to Gear's second-order. The LTspice circuit simulation was executed using a 2.8-GHz personal computer for a 100-ms simulation time. The corresponding runtime was 4.15 h. A summary of the simulation statistics is given in Table 4.2. Results of the MNA-based simulation are shown in Figures 4.7 through 4.10. As shown, each switching event is accompanied by a short-lived spike in current and voltage. It is important to note that these results reasonably match the measured data.

Table 4.2. MNA simulation statistics.

Simulation time	100 ms
Runtime	4.15 h
Simulation speed	$6.69\text{ }\mu\text{s/s}$
Integration algorithm	Gear's second-order
Number of time steps	13 498 751
Maximum time step	$0.512\text{ }\mu\text{s}$
Matrix size	221
Fill-ins	121

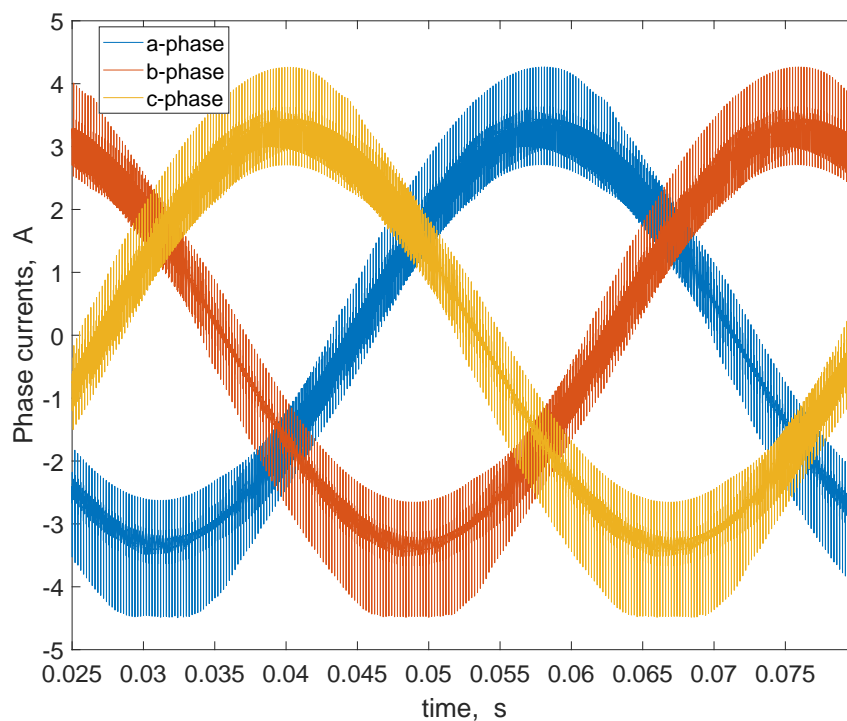


Figure 4.7. Simulated phase currents using LTspice.

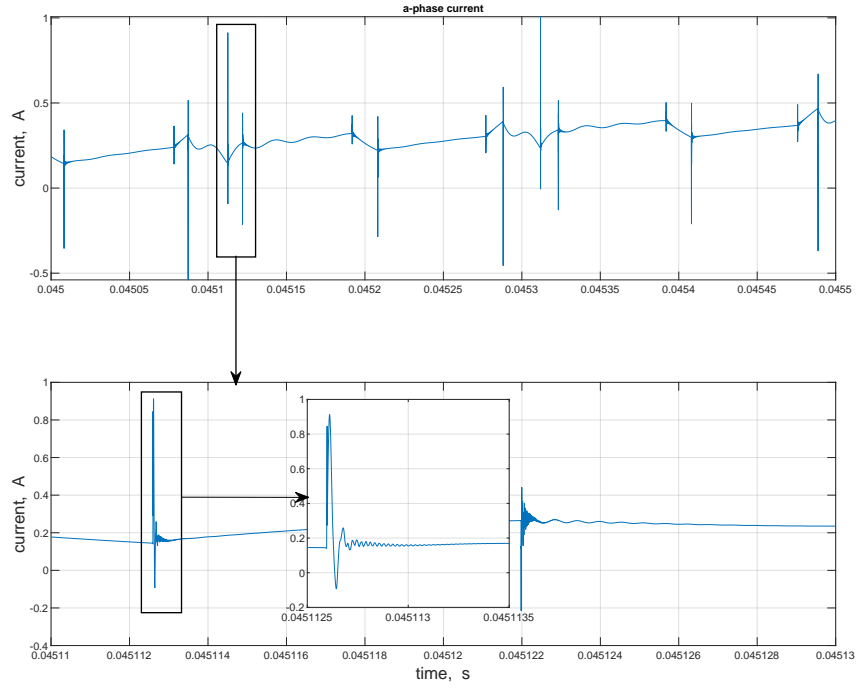


Figure 4.8. Expanded view of simulated a -phase current.

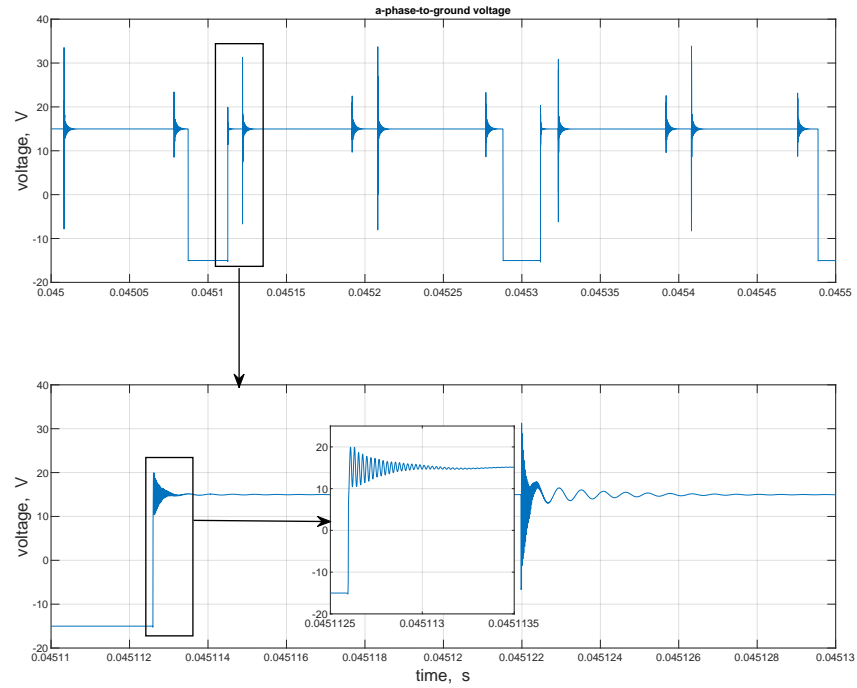


Figure 4.9. Simulated phase-to-ground voltage, v_{ag} using LTspice.

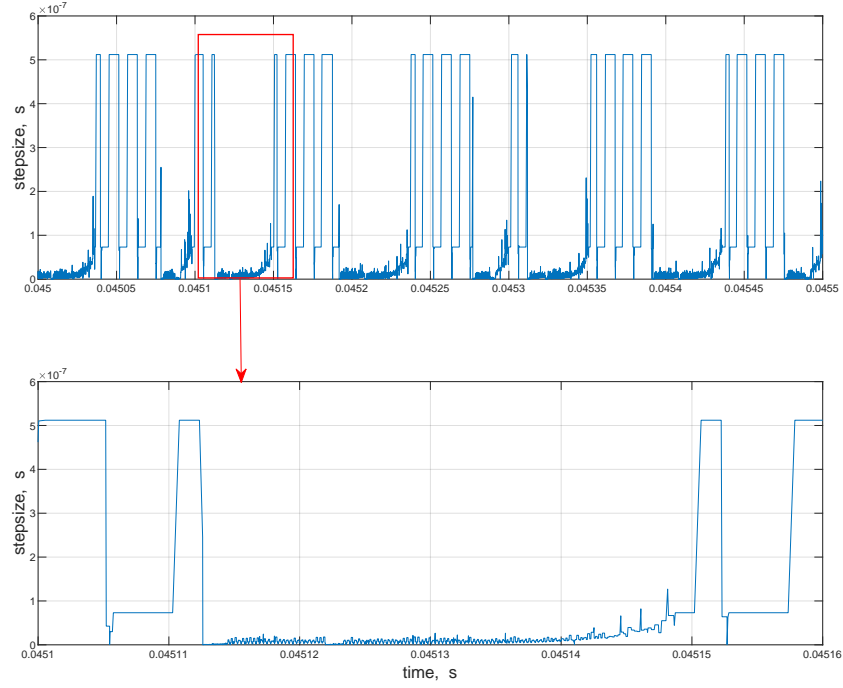


Figure 4.10. Step size taken in MNA-based simulation.

The lengthy runtime taken for the completion of the simulation can be attributed to the large number of iterations each of which involves the solution of a system of 221×221 sparse linear equations. Moreover, the disparate time scales associated with the system contribute to its numerical stiffness. As illustrated in Figures 4.8 and 4.9, every switching event results in a transient that subsides in less than a microsecond. In order to accurately capture these switching events, very small time steps must be used in the simulation. As the high-frequency events subside, the time step may grow if numerical stability can be maintained. However, this growth is not significant as shown in Figure 4.10. Although a maximum time step of $0.512 \mu\text{s}$ is registered during intervals between switching events, it can be deduced from the step size results that the time step had to be adjusted to a value less than $0.1 \mu\text{s}$ during these intervals. The reason for these phenomena is likely due to the fact that any significant growth in the time step would have resulted in convergence problems for the Newton-Raphson loop.

To avoid these problems, the time step must remain sufficiently small. In the next section, these results will be compared to a state-space-based simulation of the system model.

4.3 State-space-based Simulation of Wideband Model

System models can also be implemented using a state-space-based simulation program. In state-space-based simulators such as Simulink, the system is described in block diagram form using summer, gain, multiplier, and/or integrator blocks. The outputs of the integrator block represent the system states. Based on the graphic definition of the system, Simulink establishes a subroutine that evaluates the derivatives of state variables in terms of states and inputs. The state equations are then solved numerically, using one of the integration algorithms supported by the simulator.

A state-space-based simulation of the wideband model was implemented using Simulink. The top-level block diagram of the simulation is shown in Figure 4.11. Here, the arrows represent interconnections between component outputs and component inputs. Each block corresponds to a state model of the form

$$\frac{d\mathbf{x}}{dt} = \mathbf{f}(\mathbf{x}, \mathbf{u}) \quad (4.9)$$

$$\mathbf{y} = \mathbf{g}(\mathbf{x}, \mathbf{u}) \quad (4.10)$$

where \mathbf{u} is the component input and \mathbf{y} the component output.

The operating point chosen for this simulation is the same as in the MNA-based simulation. The absolute and relative tolerances were both set to $1e^{-6}$ and the integration algorithm was selected to be ODE23tb, suitable for stiff ordinary differential equations. The computer simulation was executed for a simulation time of 80 ms using a 3.4-GHz personal computer with 32 GB of RAM. The corresponding runtime for the simulation was 3.32 h. Although, a more powerful computer was used for the state-space-based simulation, the computational efficiency was not notably better than that of the MNA-based simulation. The simulation statistics given in Table 4.3 is indicative of the need for a more computationally efficient simulation method.

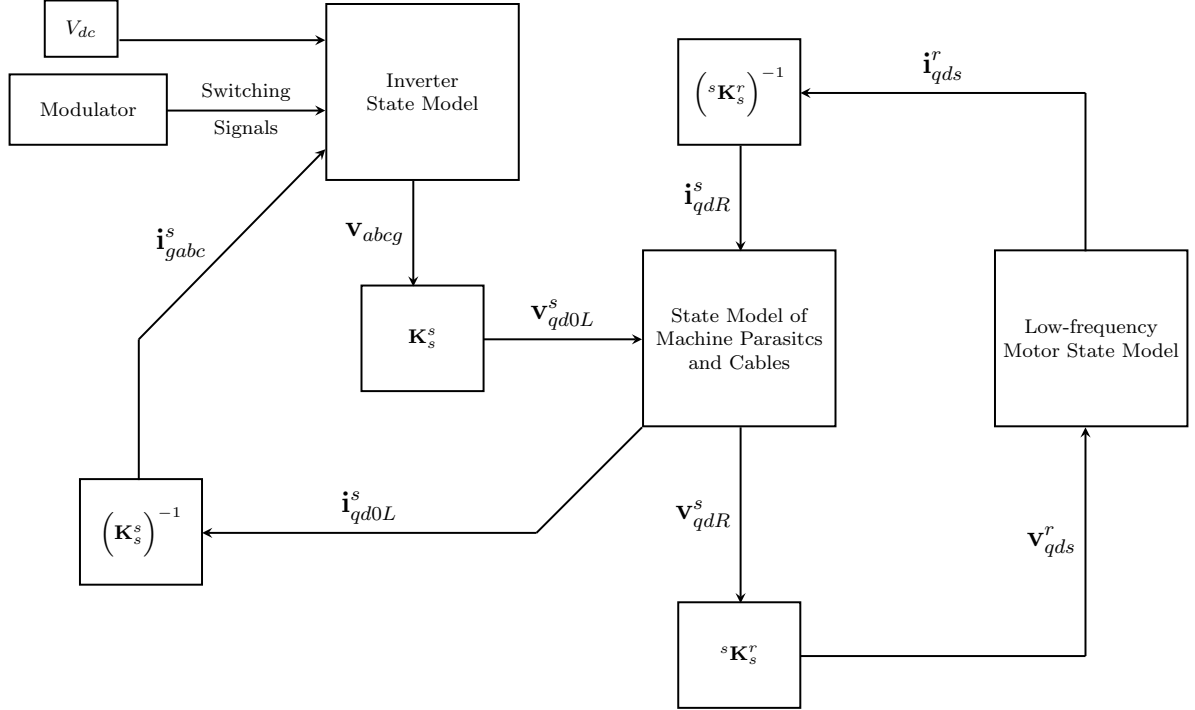


Figure 4.11. Top-level block diagram of the state-space-based simulation of the system.

The simulated phase currents are depicted in Figure 4.12. Also, zoomed-in plots of the phase current and phase-to-ground voltage of the a -phase, over a few microseconds are shown in Figures 4.13 and 4.14. The step size taken by the simulation program over this period is also shown in Figure 4.15. As depicted, the step size is varied according to the particular time scale associated with the dynamics being captured. The need to keep a strict and small time step when capturing the high-frequency dynamics gives rise to the poor computational efficiency. It is apparent that an alternative method for simulating the electric drive system must be explored since better computational efficiency is desired.

Table 4.3. State-space simulation statistics.

Simulation time	80 ms
Runtime	3.32 h
Simulation speed	6.68 $\mu\text{s/s}$
Integration algorithm	Implicit Runge-Kutta
Step size	Variable
Total time-steps	59 039 570

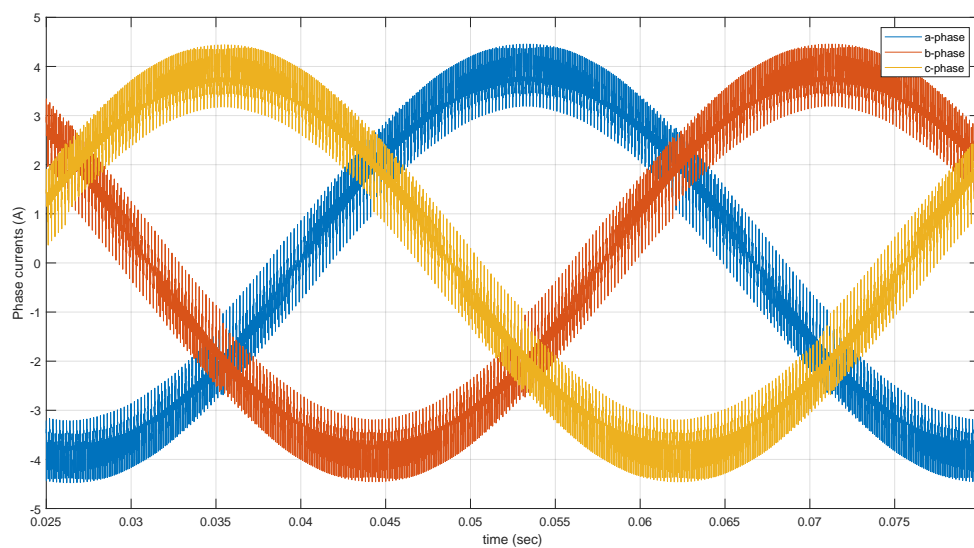


Figure 4.12. Simulated phase currents using state-space-based approach.

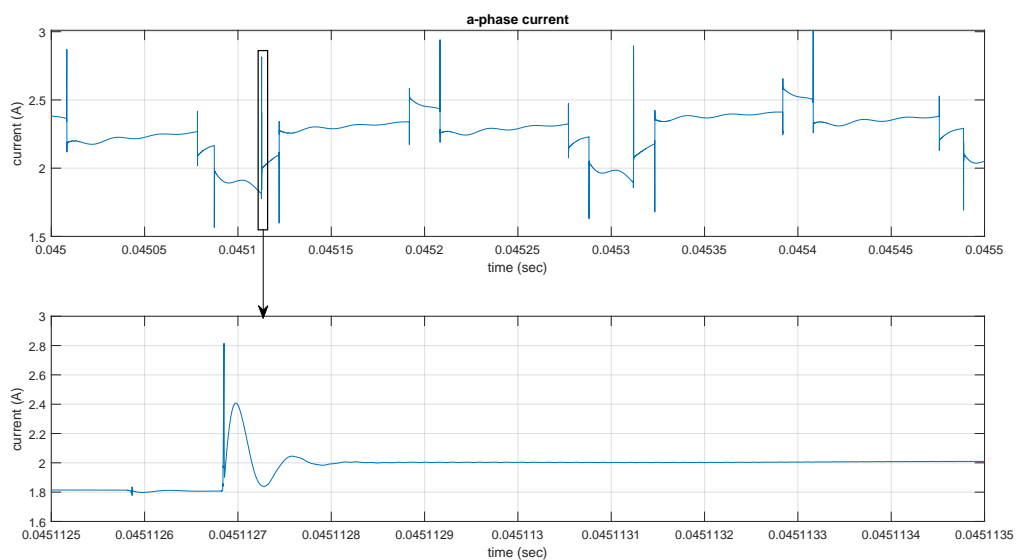


Figure 4.13. Expanded view of a -phase current.

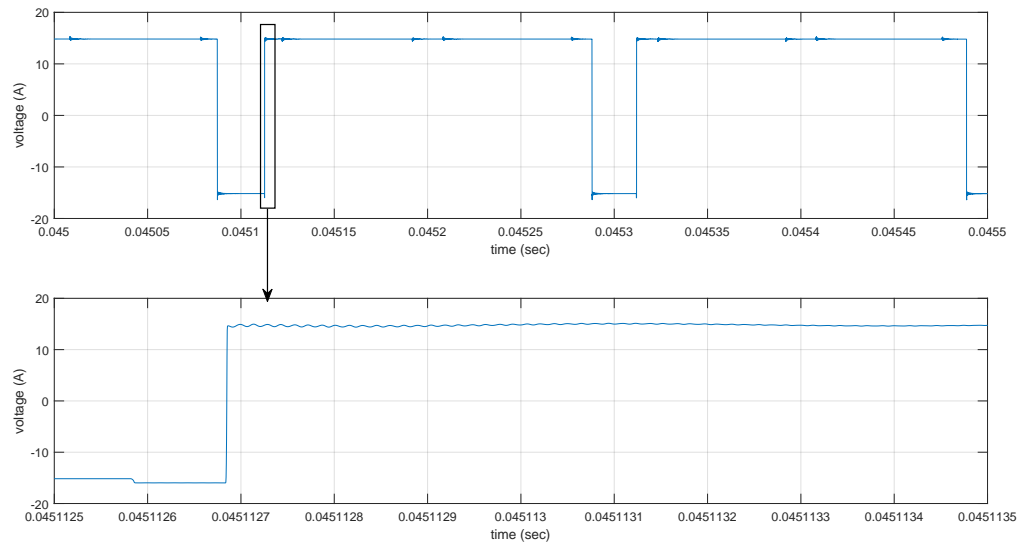


Figure 4.14. Simulated phase-to-ground voltage, v_{ag} .

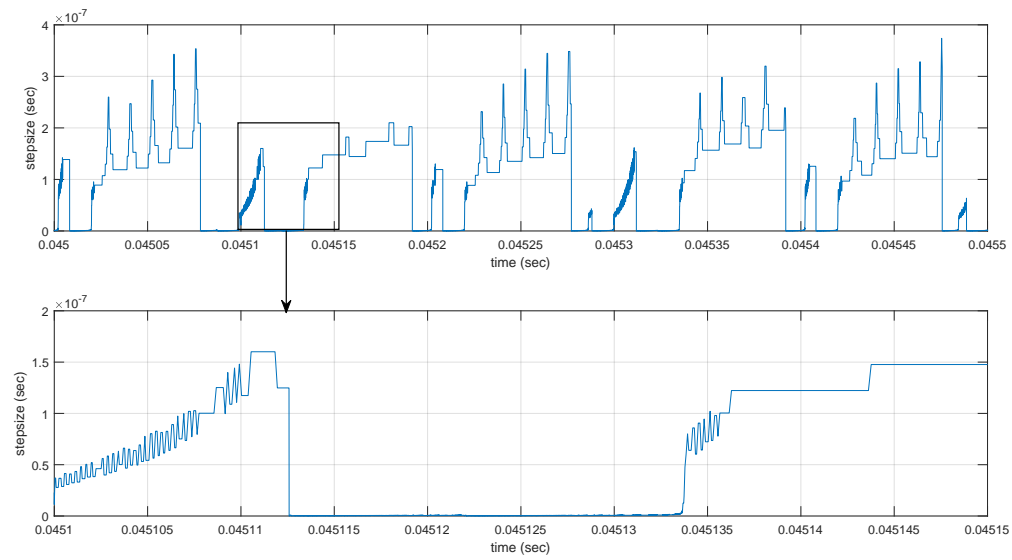


Figure 4.15. Step size taken in state-space-based simulation.

4.4 The Computational Cost of Simulation and the Stiffness Problem

The need for an efficient and accurate simulation method for WBG-based electric drive systems is emphasized by the stiff system of differential equations that define the system. To understand the implications of the stiffness of a system, it is useful to consider a set of nonlinear equations

$$p\mathbf{x} = f(\mathbf{x}, t), \quad \mathbf{x}(t_0) = \mathbf{x}_0 \quad (4.11)$$

where $\mathbf{x} \in \mathfrak{R}^n$, $f : \mathfrak{R}^n \rightarrow \mathfrak{R}^n$, and p is the derivative-with-respect-to-time (d/dt) operator. Since the differential of $f(\mathbf{x}, t)$, is generally expressed as

$$df = \frac{\partial f}{\partial \mathbf{x}} d\mathbf{x} + \frac{\partial f}{\partial t} dt \quad (4.12)$$

it follows that for small deviations from \mathbf{x}_0 , (4.11) may be approximated as

$$p\mathbf{x} = \frac{\partial f}{\partial \mathbf{x}}(\mathbf{x} - \mathbf{x}_0) + \frac{\partial f}{\partial t}(t - t_0) + f(\mathbf{x}_0, t_0) \quad (4.13)$$

For a given small time interval $[t_0, t_0 + h]$, (4.13) can be rewritten as

$$p\mathbf{x} = \mathbf{J}_x(\mathbf{x} - \mathbf{x}_0) + \mathbf{F}(\mathbf{x}_0, t_0) \quad (4.14)$$

where \mathbf{J}_x is the Jacobian of f and equal to $\partial f / \partial \mathbf{x}$ and $\mathbf{F}(\mathbf{x}_0, t_0)$ is some constant column matrix equal to $h \partial f / \partial t + f(\mathbf{x}_0, t_0)$.

For a defective or non-defective \mathbf{J}_x , the Jordan form, \mathbf{J} may be established such that

$$\mathbf{J} = \mathbf{T}_n^{-1} \mathbf{J}_x \mathbf{T}_n \quad (4.15)$$

Here, \mathbf{T}_n is some nonsingular matrix that ensures (4.15) and the matrix \mathbf{J} is given as $\mathbf{J} = \text{diag}(J_1, \dots, J_p)$, where J_1, \dots, J_p are Jordan blocks. In particular, J_i takes the form

$$J_i = \lambda_i I_{n_i} + S_{n_i} \quad (4.16)$$

In the above expression, λ_i is an eigenvalue and the i th diagonal entry of matrix \mathbf{J} , I_{n_i} is an $n_i \times n_i$ identity matrix that corresponds to the i th Jordan block, $n_1 + \dots + n_p = n$, and S_{n_i} is a block from the matrix, \mathbf{S}_n .

$$\mathbf{S}_n = \begin{bmatrix} 0 & 1 & 0 & \cdots & 0 & 0 \\ 0 & 0 & 1 & \cdots & 0 & 0 \\ 0 & 0 & 0 & \cdots & 0 & 0 \\ \vdots & \vdots & \vdots & \ddots & \vdots & \vdots \\ 0 & 0 & 0 & \cdots & 0 & 1 \\ 0 & 0 & 0 & \cdots & 0 & 0 \end{bmatrix} \quad (4.17)$$

With these definitions, (4.14) may be transformed as follows

$$\mathbf{T}_n^{-1} p\mathbf{x} = \mathbf{T}_n^{-1} \mathbf{T}_n \mathbf{J} \mathbf{T}_n^{-1} (\mathbf{x} - \mathbf{x}_0) + \mathbf{T}_n^{-1} \mathbf{F}(\mathbf{x}_0, t_0) \quad (4.18)$$

$$\mathbf{T}_n^{-1} p\mathbf{x} = \mathbf{J} \mathbf{T}_n^{-1} (\mathbf{x} - \mathbf{x}_0) + \mathbf{T}_n^{-1} \mathbf{F}(\mathbf{x}_0, t_0) \quad (4.19)$$

This may readily be simplified as

$$p\mathbf{z} = \mathbf{J}(\mathbf{z} - \mathbf{z}_0) + \mathbf{F}^*(\mathbf{z}_0, t_0) \quad (4.20)$$

where \mathbf{z} is equal to $\mathbf{T}_n^{-1} \mathbf{x}$. Now, ignoring the contributions of the term $\mathbf{F}(\mathbf{x}_0, t_0)$ in (4.14) to the solution of the test problem given by (4.14) and (4.20), a general solution may be established as

$$\mathbf{x} = \exp(\mathbf{J}_x t) \mathbf{x}_0 = \mathbf{T}_n e^{\mathbf{J} t} \mathbf{T}_n^{-1} \mathbf{x}_0 \quad (4.21)$$

where $e^{\mathbf{J}} = \text{diag}(e^{J_1}, \dots, e^{J_p})$. Specifically,

$$e^{J_i} = \exp(\lambda_i I_{n_i}) \exp(S_{n_i}) = e^{\lambda_i} \sum_{j=0}^{n_i-1} \frac{1}{j!} S_{n_i}^j$$

The given solution suggests that if some eigenvalues λ_i are in the left-half plane and larger in magnitude than the others, some components of the solution will decay faster than others. Thus, an attempt to solve the test problem using a non-stiff integration algorithm such as the forward Euler will result in long simulation runtimes since the maximum step size for

numerical stability to be maintained is usually dictated by the components with the fastest dynamics. Moreover, a long runtime may also exist if a single-rate simulation method that uses an implicit stiffly-stable algorithm is employed. This is seen in the MNA and state-space results presented in the previous sections. It follows that a new simulation strategy must be considered to achieve better computational efficiency. As a springboard for the simulation strategy described in the next chapter, the sparse tableau analysis (STA) approach is introduced next. Its capability in solving the differential equations of the wideband model is also discussed.

4.5 Sparse Tableau Formulation of System Model

The sparse tableau analysis (STA) formulation described by Hachtel et al. in [66] has been used considerably for small- and large-scale circuit analysis and design. Recent research has also seen its use in power system analysis [67]. This is made possible due to the versatility of the STA formulation. Moreover, it can also be adapted for the analysis of a system described by state equations. In this regard, the branch or device equations for a typical system is considered as having three sets of distinct variables: the state, the input, and the output.

For a system with K components, the k th component may be described by the state and output equations:

$$p\mathbf{x}^k = \dot{\mathbf{x}}^k = \mathbf{f}(\mathbf{x}^k, \mathbf{u}^k), \quad k = 1, 2, \dots, K \quad (4.22)$$

$$\mathbf{y}^k = \mathbf{g}(\mathbf{x}^k, \mathbf{u}^k) \quad (4.23)$$

Here \mathbf{x}^k , \mathbf{u}^k , and \mathbf{y}^k represent the respective state, input, and output for the k th component. Defining \mathbf{x} as the concatenation of $\mathbf{x}^1, \mathbf{x}^2, \dots, \mathbf{x}^k$, i.e. $\mathbf{x} = [\mathbf{x}^1 \ \mathbf{x}^2 \ \dots \ \mathbf{x}^k]^T$, $\mathbf{u} = [\mathbf{u}^1 \ \mathbf{u}^2 \ \dots \ \mathbf{u}^k]^T$, and $\mathbf{y} = [\mathbf{y}^1 \ \mathbf{y}^2 \ \dots \ \mathbf{y}^k]^T$, the composite state equations can be expressed as

$$p\mathbf{x} = \dot{\mathbf{x}} = \mathbf{f}(\mathbf{x}, \mathbf{u}) \quad (4.24)$$

$$\mathbf{y} = \mathbf{g}(\mathbf{x}, \mathbf{u}) \quad (4.25)$$

It is important to note that these equations do not yet incorporate the interconnections between components in the system. These interconnections can be expressed in matrix form as

$$\begin{bmatrix} \mathbf{y}^1 \\ \mathbf{y}^2 \\ \vdots \\ \mathbf{y}^k \end{bmatrix} = \begin{bmatrix} \mathbf{0} & \mathbf{L}^{1,2} & \dots & \mathbf{L}^{2,k} \\ \mathbf{L}^{2,1} & \mathbf{0} & \dots & \mathbf{L}^{2,k} \\ \vdots & \vdots & \ddots & \vdots \\ \mathbf{L}^{k,1} & \mathbf{L}^{k,2} & \dots & \mathbf{0} \end{bmatrix} \begin{bmatrix} \mathbf{u}^1 \\ \mathbf{u}^2 \\ \vdots \\ \mathbf{u}^k \end{bmatrix} \quad (4.26)$$

where $\mathbf{L}^{i,j} \in \mathbb{R}^{n,m}$ is a connection matrix connecting the outputs of component j to component i . Here, n is the number of inputs of component i and m is the number of outputs of component j . All entries of $\mathbf{L}^{i,j}$ are either 0 or 1. All diagonal elements of (4.26) are zero since there is no need to connect a component's output to its input. Equation (4.26) can be expressed symbolically as

$$\mathbf{y} = \mathbf{L}\mathbf{u} \quad (4.27)$$

where \mathbf{L} is a connection matrix. In general, it is not symmetric, it is sparse, and its entries are 0's or 1's. Equation (4.27), along with (4.24) and (4.25) represent differential-algebraic equations that define the dynamic behavior of the system.

For a time interval h , the change in state \mathbf{x} with respect to time t is

$$\dot{\mathbf{x}} = \frac{\mathbf{x}(t_0 + h) - \mathbf{x}(t_0)}{h} \quad (4.28)$$

Here, $\mathbf{x}(t_0)$ is the old state at $t = t_0$ and $\mathbf{x}(t_0 + h)$ is the new state at $t = t_0 + h$. From (4.28), it follows that the state equation may be expressed in the form

$$\mathbf{x}(t_0 + h) - \mathbf{x}(t_0) = h\mathbf{f}(\mathbf{x}(t_0 + h), \mathbf{u}(t_0 + h)) \quad (4.29)$$

where $\mathbf{u}(t_0 + h)$ is the input at $t = t_0 + h$. With old and new variables denoted with subscripts ' i ' and ' $i + 1$ ', respectively, the state equations may be rewritten for a general sense as

$$\mathbf{x}_{i+1} - \mathbf{x}_i = h\mathbf{f}(\mathbf{x}_{i+1}, \mathbf{u}_{i+1}) \quad (4.30)$$

$$\mathbf{x}_{i+1} - h\mathbf{f}(\mathbf{x}_{i+1}, \mathbf{u}_{i+1}) = \mathbf{x}_i \quad (4.31)$$

These expressions are in the backward Euler form and may serve as bases for obtaining an iterative solution. In arriving at this, the Newton-Raphson algorithm, which is based on Taylor's series expansion, may be employed. Herein,

$$\begin{aligned} \mathbf{x}_{i+1,j+1} - h \left[\mathbf{f}(\mathbf{x}_{i+1,j}, \mathbf{u}_{i+1,j}) + \frac{\partial \mathbf{f}}{\partial \mathbf{x}} \bigg|_{i+1,j} (\mathbf{x}_{i+1,j+1} - \mathbf{x}_{i+1,j}) \right. \\ \left. + \frac{\partial \mathbf{f}}{\partial \mathbf{u}} \bigg|_{i+1,j} (\mathbf{u}_{i+1,j+1} - \mathbf{u}_{i+1,j}) \right] = \mathbf{x}_{i,\infty} \end{aligned} \quad (4.32)$$

where the subscript j is notation for the j th Newton-Raphson iteration, subscript $j + 1$ denotes the $(j + 1)$ th iteration and $\mathbf{x}_{i,\infty}$ is the converged solution for the states. This expression may be further simplified as

$$\begin{aligned} \left[\mathbf{I} - h \frac{\partial \mathbf{f}}{\partial \mathbf{x}} \bigg|_{i+1,j} \right] \mathbf{x}_{i+1,j+1} - h \frac{\partial \mathbf{f}}{\partial \mathbf{u}} \bigg|_{i+1,j} \mathbf{u}_{i+1,j+1} = h\mathbf{f}(\mathbf{x}_{i+1,j}, \mathbf{u}_{i+1,j}) \\ - h \frac{\partial \mathbf{f}}{\partial \mathbf{x}} \bigg|_{i+1,j} \mathbf{x}_{i+1,j} - h \frac{\partial \mathbf{f}}{\partial \mathbf{u}} \bigg|_{i+1,j} \mathbf{u}_{i+1,j} + \mathbf{x}_{i,\infty} \end{aligned} \quad (4.33)$$

$$\mathbf{A}_{i+1,j} \mathbf{x}_{i+1,j+1} + \mathbf{B}_{i+1,j} \mathbf{u}_{i+1,j+1} = \mathbf{a}_{i+1,j} \quad (4.34)$$

Here, \mathbf{I} is an identity matrix and (4.34) is a symbolic expression of (4.33).

Following the procedures used in establishing the state equation of (4.34), a similar form may be obtained for the output equation as

$$\mathbf{y}_{i+1} = \mathbf{g}(\mathbf{x}_{i+1}, \mathbf{u}_{i+1}) \quad (4.35)$$

$$\begin{aligned} \mathbf{y}_{i+1,j+1} = \mathbf{g}(\mathbf{x}_{i+1,j}, \mathbf{u}_{i+1,j}) + \frac{\partial \mathbf{g}}{\partial \mathbf{x}} \bigg|_{i+1,j} (\mathbf{x}_{i+1,j+1} - \mathbf{x}_{i+1,j}) \\ + \frac{\partial \mathbf{g}}{\partial \mathbf{u}} \bigg|_{i+1,j} (\mathbf{u}_{i+1,j+1} - \mathbf{u}_{i+1,j}) \end{aligned} \quad (4.36)$$

$$\mathbf{y}_{i+1,j+1} - \frac{\partial \mathbf{g}}{\partial \mathbf{x}} \bigg|_{i+1,j} \mathbf{x}_{i+1,j+1} - \frac{\partial \mathbf{g}}{\partial \mathbf{u}} \bigg|_{i+1,j} \mathbf{u}_{i+1,j+1} = \mathbf{g}(\mathbf{x}_{i+1,j}, \mathbf{u}_{i+1,j}) - \frac{\partial \mathbf{g}}{\partial \mathbf{x}} \bigg|_{i+1,j} \mathbf{x}_{i+1,j} - \frac{\partial \mathbf{g}}{\partial \mathbf{u}} \bigg|_{i+1,j} \mathbf{u}_{i+1,j} \quad (4.37)$$

$$\mathbf{y}_{i+1,j+1} + \mathbf{E}_{i+1,j} \mathbf{x}_{i+1,j+1} + \mathbf{F}_{i+1,j} \mathbf{u}_{i+1,j+1} = \mathbf{b}_{i+1,j} \quad (4.38)$$

As may be inferred from the output equations, (4.38) is a symbolic expression of (4.37).

The expressions given by (4.34) and (4.38) are important in establishing the sparse tableau formulation for the state model of the system. The tableau form will also be composed of equations representing the interconnections between state models. These interconnecting equations can be expressed as

$$\mathbf{y}_{i+1,j+1} = \mathbf{L} \mathbf{u}_{i+1,j+1} \quad (4.39)$$

where \mathbf{L} is a matrix with entries nonzero $\mathbf{L}^{i,j}$ if the component j is connected to component i and $\mathbf{0}$ otherwise. Thus, the general form of the tableau can be expressed as

$$\begin{bmatrix} \mathbf{A}_{i+1,j} & \mathbf{0} & \mathbf{B}_{i+1,j} \\ \mathbf{E}_{i+1,j} & \mathbf{I} & \mathbf{F}_{i+1,j} \\ \mathbf{0} & \mathbf{I} & \mathbf{L} \end{bmatrix} \begin{bmatrix} \mathbf{x}_{i+1,j+1} \\ \mathbf{y}_{i+1,j+1} \\ \mathbf{u}_{i+1,j+1} \end{bmatrix} = \begin{bmatrix} \mathbf{a}_{i+1,j} \\ \mathbf{b}_{i+1,j} \\ \mathbf{0} \end{bmatrix} \quad (4.40)$$

which may be made equivalent to

$$\mathbf{T}_{i+1,j} \mathbf{z}_{i+1,j+1} = \mathbf{w}_{i+1,j} \quad (4.41)$$

It should be noted that $\mathbf{A}_{i+1,j}$, $\mathbf{B}_{i+1,j}$, $\mathbf{E}_{i+1,j}$, and $\mathbf{F}_{i+1,j}$ are block diagonal matrices. Consequently, the tableau matrix is very sparse.

Now, it is important to examine how to incorporate an electric circuit into the tableau. To proceed, it would be useful to consider the circuit equation for the circuit shown in Figure 4.16. Herein,

$$L \frac{di_{br}}{dt} + ri_{br} = v_{br} \quad (4.42)$$

From this, state model equations may be readily established as

$$\frac{di_{br}}{dt} = \frac{1}{L}(v_{br} - ri_{br}) \quad (4.43)$$

$$y = i_{br} \quad (4.44)$$

These imply that the rL branch has a state i_{br} , an input v_{br} , and an output i_{br} .

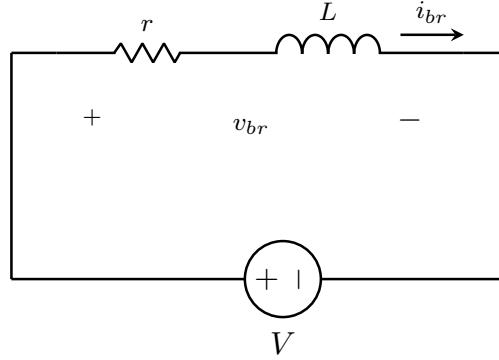


Figure 4.16. rL circuit.

Likewise, similar equations may be established for the gC branch depicted in Figure 4.17. The state model equations will be

$$\frac{dv_{br}}{dt} = \frac{1}{C}(i_{br} - gv_{br}) \quad (4.45)$$

$$y = v_{br} \quad (4.46)$$

Thus, for the gC branch, there exists a state v_{br} , an input i_{br} , and an output v_{br} .

The state model for the branches of a circuit can be accounted for when formulating (4.24) and (4.25). In particular, they will be part of the set of equations described by (4.34) and (4.38). Moreover, equations representing the interconnections between the branches may

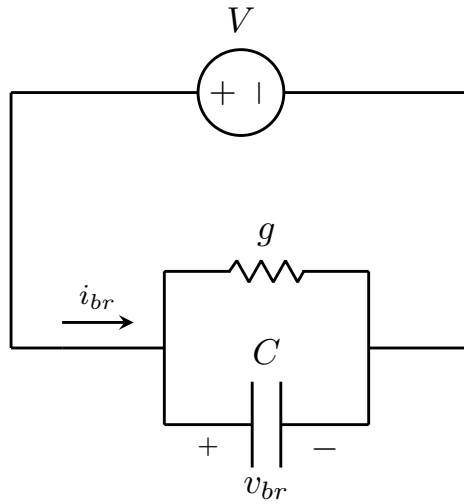


Figure 4.17. gC circuit.

easily be included in the tableau equation by taking advantage of recognized graph theory. Using these techniques, equations representing the relationship between branch currents as well as the relationship between branch voltages may be established. In order to go about this, two important matrices are necessary – the branch-to-node incidence matrix and the fundamental loop matrix.

The branch-to-node incidence matrix for a network represents the topology or structure of the network. Specifically, the entries of the incidence matrix are any of 0, +1, or -1 . The precise value of each entry is determined by the directed network graph deduced from the structure of the circuit. A directed network graph is a collection of nodes and corresponding set of edges, which correspond to the branches in the circuit. The edges (branches) are said to be incident to its vertices (or nodes). An example circuit along with the equivalent directed graph is shown in Figure 4.18.

In addition, a directed graph is characterized by loops, trees, and link branches. A loop is a subgraph wherein every node is included in exactly two edges and a path exists between the nodes in the directed graph; for the example circuit, the set of edges $\{e_3, e_4, e_5, e_6\}$ is a loop. A tree is a subgraph that has no loops but includes all nodes of the directed graph and at least a path between two nodes in the directed graph; in the directed graph given in

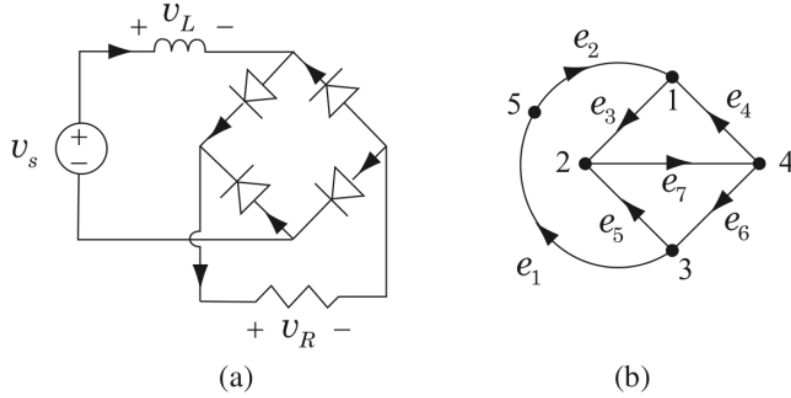


Figure 4.18. (a) Example circuit, (b) directed graph.

Figure 4.18, the set of edges $\{e_2, e_3, e_4, e_5\}$ is a tree. Branches (or edges) not found in the tree are called link branches. In a directed graph, with N_n nodes and N_b branches, there exists $(N_n - 1)$ tree branches and $(N_b - N_n + 1)$ link branches. For such a directed graph, the $N_n \times N_b$ node incidence matrix \mathbf{A}_a may be realized as

$$\mathbf{A}_a = [a_{ij}] \quad (4.47)$$

where

- $a_{ij} = 1$ if branch j is incident to node i and the edge's tail is connected to node i
- $a_{ij} = -1$ if branch j is incident to node i and the edge's head is connected to node i
- $a_{ij} = 0$ if branch j is not incident to node i

By eliminating a row in the incidence matrix, an $(N_n - 1) \times N_b$ matrix that is linearly independent may be obtained. This matrix is called the reduced incidence matrix \mathbf{A}_r , which can be used for representing the network equations that come from Kirchoff's Current Law (KCL) and Kirchoff's Voltage Law (KVL). Here,

$$\mathbf{A}_r \mathbf{i}_b = \mathbf{0} \quad (4.48)$$

$$\mathbf{v}_b = \mathbf{A}_r^T \mathbf{v}_n \quad (4.49)$$

where \mathbf{i}_b represents the vector of branch currents, \mathbf{v}_b represents the branch voltages, and \mathbf{v}_n is a vector of the nodal voltages.

The columns of \mathbf{A}_r and corresponding entries in \mathbf{i}_b can be reordered such that the first $N_n - 1$ columns correspond to tree branches with the remaining columns corresponding to link branches. This results in a partitioned incidence matrix of the form

$$\mathbf{A}_r = \begin{bmatrix} \mathbf{A}_T & \mathbf{A}_L \end{bmatrix} \quad (4.50)$$

In the structure defined above, \mathbf{A}_T is a square matrix dimensioned $(N_n - 1) \times (N_n - 1)$ whose columns correspond to the branches of a tree and \mathbf{A}_L is the $(N_n - 1) \times (N_b - N_n + 1)$ matrix whose columns define the associated link branches. These partitions allow for the introduction of the fundamental loop matrix \mathbf{B}_f that is used to express the KVL network equations in terms of the branch voltages \mathbf{v}_b .

$$\mathbf{B}_f \mathbf{v}_b = \mathbf{0} \quad (4.51)$$

It is useful to first define a loop matrix before outlining the relationship between the matrices \mathbf{B}_f , \mathbf{A}_T , and \mathbf{A}_L .

For a directed graph with N_l loops and N_b branches, there exists an $N_l \times N_b$ loop matrix defined as

$$\mathbf{B}_a = [b_{ij}] \quad (4.52)$$

where

- $b_{ij} = 1$ if branch j is in loop i and the directions agree
- $b_{ij} = -1$ if branch j is in loop i and the directions oppose
- $b_{ij} = 0$ if branch j is not in loop i

The fundamental loop matrix can be derived from this matrix by selecting the loops corresponding to the $(N_b - N_n + 1)$ link branches. Furthermore, it is a $(N_b - N_n + 1) \times N_b$ matrix that is partitioned such that

$$\mathbf{B}_f = \begin{bmatrix} \mathbf{B}_T & \mathbf{I} \end{bmatrix} \quad (4.53)$$

In (4.53), the block matrix \mathbf{B}_T is a $(N_b - N_n + 1) \times (N_n - 1)$ matrix and \mathbf{I} is a $(N_b - N_n + 1) \times (N_b - N_n + 1)$ identity matrix that correspond to the link branches.

To establish \mathbf{B}_T , it can be shown that for the fundamental loop matrix and reduced incidence matrix, one is orthogonal to the transpose of the other.

$$\mathbf{B}_f \mathbf{A}_r^T = \mathbf{0} \quad (4.54)$$

This relationship makes it possible to realize the fundamental loop matrix \mathbf{B}_f from the reduced incidence matrix \mathbf{A}_r . In particular, it implies that

$$\mathbf{B}_f \mathbf{A}_r^T = \begin{bmatrix} \mathbf{B}_T & \mathbf{I} \end{bmatrix} \begin{bmatrix} \mathbf{A}_T^T \\ \mathbf{A}_L^T \end{bmatrix} = \mathbf{0} \quad (4.55)$$

$$\begin{bmatrix} \mathbf{B}_T \mathbf{A}_T^T + \mathbf{A}_L^T \end{bmatrix} = \mathbf{0} \quad (4.56)$$

Thus,

$$\mathbf{B}_T = -(\mathbf{A}_T^{-1} \mathbf{A}_L)^T \quad (4.57)$$

Therefore, if the partitions of the reduced incidence matrix \mathbf{A}_r can be established, then the fundamental loop matrix can be obtained using (4.53) and (4.57). Consequently, the means for relating the branch voltages is simplified.

The equations given by (4.48) and (4.51) are important for defining the interconnections of branches in the STA formulation. These may easily be appended to the tableau formulation given by (4.40). A benefit of the STA is that it is readily implemented. Also, the sparsity of the tableau enables the use of established and efficient linear equation solvers. Finally, changing the structure of the model dynamically is more readily accomplished with

STA than with MNA. Specifically, a variable-structure variable-order system model is more readily implemented using the STA compared with the MNA approach.

A flowchart for the sparse tableau algorithm is shown in Figure 4.19. In the first stage, the Newton-Raphson method is used to establish a solution to the tableau equation that is formulated from the implicit stiffly-stable algorithm. The solution sets the stage for updating the tableau or reformulating the equations to be solved for the next time step. The process is continued until the time index i has exceeded a set stop time t_{stop} .

The sparse tableau algorithm, if used to implement the full-bandwidth model used in the MNA-based and state-space-based simulation, is not expected to result in a faster simulation since the resulting equations are also of large dimension. Nonetheless, the STA has several advantages: (1) state-space-based and circuit-based models are readily incorporated using any selected algorithm (explicit or implicit) without any relaxations between the circuit and state-space solvers, (2) the approach is very flexible in that new models can readily be incorporated including more advanced MOSFET models that account for voltage-dependent junction capacitances, and (3) as implemented as part of the research conducted, the STA-based simulation can be interfaced with existing Simulink models setting the stage for the heterogeneous multirate approach presented in the next chapter.

4.6 Summary

In this chapter, conventional methods used in the simulation of electric drive systems have been described. These methods include MNA-based, state-space-based, and sparse-tableau-based simulation approaches. The results from these established methods illustrate the need for a more computationally efficient simulation framework. Such a framework is set forth in the next chapter.

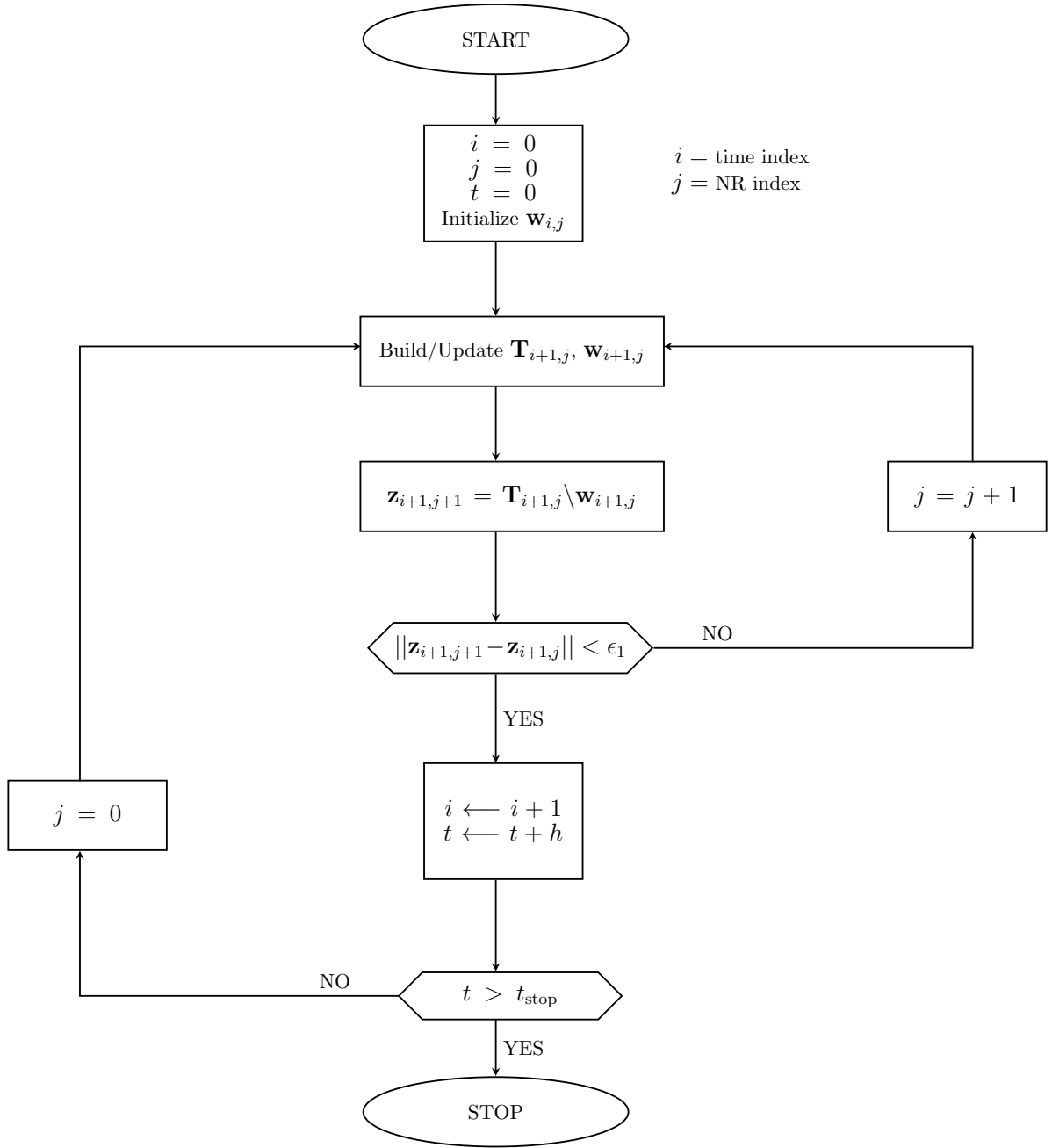


Figure 4.19. Flow chart for sparse tableau algorithm.

5. NEW HETEROGENEOUS MULTIRATE SIMULATION STRATEGY

A heterogeneous multirate simulation framework for WBG-based electric drive systems is set forth in this chapter. In this framework, short- and long-term dynamics are established separately using high- and low-frequency models of the drive system. In particular, the two models are defined by how long it takes their inherent transients to subside. The model with the longer-term transients is referred to as the low-frequency model while the other is called the high-frequency model. The simulations of these models are implemented using two separate computer programs. It is argued that synchronous communication between the two simulations is not necessary to achieve accurate results due to the following observations from the preceding chapter. First, the fast transients are initiated after each switching event. The initial conditions (capacitor voltages, inductor currents) for the fast states can be determined from the slow states at the instant switching is initiated. When the fast transients subside, the slower states would not have changed significantly. This suggests that it is advantageous to decompose the wideband model described in Chapters 2 and 3 and simulated in Chapter 4 into low- and high-frequency models, as will be described in this chapter. The simulations of the low- and high-frequency models are then carried out using computationally efficient approaches specific to each model.

5.1 The Low-frequency Model

For the purpose of establishing the long-term dynamics, a low-frequency model is realized from the wideband PMAC machine model introduced in Chapter 2 and the wideband inverter model of Chapter 3. This can be achieved by deriving reduced-order models for the inverter and surface-mount PMAC machine. In the inverter model, the inductors and capacitors associated with the source model (as shown in Figure 3.6) may be regarded as short- and open-circuits, respectively, since it is assumed that the fast transients associated with the inverter circuit have subsided when considering the long-term transients. Thus, the connecting cable between the dc source and the inverter are modeled as purely resistive

elements. In addition, the voltage drops across the MOSFETs and diodes in the inverter are modeled using lookup tables based on data provided in the CREE module datasheet. Using the measured V - I characteristics enables accurate calculation of conduction losses. The resulting model is shown in Figure 5.1. Therein, the resistive potential divider of Figure 3.6 has been represented by a pair of dc voltage sources of which the midpoint is denoted as g representing the ground or reference node. Moreover, nodes a , b , and c are connected to the low-frequency model of the electric machine and connecting cable.

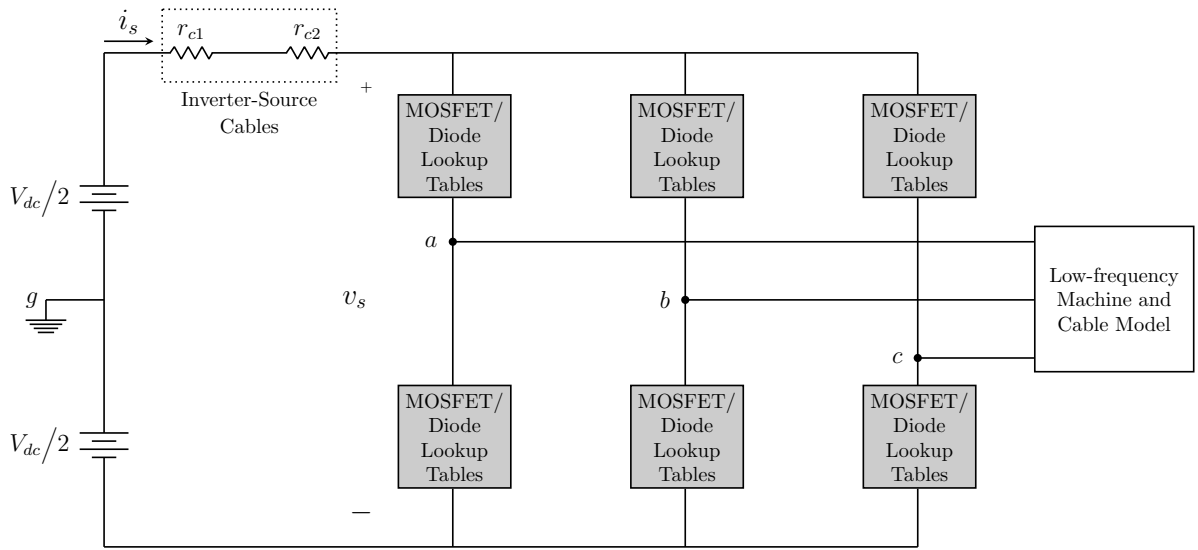


Figure 5.1. Low-frequency circuit representation of drive system.

The low-frequency PMAC machine model established in Chapter 2 is coupled with reduced-order DM and CM state models of the machine and cable as will be described in this chapter. It may be recalled from Chapter 2 that the DM and CM state models each contain three modes. It was shown that the DM state model includes

- an ultra-high-frequency (UHF) mode
- a high-frequency (HF) mode
- a low-frequency (LF) mode

On the other hand, all three modes of the CM state model may be considered to be HF modes. The implication of these observations on the formation of the reduced-order low-frequency model is that the dynamics of the CM state model may be ignored altogether since the transients associated with the HF mode are assumed to have subsided. Moreover, the transients associated with the UHF mode are assumed to have also decayed; only the dynamics associated with the LF mode are of interest in the low-frequency model. Thus, the reduced-order model may be represented by the low-frequency DM state models for the q - and d -axis. An illustration of the low-frequency model of the electric machine and interconnecting cable is shown in Figure 5.2. Here, v_{ag} , v_{bg} , and v_{cg} are inputs from the inverter model and i_{ga} , i_{gb} , and i_{gc} are outputs.

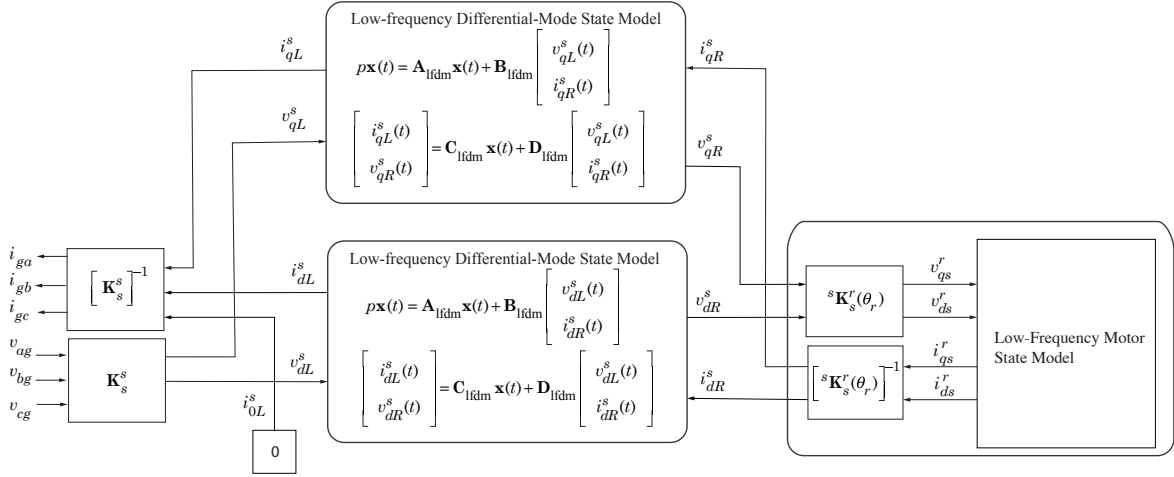


Figure 5.2. Low-frequency model of PMAC machine and interconnecting cable.

Since the CM state model only includes HF modes, it is not included in the low-frequency model where only the long-term dynamics are of paramount interest. Also, the DM state models have been substituted by their reduced forms that take into account only the low-frequency dynamics associated with the electric machine and interconnecting cable. Establishing these reduced forms is pertinent to the implementation of the low-frequency model. In this regard, singular perturbation techniques [53], [68], [69] may be employed to realize the reduced-order model.

To begin, the state and outputs equations for the three modes may be expressed symbolically as

$$\epsilon p \mathbf{x}_1 = \mathbf{A}_1 \mathbf{x}_1 + \mathbf{B}_1 \mathbf{u} \quad (5.1)$$

$$\epsilon p \mathbf{x}_2 = \mathbf{A}_2 \mathbf{x}_2 + \mathbf{B}_2 \mathbf{u} \quad (5.2)$$

$$p \mathbf{x}_3 = \mathbf{A}_3 \mathbf{x}_3 + \mathbf{B}_3 \mathbf{u} \quad (5.3)$$

$$\mathbf{y} = \mathbf{C}_1 \mathbf{x}_1 + \mathbf{C}_2 \mathbf{x}_2 + \mathbf{C}_3 \mathbf{x}_3 + \mathbf{D} \mathbf{u} \quad (5.4)$$

where \mathbf{x}_1 , \mathbf{x}_2 , \mathbf{x}_3 denote the state vectors for the UHF, HF, and LF modes respectively; \mathbf{u} is the vector of inputs, \mathbf{y} the output vector and \mathbf{A}_1 , \mathbf{A}_2 , \mathbf{A}_3 , \mathbf{B}_1 , \mathbf{B}_2 , \mathbf{B}_3 , \mathbf{C}_1 , \mathbf{C}_2 , \mathbf{C}_3 and \mathbf{D} are matrices that relate the state, input, and output vectors. In the full-order model, the variable $\epsilon = 1$. The reduced-order model is obtained by setting $\epsilon = 0$. This implies that \mathbf{x}_1 and \mathbf{x}_2 may be expressed as

$$\mathbf{x}_1 = -\mathbf{A}_1^{-1} \mathbf{B}_1 \mathbf{u}$$

$$\mathbf{x}_2 = -\mathbf{A}_2^{-1} \mathbf{B}_2 \mathbf{u}$$

and the output equation for the low-frequency reduced-order model becomes

$$\mathbf{y} = \left[-\mathbf{C}_1 \mathbf{A}_1^{-1} \mathbf{B}_1 - \mathbf{C}_2 \mathbf{A}_2^{-1} \mathbf{B}_2 + \mathbf{D} \right] \mathbf{u} + \mathbf{C}_3 \mathbf{x}_3 \quad (5.5)$$

which may be symbolically represented as

$$\mathbf{y} = \mathbf{C}_3 \mathbf{x}_3 + \mathbf{D}_{3n} \mathbf{u} \quad (5.6)$$

Thus, the low-frequency reduced-order model may be described by the state equation (5.3) and the output equation (5.6). As such, $\mathbf{A}_{\text{lfdm}} = \mathbf{A}_3$, $\mathbf{B}_{\text{lfdm}} = \mathbf{B}_3$, $\mathbf{C}_{\text{lfdm}} = \mathbf{C}_3$, and $\mathbf{D}_{\text{lfdm}} = \mathbf{D}_{3n}$. It remains to show how the matrices \mathbf{A}_1 , \mathbf{A}_2 , \mathbf{A}_3 , \mathbf{B}_1 , \mathbf{B}_2 , \mathbf{B}_3 , \mathbf{C}_1 , \mathbf{C}_2 , \mathbf{C}_3 and \mathbf{D} are established. To do this, the DM state equations are considered.

As previously introduced in Chapter 2, the state and output equations are in the form

$$p \mathbf{x} = \mathbf{A}_{\text{dm}} \mathbf{x} + \mathbf{B}_{\text{dm}} \mathbf{u} \quad (5.7)$$

$$\mathbf{y} = \mathbf{C}_{\text{dm}}\mathbf{x} + \mathbf{D}_{\text{dm}}\mathbf{u} \quad (5.8)$$

If \mathbf{T} is a 6×6 matrix whose columns are the eigenvectors of \mathbf{A}_{dm} and \mathbf{D}_g is a 6×6 diagonal matrix whose nonzero entries are the eigenvalues of \mathbf{A}_{dm} , then the matrix \mathbf{A}_{dm} may be expressed as

$$\mathbf{A}_{\text{dm}} = \mathbf{T}\mathbf{D}_g\mathbf{T}^{-1} \quad (5.9)$$

Specifically, $\mathbf{D}_g = \text{diag}[\lambda_1, \bar{\lambda}_1, \lambda_2, \bar{\lambda}_2, \lambda_3, \bar{\lambda}_3]$ where λ_1 and its conjugate $\bar{\lambda}_1$ are the eigenvalues associated with the UHF mode, λ_2 and $\bar{\lambda}_2$ are the eigenvalues for the HF mode, and λ_3 and $\bar{\lambda}_3$ are the eigenvalues for the LF mode. Also, the matrix $\mathbf{T} = [\mathbf{v}_1 | \bar{\mathbf{v}}_1 | \mathbf{v}_2 | \bar{\mathbf{v}}_2 | \mathbf{v}_3 | \bar{\mathbf{v}}_3]$ with $\mathbf{v}_1, \bar{\mathbf{v}}_1, \mathbf{v}_2, \bar{\mathbf{v}}_2, \mathbf{v}_3$, and $\bar{\mathbf{v}}_3$ being eigenvectors corresponding to the eigenvalues $\lambda_1, \bar{\lambda}_1, \lambda_2, \bar{\lambda}_2, \lambda_3$, and $\bar{\lambda}_3$, respectively. It follows that the state equation of (5.7) may be rewritten as

$$p\mathbf{x} = \mathbf{T}\mathbf{D}_g\mathbf{T}^{-1}\mathbf{x} + \mathbf{B}_{\text{dm}}\mathbf{u} \quad (5.10)$$

Assuming \mathbf{T} is a transformation matrix such that $\mathbf{x} = \mathbf{T}\mathbf{z}$, then the state and output equations become

$$\mathbf{T}p\mathbf{z} = \mathbf{T}\mathbf{D}_g\mathbf{T}^{-1}\mathbf{T}\mathbf{z} + \mathbf{B}_{\text{dm}}\mathbf{u} \quad (5.11)$$

$$\mathbf{y} = \mathbf{C}_{\text{dm}}\mathbf{T}\mathbf{z} + \mathbf{D}_{\text{dm}}\mathbf{u} \quad (5.12)$$

These equations may be simplified further as

$$p\mathbf{z} = \mathbf{D}_g\mathbf{z} + [\mathbf{T}^{-1}\mathbf{B}_{\text{dm}}]\mathbf{u} \quad (5.13)$$

$$\mathbf{y} = [\mathbf{C}_{\text{dm}}\mathbf{T}]\mathbf{z} + \mathbf{D}_{\text{dm}}\mathbf{u} \quad (5.14)$$

where $\mathbf{T}^{-1}\mathbf{B}_{\text{dm}}$ is a 6×2 matrix, $\mathbf{C}_{\text{dm}}\mathbf{T}$ is a 2×6 matrix, and \mathbf{D}_{dm} a 2×2 square matrix. Since $\mathbf{x} = \mathbf{T}\mathbf{z}$, then \mathbf{z} takes the form

$$\mathbf{z} = [z_1, \bar{z}_1, z_2, \bar{z}_2, z_3, \bar{z}_3]^T$$

with z_1, \bar{z}_1 being entries for the UHF mode, z_2, \bar{z}_2 for the HF mode, and z_3, \bar{z}_3 for the LF mode. Also, $\mathbf{T}^{-1}\mathbf{B}_{\text{dm}}$ may be expressed as

$$\mathbf{T}^{-1}\mathbf{B}_{\text{dm}} = [\mathbf{b}_1, \bar{\mathbf{b}}_1, \mathbf{b}_2, \bar{\mathbf{b}}_2, \mathbf{b}_3, \bar{\mathbf{b}}_3]^T$$

where $\mathbf{b}_1^T, \mathbf{b}_2^T, \mathbf{b}_3^T$, and their conjugates are 1×2 row vectors corresponding to the UHF, HF, and LF modes, respectively. In addition, $\mathbf{C}_{\text{dm}}\mathbf{T}$ takes the form

$$\mathbf{C}_{\text{dm}}\mathbf{T} = [\mathbf{c}_1, \bar{\mathbf{c}}_1, \mathbf{c}_2, \bar{\mathbf{c}}_2, \mathbf{c}_3, \bar{\mathbf{c}}_3]$$

with $\mathbf{c}_1, \mathbf{c}_2, \mathbf{c}_3$, and their conjugates being 2×1 columns vectors that correspond vectors to the UHF, HF, and LF modes, respectively.

Focusing on the UHF mode, the state equation may be rewritten as

$$p \begin{bmatrix} z_1 \\ \bar{z}_1 \end{bmatrix} = \begin{bmatrix} \lambda_1 & 0 \\ 0 & \bar{\lambda}_1 \end{bmatrix} \begin{bmatrix} z_1 \\ \bar{z}_1 \end{bmatrix} + \begin{bmatrix} \mathbf{b}_1^T \\ \bar{\mathbf{b}}_1^T \end{bmatrix} \mathbf{u} \quad (5.15)$$

By inspection, the complex modes of (5.15) may be handled with respect to their real and imaginary parts. If $z_n = z_{nr} + jz_{ni}$, $\lambda_n = a_{nr} + ja_{ni}$, and $\mathbf{b}_n = \mathbf{b}_{nr} + j\mathbf{b}_{ni}$, where $n = 1, 2$, or 3, then it follows that

$$pz_{nr} = \text{Re}[(a_{nr} + ja_{ni})(z_{nr} + jz_{ni})] + \mathbf{b}_{nr}^T \mathbf{u} \quad (5.16)$$

$$pz_{nr} = a_{nr}z_{nr} - a_{ni}z_{ni} + \mathbf{b}_{nr}^T \mathbf{u} \quad (5.17)$$

$$pz_{ni} = \text{Im}[(a_{nr} + ja_{ni})(z_{nr} + jz_{ni})] + \mathbf{b}_{ni}^T \mathbf{u} \quad (5.18)$$

$$pz_{ni} = a_{nr}z_{nr} + a_{ni}z_{ni} + \mathbf{b}_{ni}^T \mathbf{u} \quad (5.19)$$

Thus, new state equations for the UHF, HF, and LF modes may be formulated as

$$p \begin{bmatrix} z_{nr} \\ z_{ni} \end{bmatrix} = \begin{bmatrix} a_{nr} & -a_{ni} \\ a_{ni} & a_{nr} \end{bmatrix} \begin{bmatrix} z_{nr} \\ z_{ni} \end{bmatrix} + \begin{bmatrix} \mathbf{b}_{nr}^T \\ \mathbf{b}_{ni}^T \end{bmatrix} \mathbf{u} \quad (5.20)$$

or symbolically as

$$p\mathbf{z}_n = \mathbf{A}_n\mathbf{z}_n + \mathbf{B}_n\mathbf{u} \quad (5.21)$$

where $n = 1, 2$, or 3 for the UHF, HF, and LF modes, respectively. From this, \mathbf{A}_{lfdm} and \mathbf{B}_{lfdm} may be established from \mathbf{A}_3 and \mathbf{B}_3 , respectively. Moreover, the output equation of (5.4) may be rewritten as

$$\mathbf{y} = \begin{bmatrix} \mathbf{c}_1 & \overline{\mathbf{c}}_1 \end{bmatrix} \begin{bmatrix} z_1 \\ \overline{z}_1 \end{bmatrix} + \begin{bmatrix} \mathbf{c}_2 & \overline{\mathbf{c}}_2 \end{bmatrix} \begin{bmatrix} z_2 \\ \overline{z}_2 \end{bmatrix} + \begin{bmatrix} \mathbf{c}_3 & \overline{\mathbf{c}}_3 \end{bmatrix} \begin{bmatrix} z_3 \\ \overline{z}_3 \end{bmatrix} + \mathbf{D}_{\text{dm}}\mathbf{u} \quad (5.22)$$

which may be simplified further as

$$\mathbf{y} = 2 \operatorname{Re}[\mathbf{c}_1 z_1] + 2 \operatorname{Re}[\mathbf{c}_2 z_2] + 2 \operatorname{Re}[\mathbf{c}_3 z_3] + \mathbf{D}_{\text{dm}}\mathbf{u} \quad (5.23)$$

Assuming $\mathbf{c}_n = \mathbf{c}_{nr} + j\mathbf{c}_{ni}$ for $n = 1, 2$, and 3 , then

$$\mathbf{y} = 2 \begin{bmatrix} \mathbf{c}_{1r} & -\mathbf{c}_{1i} \end{bmatrix} \begin{bmatrix} z_{1r} \\ z_{1i} \end{bmatrix} + 2 \begin{bmatrix} \mathbf{c}_{2r} & -\mathbf{c}_{2i} \end{bmatrix} \begin{bmatrix} z_{2r} \\ z_{2i} \end{bmatrix} + 2 \begin{bmatrix} \mathbf{c}_{3r} & -\mathbf{c}_{3i} \end{bmatrix} \begin{bmatrix} z_{3r} \\ z_{3i} \end{bmatrix} + \mathbf{D}_{\text{dm}}\mathbf{u} \quad (5.24)$$

or symbolically as

$$\mathbf{y} = \mathbf{C}_1\mathbf{z}_1 + \mathbf{C}_2\mathbf{z}_2 + \mathbf{C}_3\mathbf{z}_3 + \mathbf{D}\mathbf{u} \quad (5.25)$$

which makes the output equation of the reduced-order model,

$$\mathbf{y} = \mathbf{C}_3\mathbf{z}_3 + \left[-\mathbf{C}_1\mathbf{A}_1^{-1}\mathbf{B}_1 - \mathbf{C}_2\mathbf{A}_2^{-1}\mathbf{B}_2 + \mathbf{D} \right] \mathbf{u} \quad (5.26)$$

which is equivalent to

$$\mathbf{y} = \mathbf{C}_{\text{lfdm}}\mathbf{z}_3 + \mathbf{D}_{\text{lfdm}}\mathbf{u} \quad (5.27)$$

Simulation of the low-frequency drive system model is discussed next.

5.2 Simulation of Low-frequency Model

A state-space-based simulation of the low-frequency model was implemented using Simulink. The top-level block diagram is shown in Figure 5.3. As shown, the main subsystems include the modulator, the inverter, and the PMAC machine. The modulator block implements the equations that describe the sine-triangle (with third harmonic injection) modulation strategy described in Chapter 4; specifically, these are the expressions given by (4.1), (4.2), and (4.3).

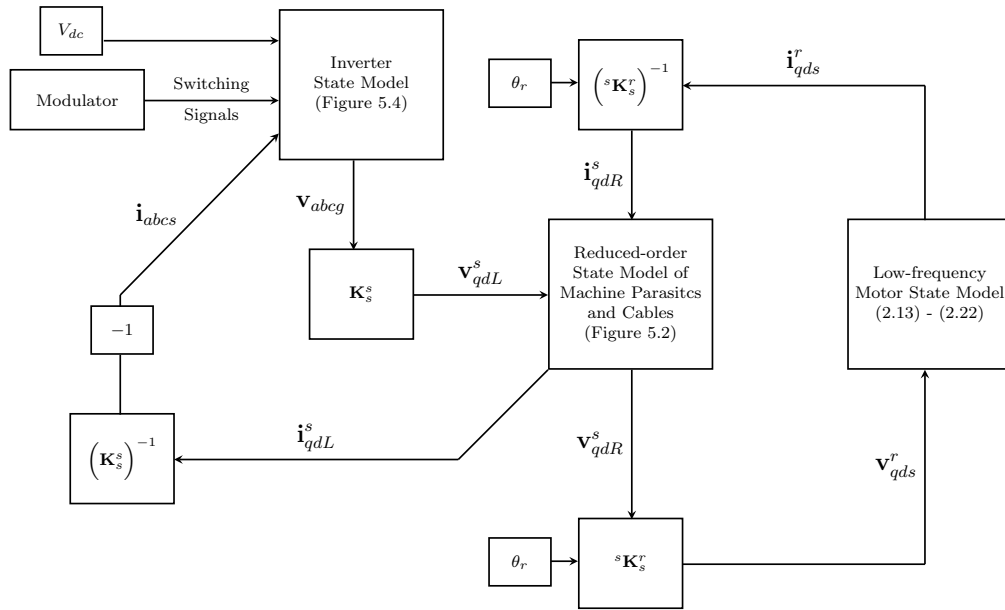


Figure 5.3. Top-level block diagram of low-frequency model.

A block-diagram of the inverter subsystem is detailed in Figure 5.4. Therein, lookup tables are used to represent the voltage drops across the MOSFETs and diodes when the switching states and currents in the devices are known. The calculated voltages are used to establish the vector of phase-to-ground voltages \mathbf{v}_{abcg} from which the voltages \mathbf{v}_{qd0L}^s may be obtained by applying the stationary reference frame (Clarke's) transformation. These voltages are inputs to the reduced-order state model of the machine and cable as shown in Figure 5.3.

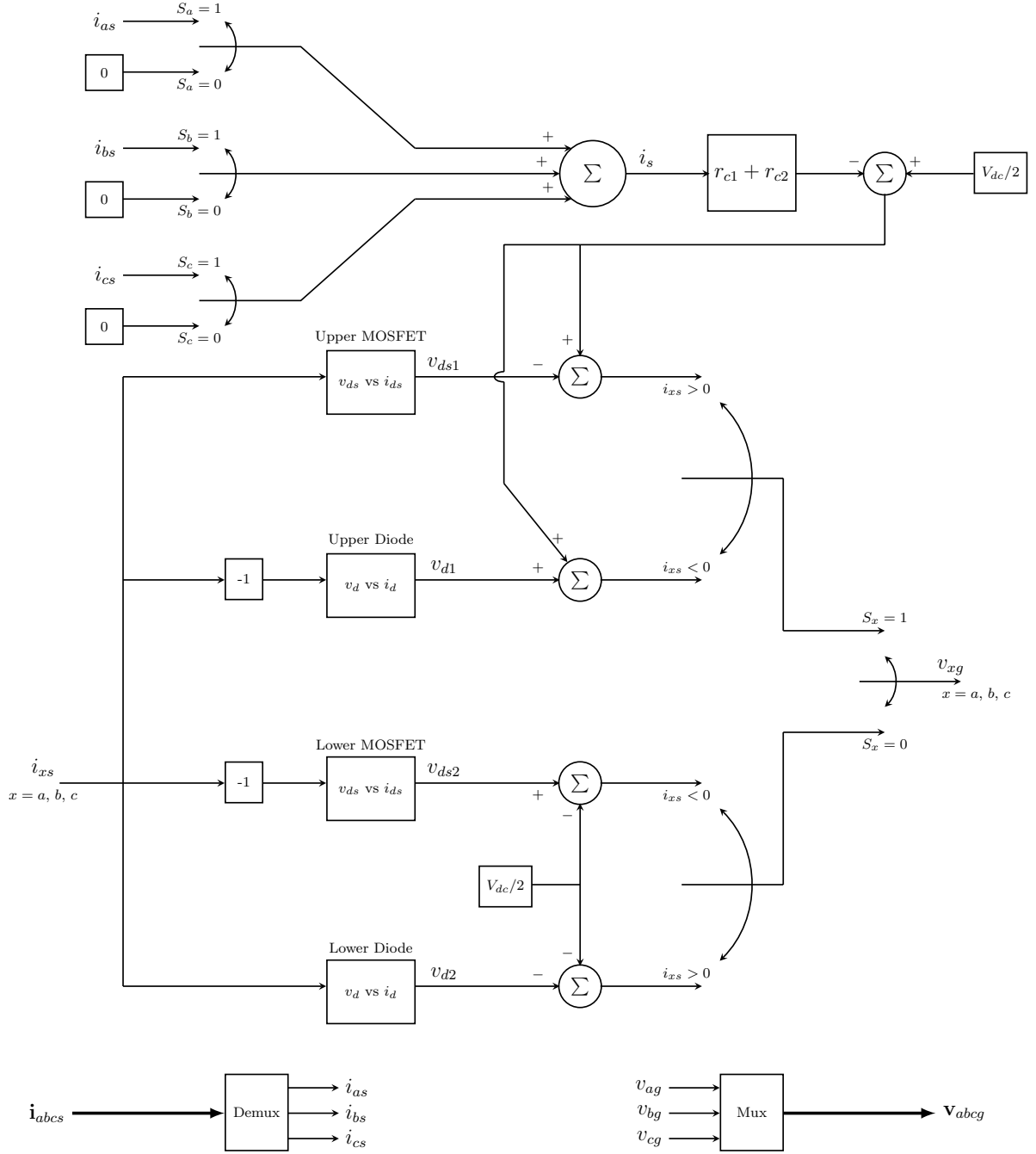


Figure 5.4. Inverter simulation block diagram (low frequency).

The given model was implemented using Simulink. The absolute and relative tolerances were set to $1e^{-3}$, and the selected solver was the variable-step ode15s (stiff/NDF), which is suitable for numerically stiff systems. Using the same machine operating point defined

in Chapter 4, the simulation required 12.8 s to run for a simulation time of 300 ms on a 2.8-GHz personal computer with 16 GB of RAM. The simulation statistics are summarized in Table 5.1.

Table 5.1. Simulation statistics using low-frequency model.

Simulation time	300 ms
Runtime	12.7838 s
Simulation speed	23.4 ms/s
Integration algorithm	Numerical Differentiation Formula
Step size	Variable
Total time-steps	304 824

The simulated phase currents are illustrated in Figures 5.5 and 5.6. It is apparent that, when zoomed in, the current waveforms do not capture the high-frequency transients observed in the simulations of the wideband model. However, these transients will be captured in the simulation of the high-frequency model as will be described later in this chapter.

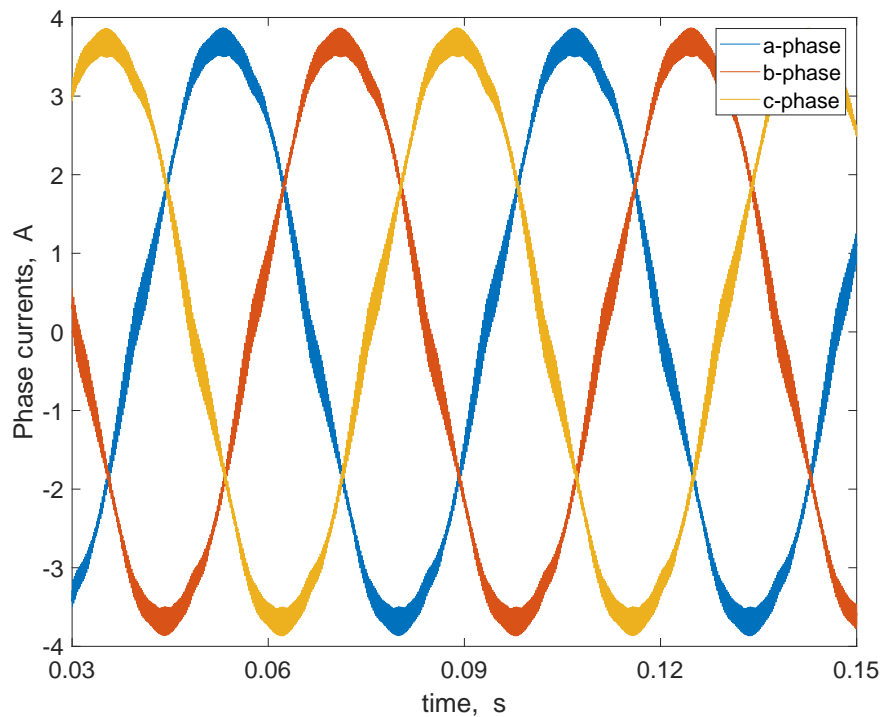


Figure 5.5. Simulated phase currents using low-frequency model.

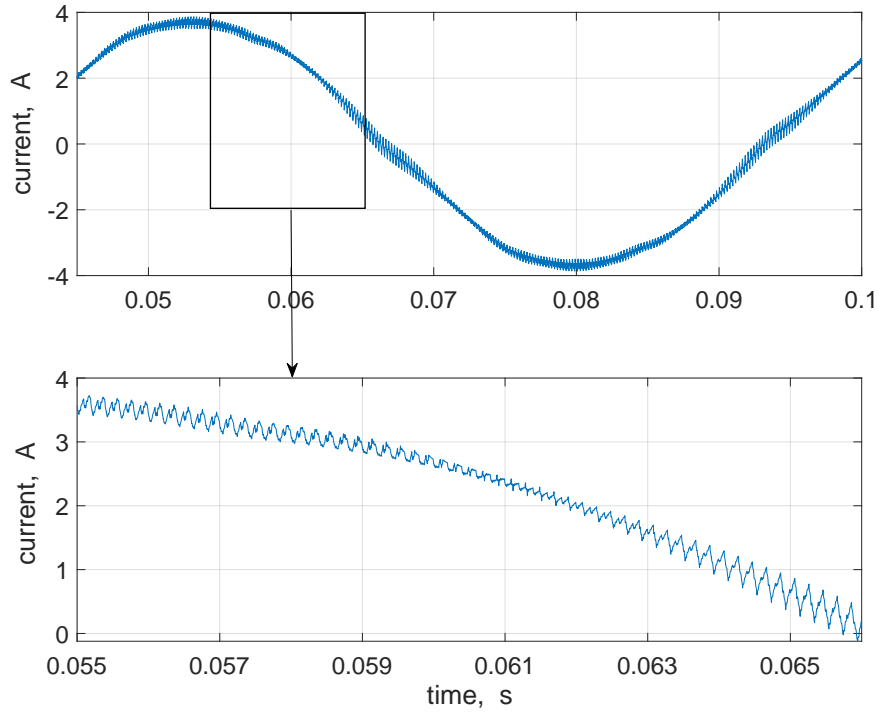


Figure 5.6. Expanded view of simulated a -phase current using low-frequency model.

It may also be observed that the current waveforms when zoomed in do not resemble the traditional sawtooth-like waveforms that would normally be predicted using a standard low-frequency model in which the transistors are represented as ideal switches and the low-to mid-frequency dynamics of the cable are neglected. The apparent contrast is due to the specific features considered in the low-frequency model. First, the conduction losses of the inverter are modeled based on measured diode and MOSFET I - V characteristics. Moreover, the electric machine model is defined by an improved low-frequency model of the PMAC machine and a reduced-order (mid-frequency) model of the machine and interconnecting cable. In particular, the low-frequency model of the PMAC machine takes into account the effects of induced eddy currents in the rotor and the reduced-order model of the machine and interconnecting cable takes into account the associated mid-frequency dynamics.

The stationary reference frame transformation of the resulting phase currents at instants of inverter switching, along with the corresponding switching states are to be used as initial

conditions in the simulation of the high-frequency transients. A description of the high-frequency model is presented next.

5.3 The High-frequency Model

The high-frequency model is set up to capture the short-lived switching transients of the electric drive system. The source, MOSFET, and high-frequency machine models are vital for establishing a high-frequency model of the complete drive system. A high-frequency circuit model of the inverter and dc source is shown in Figure 5.7. An inductance L_{stray} has been included to model the internal inductance of the Cree module. This circuit is coupled with the high-frequency model of the electric machine and interconnecting cable using dependent current sources as shown in Figure 5.7.

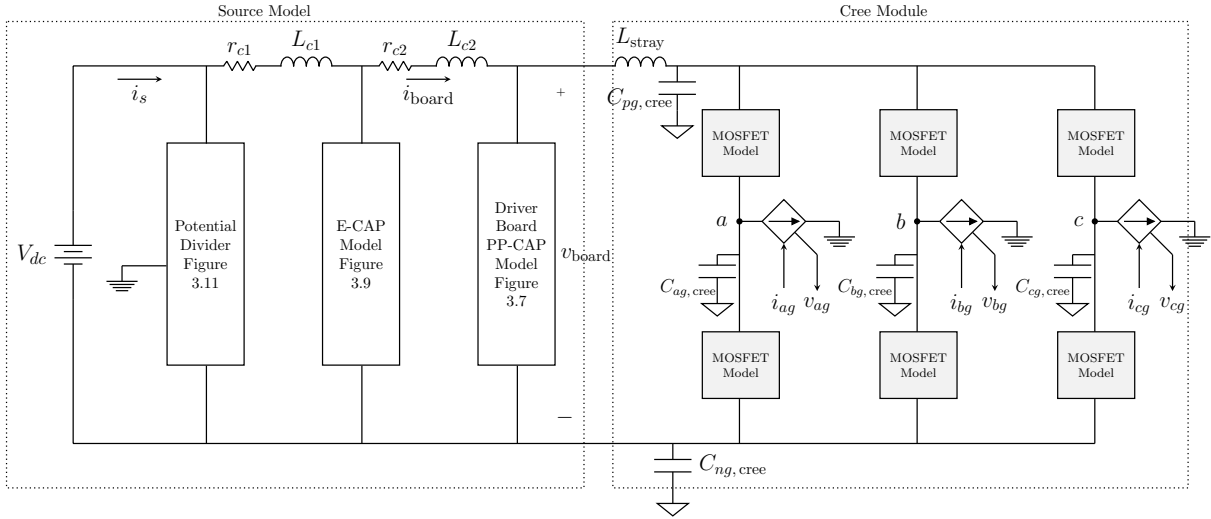


Figure 5.7. High-frequency circuit model of the inverter and source.

The source and MOSFET models in Figure 5.7 were presented in Chapter 3. The high-frequency machine model may be derived from the wideband electric machine model presented in Chapter 2 and is shown in Figure 5.8. Therein, $i_{qL}^s(t_{\text{sw}})$ and $i_{dL}^s(t_{\text{sw}})$ are the q - and d -axis components of the machine currents expressed in the stationary reference frame. These values, determined from the simulation of the low-frequency model, are set as initial

conditions of the high-frequency DM state models. The voltages v_{ag} , v_{bg} , and v_{cg} are the phase-to-ground voltages that are outputs of the inverter circuit model. They are transformed into the stationary reference frame and input to the high-frequency DM and CM state models as shown in the figure. The currents i_{qL}^s , i_{dL}^s , and i_{0L}^s are the outputs supplied to the inverter after they are transformed back to physical variables.

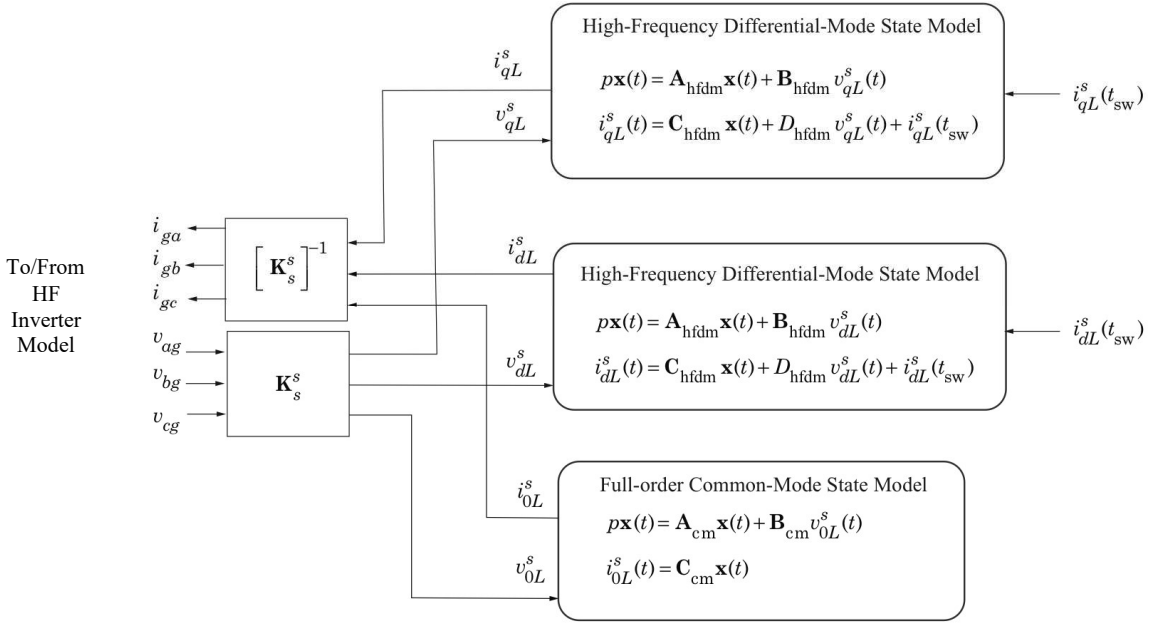


Figure 5.8. Block diagram of high-frequency model of electric machine and interconnecting cable.

Specifically, the high-frequency DM state models are realized from the wideband DM state models for the machine cable and parasitic components of the electric machine. In order to establish the high-frequency model, it is useful to recall the wideband model given by (5.1) – (5.4). The first mode has a natural frequency that exceeds 10^{11} rad/s and can be attributed to the parasitic branches in the DM equivalent circuit shown in Figure 2.13. This mode is considered superfluous and will be eliminated through singular perturbation techniques. The third mode has a natural frequency of 2.7×10^5 rad/s which is considered a long-term mode that is part of the low-frequency model described previously. As such, its

value is assumed constant in the high-frequency model. Thus, the state equations of interest are given by (5.1) and (5.2) and the output equation is

$$\mathbf{y} = \mathbf{C}_1\mathbf{x}_1 + \mathbf{C}_2\mathbf{x}_2 + \mathbf{D}\mathbf{u} + \mathbf{y}_0 \quad (5.28)$$

where \mathbf{y}_0 represents the initial conditions. Since $p\mathbf{x}_1 = 0$, then

$$\mathbf{y} = \left[-\mathbf{C}_1\mathbf{A}_1^{-1}\mathbf{B}_1 + \mathbf{D} \right] \mathbf{u} + \mathbf{C}_2\mathbf{x}_2 + \mathbf{y}_0 \quad (5.29)$$

which may be symbolically expressed as

$$\mathbf{y} = \mathbf{C}_2\mathbf{x}_2 + \mathbf{D}_{2n}\mathbf{u} + \mathbf{y}_0 \quad (5.30)$$

It should be noted that for the output equation, the variable of interest is the current, i_{qL}^s for the q -axis high-frequency DM state model and current, i_{dL}^s for the d -axis.

On the other hand, the high-frequency CM state model equations are given by (2.78) and (2.79). As only HF modes are associated with the CM circuit, no reduction techniques are necessary. Instead, it should be implemented without modification. The high-frequency model is implemented using the sparse tableau algorithm as described next.

5.4 Simulation of High-frequency Model

An STA program was developed to handle the simulation of the high-frequency model. The preference for the STA approach is instructed partly by the sparsity of the tableau matrix as well as the ease of performing structural changes to the model and the ability to combine circuit and state-space models. The simulation of the high-frequency model was performed for the instance of turn-on of the a -phase. In this study, the dc source voltage was set at 200 V and the initial phase currents set to 10, -10 , and 0 A for phases a , b , and c , respectively. These conditions were chosen to represent a prototypical switching event.

Code snippets of the high-frequency simulation are given in Figures 5.9 through 5.12. The code snippet that defines and initializes the parameters and variables used in the simulation

is shown in Figure 5.9. These parameters and variables are used in the instantiation of the high-frequency model shown in Figure 5.10. Herein, the high-frequency models of the inverter and electric machine are established along with the equations that define the connections between components. Also, a code snippet for implementing a phase leg of the inverter circuit, is given in Figure 5.11. Attention is given to defining the nodes of the inverter circuit and every element of the MOSFET model of the inverter circuit in the STA program. In addition, linear and nonlinear elements are defined and used to set up the high-frequency inverter model. The code snippet for attaining a converged solution is shown in Figure 5.12. As shown, a fixed time step of 0.1 ns is selected to achieve a converged solution for the turn-on event. The simulation routine was implemented for a simulation time of 9 μ s.

```

1 clearvars
2 globals
3 clf
4
5 % simulate inverter switching transients
6 iabc_init = [10 -10 0]; % initial currents
7
8 % iqd is 1x2 vector of initial qd currents
9 iqd(1) = (2/3)*(iabc_init(1) - 0.5*iabc_init(2) - 0.5*iabc_init(3));
10 iqd(2) = sqrt(3)/3*(-iabc_init(2)+iabc_init(3));
11
12 Sabc_init = [0 0 0]; % all lower devices initially on
13 Sabc_Δ = [1 0 0]; % turn off lower device, wait for t_dwell, then turn on upper device
14 t_dwell = 100e-9;
15
16 idc_init = Sabc_init(1) * iabc_init(1) + Sabc_init(2)*iabc_init(2) + ...
    Sabc_init(3)*iabc_init(3);
17
18 Vdc = 200.0;
19
20 vabc_init = [(Sabc_init(1)*Vdc - Vdc/2) (Sabc_init(2)*Vdc-Vdc/2) ...
    (Sabc_init(3)*Vdc-Vdc/2)];

```

Figure 5.9. Code snippet for initializing model parameters and variables.

```

1  mysys = MSystem('mysys');
2
3
4  %instantiate inverter model
5  [inverter, Slabc, S2abc, jabc_in, vabc_out, idc] = ...
6      Inverter3('Inverter', mysys, Sabc_init, Sabc_Δ, iabc_init, param, Vdc);
7  % jabc is 1x3 vector of Input objects (phase currents)
8  % vabc is 1x3 vector of Output objects (phase voltages)
9  % i_gnd is an output object
10
11 %instantiate high-frequency cable/motor model
12 [hfckt, vabc_in, iabc_out] = Hfckt2('HF_ckt', mysys, -iqd, vabc_init);
13 % vabc_in is 1x3 vector of Input objects (phase voltages)
14 % iabc_out is 1x3 vector of Output objects (phase currents)
15
16 % define connections between inputs and outputs
17 mysys.connect2(iabc_out, jabc_in, -1);
18 mysys.connect2(vabc_out, vabc_in, 1);
19
20 mysys.end;

```

Figure 5.10. Code snippet for instantiating the high-frequency model.

The results are illustrated in Figures 5.13 through 5.16. The associated voltages, currents and power losses of the a -phase MOSFETs are shown in Figures 5.13 and 5.14. As shown a triangular pulse is observed in the turn-on power loss of the upper MOSFET device. A peak loss of 4692 W is noted. For the lower MOSFET device, which was turned off in this study, a peak power loss of 3.865 W is seen.

In addition, the Miller plateau that is associated with the switching of the MOSFET device is observed in the gate-to-source voltage, v_{gs} plotted in Figure 5.14. From the same figure, the turn-on time of the upper MOSFET device may be approximated as 20 ns and the turn-on energy loss loss as 37.5 μ J. The effects of the turn-on event on the currents in the electric machine and cable are shown in Figures 5.15 and 5.16. Specifically, the currents through phases a , b , and c are shown in Figure 5.15 and the stationary reference frame currents in Figure 5.15. As shown, a high-frequency oscillations are observed in the currents. Peak currents of 15.86, -7.116 , and 2.885 A are observed for the a - b - and c -phase currents. Also, the same phenomenon is noticed in the stationary reference frame currents. It is important to note that due to the switching event, a peak of 0.1156 A and minimum of -0.1565 A are observed in the zero-sequence or common-mode current result.

```

1 function [obj, u1, u2] = PhaseLeg(name, ckt, p, o, n, param, Vdc, iload, S_Δ, S_init)
2     %PhaseLeg Construct an instance of this class
3     % u1, u2 are input objects created by instantiator
4     % sys is the MSystem object to which the PhaseLeg object
5     % is a member
6     % p, o, n, are the positive, output, and negative nodes of
7     % PhaseLeg
8     % S_Δ = 1 --> turn-on, S_Δ = 0 --> turn-off
9
10    obj.name = name;
11    % instantiate mosfets and initialuze to pre-switch state
12    if(S_Δ == 1) % a turn-on transient
13        [upper, u1] = Mosfet(strcat(name,': Upper Mosfet'), p, o, ckt, param, ...
14            Vdc, iload, 0, 'upper');
15        [lower, u2] = Mosfet(strcat(name,': Lower Mosfet'), o, n, ckt, param, ...
16            Vdc, iload, 1, 'lower');
17    elseif(S_Δ == -1) % a turn-off transient
18        [upper, u1] = Mosfet(strcat(name,': Upper Mosfet'), p, o, ckt, param, ...
19            Vdc, iload, 1, 'upper');
20        [lower, u2] = Mosfet(strcat(name,': Lower Mosfet'), o, n, ckt, param, ...
21            Vdc, iload, 0, 'lower');
22    else % a non event
23        if(S_init == 1) % phase leg on
24            [upper, u1] = Mosfet(strcat(name,': Upper Mosfet'), p, o, ckt, param, ...
25                Vdc, iload, 1, 'upper');
26            [lower, u2] = Mosfet(strcat(name,': Lower Mosfet'), o, n, ckt, param, ...
27                Vdc, iload, 0, 'lower');
28        else % phase leg off
29            [upper, u1] = Mosfet(strcat(name,': Upper Mosfet'), p, o, ckt, param, ...
30                Vdc, iload, 0, 'upper');
31            [lower, u2] = Mosfet(strcat(name,': Lower Mosfet'), o, n, ckt, param, ...
32                Vdc, iload, 1, 'lower');
33        end
34    end
35    obj.upper = upper;
36    obj.lower = lower;
37 end

```

Figure 5.11. Function for defining and instantiating the phase leg of the inverter circuit.

```

1 h = 1e-10; % time step *****
2 t1 = 1000e-9;
3
4 tic
5 mysys.solve(h, t1); % let initial conditions settle
6
7 for i = 1:3
8     if(Sabc_Δ(i) == 1) % a turn-on transient
9         S2abc(i).set(param.vgs_off);
10    elseif(Sabc_Δ(i) == -1) % a turn-off transient
11        S1abc(i).set(param.vgs_off);
12    else % a non event
13        % do nothing
14    end
15 end
16
17 mysys.contin(h, t1 + t_dwell); % simulate for another t_dwell
18
19 for i=1:3
20     if(Sabc_Δ(i) == 1) % a turn-on transient
21         S1abc(i).set(param.vgs_on);
22     elseif(Sabc_Δ(i) == -1) % a turn-off transient
23         S2abc(i).set(param.vgs_on);
24     else % a non event
25         % do nothing
26     end
27 end
28
29 t2 = 9000e-9;
30 mysys.contin(h, t2);
31
32 toc

```

Figure 5.12. Code snippet for establishing converged solution.

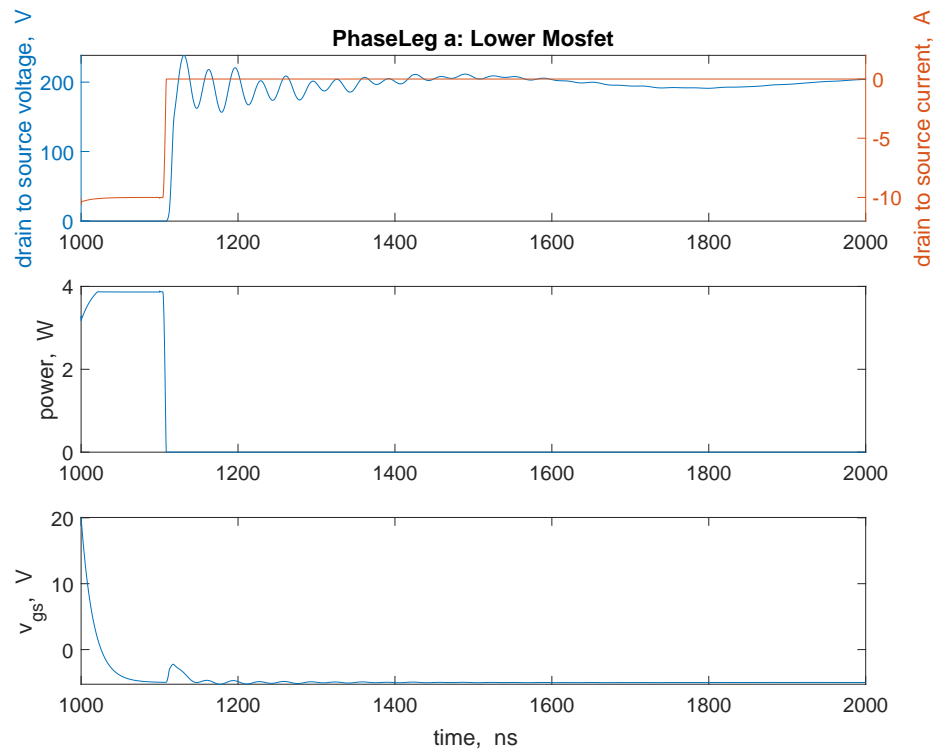


Figure 5.13. Simulated voltage, current, and power loss in lower MOSFET.

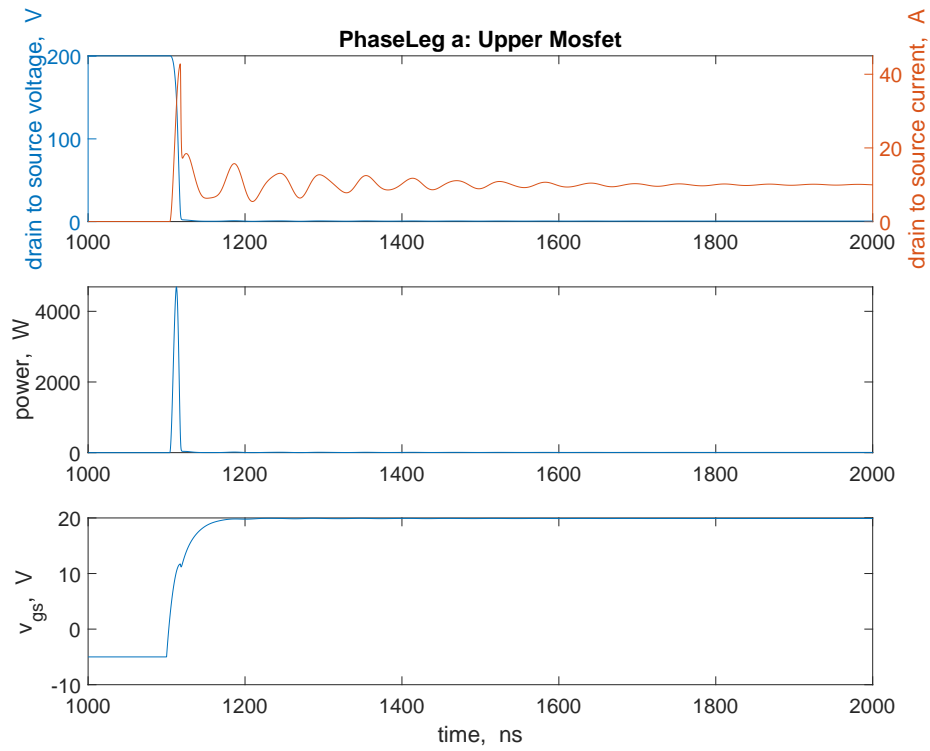


Figure 5.14. Simulated voltage, current, and power loss in upper MOSFET.

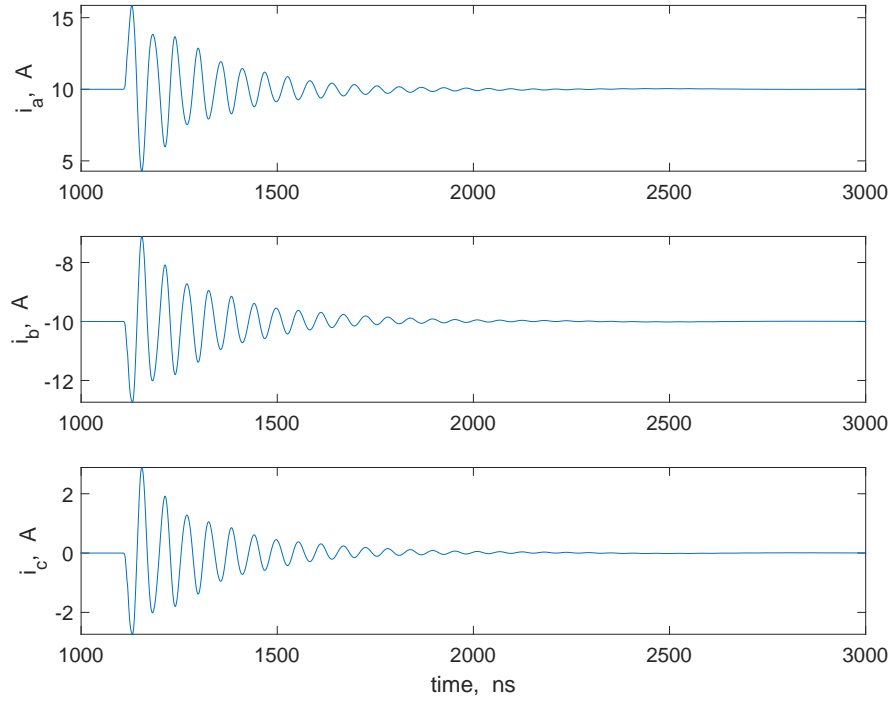


Figure 5.15. Simulated phase currents.

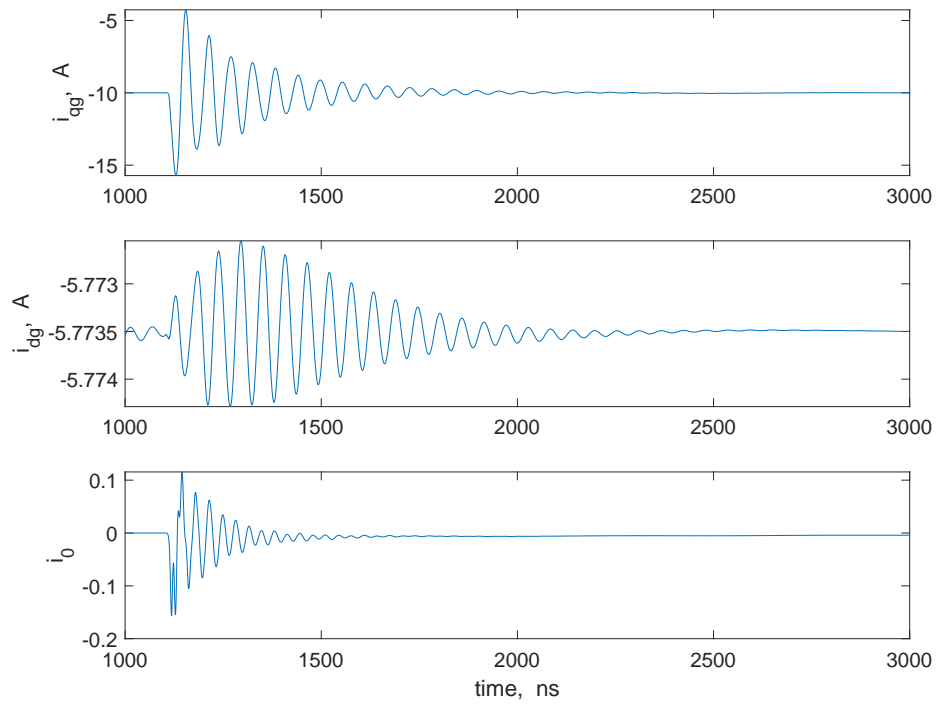


Figure 5.16. Simulated phase currents in the stationary reference frame.

5.5 High-frequency Transients with Machine Ground Wire Disconnected

In the study described in the previous section, the machine ground wire was assumed to be connected to the inverter baseplate as shown in Figures 1.2 and 4.1. It is worthwhile to observe the switching transients for the case where the ground wire is disconnected. For this purpose, the STA program was set up such that the common-mode circuit had no influence on the high-frequency dynamics.

The results shown in Figures 5.17 through 5.19 illustrate the transient behavior of the drive system following a turn-on event of a phase leg of the inverter. The operating conditions that are used to establish these results are the same as those described in the previous section. As the machine ground wire is assumed disconnected from the chassis ground, the zero-sequence current shown in Figure 5.19 remains constant at 0 A during the switching event. It is important to note that the lower and upper MOSFET switching transients are very similar to results obtained when the ground wire was assumed connected to the inverter baseplate. Thus, the results from this study indicate that the switching losses are not significantly affected by the common-mode circuit of the electric machine. In other words, the switching losses are essentially unchanged whether or not the machine ground wire is connected to the inverter baseplate (ground).

5.6 Summary

In this chapter, a heterogeneous approach for obtaining the short- and long-term dynamics of WBG-based electric drive systems has been set forth. Herein, separate high- and low-frequency models of the electric drive system are developed for establishing the short- and long-term dynamics, respectively. For the long-term dynamics, the low-frequency model was established using singular perturbation techniques on the wideband models derived in Chapter 2. Similar techniques were used to establish a high-frequency model for the short-term dynamics. The low-frequency model was implemented using a state-space-based simulation program. The high-frequency model was implemented using an STA-based simulation program. Comparisons of simulation results and analogous experimental measurements are provided in the next chapter.

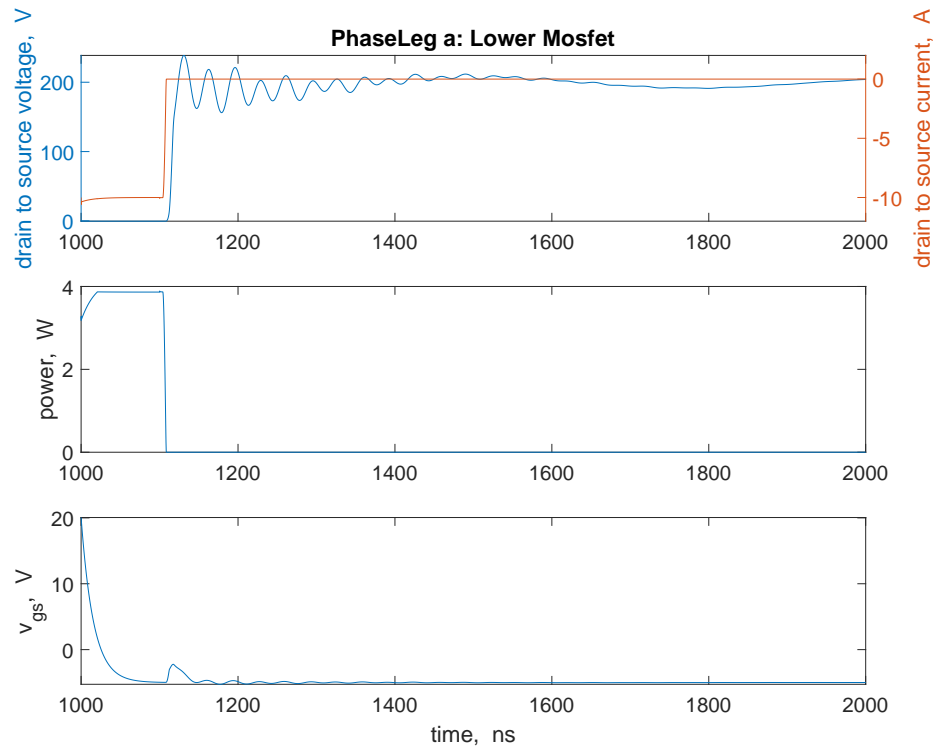


Figure 5.17. Simulated transients in lower MOSFET.

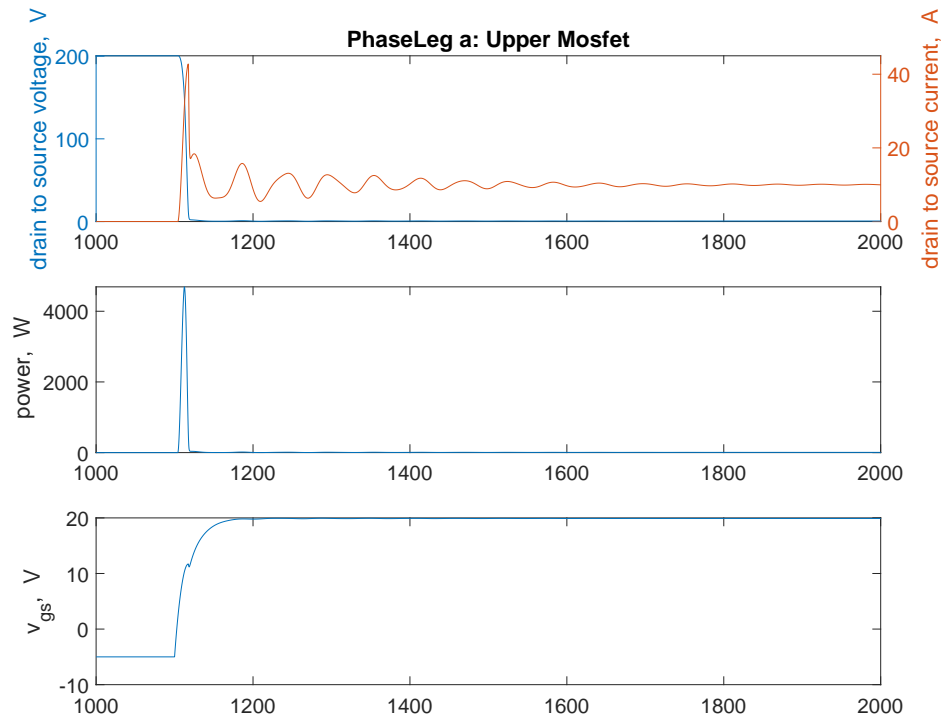


Figure 5.18. Simulated transients in upper MOSFET.

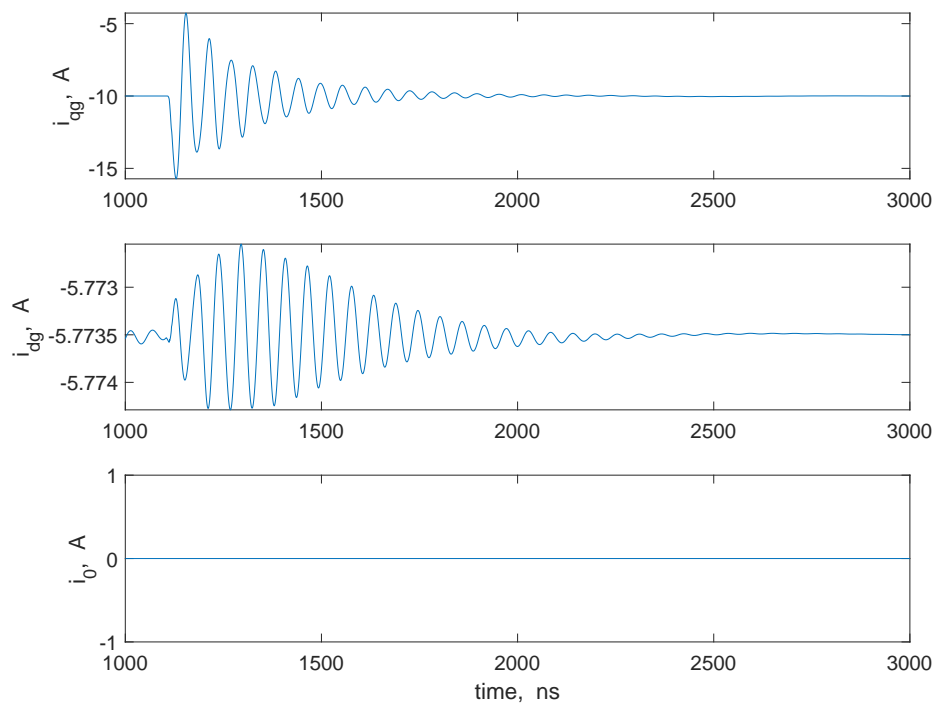


Figure 5.19. Simulated machine currents.

6. COMPARISON OF MEASURED AND SIMULATED HIGH-FREQUENCY TRANSIENTS

A two-prong simulation strategy was set forth in the preceding chapter as a method for establishing the short- and long-term dynamics of a WBG-based electric drive system. The approach involved the individual simulations of derived low- and high-frequency models of the drive system. A state-space-based approach was utilized for the long-term dynamics, and a sparse-tableau-based program was developed for establishing the short-term dynamics. In this chapter, a test simulation of the turn-on event of one phase leg of the Cree module is implemented using the sparse-tableau program. Also, a simulation of operating conditions described in Chapter 4 is implemented for a switching event. Comparisons between the simulated and measured high-frequency switching transients are provided.

6.1 Switching Transients of Inverter Test Circuit

For the purpose of comparisons, results from the inverter model simulation were established for the test setup shown in Figure 6.1. In this test, the motor and cable were disconnected from the inverter. Also, phase-leg a is turned on by switching the lower MOSFET off, then after a brief delay, turning the upper MOSFET on. The MOSFETs of the other phase legs are in the off state. In Figure 6.1, the grayed-out MOSFET blocks depict the inactive switches. Models for the resistive potential divider, electrolytic capacitor, and polypropylene capacitors, described in Chapter 3, were implemented in the simulation. It is important to note that some adjustments were made to the model parameters in order to get a good match between simulated and measured results described in the next section. In particular, changes were made to parameters C_{par2} and L_p of the polypropylene capacitor model described in Chapter 3. Herein, C_{par2} was adjusted to four times its initial value of 357.28 pF and L_p to four-fifths its original value of 15.946 nH.

Top-level MATLAB code snippets of the simulation are shown in Figures 6.2 through 6.4. In Figure 6.2, the script for initializing necessary variables is shown. These variables are used in the tableau matrix formulation, which is executed in the code snippet shown

in Figure 6.3. The solution to the simulation of the test circuit is established in the code snippet shown in Figure 6.4.

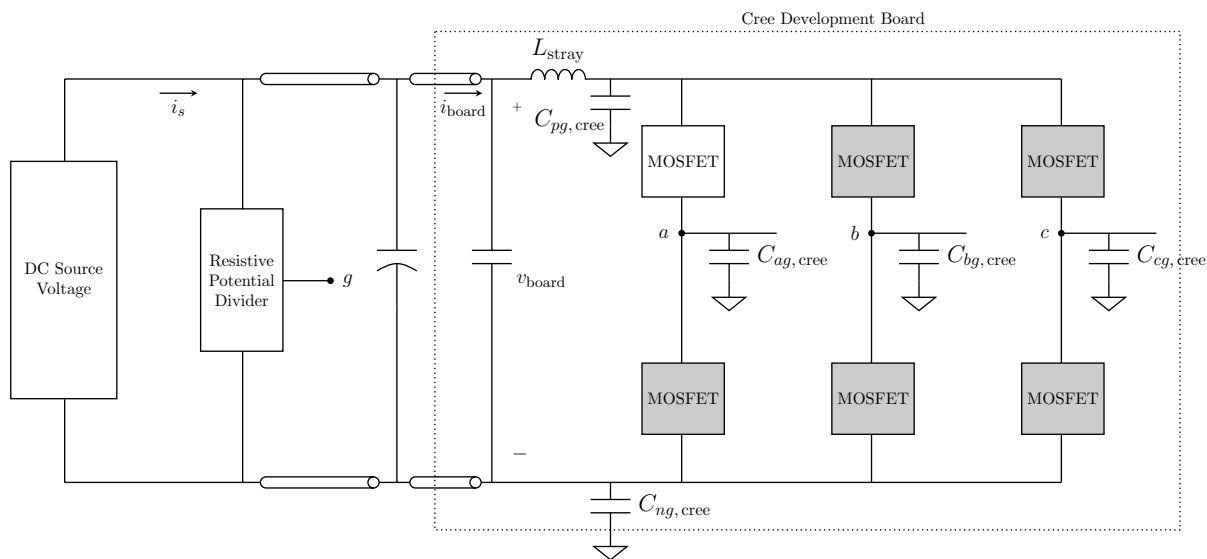


Figure 6.1. Circuit diagram for test setup.

With the dc source voltage set at 250 V, the simulation program was run for a simulation time of 5 μ s. The results of the simulation are shown in Figures 6.5 through 6.7. Here, results of the drain-to-source currents, voltages, and power losses are depicted for the upper and lower MOSFETs of the phase leg that was turned on. Also depicted are the board current i_{board} and voltage v_{board} as defined in Figure 6.1.

```

1 clearvars
2 globals
3 clf
4
5 % simulate inverter switching transients
6 iabc_init = [0 0 0]; % initial currents
7
8
9 % iqdc is 1x2 vector of initial qd currents
10 iqdc(1) = (2/3)*(iabc_init(1) - 0.5*iabc_init(2) - 0.5*iabc_init(3));
11 iqdc(2) = sqrt(3)/3*(-iabc_init(2)+iabc_init(3));
12
13 Sabc_init = [0 0 0]; % all lower devices initially on
14 Sabc_Δ = [1 0 0]; % turn off lower device, wait for t_dwell, then turn on upper device
15 t_dwell = 200e-9;
16
17 idc_init = Sabc_init(1) * iabc_init(1) + Sabc_init(2)*iabc_init(2) + ...
            Sabc_init(3)*iabc_init(3);
18
19 Vdc = 250.0;
20
21 %vng = (1/3)*(Sabc_init(1) + Sabc_init(2) + Sabc_init(3));
22
23 vabc_init = [(Sabc_init(1)*Vdc - Vdc/2) (Sabc_init(2)*Vdc-Vdc/2) ...
              (Sabc_init(3)*Vdc-Vdc/2)];

```

Figure 6.2. Definition and initialization of variables.

```

1 mysys = MSystem('mysys');
2
3 [r, ja] = Constant('Ja', mysys, iabc_init(1)); % phase current
4 [r, jb] = Constant('Jb', mysys, iabc_init(2)); % phase current
5 [r, jc] = Constant('Jc', mysys, iabc_init(3)); % phase current
6 iabc_out = [ja jb jc];
7
8 %instantiate inverter model
9 [inverter, Slabc, S2abc, jabc_in, vabc_out, idc] = ...
10   Inverter3('Inverter', mysys, Sabc_init, Sabc_Δ, iabc_init, param, Vdc);
11 % jabc is 1x3 vector of Input objects (phase currents)
12 % vabc is 1x3 vector of Output objects (phase voltages)
13
14 mysys.connect2(iabc_out, jabc_in, -1);
15
16 mysys.end;

```

Figure 6.3. Definition and instantiation of test circuit.

```

1 h = 1e-10; % time step
2 %h = 0.5e-10;
3 t1 = 1e-7;
4 tic
5 mysys.solve(h, t1); % let initial conditions settle
6
7 for i = 1:3
8     S2abc(i).set(param.vgs_off);
9     Slabc(i).set(param.vgs_off);
10 end
11
12
13 mysys.contin(h, t1 + t_dwell); % simulate for another t_dwell
14 Slabc(1).set(param.vgs_on);
15
16 t2 = 5000e-9;
17 %t2 = 1600e-9;
18 mysys.contin(h, t2);
19
20 toc

```

Figure 6.4. Code snippet for test-circuit analysis solution.

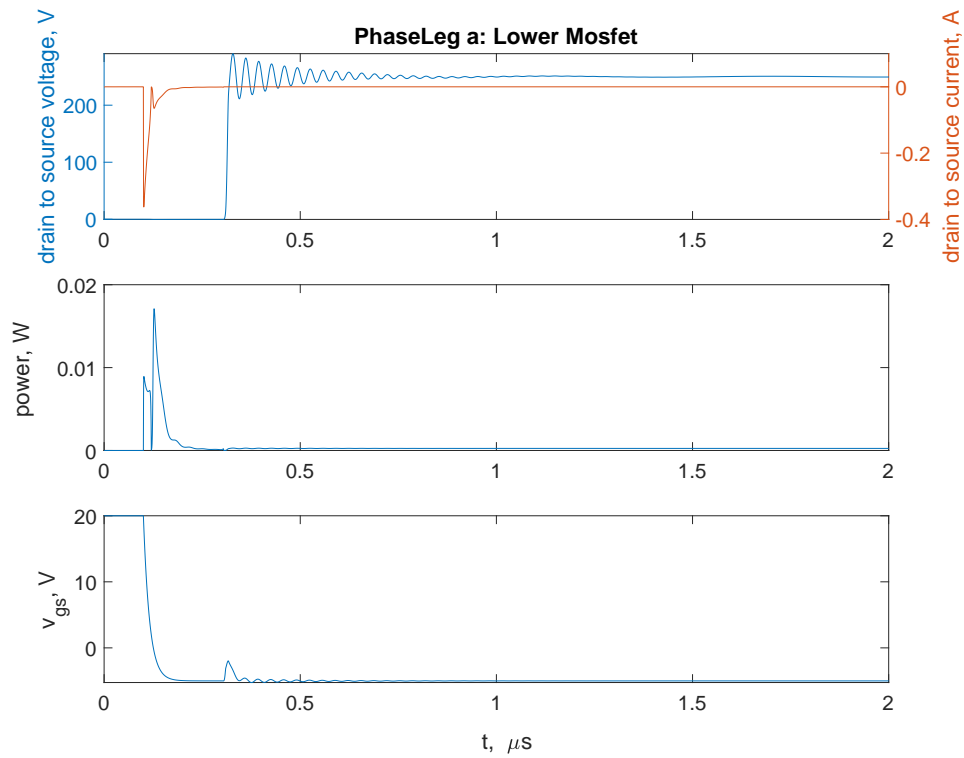


Figure 6.5. Simulated voltage, current, and power loss in lower MOSFET.

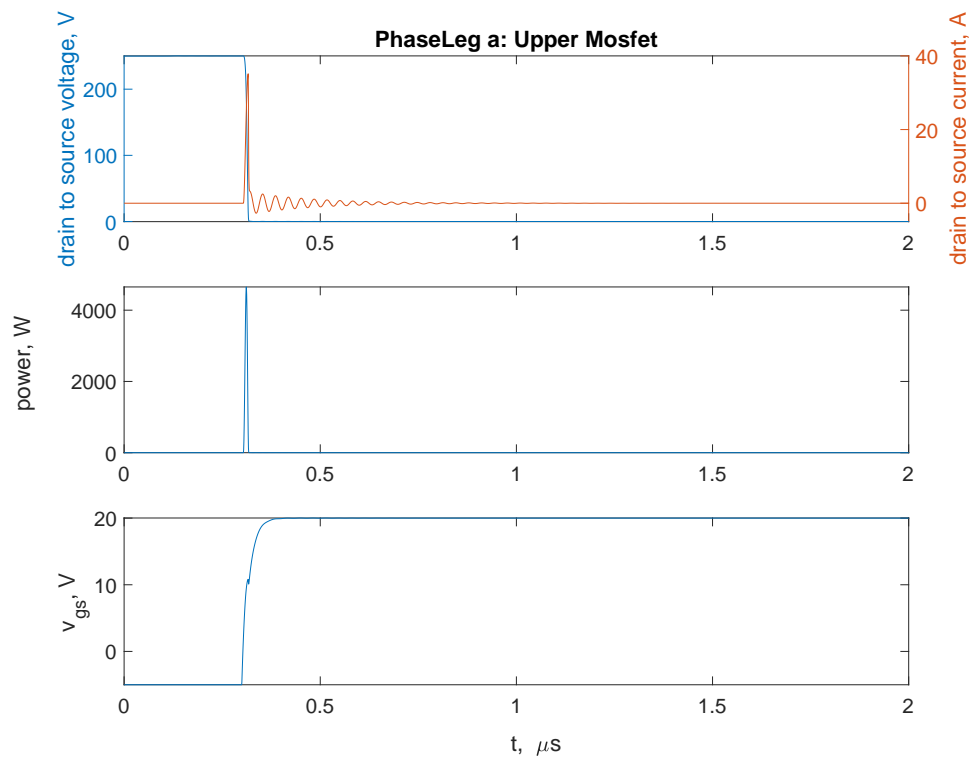


Figure 6.6. Simulated voltage, current, and power loss in upper MOSFET.

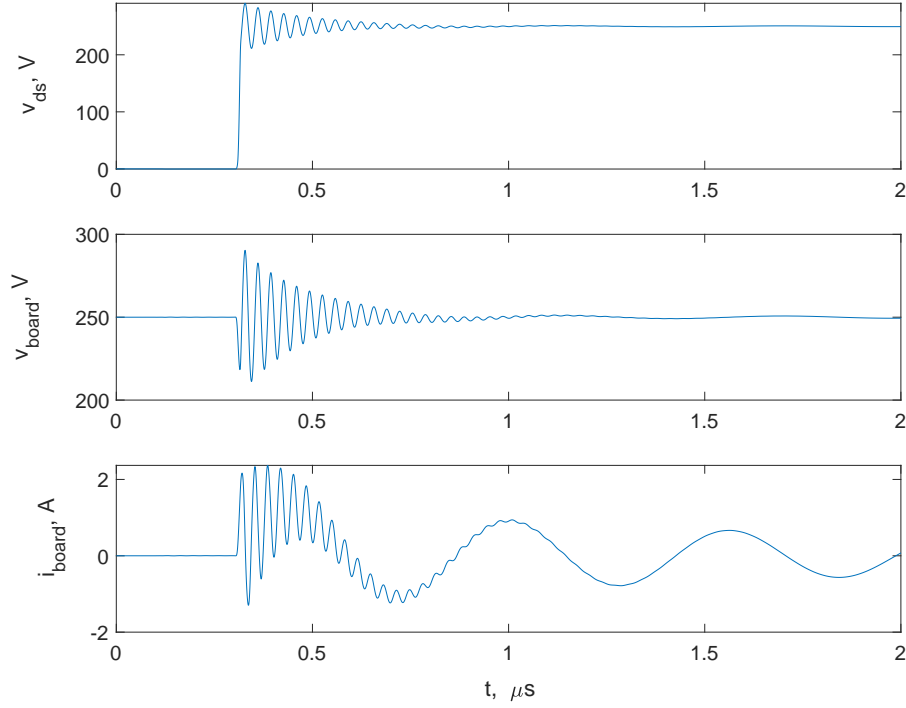


Figure 6.7. Simulated dc input voltage and currents to inverter circuit.

It is useful to consider the signals i_{board} , v_{board} , and the lower MOSFET drain-to-source voltage, v_{ds} . These signals are highlighted as they are the only signals that may be verified through experimental measurements. It was not readily possible to access contact points for the measurement of other signals. The peak values of the signals shown are 2.368 A, 290.4 V, and 290.3 V for i_{board} , v_{board} , and v_{ds} , respectively. For the signals a pair of frequencies are observed. A medium frequency of 1.8 MHz and a high frequency of 30.5 MHz. The key attributes from the simulated results are summarized in Table 6.1.

Table 6.1. Simulated results of phase leg turn-on event.

Study Signal	Simulated Peak Frequencies
i_{board}	2.368 A (1.8, 30.5) MHz
v_{board}	290.4 V (1.8, 30.5) MHz
v_{ds} (Lower MOSFET)	290.3 V (1.8, 30.5) MHz

Comparison with Measured Results

The measured switching transients were established using a Yokogawa 720210 100 MS/s module to capture the voltages and currents on a Yokogawa DL850 oscilloscope. A Yokogawa 700929 10:1 probe was used for the voltage measurements and a 701933 current probe for current measurements. The measured turn-on transients are shown in Figure 6.8. The initial portions of the transients are expanded in Figure 6.9. Therein, the lower switch drain-to-source voltage, the input dc voltage, and the board current i_{board} are displayed. A constraint set by the oscilloscope for analog voltage measurements is a 20-MHz bandwidth limit. As such, voltage measurements shown in Figures 6.8 and 6.9 have frequencies above 20 MHz attenuated. In addition, the bandwidth limit on the current probe is 50 MHz.

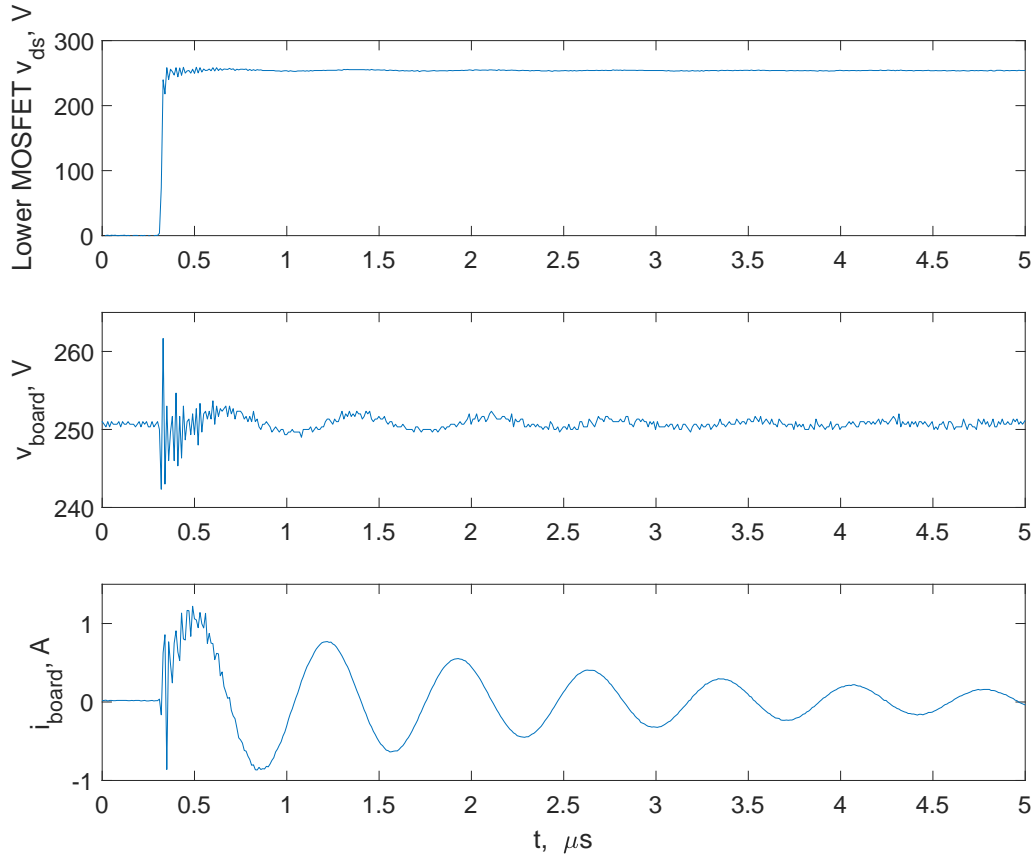


Figure 6.8. Measured results for turn-on event of a phase leg.

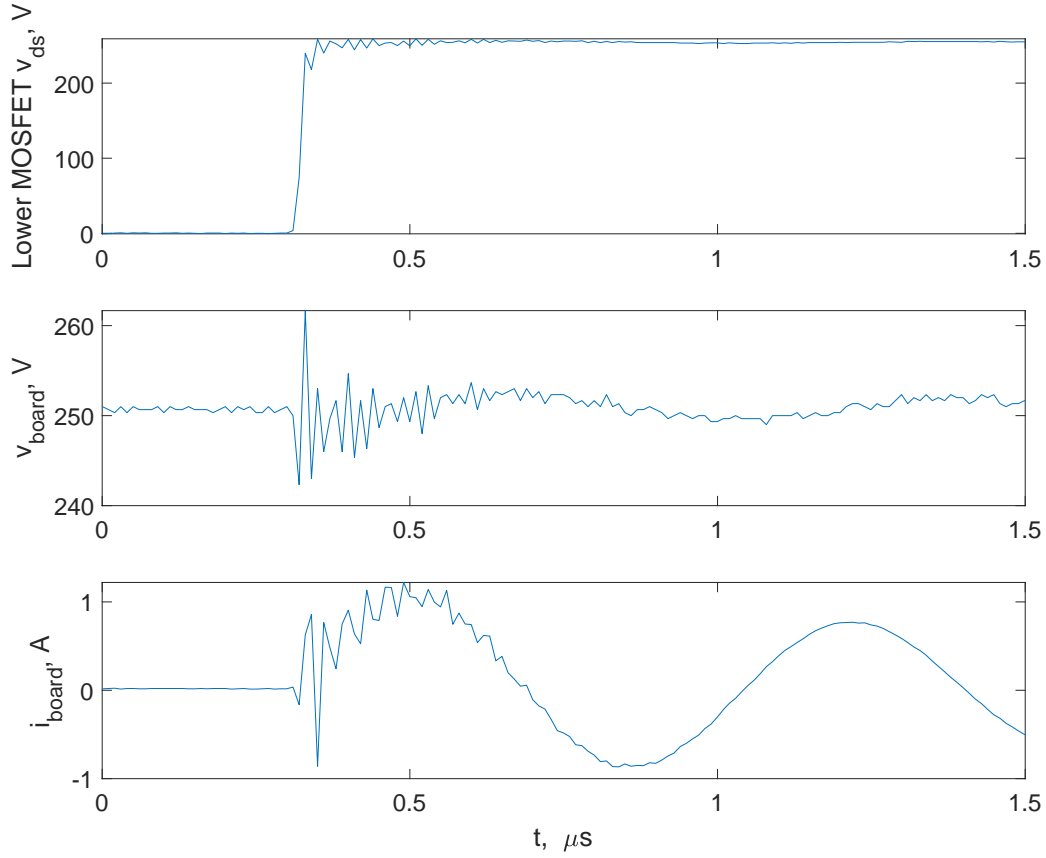


Figure 6.9. Zoomed-in measurements for turn-on event of a phase leg.

To provide a fair comparison, the simulated voltages and currents were filtered using a first-order low-pass filter with 20 and 50 MHz cutoff frequencies, respectively, and then sampled 10 ns (100 MS/s). The post-processed simulated voltages and current are depicted in Figure 6.10. Examination of these results reveals that the peak values of the predicted signals are fairly similar to those seen in the measured signals. For instance, for the simulated lower MOSFET voltage, the peak values of the raw and post-processed signals are given as 290.3 V and 263.9 V, respectively. The post-processed result reasonably matches that of the measured signal, 259 V. A summary of the key attributes, including frequencies of oscillations associated with the measured and simulated signals, are given in Table 6.2. A direct comparison of Figures 6.9 and 6.10 shows reasonable agreement.

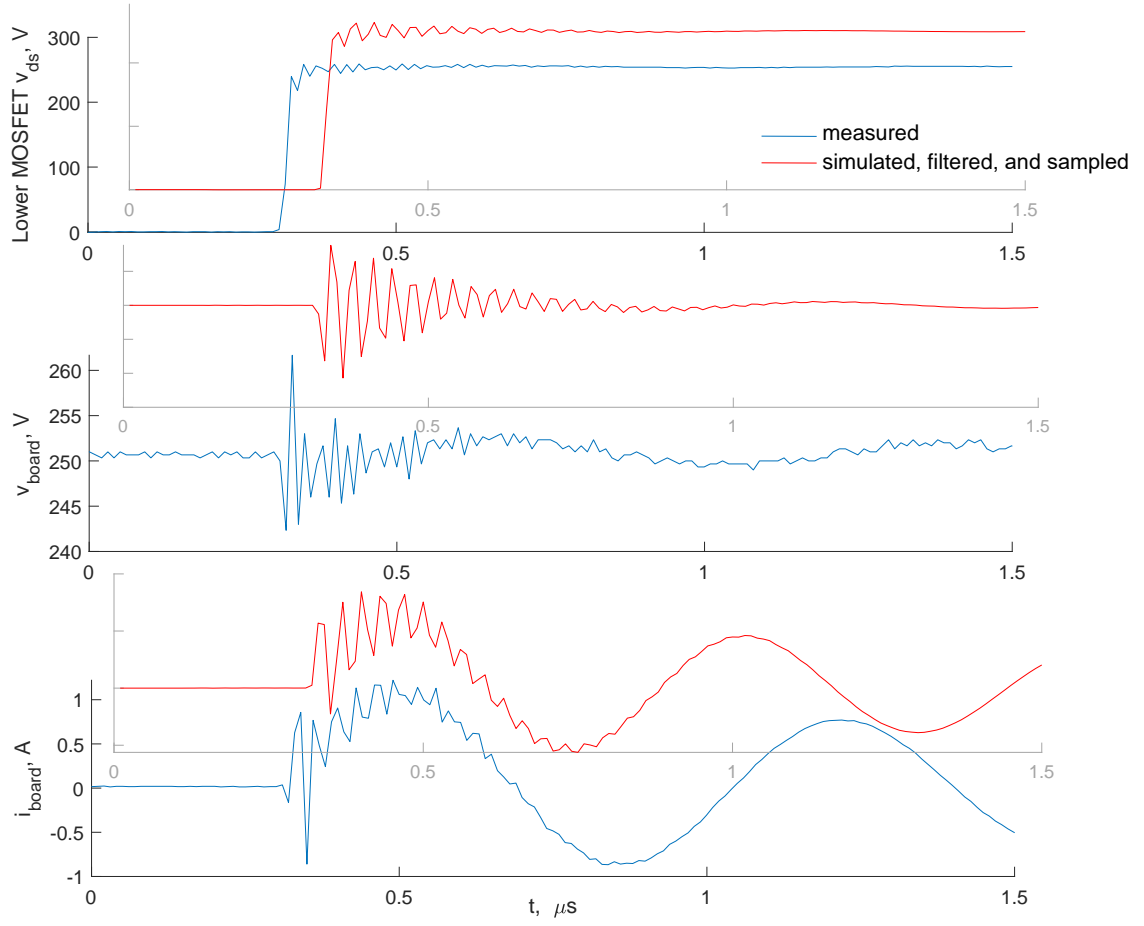


Figure 6.10. Measured and filtered simulated results for turn-on event of a phase leg of the test circuit.

Table 6.2. Results from phase leg turn-on event of inverter test circuit.

Study Signal	Measured Peak	Simulated Peak	Post-processed Peak
i_{board}	1.22 A	2.368 A	1.687 A
v_{board}	261.7 V	290.4 V	267.6 V
v_{ds} (Lower MOSFET)	259 V	290.3 V	263.9 V

The results show that the peak-transient values for the measured and post-processed results are within 1.89 % for the drain-to-source voltage of the lower MOSFET, and 2.25 % for the voltage v_{board} – the voltage across the gate-driver board of the inverter circuit. For the current i_{board} flowing into the board, the peak-transient results were within 38 % of each other.

6.2 Switching Transients of Electric Drive System

High-frequency transients of experimentally measured results established in Chapter 4 are compared with related simulated results in this section. For the purpose of comparison, the switching event for the transient highlighted in Figure 4.4 is considered. Measured phase currents and voltages during the switching event are shown in Figures 6.11 and 6.12, respectively. As shown, the initial currents through the machine are approximately 3, -1.2 , and -1.8 A for phases a , b , and c , respectively. Moreover, it is discerned from the experimentally measured data that phase-leg c is initially turned on and the others turned off before the switching event. Phase-leg a is eventually turned on to mark the switching event.

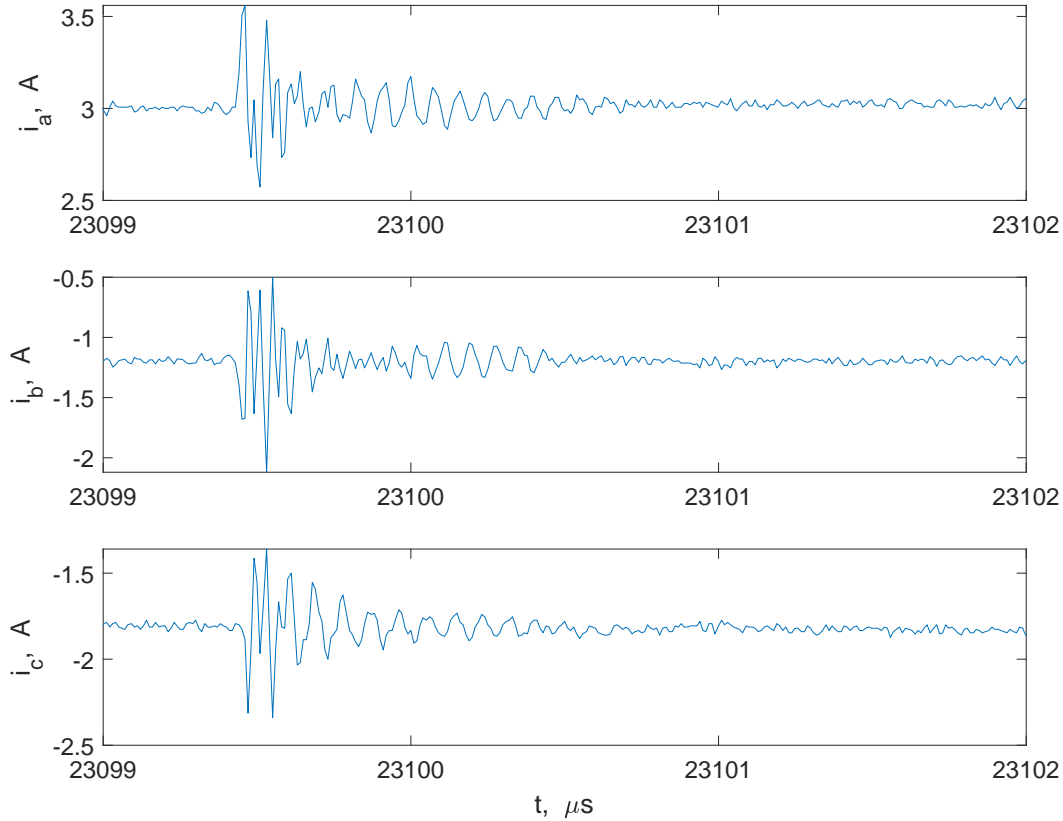


Figure 6.11. Measured currents for turn-on event of a phase leg.

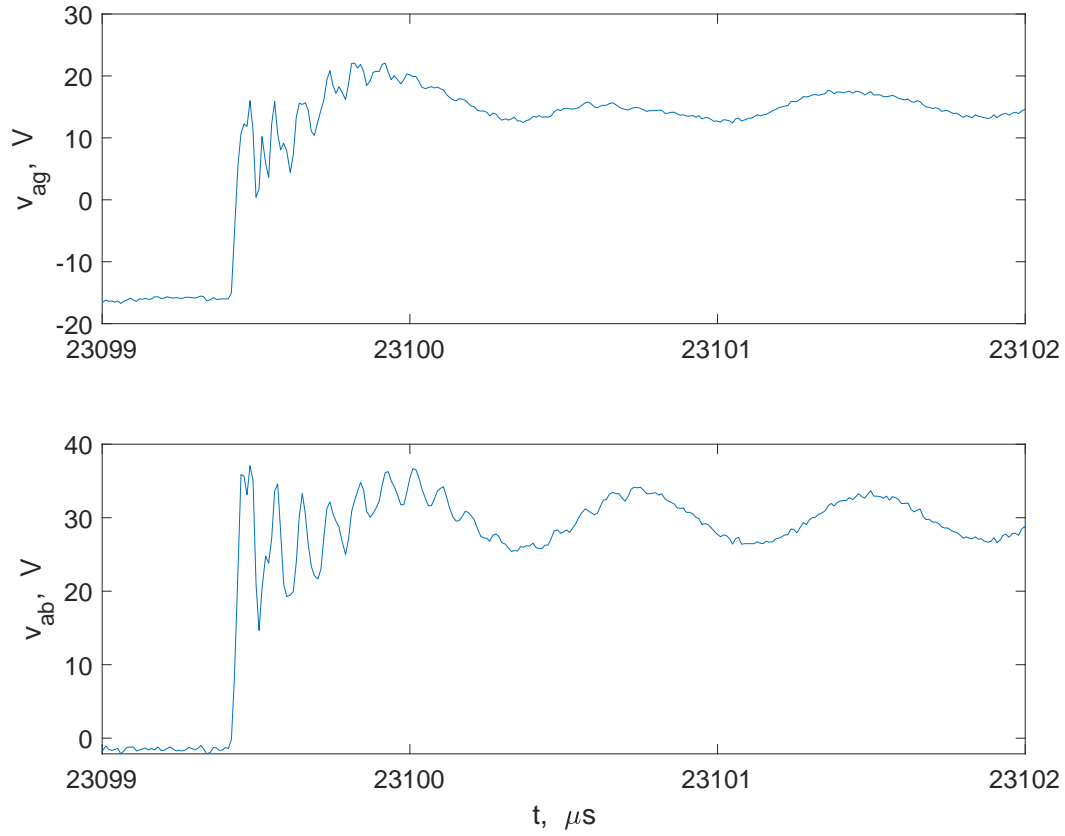


Figure 6.12. Measured voltages for turn-on event of a phase leg.

The discerned switching states and experimental conditions can be accounted for in the simulation of the high-frequency model of the electric drive system. Using the sparse tableau program, the simulation of the high-frequency model was performed for the instance of turn-on of the a -phase with the initial phase currents set to 3, -1.2 , and -1.8 A for phases a , b , and c , respectively. The simulated results are shown in Figures 6.13 and 6.14. The established simulated phase currents are illustrated in Figure 6.13. As shown, the phase currents are characterized by high-frequency oscillations due to the switching occurrence; a frequency of 18 MHz is observed for the simulated signals. Similar oscillations are observed in the plot of voltages shown in Figure 6.14. The oscillations give rise to overvoltages that peak at 27.339 and 43.399 V for voltages v_{ag} and v_{ab} , respectively.

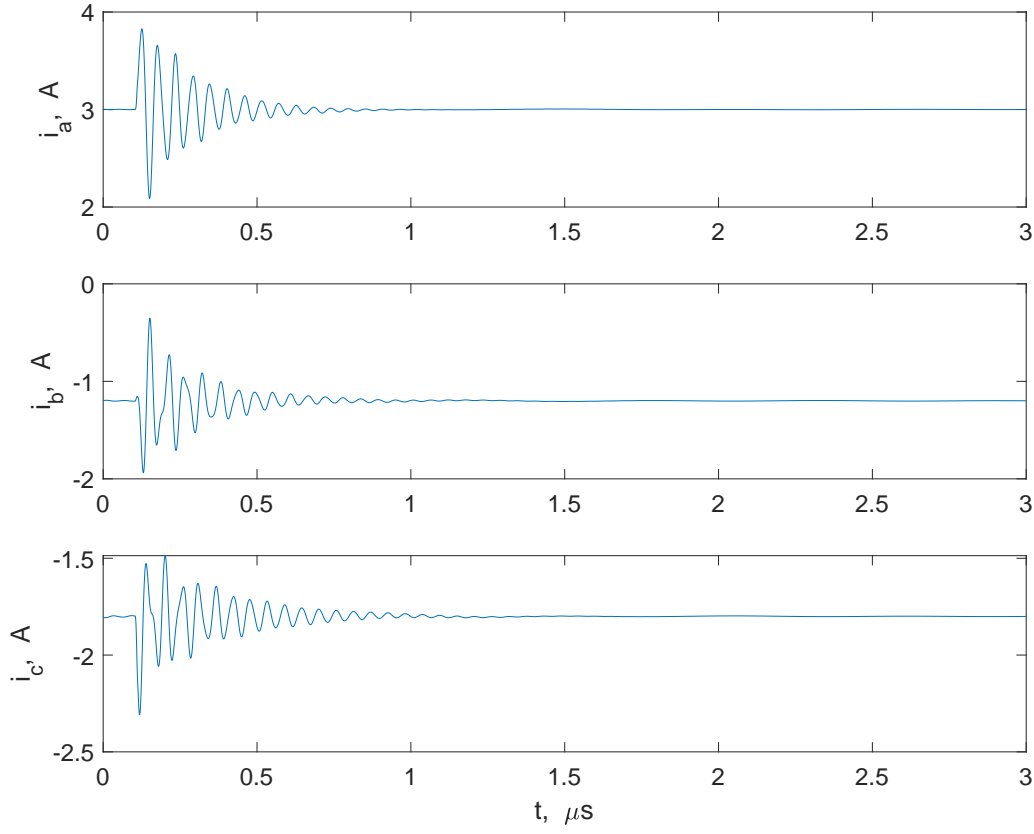


Figure 6.13. Simulated phase currents during turn-on event of a phase leg.

For a fair comparison with measured results, the simulated results were filtered and processed based on instrumentation limitations described in the previous section. The results from the post-processing routine are illustrated in Figures 6.15 and 6.16. The high-frequency oscillations observed in the current and voltage signals reasonably match those of the measured results. From the filtered phase currents shown in Figure 6.15, peak values of 3.78, -0.61 , and -1.57 A are noted for phases a , b , and c , respectively. These peak values compare reasonably with those of the measured results that are observed to be 3.56, -0.5 , and -1.36 A for the a - b - and c -phase, respectively. In addition, it is observed that the filtered voltages v_{ag} and v_{ab} depicted in Figure 6.16 peak at 32.67 and 17.43 V, respectively. These established voltages reasonably compare to the corresponding measured results. A summary of attributes of the simulated and measured signals are given in Table 6.3.

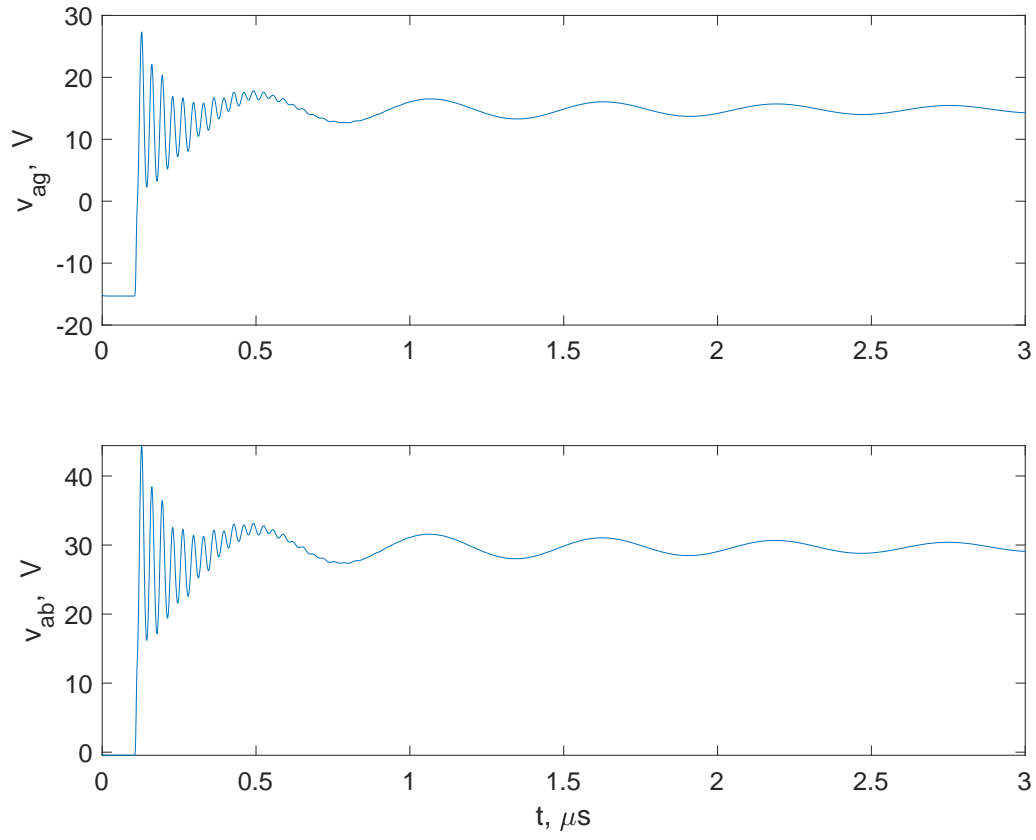


Figure 6.14. Simulated voltages during turn-on event of a phase leg.

Table 6.3. Results from turn-on event of a phase leg.

Study Signal	Measured Peak	Simulated Peak	Post-processed Peak
i_a	3.56 A	3.83 A	3.78 A
i_b	-0.5 A	-0.35 A	-0.61 A
i_c	-1.36 A	-1.49 A	-1.57 A
v_{ag}	22.07 V	27.339 V	17.43 V
v_{ab}	37.07 V	44.399 V	32.67 V

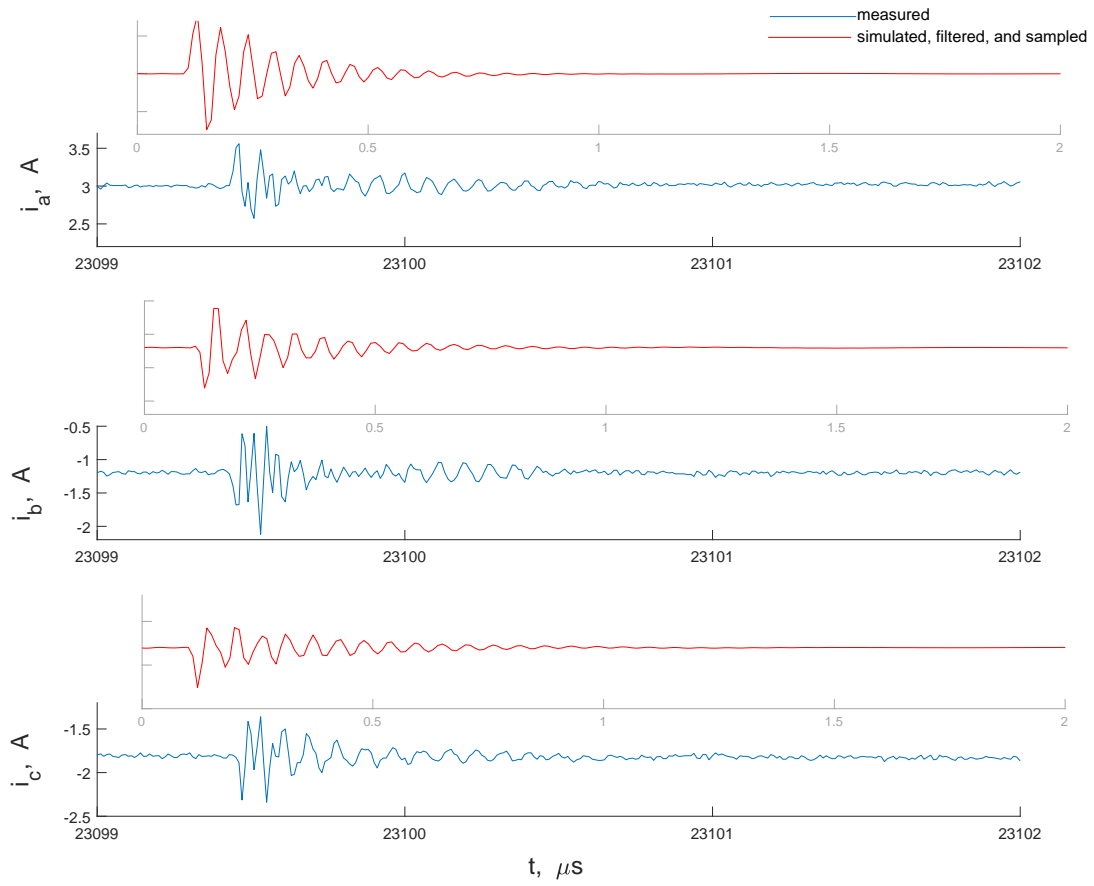


Figure 6.15. Measured and filtered simulated currents during turn-on event of a phase leg.

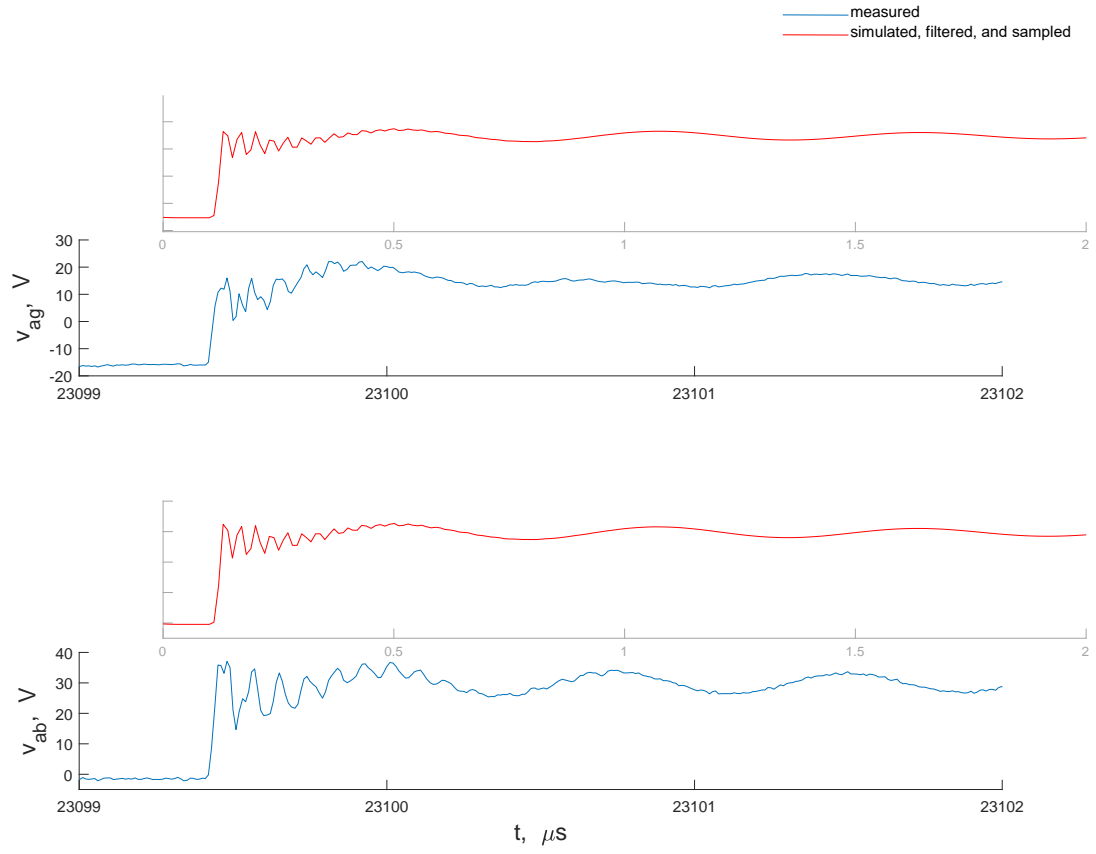


Figure 6.16. Measured and filtered simulated voltages during turn-on event of a phase leg.

6.3 Summary

In this chapter, the simulated turn-on transients of one phase leg of the inverter were compared with experimental measurements. Also, results from simulation of the high-frequency model of the electric drive system were compared with analogous experimental measurements. The simulated results were post-processed to account for oscilloscope bandwidth limitations and sampling rate. These results show that the new simulation framework is capable of predicting the short-term dynamics with reasonable accuracy.

7. FINAL RESULTS, CONCLUSIONS, AND AREAS OF POTENTIAL FURTHER RESEARCH

In previous chapters, efforts were made to develop models that can be used to predict the switching transients of a WBG-based electric drive system. These include wideband models of a surface-mount PMAC electric machine and a WBG-based inverter. Subsequently, the limitations of existing simulation approaches were demonstrated and a new heterogeneous multirate simulation framework was set forth. In this simulation framework, the short- and long-term dynamics of the drive system are established separately using individual low- and high-frequency models derived from the wideband model of the drive system. To arrive at a solution of the long-term dynamics, the simulation of the low-frequency model was implemented using an established state-space-based simulation environment. The stator currents at the switching instants may then be supplied to the high-frequency model implemented using a specially developed computer program based upon the sparse-tableau algorithm. The high-frequency model is used to determine the losses associated with the switching transients. These include the losses in the inverter as well as the electric machine and connecting cable. To enable the rapid calculation of switching losses for arbitrary operating conditions, the high-frequency model can be used to generate two-dimensional look-up tables that can be readily integrated into the low-frequency model.

In this chapter, prior results are briefly summarized. Next the simulation structure for combining the low- and high-frequency simulation results is described. Therein, results obtained from the repetitive execution of the high-frequency simulation are implemented as look-up tables. This approach is applied to the selected drive system operating near rated conditions in a state-space-based simulation. The simulated conduction losses and switching losses in the semiconductors, electric machine, and interconnecting cables are presented. This is followed by concluding comments and potential areas of further research.

7.1 Review of Prior Results

The central objectives of this research were to establish models and a simulation paradigm for WBG-based electric drive systems. In Chapter 2, a low-frequency model of a surface-mount PMAC machine is introduced. The effects of eddy currents in the rotor of the machine are represented by including rL branches in the q - and d -axis equivalent circuits of a conventional low-frequency model. The realized low-frequency model is the basis from which the wideband model is developed. To set the stage for the system-level analysis, the frequency modes of the wideband model are established, enabling its separation into individual low- and high-frequency models.

A large-displacement MOSFET model, which is a modified form of the SPICE Level 1 model, is presented in Chapter 3. Specifically, the voltage-dependent drain-to-source and gate-to-drain junction capacitances are included to accurately portray the switching transients; the static drain-to-source I - V characteristics are represented by the Shichman-Hodges equations; and the current through the body and anti-parallel diodes are described by the Shockley diode equation. The modified Level 1 MOSFET model forms the springboard for developing a wideband model of the WBG-based inverter.

Parameterization procedures for the wideband models of the surface-mount PMAC machine and WBG-based inverter are presented in Chapters 2 and 3, respectively. The wideband models and associated parameters form the basis for the simulation studies presented in Chapters 4 and 5. The deficiencies of existing state-space-based and circuit-based simulators are presented in Chapter 4. It is concluded that existing single-rate simulation methods are computationally prohibitive. As such, a heterogeneous multirate simulation framework is set forth in Chapter 5.

By considering the modal frequencies of the wideband PMAC machine model, independent low- and high-frequency models were developed for determining the long- and short-term dynamics, respectively. The simulation of the low-frequency model was performed using an established state-space-based simulation environment that saw considerable time savings compared to the single-rate simulation of the wideband model. In the simulation, the I - V characteristics of the MOSFET switches were modeled using look-up tables derived

from datasheet information. The approach enables the accurate determination of conduction losses in the inverter circuit. On the other hand, the inverter switching losses were established using high-frequency model of the drive system. For this simulation, a special-purpose computer program, based on the sparse tableau algorithm (STA), was developed to simulate the short-term dynamics.

To illustrate the accuracy of the high-frequency model, the turn-on transients of one phase leg of the inverter were simulated using the STA-based program in Chapter 6. These transients were shown to compare well with experimentally measured results.

7.2 Combining Results of Low- and High-frequency Models

In the new heterogeneous simulation framework described in Chapter 5, it was observed that the simulation of the low-frequency model for a selected steady-state operating condition yields considerable time savings compared with single-rate simulations of the wideband model. However, the execution time for the high-frequency simulation of a single switching event remains relatively high such that cascading the low- and high-frequency simulations may not yield significant savings compared to the single-rate simulation of the wideband model. Instead, due to the decoupled nature of the low- and high-frequency transients, it is possible to establish the high-frequency transients a priori for a set of initial conditions that spans the allowable operating range of the drive system. Once established, the results can be stored in look-up tables whose inputs are the initial conditions from the low-frequency simulation. These look-up tables may then be employed in a posteriori analyses of the switching losses for any selected steady-state operating condition. These tables can also be incorporated into the low-frequency simulation.

The simulation framework is illustrated in Figure 7.1. The desired torque and speed represent inputs to the low-frequency model that is implemented efficiently using an established state-space-based simulation environment such as Simulink. This simulation would include low-frequency models for all of the subsystems (including the PMAC machine, inverter, modulator, and control system) that enable the determination of the machine stator currents at the switching times t_{sw} . These currents can be transformed into their stationary

reference components $i_{qs}^s(t_{sw})$ and $i_{ds}^s(t_{sw})$. The peak value of ac current may be expressed as

$$i_{\text{peak}} = \text{magnitude}(i_{qs}^s - ji_{ds}^s) \quad (7.1)$$

and the angle as

$$\theta_e = \text{angle}(i_{qs}^s - ji_{ds}^s) \quad (7.2)$$

The corresponding switching energy losses, peak transient overvoltage, peak dv/dt , and/or energy transferred to the electric machine can be retrieved from two-dimensional look-up tables with i_{peak} , θ_e , and the initial switching states as inputs. Moreover, if a temporal plot of the stator phase currents that includes both the high- and low-frequency components is desired, the high-frequency transients established using the high-frequency simulation can also be stored in the form of a 2D by 1D look-up table. The stator phase currents can be reconstructed by splitting the low-frequency results at the switching instants t_{sw} 's and inserting the corresponding high-frequency results. In this thesis, however, the primary focus was on the calculation of long-term or accumulated switching and conduction losses.

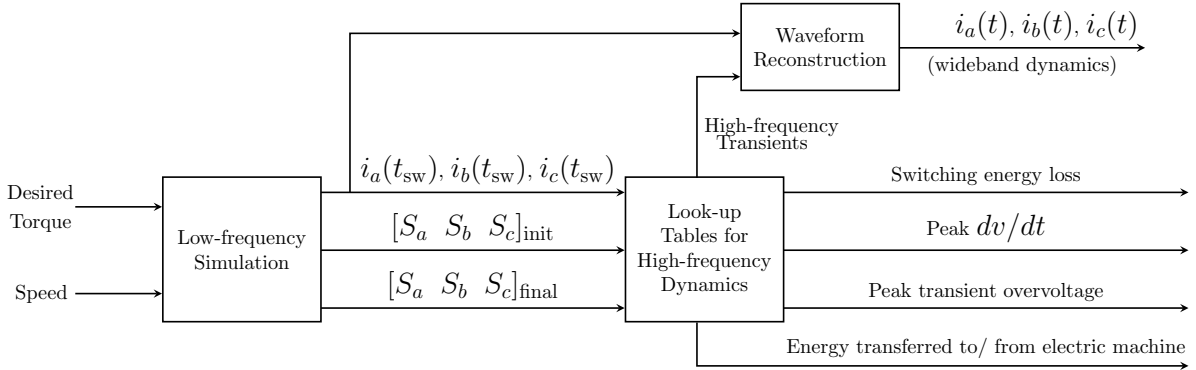


Figure 7.1. Simulation structure for establishing the high-frequency dynamics for different operating points.

Semiconductor Turn-on and Turn-off Energy Losses

Example three-dimensional surface plots that may be implemented as two-dimensional look-up tables are shown in Figures 7.2 and 7.3. Therein, maps are illustrated for turn-on and turn-off losses in phase-leg a with the other phase legs turned off. Specifically, for the phase a turn-on loss, it is assumed that initially the lower device in all three phases are on with the

corresponding upper devices off. Then, the lower device in phase a is turned off and after a 100 ns delay, the upper device in phase a is turned on. Equivalently, $[S_a \ S_b \ S_c]_{\text{init}} = [0 \ 0 \ 0]$ and $[S_a \ S_b \ S_c]_{\text{final}} = [1 \ 0 \ 0]$.

For the phase- a turn-off loss, it is assumed that, initially, the upper device in phase a and the lower devices in phases b and c are initially on with the complimentary devices off. Then, the upper device in phase a is turned off and after a 100 ns delay, the lower device is turned on. Equivalently, $[S_a \ S_b \ S_c]_{\text{init}} = [1 \ 0 \ 0]$ and $[S_a \ S_b \ S_c]_{\text{final}} = [0 \ 0 \ 0]$. In both cases, the switching energy loss is established by integrating (with respect to time) the product of voltage and current across each device over the duration of the switching transient. Sample plots of voltage, current, and power are shown later in this section.

Similar maps may be developed for the turn-on/off of phase-leg a with one of the two other phase legs initially on and the third off e.g. $[S_b \ S_c] = [1 \ 0]$ or $[S_b \ S_c] = [0 \ 1]$, or as the two other phase legs are initially on e.g. $[S_b \ S_c] = [1 \ 1]$. These maps are established by repetitively executing the high-frequency simulation for the allowable range of currents in the selected electric machine. It is useful to consider the features of these plots to determine the best procedures for their implementation as look-up tables.

It may be observed in Figures 7.2 and 7.3 that the turn-on and turn-off maps are symmetrical about $\theta_e = \pi$. The symmetry suggests that the energy losses over the range $\theta_e = [0, \pi]$ are sufficient to be implemented as look-up tables. These look-up tables may consequently be used to deduce energy losses for $\theta_e > \pi$ if desired. Also, it is argued that the look-up tables for phase-leg a can be used to evaluate the energy losses for switching conditions in the other phase legs. Since the machine phase currents form a balance three-phase set, it follows that if the a -phase turn-on energy loss $E_{a,\text{loss}}^{\text{on}}$ may be expressed as a function $g(i_{\text{peak}}, \theta_e)$

$$E_{a,\text{loss}}^{\text{on}} = g(i_{\text{peak}}, \theta_e) \quad (7.3)$$

then similar functions with θ_e shifted may be constructed for the turn-on losses in the other phase legs. In particular, the b -phase turn-on energy loss $E_{b,\text{loss}}^{\text{on}}$ will be

$$E_{b,\text{loss}}^{\text{on}} = g(i_{\text{peak}}, \theta_e - 2\pi/3) \quad (7.4)$$

and the c -phase turn-on energy loss $E_{c,\text{loss}}^{\text{on}}$ takes the form

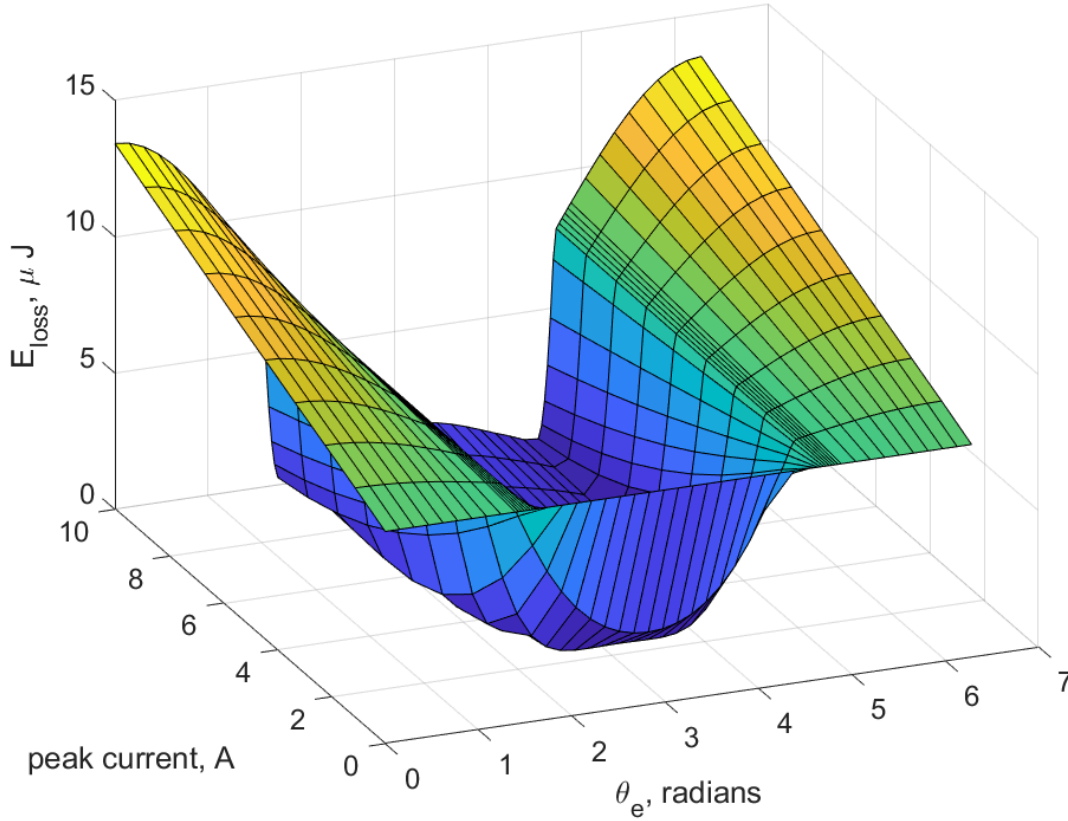


Figure 7.2. Turn-on switching energy losses for phase-leg a ; $[S_a \ S_b \ S_c]_{\text{init}} = [0 \ 0 \ 0]$; $[S_a \ S_b \ S_c]_{\text{final}} = [1 \ 0 \ 0]$.

$$E_{c, \text{loss}}^{\text{on}} = g(i_{\text{peak}}, \theta_e + 2\pi/3) \quad (7.5)$$

These relationships, which may also be applied to the turn-off energy losses, imply that the construction of look-up tables for the other phase legs are not necessary. Instead, look-up tables for phase-leg a over the range $\theta_e = [0, \pi]$ may be used to evaluate the so-called turn-on or turn-off losses in the other phase legs.

It is worthwhile to examine some important values of the look-up tables by considering the surface plots. For the turn-on map shown in Figure 7.2, a maximum energy loss of $13.42 \mu\text{J}$ is noted at $\theta_e = 0$ and 2π . The switching transients in the upper and lower MOSFETs at $\theta_e = 0$ are illustrated in Figures 7.4 and 7.5, respectively. It can be observed that the power

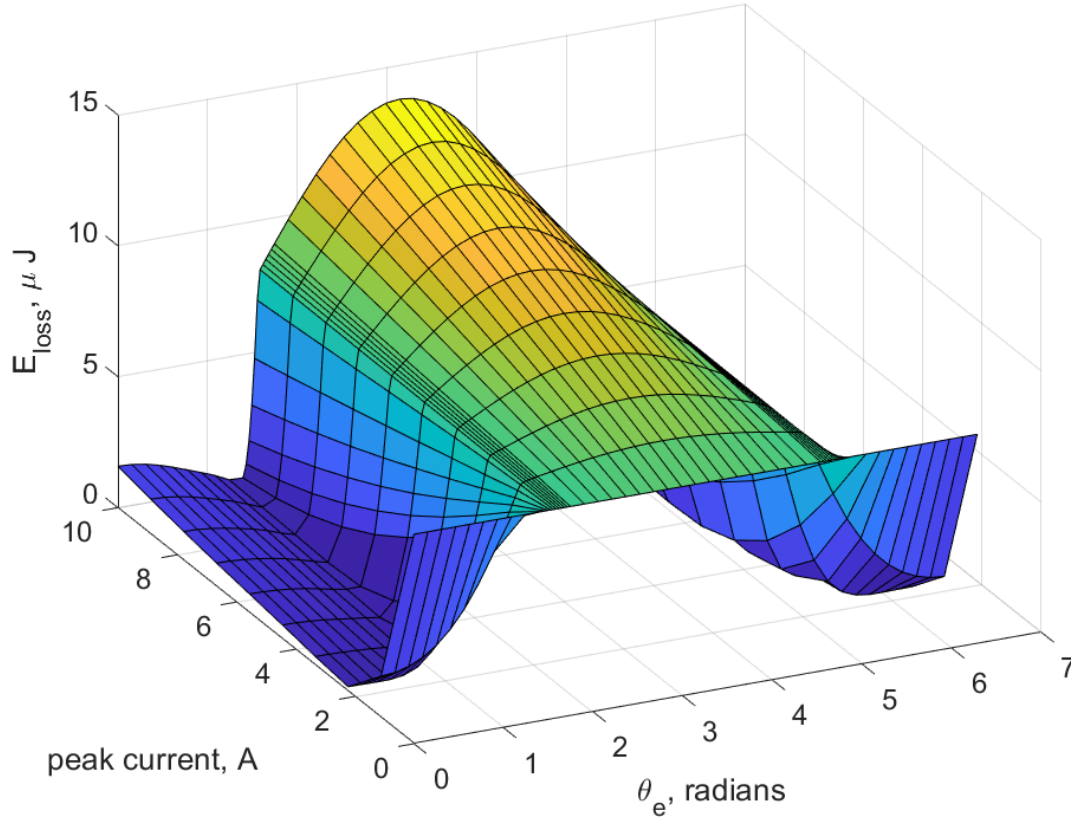


Figure 7.3. Turn-off switching energy losses for phase-leg a ; $[S_a \ S_b \ S_c]_{\text{init}} = [1 \ 0 \ 0]$; $[S_a \ S_b \ S_c]_{\text{final}} = [0 \ 0 \ 0]$.

in the lower MOSFET, which is turned off, is small in comparison to that delivered to the upper when it is turned on. It should be noted that the energy losses in the other phase legs were observed to be negligible. This implies that if the total inverter losses are desired to be estimated, it is adequate to consider only the losses in the phase leg that is switched-on/off using appropriate look-up tables.

From Figure 7.2, the smallest turn-on energy losses occur in the well or valley of the surface plot. The peak machine stator currents for which the valley exists is within the range $[2, 10]$ A and the angle θ_e within $[2\pi/3, 4\pi/3]$. To illustrate sample transients in this valley, turn-on switching transients in the lower and upper MOSFETs are shown in Figures 7.6 and 7.7, respectively, for $\theta_e = \pi$ and $i_{\text{peak}} = 10$ A. Here, the total energy loss is noted

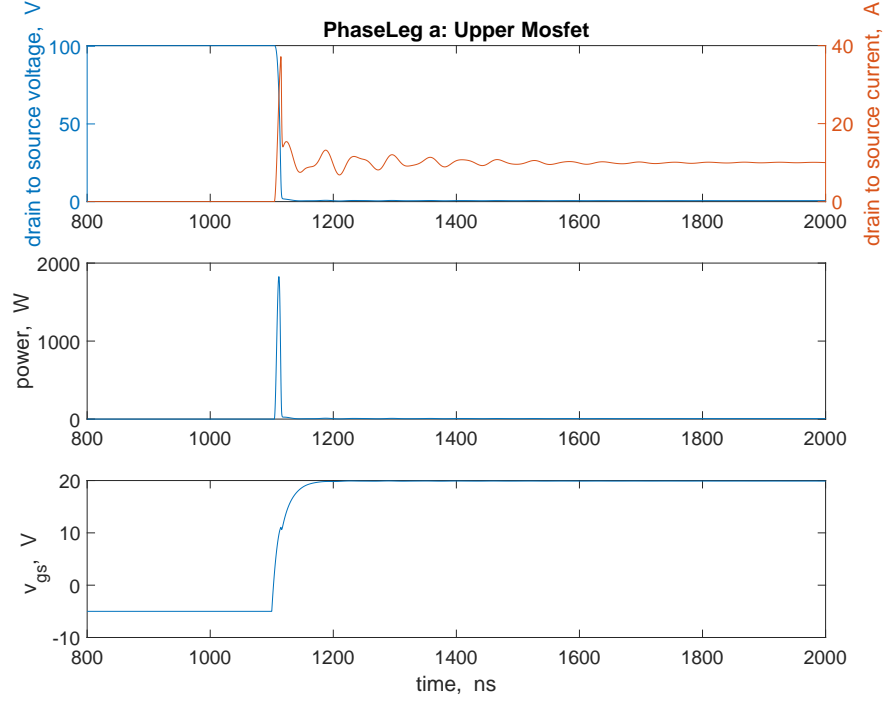


Figure 7.4. Switching transients in a -phase upper MOSFET for $\theta_e = 0$ and $i_{\text{peak}} = 10$ A; $[S_a \ S_b \ S_c]_{\text{init}} = [0 \ 0 \ 0]$; $[S_a \ S_b \ S_c]_{\text{final}} = [1 \ 0 \ 0]$.

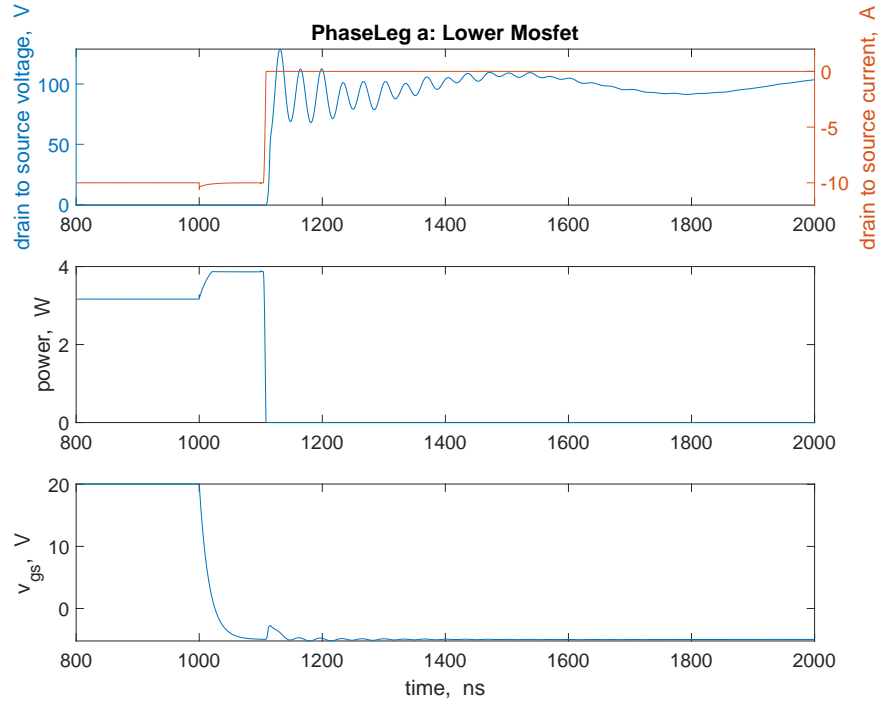


Figure 7.5. Switching transients in a -phase lower MOSFET for $\theta_e = 0$ and $i_{\text{peak}} = 10$ A; $[S_a \ S_b \ S_c]_{\text{init}} = [0 \ 0 \ 0]$; $[S_a \ S_b \ S_c]_{\text{final}} = [1 \ 0 \ 0]$.

as $1.473 \mu\text{J}$. The current in the upper MOSFET settles to -10 A as $i_{as} = i_{\text{peak}} \cos \theta_e = -10 \text{ A}$. Due to its polarity, this current flows through the diode that is connected anti-parallel to the switch. As such, a less significant current overshoot and a lower power loss is established for $\theta_e = \pi$ than that for $\theta_e = 0$. However, the ringing in the current signal results in a contribution of $1.008 \mu\text{J}$ to the total energy loss.

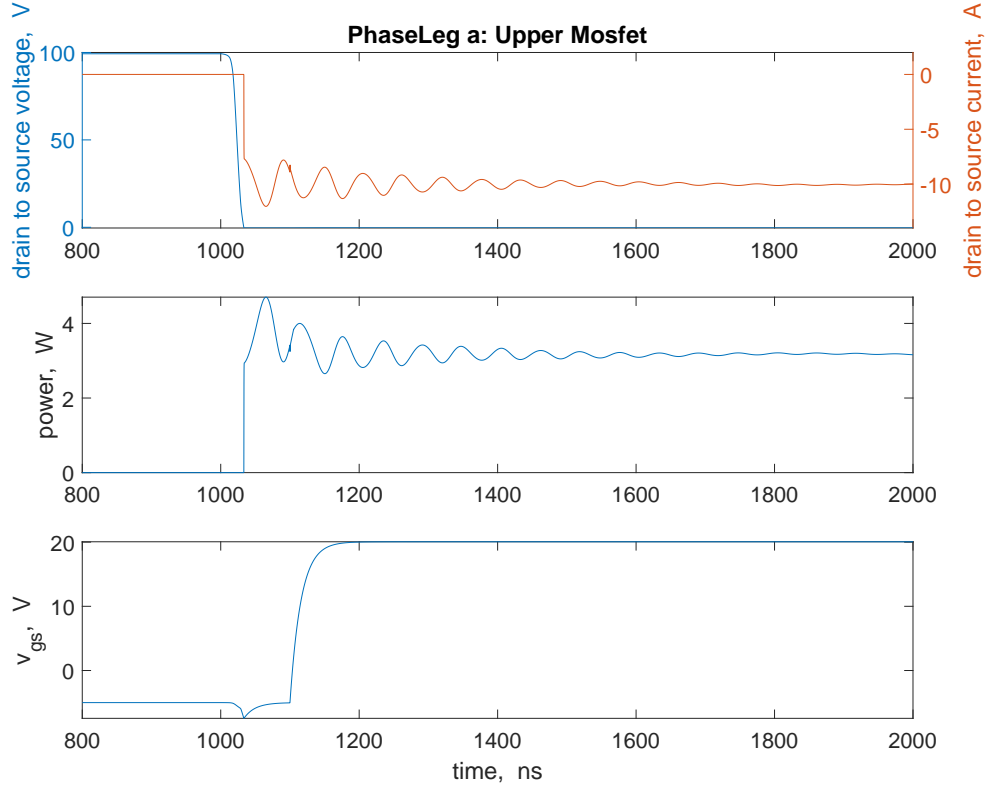


Figure 7.6. Switching transients in a -phase upper MOSFET during phase a turn-on event ($\theta_e = \pi$ and $i_{\text{peak}} = 10 \text{ A}$).

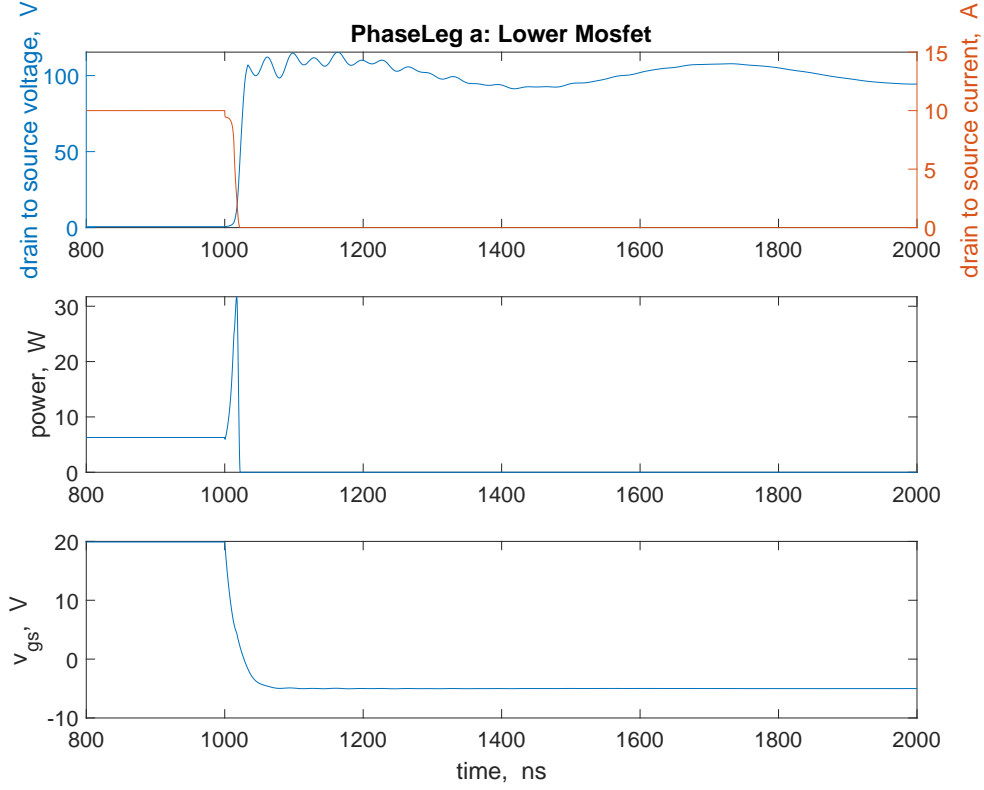


Figure 7.7. Switching transients in a -phase lower MOSFET during phase a turn-on event ($\theta_e = \pi$ and $i_{\text{peak}} = 10$ A).

For the turn-off map shown in Figure 7.3, a maximum total energy loss of $13.697 \mu\text{J}$ occurs at $\theta_e = \pi$ and $i_{\text{peak}} = 10$ A. Switching transients for these conditions are depicted in Figures 7.8 and 7.9. As shown, most of the loss is due to the lower MOSFET, which is turned on during the turn-off event of the phase leg. This significant power loss is as a result of the simultaneous presence of both voltage and current in the lower device when it is turned on.

It is interesting to note that significant energy losses are established for zero machine stator currents ($i_{\text{peak}} = 0$). From the turn-on map shown in Figure 7.2, the total energy loss is observed to be independent of θ_e and equal to $7.785 \mu\text{J}$. Similar observations are noted in the turn-off map, which shows an energy loss of $8 \mu\text{J}$. To better understand the reasons for these observations, the turn-on switching transients for $i_{\text{peak}} = 0$ are considered.

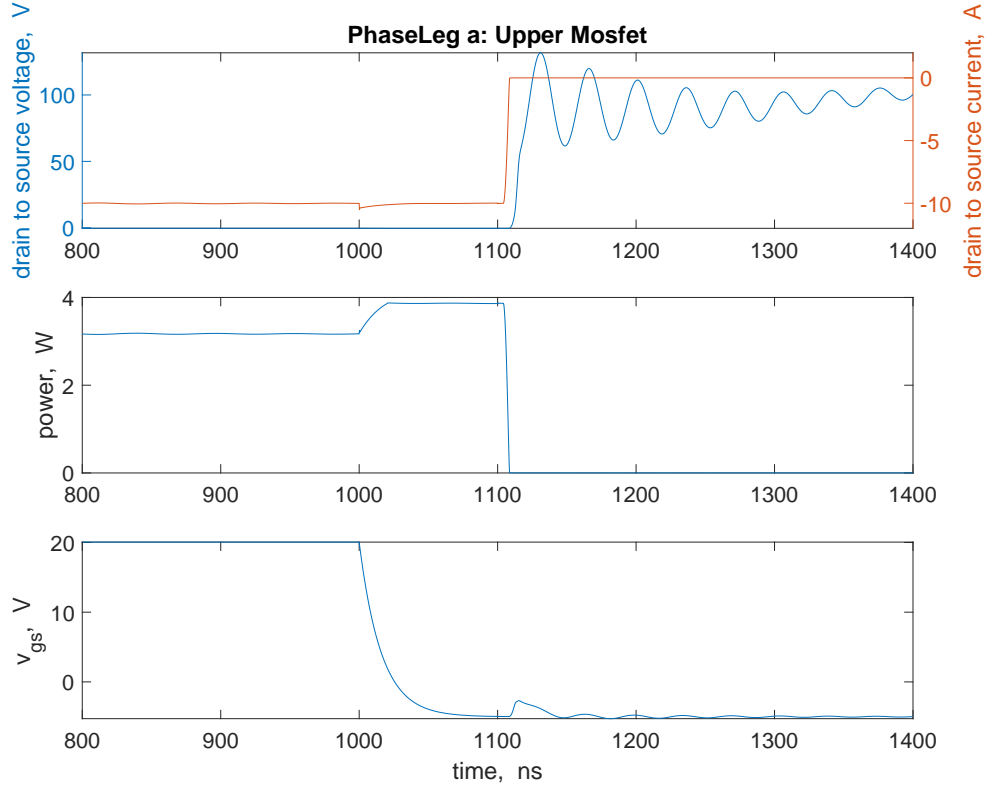


Figure 7.8. Switching transients in a -phase upper MOSFET during phase a turn-off event ($\theta_e = \pi$ and $i_{\text{peak}} = 10$ A).

The switching transients are illustrated in Figures 7.10 and 7.11. As shown, during the switching of the MOSFETs, current overshoot and undershoot are seen in the upper and lower MOSFETs, respectively. These overshoot and undershoot are due to the junction capacitances of the MOSFETs as well as the parasitic capacitances. Specifically, the voltage changes give rise to capacitive currents that consequently cause the change in the drain-to-source currents in the MOSFETs. Due to a significant current overshoot in the upper MOSFET, a peak power loss of 1360 W is registered, which is a major contribution to the total energy loss of $7.785 \mu\text{J}$.

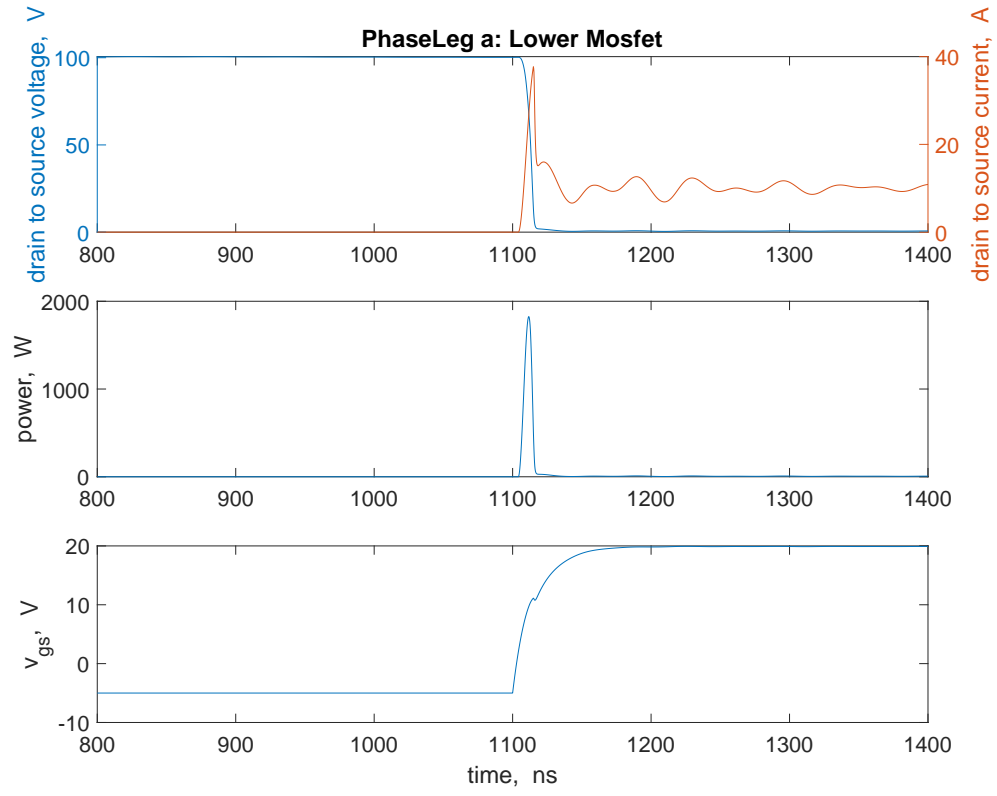


Figure 7.9. Switching transients in a -phase lower MOSFET during phase a turn-off event ($\theta_e = \pi$ and $i_{\text{peak}} = 10$ A).

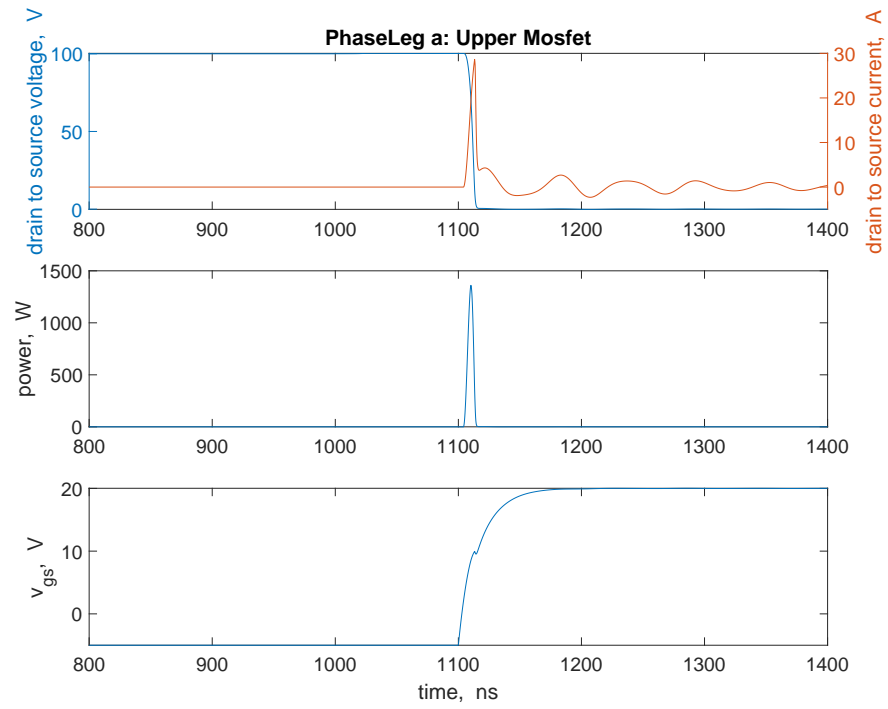


Figure 7.10. Switching transients in a -phase upper MOSFET during phase a turn-on event ($i_{\text{peak}} = 0$).

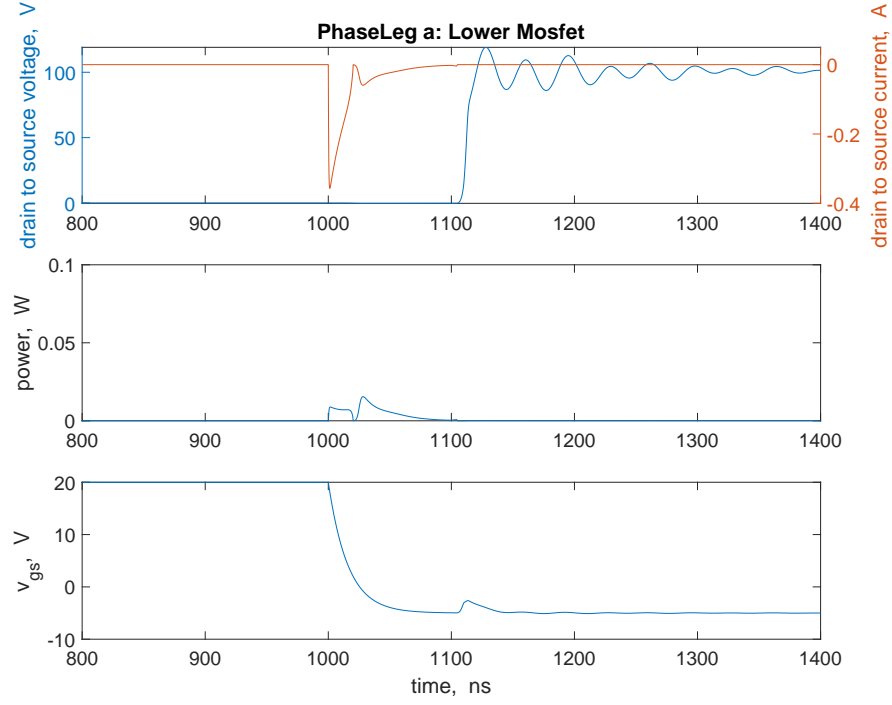


Figure 7.11. Switching transients in a -phase lower MOSFET during phase a turn-on event ($i_{\text{peak}} = 0$).

Cable and Machine Losses Attributed to Switching Transients

Similar look-up tables may be developed for calculating energy transferred to or from the high-frequency model of the electric machine during switching events. Three-dimensional surface plots that illustrate the energy transferred for phase- a turn-on and turn-off events are shown in Figures 7.12 and 7.13, respectively. These maps were constructed with the assumption that two phase legs remain turned off during the turn-on/off of the third phase leg. In particular, to establish the turn-on energy supplied by the inverter to the high-frequency circuit, it is assumed that initially the lower devices are all on. Then, the lower device in phase a is turned off and 100 ns later, the upper device is turned on. The energy supplied to the high-frequency circuit may be calculated as

$$E_{\text{xfer}} = \int_{t_{\text{sw}}}^{t_{\text{sw}}+t_{\text{f}}} \frac{3}{2} \left[v_{qL}^s(t) [i_{qL}^s(t) - i_{qL}^s(t_{\text{sw}})] + v_{dL}^s(t) [i_{dL}^s(t) - i_{dL}^s(t_{\text{sw}})] \right] dt \quad (7.6)$$

where it is assumed the turn-on transients begin at $t = t_{\text{sw}}$ and subside completely at $t = t_{\text{sw}} + t_{\text{f}}$. It is important to note that E_{xfer} is not a loss. Rather, it is the energy transferred to the high-frequency circuit, some of which goes to losses and the remainder to the increase (or decrease) of electric and magnetic energy storage in the high-frequency circuit. As shown in Figures 7.12 and 7.13, during the turn-on event, E_{xfer} is positive and during the turn-off event, E_{xfer} is negative. The difference represents the energy loss.

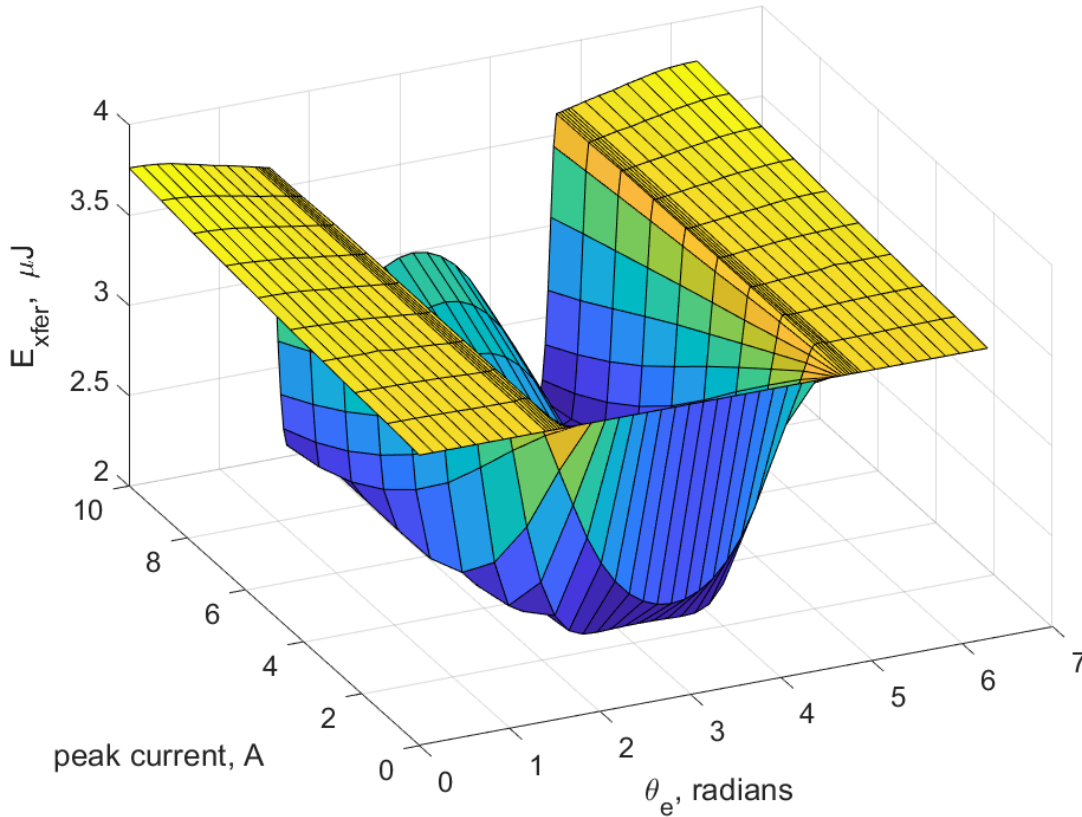


Figure 7.12. Energy transferred to electric machine during turn-on event; $[S_a \ S_b \ S_c]_{\text{init}} = [0 \ 0 \ 0]$; $[S_a \ S_b \ S_c]_{\text{final}} = [1 \ 0 \ 0]$.

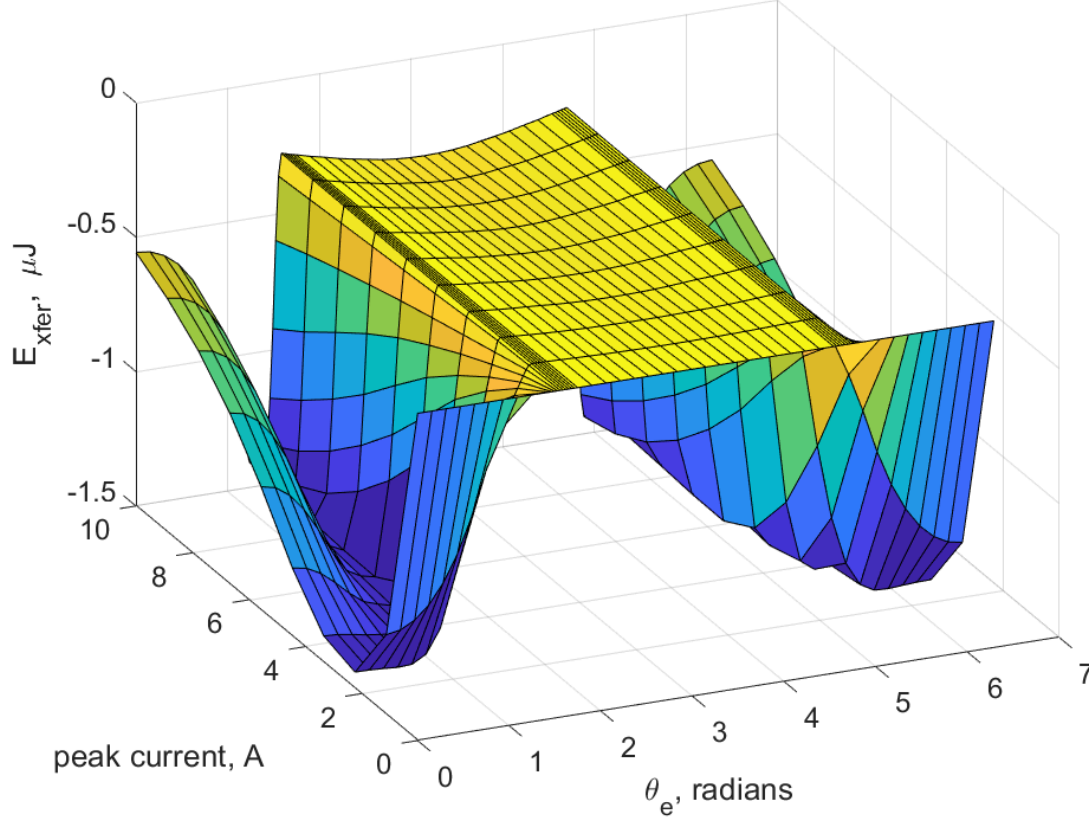


Figure 7.13. Energy transferred to electric machine during turn-off event; $[S_a \ S_b \ S_c]_{\text{init}} = [1 \ 0 \ 0]$; $[S_a \ S_b \ S_c]_{\text{final}} = [0 \ 0 \ 0]$.

In the turn-on E_{xfer} map shown in Figure 7.12, it is observed that the energy transferred in the range $2\pi/3 < \theta_e < 4\pi/3$ is smaller than that seen for other θ_e values within the range $0 < \theta_e < 2\pi$. Conversely, the turn-off map of Figure 7.13 shows that the largest energy transferred during the turn-off of the phase leg is in the range $2\pi/3 < \theta_e < 4\pi/3$. The negative energy transfer values may be interpreted as energy supplied by the high-frequency circuit. This energy supply is possible due to energy originally stored in the electric and magnetic fields - the capacitive and/or inductive components - of the high-frequency circuit.

Prototypical transients for the turn-on and turn-off of the phase leg are shown in Figures 7.14 and 7.15, respectively. As shown, it takes over $1\ \mu\text{s}$ for the switching transients to settle ($t_f \approx 1\ \mu\text{s}$). Their settling times are much greater than the MOSFET switching time, which is in the order of tens of nanoseconds. Moreover, it is observed from Figure 7.14 that the power transfer transients during the turn-on event are characterized by oscillations. This is in part due to transients in the q -axis voltage v_{qg} and current i_{qg} . On the other hand, in the power transfer plot of the turn-off event shown in Figure 7.15, a negative pulse is observed. Its non-oscillatory feature is as a result the transition of voltage v_{qg} to 0 during the switching event. The resultant negative power pulse is reason for its negative E_{xfer} plotted in Figure 7.13.

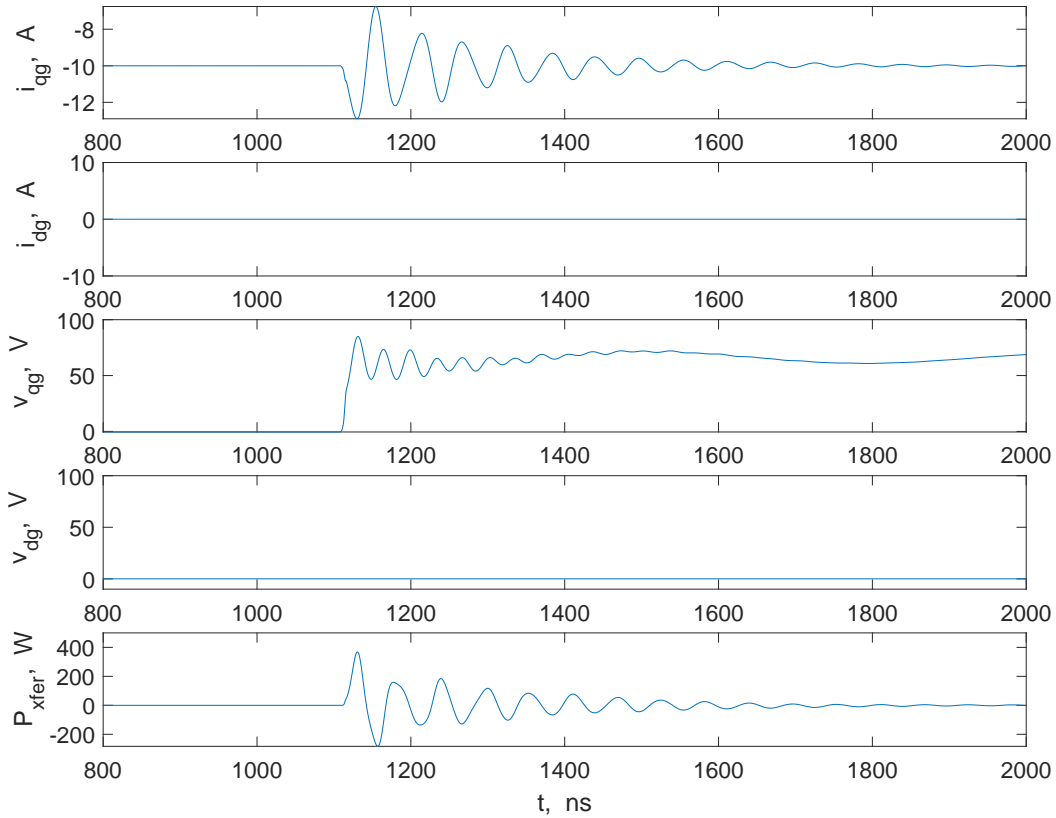


Figure 7.14. Turn-on transients in high-frequency circuit ($\theta_e = 0$ and $i_{\text{peak}} = 10\ \text{A}$); $[S_a\ S_b\ S_c]_{\text{init}} = [0\ 0\ 0]$; $[S_a\ S_b\ S_c]_{\text{final}} = [1\ 0\ 0]$.

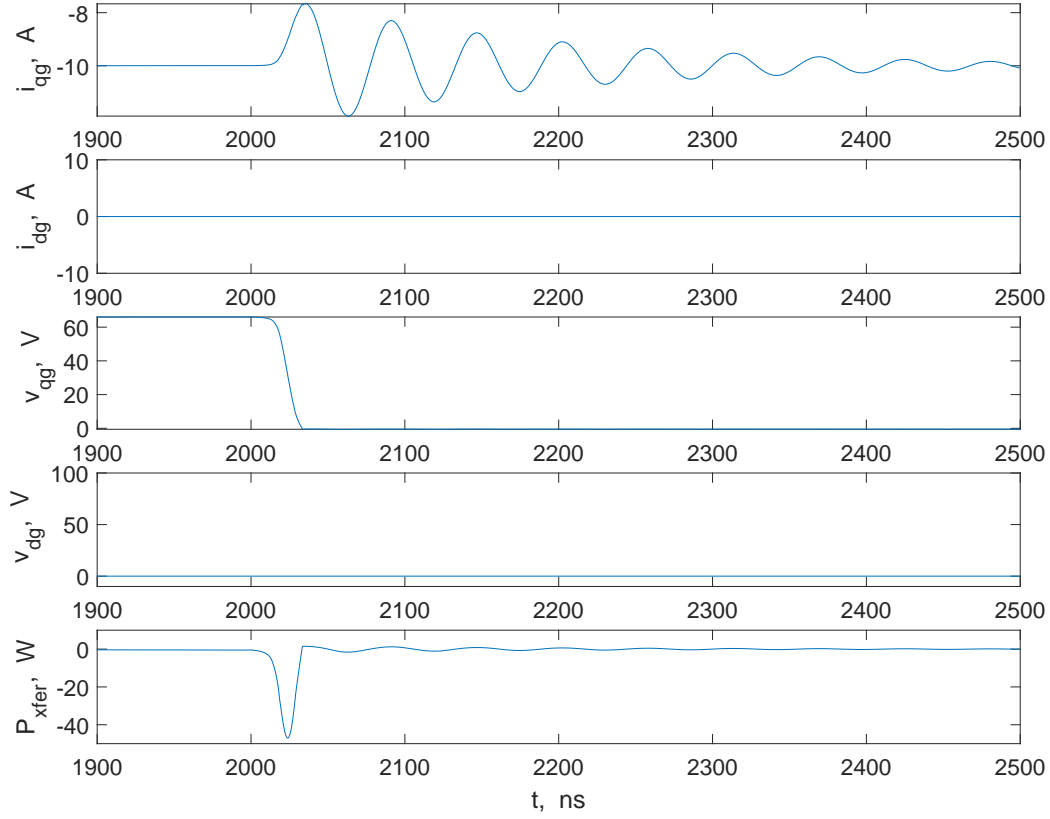


Figure 7.15. Turn-off transients in high-frequency circuit ($\theta_e = 0$ and $i_{\text{peak}} = 10$ A); $[S_a \ S_b \ S_c]_{\text{init}} = [1 \ 0 \ 0]$; $[S_a \ S_b \ S_c]_{\text{final}} = [0 \ 0 \ 0]$.

Furthermore, from the turn-on/off maps, energy transfers are noted to/from the high-frequency circuit for stator machine currents of 0 A. The apparent transfer is due to current and voltage responses in the turned-on/off phase leg and the capacitors and inductors of the high-frequency circuit of the electric machine. It will be worthwhile to see the application of the example surface plots as look-up tables in a simulation. This is the subject of the following section.

7.3 Example Study: Evaluation of Conduction and Switching Losses for Rated Operating Conditions

It is useful to illustrate the simulation framework in which the aforementioned maps are implemented as look-up tables. For this example, the electric machine is assumed to be operating at a speed of $\omega_{rm} = 1800$ rpm and at the peak rated current of 16.55 A. Herein, the d -axis component of the ac current $I_{ds}^r = 0$ and the q -axis component $I_{qs}^r = 16.55$ A. Using (7.7) and (7.8), the steady-state voltages V_{qs}^r and V_{ds}^r may be calculated as 48.45 V and -12.48 V, respectively.

$$V_{qs}^r = r_s I_{qs}^r + \omega_r (L_{ss} I_{ds}^r + \lambda_m') \quad (7.7)$$

$$V_{ds}^r = r_s I_{ds}^r - \omega_r L_{ss} I_{qs}^r \quad (7.8)$$

where $L_{ss} = L_{ls} + \frac{3}{2}L_{ms}$. With V_{dc} set to 100 V, the duty cycle d is realized as $d = 1$ and ϕ_v as 0.2521 using (4.4) and (4.6). These conditions are set in a state-space-based simulation of the simulation structure shown in Figure 7.1. Look-up tables that are used for estimating the energy losses in phase legs and energy transferred to/ from the electric machine during switching events are implemented in the simulation. The simulation required 42 s to run for a simulation time of 300 ms on a 2.8-GHz personal computer with 12 GB of RAM.

The computer traces shown in Figures 7.16 and 7.17 illustrate the phase-leg a energy losses established using the look-up tables. As shown in Figure 7.16, the energy loss in phase-leg a peaks at $13.52 \mu\text{J}$. Moreover, the accumulated switching energy loss ΣE_{loss} in phase-leg a at the termination of the simulation is given as 18.2 mJ. From the ΣE_{loss} plot, the average switching power loss in the phase leg is noted to be approximately 60.73 mW. This switching power loss is small in comparison to the net conduction loss observed from Figure 7.18. Therein, the average conduction power loss is observed to be approximately 28.85 W. Further, plots of the conduction losses for each phase in Figure 7.18 show that the conduction power loss is more than two orders of magnitude larger than the switching power loss.

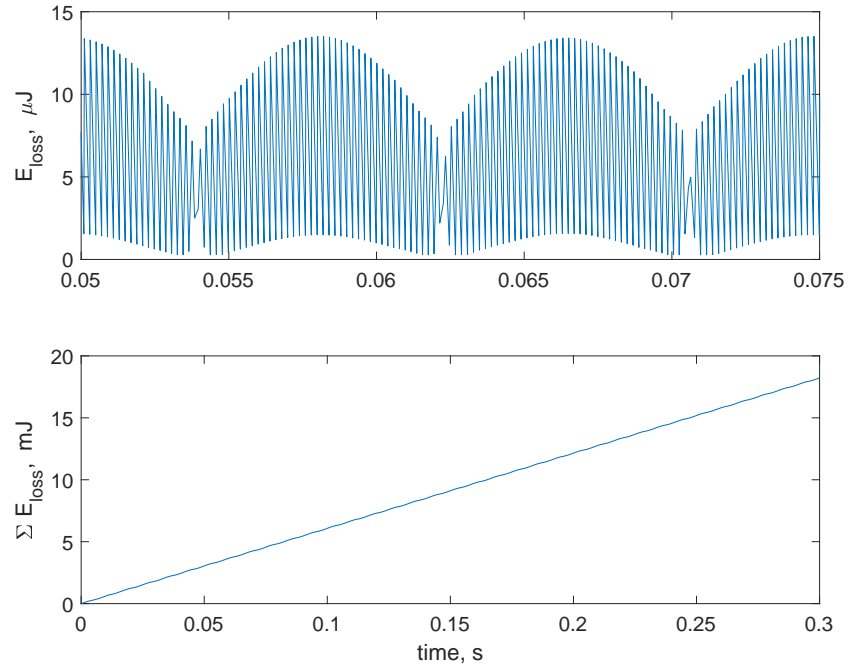


Figure 7.16. Switching energy loss in phase-leg a .

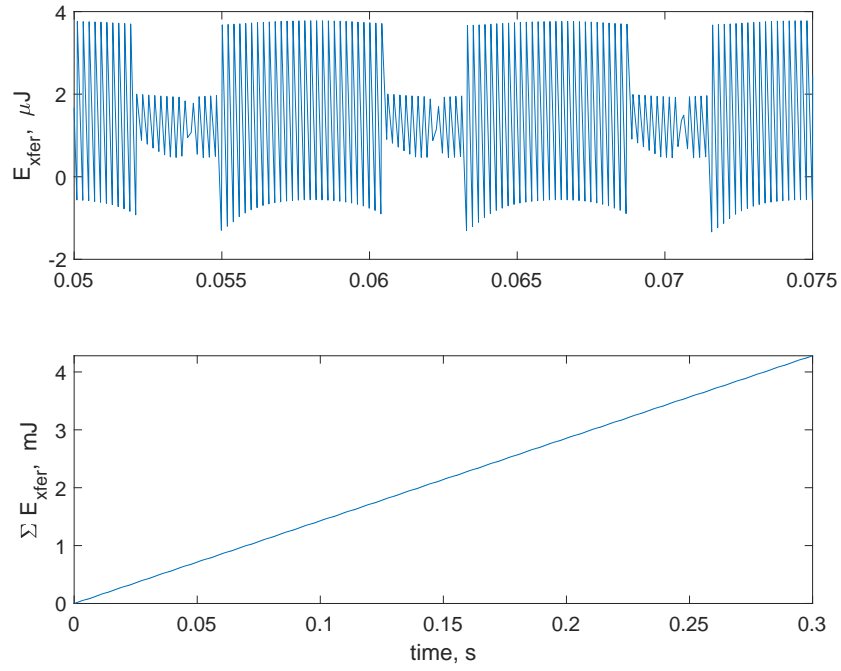


Figure 7.17. Energy transferred to/ from electric machine during switching of phase-leg a .

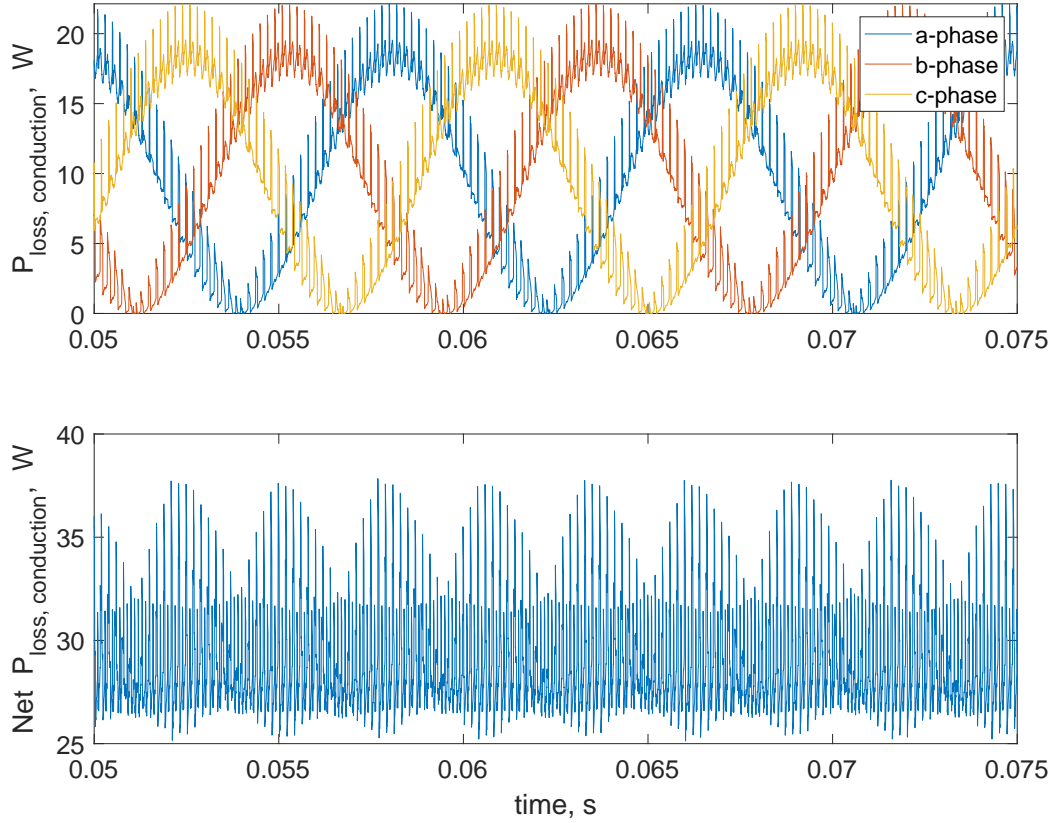


Figure 7.18. Conduction loss in inverter.

In Figure 7.17, plots of energy transferred to/ from the electric machine are shown. Examination of the aggregate energy transferred to/ from the machine shows its value to be an order of magnitude smaller than that of the switching loss. Specifically, the net energy transferred at the termination of the simulation is noted to be approximately 4.28 mJ. From the ΣE_{xfer} plot, the average power loss in the cable/ machine is noted to be approximately 14.27 mW. A summary of key results is given in Table 7.1. It is important to note that the conduction losses in the MOSFETs are significantly greater than the losses attributed to switching transients.

Table 7.1. Summary of average power losses and efficiency

Ave P_{motor}	1202.8 W
Ave $P_{\text{loss, semiconductor}}$	60.73 mW
Ave $P_{\text{loss, cable/machine}}$	14.27 mW
Net $P_{\text{loss, conduction}}$	28.85 W
Efficiency	97.6 %

7.4 Conclusions

In this thesis, a heterogeneous multirate simulation approach for wide-bandgap-based inverter drives was set forth. In this approach, the short- and long-term transients are established separately using high- and low-frequency models implemented using different computer programs that are best suited for the respective time scales and transients. Repetitive execution of the high-frequency model yields look-up tables for the switching losses in the semiconductors, electric machine, and interconnecting cables. These look-up tables can be integrated into the low-frequency simulation that establishes all other losses including conduction losses in the semiconductors and electric machine.

This simulation strategy was applied to a wide-bandgap-based drive system consisting of a SiC-based inverter and permanent-magnet ac machine. It was shown that the conduction losses are more than two orders of magnitude larger than the switching losses, which is consistent with expectation. The simulation approach set forth yields significant time savings compared with conventional single-rate simulation approaches wherein all transients, fast and slow, are established using a single fixed- or variable-time-step integration algorithm.

7.5 Areas of Future Research

In this thesis, the primary focus was on the prediction of switching and conduction losses attributed to fast wide-bandgap semiconductor devices. Also of interest, however, are peak transient overvoltages and the peak dv/dt applied to the electric machine. Both of these can readily be established through repetitive execution of the high-frequency simulation with results stored in look-up tables.

Other areas of potential exploration involve the extension of the simulation method to other types of drive systems such as induction or salient-rotor permanent-magnet ac machine drives or those utilizing multi-level, soft-switching, and/or current-source inverter topologies.

Another avenue of research involves the improvement in computational speed of the high-frequency simulation. Efforts in this area may likely involve the use of parallel direct or iterative sparse linear equation solvers. The use of a commercial or custom MNA-based program to establish high-frequency transients is also possible as long as the objective for reducing the computational expense is met.

REFERENCES

- [1] M. Chinthavali, P. Otaduy, and B. Ozpineci, “Comparison of si and sic inverters for ipm traction drive,” in *2010 IEEE Energy Conversion Congress and Exposition*, 2010, pp. 3360–3365. DOI: [10.1109/ECCE.2010.5618319](https://doi.org/10.1109/ECCE.2010.5618319).
- [2] T. Zhao, J. Wang, A. Q. Huang, and A. Agarwal, “Comparisons of sic mosfet and si igbt based motor drive systems,” in *2007 IEEE Industry Applications Annual Meeting*, 2007, pp. 331–335. DOI: [10.1109/07IAS.2007.51](https://doi.org/10.1109/07IAS.2007.51).
- [3] H. Zhang, L. M. Tolbert, and B. Ozpineci, “Impact of sic devices on hybrid electric and plug-in hybrid electric vehicles,” *IEEE Transactions on Industry Applications*, vol. 47, no. 2, pp. 912–921, 2011, ISSN: 0093-9994. DOI: [10.1109/TIA.2010.2102734](https://doi.org/10.1109/TIA.2010.2102734).
- [4] T. Evans, T. Hanada, Y. Nakano, and T. Nakamura, “Development of sic power devices and modules for automotive motor drive use,” in *2013 IEEE International Meeting for Future of Electron Devices, Kansai*, 2013, pp. 116–117. DOI: [10.1109/IMFEDK.2013.6602266](https://doi.org/10.1109/IMFEDK.2013.6602266).
- [5] M. Bhatnagar and B. J. Baliga, “Comparison of 6h-sic, 3c-sic, and si for power devices,” *IEEE Transactions on Electron Devices*, vol. 40, no. 3, pp. 645–655, 1993.
- [6] B. J. Baliga, “Power semiconductor devices for variable-frequency drives,” *Proceedings of the IEEE*, vol. 82, no. 8, pp. 1112–1122, 1994.
- [7] B. J. Baliga, “Trends in power semiconductor devices,” *IEEE Transactions on Electron Devices*, vol. 43, no. 10, pp. 1717–1731, 1996.
- [8] J. Wang, T. Zhao, J. Li, A. Q. Huang, R. Callanan, F. Husna, and A. Agarwal, “Characterization, modeling, and application of 10-kv sic mosfet,” *IEEE Transactions on Electron Devices*, vol. 55, no. 8, pp. 1798–1806, 2008.
- [9] Q. Zhang, R. Callanan, M. K. Das, S. Ryu, A. K. Agarwal, and J. W. Palmour, “Sic power devices for microgrids,” *IEEE Transactions on Power Electronics*, vol. 25, no. 12, pp. 2889–2896, 2010.
- [10] H. A. Mantooth, M. D. Glover, and P. Shepherd, “Wide bandgap technologies and their implications on miniaturizing power electronic systems,” *IEEE Journal of Emerging and Selected Topics in Power Electronics*, vol. 2, no. 3, pp. 374–385, 2014.
- [11] J. Millán, P. Godignon, X. Perpiñà, A. Pérez-Tomás, and J. Rebollo, “A survey of wide bandgap power semiconductor devices,” *IEEE Transactions on Power Electronics*, vol. 29, no. 5, pp. 2155–2163, 2014.

- [12] H. A. Mantooth, K. Peng, E. Santi, and J. L. Hudgins, "Modeling of wide bandgap power semiconductor devices — part i," *IEEE Transactions on Electron Devices*, vol. 62, no. 2, pp. 423–433, 2015.
- [13] M. Guacci, J. A. Anderson, K. L. Pally, D. Bortis, J. W. Kolar, M. J. Kasper, J. Sanchez, and G. Deboy, "Experimental characterization of silicon and gallium nitride 200v power semiconductors for modular/multi-level converters using advanced measurement techniques," *IEEE Journal of Emerging and Selected Topics in Power Electronics*, pp. 1–1, 2019.
- [14] Z. Wang, Y. Wu, M. H. Mahmud, Z. Zhao, Y. Zhao, and H. A. Mantooth, "Design and validation of a 250-kw all-silicon carbide high-density three-level t-type inverter," *IEEE Journal of Emerging and Selected Topics in Power Electronics*, vol. 8, no. 1, pp. 578–588, 2020.
- [15] Z. Zhang, W. Zhang, F. Wang, L. M. Tolbert, and B. J. Blalock, "Analysis of the switching speed limitation of wide band-gap devices in a phase-leg configuration," in *2012 IEEE Energy Conversion Congress and Exposition (ECCE)*, 2012, pp. 3950–3955. DOI: [10.1109/ECCE.2012.6342164](https://doi.org/10.1109/ECCE.2012.6342164).
- [16] B. J. Baliga, "Power semiconductor devices for variable-frequency drives," *Proceedings of the IEEE*, vol. 82, no. 8, pp. 1112–1122, 1994, ISSN: 0018-9219. DOI: [10.1109/5.301680](https://doi.org/10.1109/5.301680).
- [17] D. Kranzer, C. Wilhelm, F. Reiners, and B. Burger, "Application of normally-off sic-jfets in photovoltaic inverters," in *2009 13th European Conference on Power Electronics and Applications*, 2009, pp. 1–6.
- [18] T. J. Han, J. Nagashima, S. J. Kim, S. Kulkarni, and F. Barlow, "High density 50 kw sic inverter systems using a jfet based six-pack power module," in *8th International Conference on Power Electronics - ECCE Asia*, 2011, pp. 764–769. DOI: [10.1109/ICPE.2011.5944668](https://doi.org/10.1109/ICPE.2011.5944668).
- [19] Y. Xie, C. Chen, Z. Huang, T. Liu, Y. Kang, and F. Luo, "High frequency conducted emi investigation on packaging and modulation for a sic-based high frequency converter," *IEEE Journal of Emerging and Selected Topics in Power Electronics*, vol. 7, no. 3, pp. 1789–1804, 2019.
- [20] P. Bogónez-Franco and J. B. Sendra, "Emi comparison between si and sic technology in a boost converter," in *International Symposium on Electromagnetic Compatibility - EMC EUROPE*, 2012, pp. 1–4.

- [21] T. Lee, H. Kim, N. Lee, T. Chin, H. Bu, and Y. Cho, "Performance evaluation of gan fet-based matrix converters with dv/dt filters for variable frequency drive applications," *Journal of Power Electronics*, pp. 1–10, 2020.
- [22] S. Chen, T. A. Lipo, and D. Fitzgerald, "Source of induction motor bearing currents caused by pwm inverters," *IEEE Transactions on Energy Conversion*, vol. 11, no. 1, pp. 25–32, 1996, ISSN: 1558-0059. DOI: [10.1109/60.486572](https://doi.org/10.1109/60.486572).
- [23] A. von Jouanne, P. Enjeti, and W. Gray, "Application issues for pwm adjustable speed ac motor drives," *IEEE Industry Applications Magazine*, vol. 2, no. 5, pp. 10–18, 1996, ISSN: 1558-0598. DOI: [10.1109/2943.532149](https://doi.org/10.1109/2943.532149).
- [24] R. J. Kerkman, D. Leggate, and G. L. Skibinski, "Interaction of drive modulation and cable parameters on ac motor transients," *IEEE Transactions on Industry Applications*, vol. 33, no. 3, pp. 722–731, 1997, ISSN: 1939-9367. DOI: [10.1109/28.585863](https://doi.org/10.1109/28.585863).
- [25] D. F. Busse, J. M. Erdman, R. J. Kerkman, D. W. Schlegel, and G. L. Skibinski, "The effects of pwm voltage source inverters on the mechanical performance of rolling bearings," *IEEE Transactions on Industry Applications*, vol. 33, no. 2, pp. 567–576, 1997.
- [26] O. T. Fulani, "High-frequency switching transients and power loss estimation in electric drive systems that utilize wide-bandgap semiconductors," Master's thesis, Purdue University, 2017, p. 71, ISBN: 978-0-355-26270-4. [Online]. Available: <https://search.proquest.com/docview/1975367003?accountid=13360>.
- [27] A. E. Fitzgerald, C. Kingsley, S. D. Umans, and B. James, *Electric machinery*. McGraw-Hill New York, 2003, vol. 5.
- [28] P. Krause, O. Wasynczuk, and S. D. Pekarek, *Electromechanical motion devices*. John Wiley & Sons, 2012, vol. 90.
- [29] The Math Works Inc., *Simulink User's Guide*, Natick, Massachusetts, 2019.
- [30] M. Cai, T. Craddock, and O. Wasynczuk, "High-frequency modeling, parameterization, and simulation of ipm motor drive systems," in *2017 IEEE Power and Energy Conference at Illinois (PECI)*, 2017, pp. 1–8. DOI: [10.1109/PECI.2017.7935769](https://doi.org/10.1109/PECI.2017.7935769).
- [31] Y. Xu and D. C. Aliprantis, "Wound-rotor induction machine model with saturation and high-frequency effects," in *2014 International Conference on Electrical Machines (ICEM)*, 2014, pp. 1838–1844. DOI: [10.1109/ICELMACH.2014.6960433](https://doi.org/10.1109/ICELMACH.2014.6960433).

- [32] A. Boglietti and E. Carpaneto, "Induction motor high frequency model," in *Conference Record of the 1999 IEEE Industry Applications Conference. Thirty-Forth IAS Annual Meeting (Cat. No.99CH36370)*, vol. 3, 1999, 1551–1558 vol.3.
- [33] M. Schinkel, S. Weber, S. Guttowski, W. John, and H. Reichl, "Efficient hf modeling and model parameterization of induction machines for time and frequency domain simulations," in *Twenty-First Annual IEEE Applied Power Electronics Conference and Exposition, 2006. APEC '06.*, 2006, 6 pp.–.
- [34] L. Wang, C. Ngai-Man Ho, F. Canales, and J. Jatskevich, "High-frequency modeling of the long-cable-fed induction motor drive system using tlm approach for predicting overvoltage transients," *IEEE Transactions on Power Electronics*, vol. 25, no. 10, pp. 2653–2664, 2010, ISSN: 1941-0107. DOI: [10.1109/TPEL.2010.2047027](https://doi.org/10.1109/TPEL.2010.2047027).
- [35] A. Boglietti, A. Cavagnino, and M. Lazzari, "Experimental high-frequency parameter identification of ac electrical motors," *IEEE Transactions on Industry Applications*, vol. 43, no. 1, pp. 23–29, 2007.
- [36] S. D. Sudhoff, J. L. Tichenor, and J. L. Drewniak, "Wide-bandwidth multi-resolutional analysis of a surface-mounted pm synchronous machine," *IEEE Transactions on Energy Conversion*, vol. 14, no. 4, pp. 1011–1018, 1999, ISSN: 1558-0059. DOI: [10.1109/60.815021](https://doi.org/10.1109/60.815021).
- [37] L. W. Nagel and D. Pederson, "SPICE (Simulation Program with Integrated Circuit Emphasis)," EECS Department, University of California, Berkeley, Tech. Rep. UCB/ERL M382, 1973. [Online]. Available: <http://www2.eecs.berkeley.edu/Pubs/TechRpts/1973/22871.html>.
- [38] H. Shichman and D. Hodges, "Modeling and simulation of insulated-gate field-effect transistor switching circuits," *IEEE Journal of Solid-State Circuits*, vol. 3, no. 3, pp. 285–289, 1968.
- [39] T. Liu, R. Ning, T. T. Y. Wong, and Z. J. Shen, "Modeling and analysis of sic mosfet switching oscillations," *IEEE Journal of Emerging and Selected Topics in Power Electronics*, vol. 4, no. 3, pp. 747–756, 2016.
- [40] L. Wu and M. Saeedifard, "A simple behavioral electro-thermal model of gan fets for spice circuit simulation," *IEEE Journal of Emerging and Selected Topics in Power Electronics*, vol. 4, no. 3, pp. 730–737, 2016.
- [41] A. Subbiah, "A variable-structure variable-order simulation paradigm for power electronic circuits," PhD thesis, Purdue University, 2015, p. 165, ISBN: 978-1-339-58237-5. [Online]. Available: <https://search.proquest.com/docview/1778511264?accountid=13360>.

- [42] J. Vlach and K. Singhal, *Computer methods for circuit analysis and design*, eng, 2nd ed. New York: Van Nostrand Reinhold, 1994, ISBN: 0442011946.
- [43] F. N. Najm, *Circuit Simulation*. Hoboken, New Jersey: John Wiley & Sons Inc., 2010.
- [44] C. Gear, "Multirate methods for ordinary differential equations," Illinois Univ., Urbana (USA). Dept. of Computer Science, Tech. Rep., 1974.
- [45] J. Chen and M. L. Crow, "A variable partitioning strategy for the multirate method in power systems," *IEEE Transactions on Power Systems*, vol. 23, no. 2, pp. 259–266, 2008.
- [46] J. Chen, M. L. Crow, B. H. Chowdhury, and L. Acar, "An error analysis of the multirate method for power system transient stability simulation," in *IEEE PES Power Systems Conference and Exposition, 2004.*, 2004, 982–986 vol.2.
- [47] M. L. Crow and J. G. Chen, "The multirate method for simulation of power system dynamics," *IEEE Transactions on Power Systems*, vol. 9, no. 3, pp. 1684–1690, 1994.
- [48] M. L. Crow and J. G. Chen, "The multirate simulation of facts devices in power system dynamics," *IEEE Transactions on Power Systems*, vol. 11, no. 1, pp. 376–382, 1996.
- [49] S. D. Pekarek, *A partitioned state model of synchronous machines for simulation and analysis of power/drive systems*. eng, 1996.
- [50] S. D. Pekarek, O. Wasynczuk, E. A. Walters, J. V. Jatskevich, C. E. Lucas, Ning Wu, and P. T. Lamm, "An efficient multirate simulation technique for power-electronic-based systems," *IEEE Transactions on Power Systems*, vol. 19, no. 1, pp. 399–409, 2004, ISSN: 1558-0679. DOI: [10.1109/TPWRS.2003.821452](https://doi.org/10.1109/TPWRS.2003.821452).
- [51] F. A. Moreira, J. R. Marti, L. C. Zanetta, and L. R. Linares, "Multirate simulations with simultaneous-solution using direct integration methods in a partitioned network environment," *IEEE Transactions on Circuits and Systems I: Regular Papers*, vol. 53, no. 12, pp. 2765–2778, 2006.
- [52] T. Kato, K. Inoue, T. Fukutani, and Y. Kanda, "Multirate analysis method for a power electronic system by circuit partitioning," *IEEE Transactions on Power Electronics*, vol. 24, no. 12, pp. 2791–2802, 2009.
- [53] P. V. Kokotovic, R. E. O'Malley Jr, and P. Sannuti, "Singular perturbations and order reduction in control theory - an overview," *Automatica*, vol. 12, no. 2, pp. 123–132, 1976.

- [54] A. Davoudi, J. Jatskevich, P. L. Chapman, and A. Bidram, "Multi-resolution modeling of power electronics circuits using model-order reduction techniques," *IEEE Transactions on Circuits and Systems I: Regular Papers*, vol. 60, no. 3, pp. 810–823, 2013.
- [55] P. Krause, O. Wasynczuk, S. Sudhoff, and S. Pekarek, *Analysis of Electric Machinery and Drive Systems*, Third. Hoboken, New Jersey: John Wiley & Sons Inc., 2013.
- [56] R. H. Park, "Two-reaction theory of synchronous machines generalized method of analysis-part i," *Transactions of the American Institute of Electrical Engineers*, vol. 48, no. 3, pp. 716–727, 1929. DOI: [10.1109/T-AIEE.1929.5055275](https://doi.org/10.1109/T-AIEE.1929.5055275).
- [57] K. Yoshida, Y. Hita, and K. Kesamaru, "Eddy-current loss analysis in pm of surface-mounted-pm sm for electric vehicles," *IEEE Transactions on Magnetics*, vol. 36, no. 4, pp. 1941–1944, 2000. DOI: [10.1109/20.877827](https://doi.org/10.1109/20.877827).
- [58] S. Sudhoff, *Genetic Optimization System Engineering Toolbox 2.6*, 2014. [Online]. Available: <https://engineering.purdue.edu/ECE/Research/Areas/PEDS/>.
- [59] E. Clarke, *Circuit analysis of AC power systems; symmetrical and related components*. Wiley, 1943, vol. 1.
- [60] R. A. Minasian, "Power mosfet dynamic large-signal model," *IEE Proceedings I - Solid-State and Electron Devices*, vol. 130, no. 2, pp. 73–79, 1983. DOI: [10.1049/ip-i-1.1983.0018](https://doi.org/10.1049/ip-i-1.1983.0018).
- [61] Aloisi and Pierre, "Power MOSFET Transistors," in *Power Electronics Semiconductor Devices*. ISTE, 2010, pp. 1–56, ISBN: 9780470611494. DOI: [10.1002/9780470611494.ch1](https://doi.org/10.1002/9780470611494.ch1). [Online]. Available: <http://dx.doi.org/10.1002/9780470611494.ch1>.
- [62] W. Shockley, "The theory of p-n junctions in semiconductors and p-n junction transistors," *The Bell System Technical Journal*, vol. 28, no. 3, pp. 435–489, 1949, ISSN: 0005-8580. DOI: [10.1002/j.1538-7305.1949.tb03645.x](https://doi.org/10.1002/j.1538-7305.1949.tb03645.x).
- [63] J. Doke, *GRABIT*, version 2.3, 2007. [Online]. Available: <https://www.mathworks.com/matlabcentral/fileexchange/7173-grabit>, MATLABCentralFileExchange.
- [64] Chung-Wen Ho, A. Ruehli, and P. Brennan, "The modified nodal approach to network analysis," *IEEE Transactions on Circuits and Systems*, vol. 22, no. 6, pp. 504–509, 1975.
- [65] F. Lannutti, P. Nenzi, and M. Olivieri, "Klu sparse direct linear solver implementation into ngspice," in *Proceedings of the 19th International Conference Mixed Design of Integrated Circuits and Systems - MIXDES 2012*, 2012, pp. 69–73.

- [66] G. Hachtel, R. Brayton, and F. Gustavson, “The sparse tableau approach to network analysis and design,” *IEEE Transactions on Circuit Theory*, vol. 18, no. 1, pp. 101–113, 1971.
- [67] B. Park, J. Netha, M. C. Ferris, and C. L. DeMarco, “Sparse tableau approach for power system analysis and design,” in *2018 North American Power Symposium (NAPS)*, 2018, pp. 1–6.
- [68] P. Kokotović, H. K. Khalil, and J. O’reilly, *Singular perturbation methods in control: analysis and design*. SIAM, 1999.
- [69] X. Xu, R. M. Mathur, J. Jiang, G. J. Rogers, and P. Kundur, “Modeling of generators and their controls in power system simulations using singular perturbations,” *IEEE Transactions on Power Systems*, vol. 13, no. 1, pp. 109–114, 1998.

A. MNA-BASED SIMULATION OF THE ELECTRIC DRIVE SYSTEM

Circuit diagrams for the controller, inverter, machine cable and motor are shown in Figures A.1 through A.4. As shown in Figure A.1, SR flip-flops are used to establish a modulation scheme for the switches in the inverter. In Figure A.2, LTspice models for the resistor, capacitor, and inductor are used to lay out the inverter circuit model shown in Figure 3.6. The MOSFET model was established by wrapping capacitors, which represent the junction capacitances, around an LTspice VDMOS model.

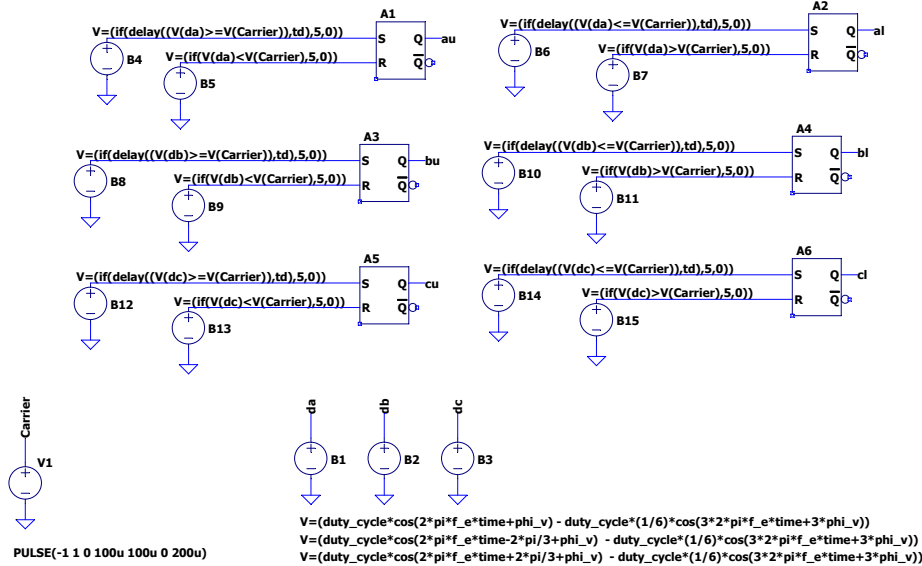


Figure A.1. LTspice implementation of the extended sine-triangle modulation strategy.

For the machine cable, the *a*- *b*- and *c*-phase cable connections are extracted from the WB model of the electric machine model illustrated in Figure 2.17. In particular, LTspice resistor, capacitor, and inductor models are used to model the line impedances as well as the line-to-ground parasitics. Also, the WB model of the machine is shown in Figure A.3. By using dependent voltage and current sources, a procedure for taking account of the low-

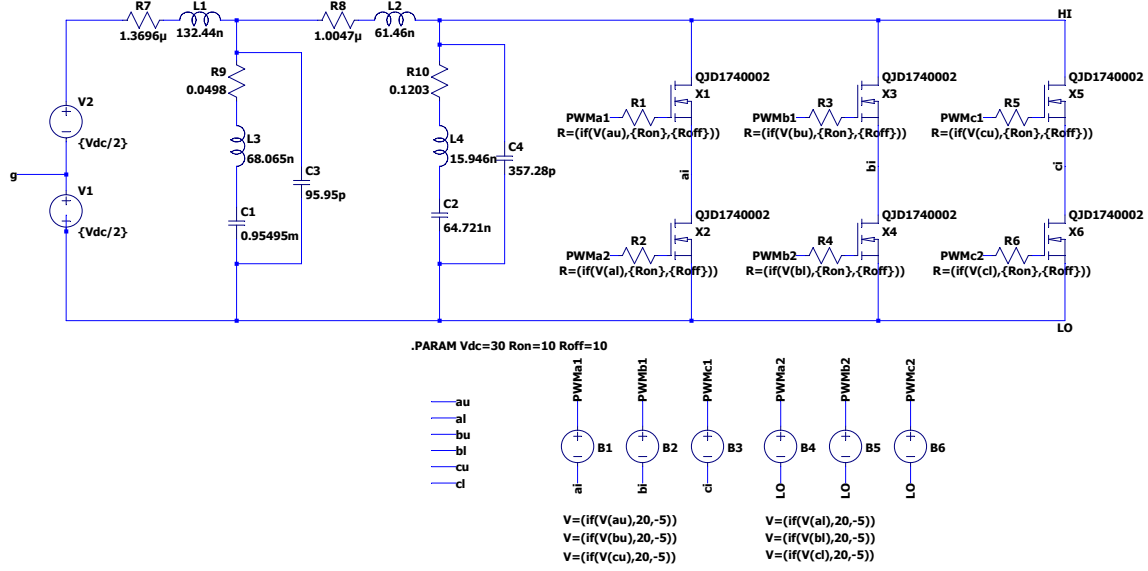


Figure A.2. LTspice circuit diagram of the inverter.

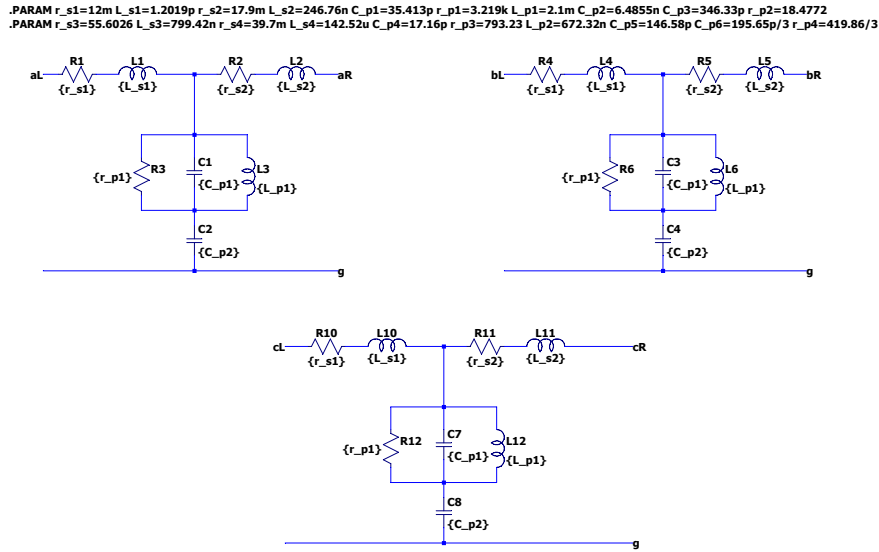


Figure A.3. LTspice circuit diagram of the machine cables.

frequency q - and d -axis equivalent circuits is implemented. The *qdmmodel* block may be set up by using custom-made blocks that mirror the standard constant, gain, integrator, and sum blocks of a state-space-based simulator.

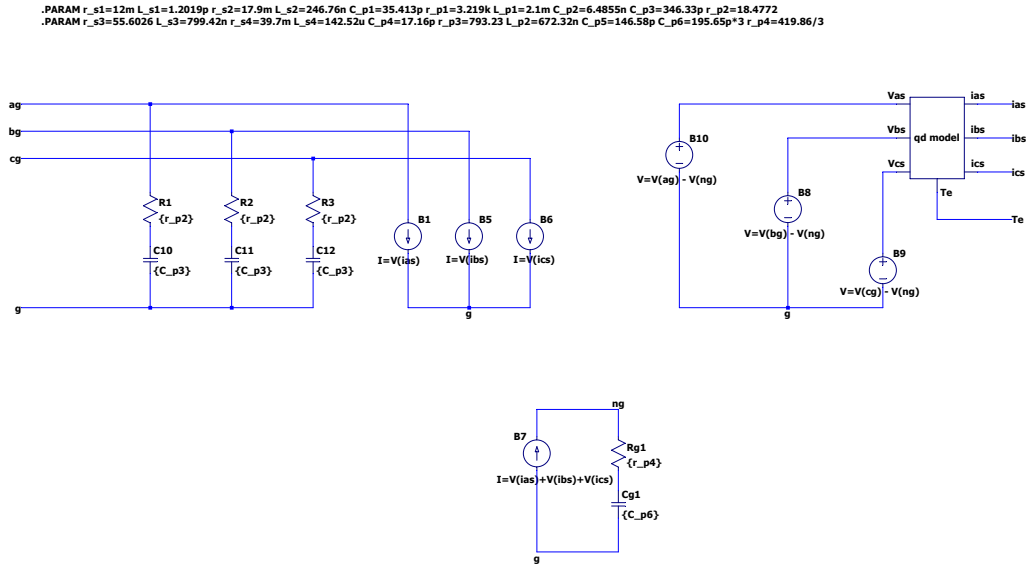


Figure A.4. LTSpice circuit diagram of the surface-mount PMAC machine.

VITA

Olatunji Fulani received a B.Sc.(Hons) degree in Electrical and Electronics Engineering from the University of Lagos, Nigeria, in the 2012/2013 academic session and the MSECE degree from Purdue University in 2017. He is currently pursuing his Ph.D. in Electrical and Computer Engineering at Purdue. His research interests include the modeling and analysis of power electronic and electric machine drive systems.